

Molecularly Distinct Sympathetic Populations Control Brown Adipose Tissue Functions

Daniele Neri

Submitted in partial fulfillment of the
requirements for the degree of
Doctor of Philosophy
under the Executive Committee
of the Graduate School of Arts and Sciences

COLUMBIA UNIVERSITY

2024

© 2024

Daniele Neri

All Rights Reserved

Abstract

Molecularly Distinct Sympathetic Populations Control Brown Adipose Tissue Functions

Daniele Neri

Brown adipose tissue (BAT) serves as a crucial thermogenic organ, extracting glucose and lipids from circulation to generate heat. Enhancing BAT activity holds potential as a therapy for treating metabolic diseases, such as obesity and diabetes. The sympathetic nervous system (SNS) is the main regulator of BAT activity by increasing extraction and oxidation of substrates. However, the SNS role in metabolic disorders is complex. In obesity, there is increased sympathetic tone, yet reduced BAT responsiveness.

Furthermore, increasing systemic sympathetic tone in individuals already at heightened cardiovascular risk leads to adverse complications, as demonstrated by recent clinical trials. As a result, BAT's impact on overall health in humans has been challenged in recent years, largely due to the lack of methods to selectively activate BAT without affecting other organs.

Here, I used chemogenetics and retrograde viral injections in the interscapular BAT (iBAT) of mice to selectively activate only the neurons projecting to this tissue. Targeted activation of BAT did increase thermogenesis and improved glucose homeostasis.

Leveraging on the single-cell RNA sequencing from our laboratory, we identified two sympathetic populations innervating iBAT: one primarily targets the small arterioles, while the other innervates the parenchyma. These populations mediate non-overlapping sympathetic-functions in iBAT: activating only the vascular projecting neurons lowers blood glucose without affecting thermogenesis, while activating the other population results in increased energy expenditure, local thermogenesis, and blood flow, with no effect on glycemia.

The findings from this work could pave the way to the development of targeted strategies against metabolic disorders characterized by hyperglycemia, highlighting the potential of selectively activating specific SNS components to normalize blood glucose levels.

Table of Contents

List of Charts, Graphs, Illustrations.....	viii
Acknowledgments.....	x
Dedication.....	xi
Chapter 1: Background and Introduction.....	1
The Sympathetic Nervous System.....	2
1.1.1 Development and Neuroanatomy of the SNS.....	3
1.1.2 SNS neurotransmitters.....	7
1.1.2.1 NE.....	7
1.1.2.2 NPY.....	8
1.1.2.3 ATP.....	9
1.1.2.4 Oxytocin.....	10
1.1.3 SNS receptors.....	10
1.1.3.1 Adrenergic receptors.....	10
1.1.3.2 NPY receptors.....	12
1.1.3.3 Purinergic receptors.....	13
1.1.4 SNS and blood glucose homeostasis.....	14
1.1.4.1 SNS regulation of the Pancreas.....	15
1.1.4.2 SNS regulation of the Liver.....	15
1.1.4.3 SNS regulation of adipose tissue and its role in insulin resistance.....	16
1.1.5 Evidence for different sympathetic populations.....	18

Brown Adipose Tissue.....	20
1.2.1 Differences between BAT and WAT.....	20
1.2.2 Brief history of BAT research.....	22
1.2.3 Anatomy of BAT and its depots in humans and rodents	24
1.2.4 Impact of BAT on metabolism	25
1.2.4.1 BAT impact on Energy Expenditure.....	26
1.2.4.2 BAT impact on glucose homeostasis	28
1.2.5 BAT as an endocrine organ.....	30
1.2.6 Role of vasculature in BAT function	32
SNS control of BAT.....	33
1.3.1 Evidence of sympathetic control of BAT activity	36
1.3.2 Sympathetic and Sensory cross-talk in BAT	41
1.3.3 Sympathetic control of vascular tone in BAT.....	43
Open questions in the field	45
Chapter 2: Rearing mice at 22°C programs increased capacity to respond to chronic exposure to cold but not high fat diet.....	48
Abstract.....	50
Introduction.....	51
Materials and Methods.....	53
1.3.4 Animals.....	53
1.3.5 Responses to cooling.....	53
1.3.6 Responses to HFD.....	54

1.3.7	Statistical analyses of CLAMS data (all experiments)	55
1.3.8	Glucose homeostasis	57
Results		57
1.4.1	Influence of rearing temperature on metabolic responses to a cold challenge	57
2.4.1.1	Effects on body composition	57
2.4.1.2	Effects on energy expenditure	58
2.4.1.3	Partitioning of total energy expenditure	58
1.4.2	Influence of rearing temperature on metabolic responses to HFD at thermoneutrality	60
2.4.2.1	Effects on body composition	61
2.4.2.2	Effects on glucose homeostasis	61
2.4.2.3	Effects on energy expenditure	61
2.4.2.4	Partitioning of total energy expenditure	62
Discussion		63
1.5.1	Rearing at 22°C enhances long-term adaptations to cold.	63
1.5.2	Distinguishing between effects on thermogenic capacity vs. defended body temperature.	64
1.5.3	Effects of rearing at 22°C on thermogenic responses to HFD change over time.	64
1.5.4	Rearing at 22°C has a modest, but protective, effect on glucose homeostasis.	65
1.5.5	Limitations	66
1.5.6	Summary and Future Research Questions	66
Author Contributions		67

Acknowledgements.....	67
Conflict of Interest	67
Data availability	68
Figures.....	69
1.6.1 Figure 5 Supplementary File.....	78
1.6.2 Figure 6 Supplementary File.....	84
1.6.3 Figure 7 Supplementary File.....	86
1.6.4 Figure 8 Supplementary File.....	89
Chapter 3: Measuring real-time temperature and blood flow changes in brown adipose tissue in anesthetized mice	91
Abstract.....	93
Introduction.....	94
Protocol.....	97
1.6.5 Anesthetic preparation	97
1.6.6 Set up the heatpad	98
1.6.7 Set up the thermocouple meter	99
1.6.8 Connect the thermocouple meter to a computer via a data acquisition system	99
1.6.9 Prepare the continuous perfusion of anesthetic	101
1.6.10 Prepare the animal for recording.....	103
1.6.11 Set up the recording	104
1.6.12 Set up the laser doppler imager.....	105
1.6.13 Experimental Recording	107
1.6.14 Collect and decode data	108

1.6.15	Data Analysis and Statistics.....	110
	Representative results	112
	Figures.....	113
	Discussion.....	120
	Author Contributions	122
Chapter 4: Identification and functional characterization of two distinct sympathetic neuronal populations regulating brown adipose tissue functions		
	Summary.....	125
	Introduction.....	125
	Results.....	127
1.6.16	Selective targeting of sympathetic nerves projecting to interscapular brown adipose tissue in mice	127
1.6.17	iBAT-projecting SNS acutely regulate blood glucose and metabolism, and increase local thermogenesis and blood flow	128
1.6.18	Characterization of subtypes of Stellate Ganglion neurons innervating distinct targets	129
1.6.19	The molecular signature of vasomotor neurons is not conserved across the Sympathetic chain.....	131
1.6.20	Cre-driver mouse lines confirm vascular projection of Npy ^{HI} Stellate Ganglion neurons	132
1.6.21	Two sympathetic subpopulations of neurons control complementary processes of iBAT physiology.....	133
	Discussion.....	134

Materials and Methods.....	136
1.7.1 Animals.....	136
1.7.2 Retrograde tracing with CTb	137
1.7.3 Virus injection.....	138
1.7.4 Temperature and Blood Flow Recordings	138
1.7.5 Dissociation of stellate ganglion neurons	140
1.7.6 Cell sorting.....	141
1.7.7 Plate-based scRNA sequencing of stellate ganglion neurons	142
1.7.8 Analysis of scRNA-Seq datasets	142
1.7.9 Metabolic cages	144
1.7.10 Oral Glucose Tolerance Tests.....	145
1.7.11 Immunofluorescence staining and counting	146
1.7.12 In Situ Hybridization.....	147
1.7.13 Imaging from Virus-injected mice.....	148
Figures.....	149
Supplementary Figures	159
Author Contributions	167
Competing Interest Statement.....	167
Chapter 5: Conclusion and future directions	168
Summary.....	169
Limitations	169
Impact and future steps	172
References.....	175

Appendix A.....	202
Transcriptomics and lipidomics on acutely activated mice iBAT	202
Methods.....	203
Figures.....	204
Appendix B.....	206
Systemic effects of sympathetic transmitters and peptides on glucose tolerance.....	206
Methods.....	207
Figures.....	209

List of Charts, Graphs, Illustrations

Figure 1. Anatomy of the Sympathetic Nervous System.....	4
Figure 2. Representative schematics of spinal nerve organization.	6
Figure 3: BAT depots distribution in humans.....	24
Figure 4: Schematics of different sympathetic innervation in blood vessels, WAT, and BAT....	34
Figure 5. Rearing temperature does not affect body weight and composition during a chronic cold challenge	71
Figure 6. Rearing temperature affects baseline glycemia in mice fed a high fat diet at 30°C.....	73
Figure 7. Rearing temperature programs lasting effects on metabolic responses to acute, but not chronic, feeding on high fat diet.	76
Figure 8. Rearing temperature influences short term adaptations to high fat diet feeding that dissipate with time	77
Figure 9. Schematics of the experimental setup	114
Figure 10. Drawing of probe placement in an experimental animal.....	115
Figure 11. Representative traces obtained with the set up.....	116
Figure 12. NE effects on Thermogenesis and Blood flow.....	117
Figure 13. CL effects on Thermogenesis and Blood flow.....	118
Figure 14. Effects of IP injection of Propranolol (PRP) 5 mg/kg following NE 0.5 mg/kg IP..	119
Figure 15. Selective targeting of the interscapular brown fat-projecting sympathetic neurons is achieved via Cre-lox system.	150

Figure 16. Figure 2: Acute chemogenetic activation of iBAT-projecting SNS neurons results in increased thermogenesis, blood flow, energy expenditure, decreased RER, and better glycemic profile in mice.	151
Figure 17. Identifying subpopulations of stellate ganglion neurons with scRNA-Seq.....	154
Figure 18. Validation of mouse Cre driver lines for the two sympathetic subpopulations.	155
Figure 19. High Npy expressing neurons target large arterioles in iBAT in mice and regulate glucose uptake, while low Npy expressing neurons target parenchyma in iBAT in mice and regulate thermogenesis and blood flow.	156
Figure 20. Comparison of retrolabeling efficiency between CTb, AAVrg, and MaCPNS1.	160
Figure 21. Average blood glucose curve under DCZ in Th-Cre mice expressing hM3D against Th-Cre mice injected with a control virus.	161
Figure 22. Strategy for scRNA-Seq in conjunction with retrograde tracing.	162
Figure 23. Expression of stellate cluster markers in mouse superior cervical and mouse celiac ganglia.....	163
Figure 24. Developmental expression of Cre observed in Vmat1-Cre::tdTomato mice.	165
Figure 25. Coexpression of Vmat1 and Rxfp1 in iBAT projecting neurons fom scRNASeq....	166
Figure 26. Transcriptomic analysis of chemogenetically activated iBAT-projecting sympathetic nerves reveals metabolic activation in iBAT	204
Figure 27. Lipidomics analysis suggests iBAT involvement with circulating TGs clearance and different lipid metabolism based on sex	205
Figure 28. OGTTs on mice under stimulation of adrenergic-related peptides	209
Figure 29. OGTTs using combinations of adrenergic transmitters and adrenergic-related receptor antagonists.....	210

Acknowledgments

I am deeply grateful to my advisor, Lori Zeltser, for her invaluable guidance, support, knowledge, and wisdom throughout my PhD journey. I also thank Anthony Ferrante for his steady support and Joerg Heeren for his vital contributions to the lipidomics analysis. I am grateful to Dave Sulzer, Sabrina Diano, and Gary Schwartz for the stimulating discussions that enriched my research.

Special thanks to my Zeltser lab colleagues, particularly Alexis Fohn, Angela Maria Ramos Lobo, and Natalia Bobba, for their camaraderie and collaboration. I am also indebted to the NMB PhD staff and support team, especially Zachary Corter, Charmain Watson, and Bernadette Spina, for their assistance along the way.

To my friends Kunheng Cai, Pedro Javier Del Rivero Morfin, Chrystal Mavros, Luca Milani, and Alessandro Gorini—your friendship has been invaluable.

I am profoundly grateful to my wife, Maddie, my greatest supporter and biggest fan, and my cat, Cacio, who kept me grounded.

Lastly, I dedicate this work to my parents, Sandro and Lucia, whose unwavering support made this possible, and to my extended family—Francesco, Barbara, Matteo, my great-uncle Graziano, my grandma Lidia, zia Simona, Cristian, and Francesco—whose encouragement I cherish deeply.

Dedication

To my beloved grandma Lina, and my great-aunts Maria and Rosa. Though you are no longer here, your unwavering support and encouragement through even the most challenging moments will forever be with me. This work is a testament to your enduring love and belief in my journey.

Chapter 1: Background and Introduction

The Sympathetic Nervous System

The Sympathetic Nervous System (SNS) is one of the branches of the Autonomic Nervous System (ANS), along with the Parasympathetic Nervous System (PNS) and the Enteric Nervous System (ENS). The ANS is involved in regulating several body functions and adaptive responses that we do not consciously control, such as heart rate and function, gut motility, blood pressure, body temperature, immune response, and breathing. As such, the primary function of the ANS is to ensure whole-body homeostasis and the survival of the organism^{5,6}.

The SNS and PNS innervate most peripheral organs, exerting antagonistic effects on their downstream targets. The SNS is activated in catabolic states, such as arousal and metabolic activation: increased sympathetic activity generally leads to an increased heart and respiration rate, increased blood pressure, energy expenditure, body temperature, lipolysis, glycemia, and nutrient utilization. On the other hand, the PNS is involved in postprandial and relaxed states, often referred to as “rest and digest”⁷. Some authors refer to SNS activity as the “fight or flight” response⁸. However, although the SNS is active during stressful and threatening events, and all the processes mentioned above can be interpreted as preparing the body to perform a particularly energy-demanding task (such as fighting or running), the “fight or flight” concept was formulated at a time when sympathetic and adrenomedullary activity were thought to function as a single unit and to be strictly active during stressful events⁹. Simply put, there was no functional difference between the hypothalamic-pituitary-adrenocortical (HPA) axis and the whole SNS at that time. Although the SNS is recruited during life-threatening events, we now know that the SNS has a basal tone and it shows adaptive responses to many non-life-threatening challenges (such as mild cold environments or post-prandial thermogenesis)¹⁰. As such, the term “fight or flight” reflects only a small portion of the processes in which the SNS is involved.

1.1.1 Development and Neuroanatomy of the SNS

The components of the ANS share a common origin from neural crest cells. These cells originate during early embryonic development in vertebrates, arising from the edges of the neural plate. After the formation of the neural tube and the notochord, neural crest cells continue forming in the dorsolateral portion of the neural tube, from where they start migrating to the periphery, differentiating into various types of SNS neurons and glial cells. The mechanisms behind lineage determination and differentiation are quite complex and they have been extensively reviewed by other authors¹¹, and they are not the primary focus of this introduction.

Neural crest cells that migrate ventrally, toward the forming aorta, differentiate into ganglionic sympathetic neurons. These neurons start expressing typical markers of these cells, such as tyrosine hydroxylase (TH) and dopamine β -hydroxylase (DBH)^{12,13}, and they aggregate in paravertebral ganglia.

The SNS is organized in a two-order model: first order neurons, residing in the spinal cord, and second order neurons, which are grouped in paravertebral ganglia along the trunk. First order neurons are generally referred to as pre-ganglionic, while second order neurons are called ganglionic or post-ganglionic. Pre-ganglionic neurons are located in the intermediolateral (IML) nucleus of the spinal cord, which, in vertebrates, extends throughout the thoracic portion of the cord up until the upper lumbar section (L2 or L3 are generally considered the maximal extension). Sympathetic ganglia are located next to the vertebral column, hence the name “paravertebral”, and they usually take the name from the closest vertebra (e.g., T1 from the first thoracic vertebra). There are some exceptions to this nomenclature, such as for the three cervical ganglia (superior, middle, and inferior cervical ganglia), the stellate ganglion (SG) and the

abdominal ganglia (such as the coeliac ganglion) (Figure 1). As such, sympathetic ganglia extend from the cervical portion of the trunk, up to the lumbar section⁴.

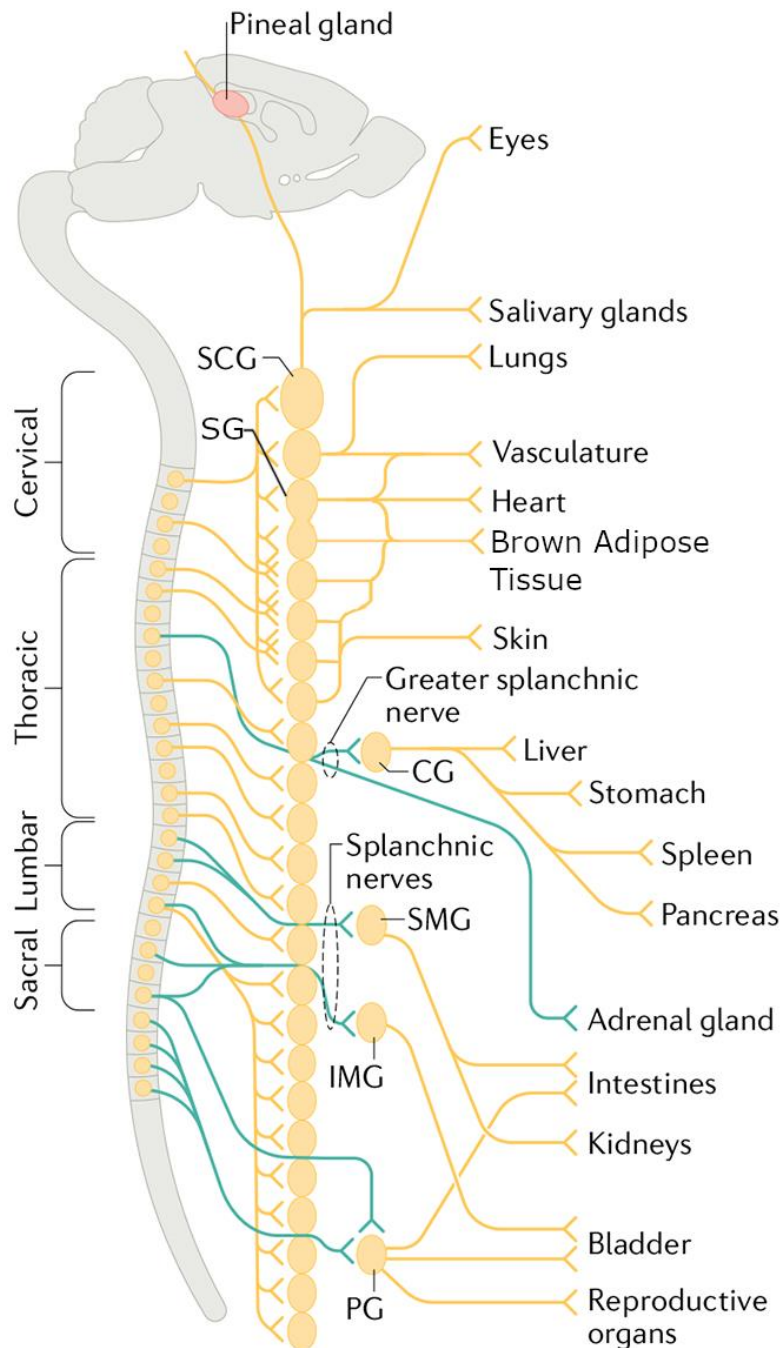


Figure 1. Anatomy of the Sympathetic Nervous System

Adapted from⁴. SCG: superior cervical ganglion, SG: stellate ganglion, CG: coeliac ganglion, SMG: superior mesenteric ganglion, IMG: inferior mesenteric ganglion, PG: pelvic ganglion.

Pre- and post- ganglionic neurons present several differences, both morphological and neurochemical. Pre-ganglionic neurons have short, myelinated axons that are collected in nerves exiting the spine from the ventral root, joining the nerves from the dorsal root to form the spinal nerve. Sympathetic axons then leave the spinal nerves to contact the ganglionic neurons through the white rami communicantes. Ganglionic neurons send their unmyelinated axons back to the spinal nerves via the grey rami communicantes, and these axons travel along motor and sensory nerves until they reach their final targets¹⁴ (Figure 2). Sympathetic ganglia are interconnected along the rostral-caudal axis by the sympathetic trunk, forming a structure referred to as the “sympathetic chain”. Due to the interconnected nature of the sympathetic chain, it is not uncommon for pre- and post-ganglionic axons to travel up or down the chain before looping back into the spinal nerves. As such, target organs are generally innervated by ensembles of ganglionic neurons whose somas reside in different neighboring ganglia, rather than in a single ganglion. Despite the interconnected nature of this system, each ganglionic neuron sends its axon exclusively to one target organ, as demonstrated by several tracing studies¹⁵⁻¹⁷.

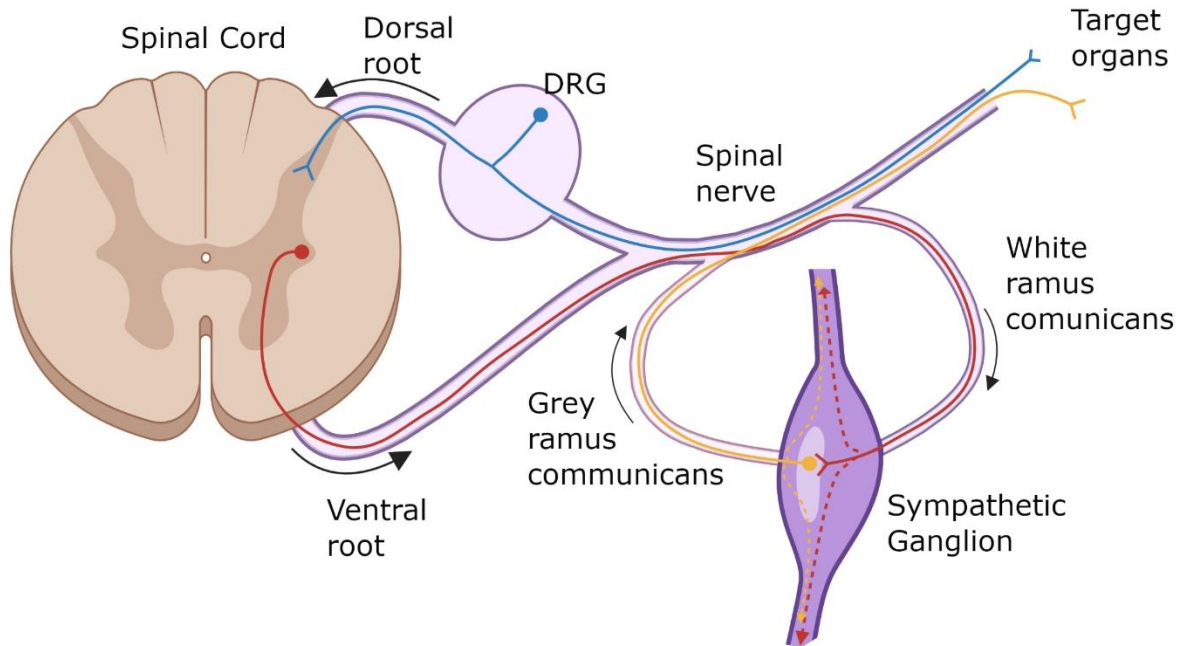


Figure 2. Representative schematics of spinal nerve organization.

DRG: Dorsal root ganglion. The sensory neuron is represented in blue, pre-ganglionic sympathetic neuron in red, and post-ganglionic neuron in yellow. Dashed lines represent the possibility for pre- and post-ganglionic neurons to travel up and down the sympathetic chain before forming a synapse or leaving the ganglion, respectively. Created with BioRender

The main neurotransmitter released by pre-ganglionic sympathetic neurons is acetylcholine (ACh), which stimulates the post-ganglionic neurons via nicotinic cholinergic receptors (nAChRs)¹⁸. Post-ganglionic neurons predominantly release norepinephrine (NE). In some cases, such as the neurons innervating sweat glands, adrenergic neurons switch to a cholinergic nature, and a small number of cholinergic neurons are observed within sympathetic ganglia^{19,20}. Finally, sympathetic nerves do not form the typical synaptic structure we are used to seeing in the Central Nervous System (CNS), which is composed of a presynaptic terminal, a synaptic cleft of approximately 20 nm²¹, and a post-synaptic structure called a dendrite. Instead, a single axon, once it reaches the target organ, can have hundreds of bulbous structures called

“varicosities”, positioned in series along the axon, from which neurotransmitters are released into the interstitial space²². The distance between a varicosity and its target can vary a lot in different organs, spanning from 20 nm up to 500 nm²³. There is no clear hypothesis as to why the SNS has this type of non-synaptic structure. However, Geoffrey Burnstock proposed that cleft size determines the degree of neuromodulation exerted by sympathetic co-transmitters²⁴.

1.1.2 SNS neurotransmitters

Most sympathetic ganglionic neurons are considered adrenergic due to their release of NE. However, they also release co-transmitters such as neuropeptide Y (NPY) and adenosine triphosphate (ATP)²⁵. Co-transmitters have generally been considered modulators of NE activity, increasing or decreasing NE effect on target cells based on different combinations of membrane receptors expressed. Although there is evidence of direct action by sympathetic co-transmitters that are non-adrenergic and non-cholinergic (NANC)²⁶, these neurotransmitters are either colocalized with NE in presynaptic vesicles (ATP) or always co-released with NE (NPY)²⁷. As such, they cannot be considered independent transmitters in the context of sympathetic transmission. A very small proportion of ganglionic neurons are cholinergic. Although proportions reported by different authors vary slightly, it is generally believed that at least 90% of ganglionic neurons are adrenergic, and cholinergic neurons make up around 5% of the ganglionic population (reviewed in ²⁸).

1.1.2.1 NE

NE is an endogenous catecholamine, along with dopamine (DA), and epinephrine (EPI). NE synthesis begins with the conversion of tyrosine to dihydroxyphenylalanine (DOPA) by TH, which is the rate-limiting step in NE production. DOPA is then processed by DOPA

decarboxylase into DA, and finally DBH catalyzes the conversion of DA to NE. In chromaffin cells, located in the adrenal medulla, and in some neurons of the brainstem, phenylethanolamine-N-methyltransferase (PNMT) converts NE to EPI. No sympathetic neurons in the paravertebral ganglia have shown expression of PNMT. As such, EPI secretion is mostly restricted to adrenal activation.

TH and DBH are the most used markers to measure sympathetic innervation in a tissue²⁹ and they are traditionally considered sympathetic markers. It should be noted that TH is also expressed in dopaminergic neurons, as it is necessary for DA production, and that DA is stored in large vesicles within sympathetic presynaptic terminals. However, the general consensus is that these vesicles are pools of substrates waiting to be converted to NE by DBH, and sympathetic DA release occurs as a result of NE depletion during prolonged stimulation, when DBH conversion struggles to match the depletion rate³⁰. Therefore, DA is not considered a sympathetic neurotransmitter.

NE is stored in small vesicles near the plasma membrane of varicosities by vesicular monoamine transporter 2 (VMAT2 or SLC18A2)³¹. Once released, NE is quickly removed from the interstitial space either through metabolization by monoamine oxidase (MAO) or reuptake into sympathetic neurons via the NE transporter (NET).

1.1.2.2 NPY

NPY is a small neuropeptide (36 aminoacids) that is synthesized and stored in large, core-dense vesicles by neurons and co-released with NE. NPY is expressed by a large subset of adrenergic neurons, and the proportion of NPY-positive neurons varies across developmental stages and anatomical locations³². In mice, 60% of neurons in thoracic ganglia express NPY during embryonic development, but this percentage drops to 40% during the first three weeks post-

partum. In abdominal ganglia, ~90% of neurons are NPY-positive, with no age-associated variations. Other authors have reported a similar proportion in the SG of rats, although they observed an opposite age effect³³. Nonetheless, it is safe to assume that ~50% of thoracic ganglionic neurons co-express NPY and NE. The storage in large vesicles, as opposed to the NE-loaded small vesicles, could be related to different release dynamics: NPY release is primarily observed during prolonged sympathetic stimulations³⁴.

NPY has been extensively studied in the context of the CNS due to its orexigenic effects on food intake by neurons from arcuate nucleus of the hypothalamus³⁵. However, the role of central NPY seems to be completely separated from the role of peripheral SNS-derived NPY. Peripheral NPY is considered a vasoconstrictor, and it is involved in three mechanisms: direct vasoconstriction, modulation of NE-induced vasoconstriction (via receptors on target cells), and negative feedback on NE release by SNS (via autoreceptors on sympathetic axons)³⁶⁻³⁸. There is anatomical evidence showing that NPY-positive sympathetic nerves are more abundant around blood vessels, especially those of smaller diameter³⁹, suggesting an important role for SNS-derived co-release of NPY and NE in regulating arteriolar blood flow.

1.1.2.3 ATP

ATP neurotransmission in autonomic nerves was first described in the mid-60s as NANC. It was only a few years later that the neurotransmitter responsible for NANC was identified as ATP⁴⁰. Following this discovery, ATP transmission was renamed “purinergic transmission”⁴¹. ATP is also one of the first co-transmitters ever discovered, as it was observed to be co-released with NE from sympathetic nerves. In the SNS, ATP is co-stored with NE in small vesicles, ready to be released. However, ATP has also been observed as co-transmitter in other branches of the ANS⁴². In the context of SNS, ATP is a fast-acting, early-onset vasoconstrictor. Upon release

from SNS vesicles, ATP acts first on smooth muscle cells (SMCs) with a rapid contraction, while NE works at a relatively slower pace, with a gradual, but more persistent contraction. Extracellular ATP is quickly processed by ectoATPases, and the metabolites are either taken up by neurons or spilled into circulation.

1.1.2.4 Oxytocin

A recent study from Rosen group has shown the presence of a small population of oxytocinergic sympathetic neurons that innervate adipose tissue in mice⁴³. In this paper, the authors demonstrate that oxytocin (OXT) from sympathetic neurons increases lipolysis in adipose tissue through an enzymatic cascade that is distinct from the NE-induced cascade. This study is the first to identify the presence of sympathetic oxytocinergic neurons, raising the possibility that many other neuronal populations remain to be discovered within the SNS.

1.1.3 SNS receptors

NE can have a wide array of effects on target organs, ranging from constriction to relaxation. This is because the effects of NE are mediated by its receptors, known as adrenergic receptors (ARs). Each ARs activation has its own downstream effects, and cells can express one or more ARs in different proportions, resulting in the variety of NE-induced effects observed.

1.1.3.1 Adrenergic receptors

There are five different types of adrenergic receptors: α_1 , α_2 , β_1 , β_2 , and β_3 . ARs are all G-protein coupled receptors (GPCRs), although different types associate with different G proteins⁴⁴.

α_1 is expressed by SMC on blood vessels, and its activation results in vasoconstriction and increase in blood pressure. Upon binding to NE, the receptor couples with G_{α_q} protein, activating phospholipase C (PLC), which then cleaves phosphatidylinositol 4,5-bisphosphate (PIP2),

increasing the levels of inositol triphosphate (IP3) and diacylglycerol (DAG). Finally, IP3 opens the intracellular Ca^{2+} channels from the endoplasmic reticulum, resulting in increased Ca^{2+} levels, which leads to contraction in SMCs⁴⁵. α_1 is also expressed in brown adipocytes, where it has been shown to have an important role in promoting thermogenesis⁴⁶.

α_2 is coupled to the $G_{i/o}$ protein, and its activation results in reduction in cyclic adenosine monophosphate (cAMP) levels, which leads to a decrease in intracellular Ca^{2+} levels. α_2 receptors can be autoreceptors, and they are expressed on the varicosities of sympathetic neurons. As such, activation of α_2 results in suppression of sympathetic activity and a lowering of blood pressure as a consequence⁴⁷. These receptors are also expressed by β cells in pancreas, and their activation results in suppression of insulin release⁴⁸. Finally, adipocytes also express α_2 ARs, and their activation leads to inhibition of lipolysis.

β_1 ARs are highly expressed in cardiac tissue, coupled with $G_{s\alpha}$, and their activation results in increased cAMP levels, which ultimately leads to increased intracellular Ca^{2+} levels. β_1 stimulation results in positive inotropism (increased contractility) and chronotropism (increase heart rate)⁴⁹, which can lead to increased blood pressure. β_1 antagonism is a common pharmacological therapy for the treatment of hypertension⁵⁰. Importantly, β_1 is also expressed in adipocytes, where their activation results in increased lipolysis⁵¹.

β_2 ARs are mostly expressed by SMCs, similarly to α_1 . However, their activation results in relaxation, leading to vasodilation, increased perfusion, and lowering of blood pressure. In lungs, β_2 mediates bronchodilation, and it is a pharmacological target for the treatment of asthma⁵². Similarly to the α and β opposition in SMCs, β_2 stimulation in pancreatic β cells results in increased glucose-dependent insulin secretion⁵³.

Finally, β_3 is expressed in brown and beige adipocytes, in certain myocytes like cardiomyocytes⁵⁴, the detrusor muscle of the urinary bladder⁵⁵, and in endothelial cells (ECs) in tissues like coronary micro-arteries in humans⁵⁶. In myocytes, β_3 activation generally induces relaxation, leading to reduced cardiac contractility⁵⁷ and increased bladder capacity⁵⁵. In ECs, β_3 activation promotes vasodilation⁵⁶. For adipocytes, activation results in increased lipolysis, thermogenesis, energy expenditure, and browning of the tissue⁵⁸. β_3 agonists produce robust weight loss in rodent preclinical models, and are among the most sought-after targets for treatment of metabolic diseases⁵⁹. However, results on humans have not recapitulated those obtained in rodents, and further studies are necessary to determine to what extent we can stimulate this family of receptors before facing negative off-site effects due to excessive adrenergic stimulation⁶⁰.

These different ARs show both different affinities for NE and EPI, and different sensitivity to NE. Both α_2 and β_2 show higher affinity for EPI, whereas other receptors have greater affinity for NE. Among the β ARs, β_3 seems to be activated at higher concentrations of catecholamines compared to the other two types, indicating that β_3 is more likely to be active during prolonged sympathetic activity, while other receptors will undergo through desensitization⁶¹. This characteristic could be due to the lack of some aminoacidic residues mediating receptor desensitization, which are present on β_1 and β_2 ^{62,63}.

1.1.3.2 NPY receptors

NPY receptors (NPYRs) have been extensively studied in the context of the CNS, given their fundamental role as neurotransmitters in regulating energy and glucose homeostasis via hypothalamic circuits⁶⁴. However, their role in the periphery has remained relatively underexplored. NPY has five known receptors: Y1, Y2, Y4, Y5, and y6⁶⁵. Y1 and Y2 are the

most highly expressed receptors in this family, and, in the periphery, they can be found on both skeletal and smooth muscle cells⁶⁶, adipose tissue⁶⁷, liver, and pancreas⁶⁸, indicating a role in regulating energy metabolism beyond their CNS effects. These receptors are all GPCRs, with G_i as their G protein companion. As such, NPYR activation results in a reduction of cAMP levels⁶⁹, which leads to increased PLC activity and increased intracellular Ca²⁺ levels, inducing contractions in muscle cells. In SMCs, NPYRs enhance ARs-induced vasoconstriction by increasing PLC activity and, consequently, intracellular Ca²⁺ levels further. NPYR activation on sympathetic varicosities, however, leads to suppression of NE release⁷⁰, although the molecular mechanisms have not been fully elucidated. The role of non-vascular NPYRs in the periphery and their impact on energy metabolism is still under debate. Some authors suggest that antagonizing NPYRs can be protective against metabolic diseases⁷¹, whereas others have reported that SNS-derived NPY is fundamental for the optimal regulation of whole-body glucose balance³².

1.1.3.3 Purinergic receptors

ATP receptors are grouped into two families: P2X, which are ligand-gated ion channel receptors, and P2Y, which are GPCRs⁴². P2Xs are generally expressed on SMCs and on neurons, both in CNS and ANS. P2Ys are expressed on endothelial, epithelial, and immune cells; however, there is evidence of P2Ys expression in some adrenergic spinal neurons⁷², where they serve as autoreceptors, and their activation decreases NE release. P2Xs are considered to be the main purinergic receptors involved in fast neurotransmission, and the primary effector of the fast initial contraction during the early phase upon SNS release of NE and ATP on SMCs²⁵, as they directly increase intracellular cation concentrations like Na⁺ and Ca²⁺. ANS terminals also

express P1 receptors, which are activated by adenosine. This mechanism is postulated to be a feedback loop in the ANS to regulate blood pressure: after ectoATPases process ATP to adenosine, P1 presynaptic receptors are activated, producing opposite effects on different aspects of the ANS. On the SNS, P1 activation results in suppression of neuronal activity. Conversely, P1 activation on sensory neurons, such as those in the Nucleus of the Solitary Tract (NTS), causes neuronal excitation, ultimately leading to a reduction in SNS activity⁷³.

1.1.4 SNS and blood glucose homeostasis

Glucose concentration in blood (glycemia) homeostasis is a tightly regulated balance fundamental to survival. Although oscillations in glycemia are normal and physiological in the context of circadian rhythms and daily life routines, such as postprandial increases or decreases during physical activity, chronic and uncontrolled variations can have catastrophic consequences. Chronic low blood glucose (hypoglycemia) prevents organs from functioning properly, and in severe cases, it can lead to death. On the other side of the spectrum, chronic high blood glucose (hyperglycemia) can lead to dysfunction of the cardiovascular system, kidneys, blindness, and peripheral neuronal damage (neuropathy)⁷⁴.

Two of the most important organs in regulating glycemia in mammals are the pancreas, via the secretion of insulin and glucagon, and the liver. The most well-known mechanism is glucose-sensitive insulin secretion (GSIS). Briefly, high levels of glucose in the blood are directly detected by β cells within Langerhans islets in the pancreas, which undergo depolarization, releasing insulin into the bloodstream. Insulin will then instruct all the other organs in the body to extract glucose from circulation, restoring normal glucose levels (euglycemia). Under this paradigm, there is no role for the nervous system. However, as we will soon discuss, both pancreatic Langerhans islets and the organs involved in the insulin response receive dense

sympathetic innervation that can strongly influence their function, impacting on blood glucose levels. The involvement of the SNS in glucose balance is not restricted to β cells modulation. We will explore the insulin-independent effects of SNS in liver and adipose tissue and their repercussions on systemic blood glucose levels later on.

1.1.4.1 SNS regulation of the Pancreas

Both the PNS and the SNS innervate the Langerhans islets, and as expected, their activities has opposite effects. SNS innervation of the pancreas originates from the CG and the SMG⁷⁵. NE release from SNS acts primarily on α_2 ARs on β cells, suppressing insulin release⁷⁶. At the same time, NE stimulates α cells to produce glucagon, mainly via β_2 AR stimulation⁷⁷, but also, to a lesser extent, via α ARs⁷⁸. Some authors have reported that β_2 AR stimulation on β cells potentiates GSIS⁷⁹. However, it seems that the effects of α_2 ARs override the positive effects of β_2 ARs on insulin secretion, as stimulation of the pancreas-projecting nerves results in a reduction in circulating insulin levels⁸⁰, and stimulation of the upstream CNS circuits controlling those nerves have the same effects¹⁶. Ultimately, SNS stimulation of pancreas results in hyperglycemia by reducing insulin secretion and increasing glucagon production.

1.1.4.2 SNS regulation of the Liver

The liver is the organ that stores the largest quantity of glucose in the body as glycogen. During hypoglycemia, the liver breaks down glycogen into glucose molecules (glycogenolysis) and generates new glucose molecules from precursors via gluconeogenesis, releasing them in the blood stream to replenish physiological glucose levels⁸¹. During hyperglycemia, the liver takes glucose from circulation to store it as glycogen⁸². SNS activity on liver function presents many similarities to what we have just seen in the pancreas. Sympathetic innervation of hepatic tissues originates from the CG and the SMG⁸³, and increased sympathetic activity in the liver results in

hyperglycemia via enhanced hepatic glucose production by stimulating glycogenolysis and gluconeogenesis⁸⁴, primarily through the activation of α_1 and β_2 ARs⁸⁵. Many of the hyperglycemic effects of SNS on liver function are also synergized by the SNS-induced effects on the pancreas we previously discussed, such as increased levels of glucagon, which independently promote increased hepatic glucose production.

1.1.4.3 SNS regulation of adipose tissue and its role in insulin resistance

SNS abundantly innervates adipose tissue (AT), both white⁸⁶ (WAT) and brown¹⁵ (BAT). Contrary to many other peripheral organs, AT does not receive any innervation from the PNS⁸⁷. Sympathetic stimulation of AT leads to increased lipolysis through ARs. While other factors can induce lipolysis in AT, the SNS is the primary and strongest initiator of this process⁸⁸. Further studies on adipocytes have shown that β_1 and β_3 ARs increase lipolysis, while α_2 decreases lipolysis⁸⁹. Thus, although SNS stimulation of AT generally results in increased lipolysis, the degree of this process can change between depots according to the relative expression of α_2 vs β ARs. Stimulation of β ARs in adipocytes results in $G_{s\alpha}$ activation, increasing of cAMP levels, activation of protein kinase A (PKA), which ultimately phosphorylates and activates hormone sensitive lipase (HSL), a neutral lipase and a critical enzyme involved in lipolysis, as well as perilipin 1, a regulator of neutral lipase activity, especially that of adipose triglyceride lipase (ATGL). In BAT, where β_3 ARs are abundantly expressed by brown adipocytes, NE stimulation leads to uptake of glucose and fatty acids from circulation and increased fatty acid oxidation due to this specific type of AR^{90,91}. Insulin and NPY both reduce lipolysis in adipocytes via their respective receptors⁹².

There is a positive association between AT lipolysis and insulin resistance in obese patients⁹³, although sensitivity to NE-induced lipolysis is reduced as well in obesity⁹⁴. The exact

mechanisms behind this process are still unclear. The working hypothesis is that SNS activity is increased during weight gain to balance excessive caloric intake. However, this results in increased lipolysis and high levels of circulating free fatty acids (FFAs). These FFAs accumulate in the liver and other insulin-responsive tissues (ectopic lipid accumulation), disrupting physiological insulin receptor function through multiple mechanisms and causing insulin resistance⁹⁵. Reduction of AT lipolysis in obese mice partially rescues insulin sensitivity⁹⁶. Increased SNS activity in obesity can also be caused through other circuits. Both WAT and BAT are endocrine organs, with their respective adipocytes releasing adipokines or batokines, respectively. These molecules have been shown to have a wide plethora of paracrine and endocrine effects both on CNS and other peripheral organs. As such, AT influence on systemic metabolism goes beyond the management of lipid storage. The most famous adipose-secrete hormone is leptin, which is secreted by white adipocytes in proportional levels to total fat mass⁹⁷. Leptin acts on a wide range of targets, with the most widely described circuit being the arcuate nucleus of the hypothalamus, where two groups of neurons express leptin receptors and have opposite responses to its activation and their downstream target. Briefly, an increase in leptin levels signals the brain to increase energy expenditure and reduce food intake. The increase in energy expenditure is achieved in part via activation of the SNS, as neurons in the CNS circuit controlling thermogenesis express leptin receptors^{98,99}. However, during chronic overfeeding, such as in obesity, leptin resistance is established, leading to permanent weight gain even in presence of high levels of plasma leptin. Interestingly, some authors have proposed a “selective leptin resistance” theory, whereby the CNS circuits that control SNS activity are not desensitized, and adrenergic activity remains elevated even after leptin resistance is established¹⁰⁰, sustaining unrestrained lipolysis.

The picture drawn from these results is the typical patient affected by metabolic syndrome: high level of plasma FFA and triglycerides, insulin resistance or type 2 diabetes (T2D), increased sympathetic activity, which ultimately leads to increased cardiovascular risk. However, as we have discussed earlier, SNS activity on AT is necessary for the correct functioning of these tissues in healthy patients. As such, therapeutic targets should try to modulate SNS outflow to specific targets rather than completely suppress it, since downregulation of this system can lead to other negative side effects. In the next chapters, we will explore the relationship between SNS and BAT, and how selective increase in sympathetic activity can lead to several health benefits.

1.1.5 Evidence for different sympathetic populations

We have discussed the complexity of SNS-mediated effects, and how the response to sympathetic activity depends on receptor expression, temporal dynamics, and interaction with co-transmitters or other hormonal signals. This view, however, assumes that SNS activity is generally uniform, as if, once the sympathetic neurons are engaged, the determinants of the target response rely solely on the receptors present beyond the sympathetic varicosities. This viewpoint only provides a partial understanding, as the existence of different sympathetic subpopulations and their proportions can further complicate SNS-mediated effects.

We have already noted that approximately half of the ganglionic sympathetic neurons express NPY, and how these NPY-positive sympathetic neurons preferentially innervate the vasculature, suggesting a specific role for this NPY+NE secreting neurons. Moreover, we have presented recent highlighting a small population of oxytocinergic sympathetic neurons that enhance lipolysis in WAT. To gain a better understanding of whether ganglionic sympathetic neurons are composed of different subgroups, we must examine recent transcriptomic analysis.

Single cell sequencing (scSeq) is a relatively recent technique that enables the measurement of gene expression at a cellular level within tissue¹⁰¹. When combined with linear algebra calculations, this technique has facilitated the discovery of numerous new cell types across virtually all tissues. scSeq, and its variation single nuclei sequencing (snSeq), have been extensively used in the CNS, uncovering hundreds of new neuronal groups¹⁰², which have led to deeper understanding of behavioral processes¹⁰³ and development of new treatments¹⁰⁴. However, the ANS has lagged behind in this area. To date, most peripheral sequencing efforts have been directed toward the Sensory Nervous System (see ¹⁰⁵ for a comprehensive list). Nonetheless, there have been a few but significant studies focused on the SNS. In 2016, the Linnarson group performed single cell sequencing on mouse sympathetic ganglia¹⁰⁶, identifying five noradrenergic and two cholinergic clusters, with cholinergic neurons account for less than 10% of the SNS neurons. Although this was a great breakthrough in identifying sympathetic subpopulations, it is essential to note that the authors grouped sympathetic ganglia from different levels of the chain, potentially losing valuable information about spatial specificity. More recently, Ajjola's group sequenced mouse SG neurons, focusing on neurons that innervate heart vs forelimbs¹⁰⁷. Their results partially overlap those presented Linnarson's group, revealing the presence of clusters of neurons characterized by high vs low expression of *Npy* (NPY^{HI} and NPY^{LO}), suggesting that low-level stimulation of the heart is mediated by NPY^{LO} neurons, and NPY^{HI} neurons are recruited upon higher stimulation to induce maximal positive inotropism and chronotropism. Additional sequencings on sympathetic ganglia have been conducted^{108,109}, including analysis of human samples¹¹⁰. However, in these three studies, no specific investigation of SNS subclusters was carried out, as that was not their primary objective.

There is substantial evidence supporting the existence of SNS subpopulations; however, information regarding their functional roles remains largely elusive. The only study to investigate these roles is the one conducted by Ajijola's group, which focused solely on cardiac function. One of the primary challenges in studying these populations is the absence of specific markers that would allow molecular access to them. While NPY is often cited, it cannot serve as a reliable marker, as it is also expressed by other sympathetic neurons, albeit at lower levels¹⁰⁷. In the research I will present, I leveraged single cell sequencing of mouse SG performed by Seo Eun Lee, a former PhD student in our lab, to identify reliable markers for vasculature-projecting SNS in the interscapular BAT (iBAT). With this information, we developed a mouse model to investigate their functional role in the context of glucose homeostasis.

Brown Adipose Tissue

BAT is a specialized type of AT that utilizes fatty acids and glucose to produce heat in a process called thermogenesis^{111,112}. This organ is relatively recent in evolutionary terms, appearing only in mammals^{113,114}. However, BAT thermogenesis is not the only mechanism mammals employ to defend body temperature in cold environments, as shivering, originating from skeletal muscle contraction, is a commonly shared mechanism among the animal kingdom¹¹⁵. Thus, BAT thermogenesis is also referred to as non-shivering thermogenesis (NST).

1.2.1 Differences between BAT and WAT

While both WAT and BAT serve as forms of adipose tissues, they exhibit notable differences. Histologically, BAT has denser innervation, receiving input from both the Sympathetic and Sensory Nervous System, and it is more densely vascularized than WAT^{116,117}. BAT appears dark red compared to the pale appearance of WAT, a hue thought to result from Fe²⁺ ions in

heme groups within the blood supply and the high concentration of mitochondria in brown adipocytes, although this hypothesis has not been directly studied¹¹⁸. On a cellular level, brown adipocytes contain multiple small lipid droplets, abundant mitochondria, and exhibit high expression of β_3 ARs and uncoupling protein 1 (UCP1)¹¹⁹. UCP1 is critical for NST; its activity and expression increase with ARs stimulation, and BAT cannot perform thermogenesis without it¹²⁰. Activation of β_3 ARs raises intracellular cAMP¹²¹, leading to the activation of PKA. This cascade results in enhanced lipolysis (as discussed in a previous section), activation of transcription factor cAMP response element-binding protein (CREB)—which promotes expression of genes including *UCP1*¹²²—and activation of the Erk1/2 pathway through Src phosphorylation¹²³. Although the exact mechanisms by which UCP1 is activated are still under investigation, increased lipolysis is consistently followed by elevated UCP1 activity in brown adipocytes¹¹². UCP1 resides in the inner mitochondrial membrane, enabling proton (H^+) flow from the intermembrane space into the mitochondrial matrix along the gradient, producing heat. Normally, this proton gradient, generated by the respiratory chain complex, powers ATP synthesis from ADP in a process called coupled respiration. BAT, however, utilizes UCP1 to bypass ATP production, using the energy released from proton movement to produce heat instead, hence the “uncoupling” name¹²⁴. This UCP1 activity is also associated with what’s known as “metabolic inefficiency” or “futile cycle”. Although it may sound negative, this term refers to the fact that the energy from food is “wasted” on thermogenesis rather than on ATP production. While UCP1-related thermogenesis is one of several cellular futile cycles (reviewed in recent studies^{125,126}), it is the most prominent in BAT, playing a crucial role in NE-induced thermogenesis. Mice lacking UCP1 (*Ucp1*^{-/-}) lack NE-induced thermogenic responses in BAT and experience difficulty maintaining body temperature in cold environments¹²⁷.

Activation of brown adipocytes also promotes the uptake of lipids¹²⁸ and glucose¹²⁹ from circulation. Fatty acid uptake is essential for BAT thermogenesis, as blocking lipolysis specifically within BAT does not inhibit thermogenesis¹³⁰; however, systemic inhibition of lipolysis does¹³¹, as does blocking lipids uptake (reviewed in ¹³²). The role of glucose in BAT remains under study; some researchers propose it may support glycolysis, while others suggest it aids in regenerating fatty acids to sustain β -oxidation. Despite these uncertainties, BAT's role in glucose clearance is well-supported by findings from various animal and human studies¹³³⁻¹³⁵.

1.2.2 Brief history of BAT research

The earliest description of BAT dates back to 1551, when Swiss naturalist Conrad Gessner identified this tissue in marmots¹³⁶, hypothesizing a connection to hibernation due to their seasonal dormancy (reviewed in ^{137,138}). Without advanced tools, Gessner speculated that might serve as a hibernation-related organ, since marmots are hibernating animals. For centuries, BAT was thought to play roles in sleep and hibernation¹³⁹, including the possibility that BAT could act as a nutrient reservoir during this time. BAT is indeed abundantly present in hibernating mammals, and it plays a role in hibernation: a recent study has shown that BAT activity in hibernating squirrels is engaged in interbout arousals both during hibernation (to prevent excessive drops in body temperature) and is active in warming up the body when exiting hibernation¹⁴⁰. Despite its well-documented function in hibernating species, BAT is also present in non-hibernating mammals like mice, rats, and humans. Although there was evidence of high metabolic activity of BAT during hibernation¹⁴¹, it is not until 1961 that the first evidence of thermogenesis of brown fat was shown in rats¹⁴². From that moment on, BAT was known as a “thermogenic organ”. Subsequent decades of research clarified the molecular mechanisms underlying thermogenesis (discussed previously). Notably, scientists observed that BAT plays a

role in diet-induced thermogenesis (DIT)—an adaptive NST response to excess calorie intake. Impairment of DIT in genetically obese mice (e.g., *ob/ob* mice)¹⁴³ supported the idea of BAT as a potential therapeutic target for obesity, as BAT activation in rodents, whether by NE or selective β_3 agonists, promoted to significant weight loss¹⁴⁴. However, results in humans were conflicting.

BAT is abundant in newborns and infants, but its presence decreases with age, leading to the belief that it gradually converts to WAT, based on histological evidence¹⁴⁵. However, UCP1 remains detectable “ex” BAT depots in adults¹⁴⁶, and evidence of BAT plasticity emerged in patients with pheochromocytoma¹⁴⁷, an adrenal tumor associated with chronically high plasma levels of EPI and NE. This evidence suggests that BAT “whitening” may occur from insufficient stimulation rather than atrophy, hinting at potential reversibility through reactivation, a topic explored further in section 1.3 on environmental temperature’s impact on BAT plasticity.

Interest in BAT research waned in the 1980s, as it appeared evident that adult humans did not possess significant quantities of BAT. However, in the early 2000s, the introduction of Positron Emission Tomography (PET) inadvertently revived interest in BAT. Briefly, a radioactive molecule is administered to the patient, and the signal from the molecule is then detected by scanning the whole body. Certain cancer cells uptake glucose at high rates¹⁴⁸. As such, by using a radioactive analog of glucose (¹⁸Fluorodeoxyglucose, ¹⁸FDG), tumors will glow in scans, revealing the position and size of the neoplasms. However, it soon became evident to clinicians that there were regions other than tumors that showed up in these scans. It turned out that, in a significant proportion of the adult population, BAT is active and uptakes large quantity of glucose from the circulation, especially under mild cold stimulation¹⁴⁹⁻¹⁵¹. This discovery

renewed interest in BAT's potential role in metabolic health, particularly in glucose management for diseases like T2D¹³⁴, highlighting its capacity to lower glycemia upon activation¹²⁹.

1.2.3 Anatomy of BAT and its depots in humans and rodents

BAT is composed of several distinct depots distributed in the thoracic and abdominal regions, symmetrically on each side of the body. In humans, known depots are cervical, supraclavicular, paraspinal, mediastinal, axillary, and abdominal¹⁵². Of these the cervical and supraclavicular depots¹ are the most prominent and metabolically active, as measured by ¹⁸FDG intensity (Figure 3A). Rodents exhibit a similar pattern of BAT depot distribution, with some anatomical differences (Figure 3B).

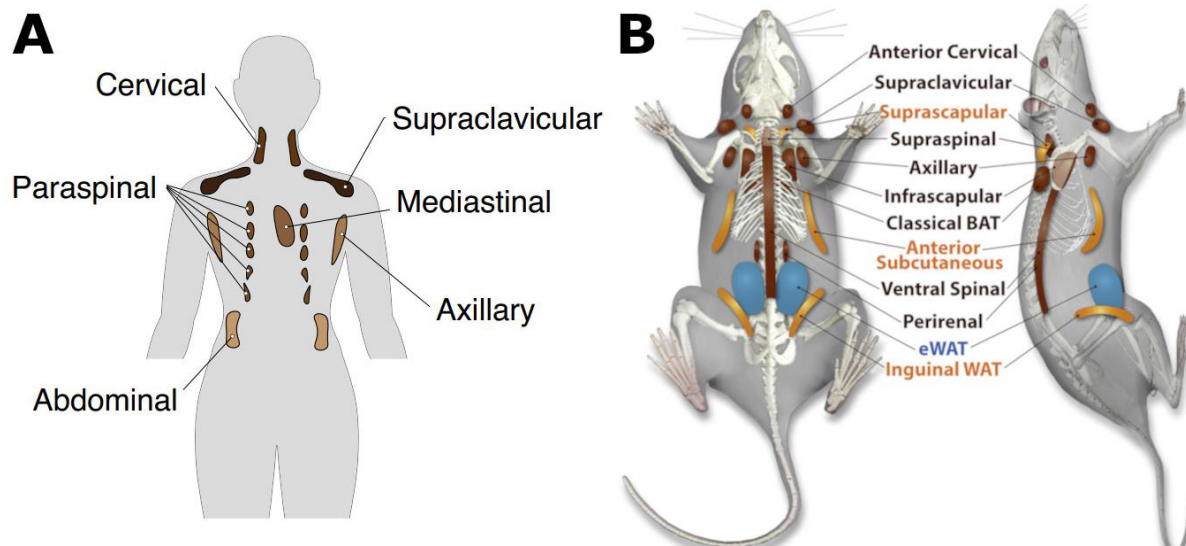


Figure 3: BAT depots distribution in humans.
(A, adapted from¹) and in rodents (B, adapted from²)

The main BAT depot in rodents is the interscapular BAT (iBAT)², which accounts for ~50% of total UCP1 content in mice housed at 30°C¹⁵³. Due to its prominence, iBAT is commonly used in translational research on rodents as a representative for all BAT depots. Another significant fat depot in rodents, although not primarily brown, is the inguinal WAT (iWAT). This depot contains a substantial number of beige adipocytes and has the highest browning capacity,

meaning that, under appropriate conditions, beige adipocytes can acquire many characteristics typical of brown adipocytes¹⁵⁴. Consequently, iWAT is often studied to uncover the mechanisms driving the browning process and to explore their potential health benefits.

Both BAT and WAT are typically found within the same fat depots, and their distinction is visible to the naked eye. The colocalization of brown and white fat within most depots is an indication of the plasticity of the AT and the potential for browning. Upon BAT activation, this tissue can expand through mature brown adipocytes proliferation, differentiation of new brown adipocytes from precursor, and the browning of beige adipocytes¹⁵⁵⁻¹⁵⁷. However, the absence of stimulation, a reverse process called whitening can occur^{158,159}. This plasticity has led some researchers to suggest that every adipocyte may have the potential to transition from white to brown and vice versa given the right stimuli¹⁶⁰. However, substantial evidence indicates that brown adipocytes do not convert to white adipocytes, even under prolonged absence of stimulation¹⁵⁹. Developmentally, white and brown adipocytes arise from distinct lineages, with brown adipocytes having closer similarities to SMCs than to white adipocytes¹⁶¹. Consensus holds that classic brown adipocytes tissue are established during embryonal development and form classic BAT¹⁶², while beige adipocytes derive from a separate precursor lineage and reside within WAT depots between white adipocytes¹⁶³. Beige adipocytes are unique in their ability to transition between white and brown phenotypes.

1.2.4 Impact of BAT on metabolism

We have briefly discussed how BAT activation can increase energy expenditure and lowers glycemia in both mice and in humans. However, considerable debate remains around the extent of BAT's impact on whole-body metabolism in humans and how this knowledge can be

translated into practical therapeutic approaches. To delve deeper into this topic, let's examine the evidence from both human studies and preclinical models.

1.2.4.1 BAT impact on Energy Expenditure

Acute pharmacological stimulation of BAT in mice can lead to doubling of total energy expenditure (EE), as measured by O₂ consumption¹⁶⁴. However, isolating BAT's exclusive contribution to EE is challenging. Pharmacological stimulation of ARs affects multiple organs, such as the skeletal muscle, which can mask BAT's precise effect on EE. Stress also influences energy balance via the ANS; even handling, like scruffing, can trigger stress-induced hyperthermia and elevate EE¹⁶⁵. The complexity increases with findings that *Ucp1*^{-/-} mice do not gain more weight than their wild type (WT) counterparts and, in fact, gain less weight¹⁶⁶. Interestingly, when these mice are housed at a higher environmental temperature (27°C), their weight gain is similar to that of WT mice. Although the mechanisms remain unclear, the prevailing hypothesis is that housing mice at room temperature (typically 20-24°C) exposes them to mild, chronic cold stress¹⁶⁷. This requires mice to maintain body temperature by other means, which for *Ucp1*^{-/-} mice may involve upregulating alternative futile cycles or relying more on shivering thermogenesis. Supporting this view, experiments conducted on WT vs *Ucp1*^{-/-} mice, both born and raised at 30°C and anesthetized during the experiments, showed that WT mice exhibited a two-fold increase in energy consumption following NE injection¹⁶⁸, underscoring BAT potential to increase EE.

Chronic stimulation of BAT in mice using daily injections of CL-316,243 (CL), a selective β₃ AR agonist, has been shown to prevent weight gain when exposed to high fat diet (HFD)¹⁶⁹ and induce weight loss in diet-induced obese mice¹⁷⁰. This effect occurs by increasing EE, without affecting food intake or locomotor activity. Other authors reported similar effects, but also noted

an anorexigenic effect of CL¹⁷¹. However, some researchers argued that such pharmacological stimulation leads to supraphysiological BAT activity, potentially overriding other adaptive counterregulatory mechanisms that help defend body weight. Subsequently, it was demonstrated that mice exposed to chronic cold environment, which physiologically activates BAT, increased their food intake to counterbalance the EE increase from BAT, resulting in no net weight change¹⁷². This evidence challenged the notion that BAT activation alone could induce weight loss in humans.

The situation in humans is more complex due to technical limitations. One of the primary challenges is that BAT activity in humans is almost exclusively measured via ¹⁸FDG uptake, a method that may deter many healthy volunteers. Consequently, these studies often involve very small sample sizes. Moreover, the origin of the sample can significantly influence results, as younger individuals tend to have a higher incidence of active BAT than older adults. Reports on prevalence of active BAT in the human population vary widely, with estimates ranging from 5%¹⁷³ to 50%¹⁷⁴. Nevertheless, acute stimulation of BAT, whether pharmacological or through cold exposure, has been shown to increase EE by approximately 50%¹⁷⁵.

The selective β_3 AR drug studied in humans is Mirabegron, which is currently prescribed for overactive bladder at a daily oral dose of 50 mg. However, the dose necessary to elicit effects on BAT activity in humans appears to be at least 100 mg¹⁷⁶. Despite a small but significant increase in energy expenditure, treatments with Mirabegron have failed to produce meaningful weight loss, even at a 200 mg dose¹⁷⁷. Additionally, negative side effects related to off-target ARs stimulation, related to increased cardiovascular risk^{178,179}, have been reported. As a result, Mirabegron has not been approved for weight management purposes.

The reasons behind Mirabegron's ineffectiveness in promoting weight loss remain under investigation. Recent evidence suggests that human BAT expresses high levels of β_2 AR, which are coexpressed with UCP1, and that β_2 AR might be the receptor responsible for BAT thermogenesis rather than β_3 ¹⁸⁰⁻¹⁸². Ongoing studies are exploring whether β_2 AR agonists, rather than β_3 ARs agonists, could be viable weight loss therapies. However, unless new studies yield different outcomes, it seems clear that BAT activity in humans may not be a viable strategy to induce weight loss.

1.2.4.2 BAT impact on glucose homeostasis

Adipose tissue, both brown and white, plays a crucial role in whole-body glucose homeostasis and the development of insulin resistance. There are three primary mechanisms by which AT can enhance insulin sensitivity¹⁸³: i) reduction of circulating lipids, either by decreasing lipolysis or by increasing the uptake of lipids from circulation, which helps prevent ectopic lipid accumulation in other tissues, a known contributor to insulin resistance; ii) increased oxidation of substrates like lipids and glucose to reduce their circulating levels; iii) release of molecules that can influence the activity of other tissues. In this context, BAT can exert a direct positive effect by sequestering and oxidizing circulating glucose and fatty acids, as well as an indirect effect through the secretion of insulin-sensitizing hormones. We will explore the endocrine role of BAT in more detail in section 1.2.5.

We have previously discussed how acute BAT activation leads to the uptake of circulating glucose in both rodents and humans. A pertinent question arises: can chronic BAT activation help fight T2D and insulin resistance? Evidence from mouse studies indicates that chronic pharmacological stimulation with CL¹⁸⁴ or cold exposure^{172,185} in diet-induced obese mice can

reduce resting glycemia, improve glucose tolerance, and enhance insulin sensitivity. However, it is important to note that preclinical findings do not always translate effectively to humans. In contrast to the challenges observed with weight loss interventions, treatments with Mirabegron have demonstrated improvements in insulin sensitivity, even in the absence of weight loss^{59,177,179}. A relatively recent retrospective study from Paul Cohen's group¹, involving over 50,000 oncology patients, found that detection of active BAT was associated with lower resting glycemia and plasma triglycerides. Notably, when patients were stratified by BMI, the benefits of active BAT on glycemia and triglycerides became more pronounced as BMI increased. Although this finding is correlational, it suggests that enhancing BAT may be particularly beneficial for those patients with excessive weight, who are often affected by metabolic syndrome. Interestingly, environmental colder temperatures are linked to improved glucose homeostasis and insulin sensitivity¹⁸⁶, and repeated cold exposure has been shown to enhance insulin sensitivity in T2D patients¹⁸⁷. However, some people argue that, in humans, most of the metabolic benefits derived from cold stimulation may be mediated by skeletal muscles rather than BAT¹⁸⁸. While it is true that skeletal muscle plays an important role in facilitating cold exposure-related metabolic benefits and may exert more immediate effects on lowering glycemia, pharmacological evidence supports the idea that BAT activity contributes to improved glucose homeostasis and insulin sensitivity. Additionally, the role of skeletal muscle does not negate the endocrine functions of BAT and its capacity to enhance insulin sensitivity in other organs through recently identified signaling molecules. We will further discuss this aspect of BAT in the following section.

1.2.5 BAT as an endocrine organ

We have briefly touched on the role of AT as an endocrine organ in section 1.1.4.3, particularly in relation to leptin. Since the discovery of leptin, numerous factors released from WAT have been identified, including fibroblast growth factor 21 and adiponectin. Collectively, these WAT-secreted molecules are referred to as “adipokines”¹⁸⁹. While much of the research has focused on WAT, the secretory role of BAT has remained relatively understudied until more recently^{190,191}. Over the last 15 years, however, substantial evidence has emerged demonstrating a diverse range of molecules secreted by BAT. These molecules can exert autocrine, paracrine (acting on blood vessels and nerves within BAT) or endocrine (targeting other organs, like liver or pancreas) functions. This class of BAT-secreted molecules are known as “batokines”, distinguishing them from adipokines released by WAT. Batokines are characterized by their increased expression or secretion in response to brown adipocyte stimulation.

Bone morphogenic protein 8b (BMP8B) was one of the first batokines identified¹⁹². It enhances thermogenesis through at least three distinct mechanisms: acting centrally on the hypothalamus, stimulating axonal growth and vascularization in BAT¹⁹³, and increasing cAMP levels in brown adipocytes. Another notable batokine is neuregulin 4 (NRG4), which influences the liver, the SNS, and vascularization. In vitro, NRG4 mediates the BMP8b-induced axonal growth in sympathetic neurons¹⁹³. Within BAT, NRG4 promotes vascularization by stimulating ECs¹⁹⁴. Finally, NRG4 acts on the liver by binding to its receptor on hepatocytes, triggering an enzymatic cascade that reduces the expression of genes involved in *de novo lipogenesis*. This effect provides protection against hepatic steatosis during HFD feeding, resulting in improved insulin sensitivity in diet-induced obese mice^{195,196}.

Many batokines exhibit neurotrophic activity, promoting the sympathetic innervation of BAT. Neurotrophic factor 3 (NT-3) is one of such batokines that stimulates SNS growth, promoting the innervation and expansion of BAT, as well as browning in WAT¹⁹⁷. Increased levels of NT-3 confer protection against diet-induced obesity and enhanced thermogenesis, while reduced NT-3 levels increase susceptibility to weight gain in diet-induced obesity models and impair the ability to maintain body temperature when challenged with cold. Additionally, mice overexpressing *Nt3* exhibit lower fasting glycemia and improved insulin sensitivity when fed a HFD, although these effects appear to be primarily linked to reduced body weight compared to control animals.

Another neurotrophic batokine worth noting is S100b¹⁹⁸, which has been shown to promote SNS innervation of thermogenic fat, including both BAT and beige AT.

AT can also release certain lipid species that function similarly to adipokines and batokines, influencing glucose homeostasis and insulin sensitivity. These lipid molecules are referred to as “lipokines”¹⁹⁹. Recent technological advancements, particularly in lipidomics, have led to the identification of BAT-exclusive lipokines. One such lipokine is 12,13-dihydroxy-9Z-octadecenoic acid (12,13-diHOME), which is produced by and acts on brown adipocytes²⁰⁰. 12,13-diHOME enhances the translocation of FATP1 and CD36 to the membrane of brown adipocytes, resulting in increased uptake of circulating lipids and subsequently lowering lipidemia. In a separate study, the same research group demonstrated that plasma levels of 12,13-diHOME increase following bouts of moderate physical activity in humans, and this lipokine also promotes the uptake and oxidation of fatty acids by skeletal muscle²⁰¹. Another important BAT lipokine is 12-hydroxyeicosapentaenoic acid (12-HEPE), which is also produced by brown adipocytes, and it acts in an autocrine manner, triggering an insulin-like signaling pathway that

leads to increased translocation of Glut4 to the membrane and increased glucose uptake into brown adipocytes²⁰².

Finally, a recent study from Shingo Kajimura's group has highlighted the relationship between BAT metabolism of branched chain amino acids (BCAAs) and insulin sensitivity²⁰³. In the mechanisms described, brown adipocytes take up BCAAs from circulation and utilize the nitrogen group to generate and release a series of derived metabolites, including glutathione, as well as amino acids like glutamate, alanine, and aspartate. These BAT-derived metabolites subsequently act on other organs, such as the liver, to reduce oxidative stress and enhance insulin sensitivity. Notably, these improvements in insulin sensitivity were not accompanied by changes in EE or weight, aligning with observation from human studies where BAT stimulation leads to better glucose management without significant weight loss.

In conclusion, the evidence presented in this section underscores the fundamental role that BAT plays in glucose homeostasis. Although BAT might not function as the calorie-burning powerhouse seen in rodents, and its thermogenic activity in humans might not significantly influence energy balance, the molecules secreted by active BAT can positively impact metabolic health. The endocrine role of BAT could be pivotal in developing new therapies for T2D.

1.2.6 Role of vasculature in BAT function

BAT is one of the most densely vascularized organs in the body, and its activity is highly dependent on access to systemic circulation. As previously discussed, BAT requires circulating lipids to sustain thermogenesis^{130,131}, and brown adipocyte lipolysis is not necessary for thermogenesis as long as they can import lipids from bloodstream²⁰⁴. Therefore, a tight coordination of vascular tone and blood flow is crucial for the proper functioning of BAT, both during acute and chronic activation. Historical evidence dating back to the early 1970s

demonstrated that SNS activation in WAT can enhanced capillary permeability²⁰⁵, in conjunction with promoting lipolysis, likely to facilitate the transfer of lipids from the depot into circulation. Similar processes may occur in BAT, as studies have shown that blood perfusion to BAT increases during cold exposure^{149,206}.

We have also noted the presence of NE and NPY double-positive fibers lining small arterioles in peripheral organs, including BAT. Whole-body knockout of NPY in sympathetic nerves has been associated with impaired glucose homeostasis³². In the next section, we will explore the role of the SNS in regulating BAT activity and the evidence surrounding local blood flow modulation in BAT.

SNS control of BAT

In this section we are going to review the evidence for SNS control of BAT activity and examine why increased SNS outflow to BAT is typically considered beneficial. However, systemic sympathetic activity is generally undesirable in overweight and obese patients, as it is linked to heightened cardiovascular risk and insulin resistance. How can we address this apparent dichotomy? Let's review some of the major theories that may resolve this question.

SNS activity has distinct effects on BAT and WAT. Sympathetic stimulation of WAT promotes lipolysis, which increases circulating lipid levels, while stimulation of BAT has the opposite effect, lowering lipid and glucose levels in the blood. This raises the question: could there be differences in sympathetic drive between the two types of fat? We already know that BAT and WAT have different magnitudes of sympathetic innervation, with BAT exhibiting a much higher density of sympathetic fibers compared to WAT. This increased innervation is also a hallmark of browning in WAT, as highlighted by imaging studies^{29,207-209} (Figure 4).

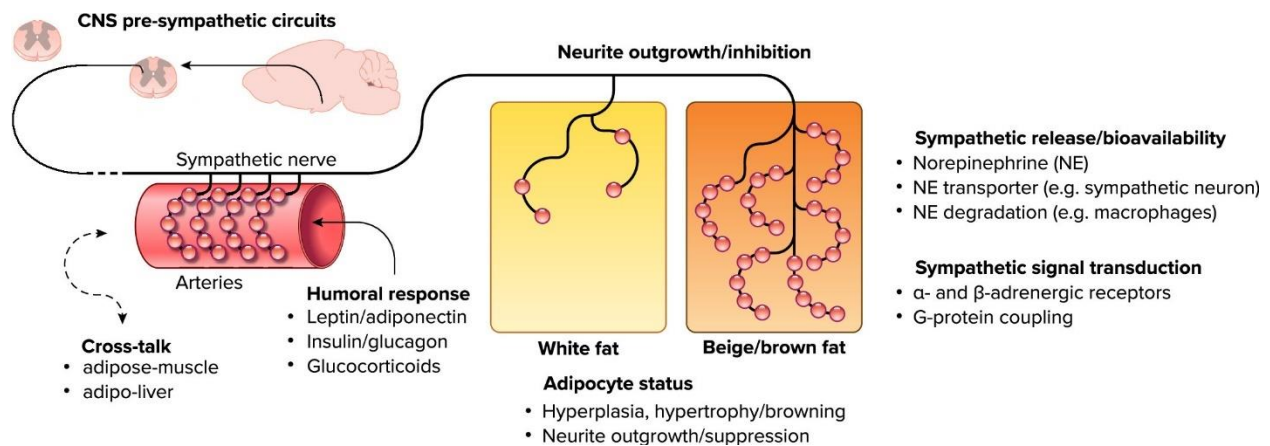


Figure 4: Schematics of different sympathetic innervation in blood vessels, WAT, and BAT.
Adapted from³.

There is evidence supporting a shift in sympathetic outflow to different adipose depots in response to specific stimuli in rodents²¹⁰. For instance, food and glucose deprivation are associated with increased sympathetic activity in epididymal WAT (eWAT), a depot considered to be pure WAT with no browning potential, while cold exposure does not increase sympathetic outflow to this depot²¹¹. In contrast, iBAT shows increased sympathetic activity specifically during cold exposure²¹¹. Interestingly, iWAT blood flow appears to increase across all tested conditions, likely due to its beige nature. Stimulation of central melanocortin receptor 4 (MC4R)- expressing neurons, a downstream node of the leptin-inducible circuit in the CNS, also leads to increased outflow to iBAT and iWAT, but not eWAT²¹².

In humans, the role of sympathetic activity in BAT among obese patients remains unclear. Most studies report that sympathetic activity decreases as body fat accumulates²¹³, while other show no significant change²¹⁴, as measured by ¹⁸FDG uptake. A more recent study²¹⁵ found that the intensity of BAT activity may not significantly differ between lean and obese individuals with detectable BAT. However, the prevalence of active BAT is notably lower in obese patients, aligning with the large-scale retrospective study on over 50,000 patients¹. Additionally, BAT

activity in obese patients is negatively correlated with visceral adiposity, a key factor linked to cardiovascular risk²¹⁶. In another human study, sympathetic innervation in cervical and supraclavicular depots was measured in lean and obese women by using a radioligand for NET, the NE transporter expressed by sympathetic neurons²¹⁷. The results indicated that NET levels were lower in obese patients, suggesting reduced sympathetic innervation in their BAT. Obese patients also show impaired uptake and oxidation of fatty acids by BAT²¹⁸. Interpreting these findings in human patients is challenging, as many are derived from association studies that cannot determine causality between decreased BAT activity and increased weight gain. However, the majority of evidence points toward reduced BAT activity in overweight and obese individuals.

A crucial component in the pathophysiology of obesity is the role of immune system in AT function, an area often referred to as immunometabolism²¹⁹. In recent years, research has expanded on the interaction between adipose tissue, local immune cells, and adipose-innervating neurons, leading to the emerging field of neuroimmunometabolism (reviewed in ²²⁰ and in ²²¹). Immune cells in adipose tissue can influence adipocyte activity in positive or negative ways, depending on the nature of the stimulus. Overweight and obesity are typically associated with chronic adipose tissue inflammation, which can drive or exacerbate insulin resistance²²². Notably, resident macrophages in both WAT and BAT can modulate adipocyte function by sequestering NE released from sympathetic varicosities, resulting in attenuated responses to SNS activity²²³. This immune-mediated disruption of adipocyte function is considered a fundamental aspect of catecholamine resistance²²⁴, observed in overweight individuals as blunted lipolytic response of adipocytes to adrenergic stimulation^{94,225-227}. Downregulation of β_3 AR in BAT of mice has been observed following diet-induced obesity, contributing to catecholamine

resistance²²⁸. The proposed picture from this line of research is that, during early weight gain phase, the CNS increases SNS outflow to both WAT and BAT to offset excess energy intake. However, if a positive energy balance persists, ATs become desensitized to this response, resulting in reduced SNS-mediated effects. Despite this blunted response²²⁹, basal WAT lipolysis appears elevated in obesity²³⁰, potentially due to insulin resistance, given that insulin is a potent inhibitor of lipolysis. Moreover, elevated leptin levels from WAT expansion can exacerbate insulin resistance by promoting lipolysis²³¹, countering insulin's effects. This hypothesis is further supported by findings showing that catecholamine resistance can be reversed with weight loss²³² and that partial reductions in circulating leptin can restore insulin sensitivity in obese animals, promoting weight loss^{233,234}.

These insights suggest that restoring or enhancing BAT activity could hold promise for future therapies. However, since BAT activation is driven by SNS stimulation, strategies to increase systemic SNS activity must be managed carefully, as elevated sympathetic tone can adversely impact cardiovascular health. In the next section, we will review relevant studies on SNS control of BAT activity and what we can learn from these studies to understand how to selectively activate BAT-projecting SNS.

1.3.1 Evidence of sympathetic control of BAT activity

The first evidence of sympathetic innervation of BAT was presented by Claes Wirsén, which published two consecutive papers illustrating images of sympathetic varicosities, first in BAT vessels²³⁵ and later in the parenchyma²³⁶. Rodent iBAT has visible nerve bundles that enter dorsolateral on each side, indicating that each side of the SNS innervates ipsilaterally^{15,237,238}, although some authors report a small proportion (~10%) of contralateral innervation²³⁹. The relative ease of access to these bundles has made surgical denervation a common method in

functional studies. In these studies, cold-induced thermogenesis²⁴⁰, increased blood flow²⁴¹, and BAT glucose uptake²⁴² were abolished after denervation. When NE injections were administered to denervated rodents, BAT functionality was restored²⁴⁰, further confirming that SNS-derived NE is essential for BAT activity. However, surgical denervation results should be interpreted cautiously, as these bundles also contain sensory nerves and are in close contact with arteries supplying the tissue²⁴³, which can be damaged during surgery, leading to more than just sympathetic denervation. An alternative to surgical denervation is chemical denervation, achieved through local injection of the catecholaminergic neurotoxin 6-hydroxy-dopamine (6-OHDA)²⁴⁴. Chemical denervation results aligned with surgical outcomes²⁴⁵, eliminating thermogenesis and increased blood flow and reinforcing the SNS role in iBAT activity. Interestingly, sympathetic regeneration was observed in this study, with the process accelerated in mice housed at colder temperatures.

BAT thermogenesis depends on SNS activity²⁴⁶, which, in the context of thermoregulation, is triggered by cold exposure. Exposing mice to colder temperatures increases the sympathetic signal intensity to BAT, while warmer temperatures decrease it. SNS outflow to iBAT rises upon acute cold exposure, as measured by nerves activity projecting to iBAT^{238,247}. Chronic cold exposure, often referred to as cold acclimation, leads to an increased cold-evoked sympathetic response in iBAT²⁴⁸, accompanied by increased TH protein expression in brown and beige adipose tissue²⁴⁹, along with other tissue adaptations such as neoangiogenesis²⁵⁰ and increased *UCPI* expression. The increase in TH expression suggests an increased innervation density of thermogenic depots, which is confirmed by whole-tissue imaging²⁵¹. This remodeling is reversible: in warmer temperatures, sympathetic activity in thermogenic adipose tissues diminishes, reducing innervation and vascular density. Remarkably, this neurovascular

remodeling of thermogenic adipose tissue demonstrates high plasticity, with innervation and vascularization reverting to their original level once animals return to previous temperatures²⁵². However, when temperature manipulation occurs between birth and weaning—a period when the SNS is still developing in rodents—permanent changes in iBAT innervation can result; for instance, rats reared at 30°C have fewer neurons innervating iBAT than those reared at 18°C²⁵³. Despite this phenotype, no lasting metabolic effects or cold-evoked responses appear in mice reared at thermoneutrality if they first adapt to room temperature²⁵⁴. However, in the latter study, mice were kept at 4°C for only a week, a brief but intense cold stimulus unlikely to show long-term cold adaptation effects. In chapter 2, I present our study that we published in 2023 exploring the effects of early environmental temperature manipulation on long-term adaptations in mice, showing that while mice raised at thermoneutrality exhibit intact acute response to cold, they fail to adapt to prolonged cold exposure beyond two weeks.

The neural circuitry involved in thermoregulation has been extensively studied using both viral tracing²⁵⁵⁻²⁵⁷ and via electrophysiological studies²⁵⁸ (reviewed in²⁵⁹ and in²⁶⁰). Briefly, two groups of neurons in the median preoptic subnucleus (mnPO) of the preoptic area (POA) in the CNS—one glutamatergic (excitatory) and the other GABAergic (inhibitory)—project to GABAergic neurons in the medial POA (MPA). These MPA neurons, in turn, project to glutamatergic neurons in the dorsomedial hypothalamus (DMH). DMH neurons then extend to the rostral ventromedial medulla, where they connect to glutamatergic and serotonergic neurons in the rostral raphe pallidus and the parapyramidal area, which subsequently project to first order sympathetic neurons in the IML, contacting ganglionic neurons. Due to the GABAergic nature of the MPA neurons and the two groups of neurons in the upstream mnPO, thermogenesis activation depends on which mnPO group is activated. During cold exposure, the

GABAergic mnPO group activates, inhibiting MPA and disinhibiting DMH; in warmer conditions, the glutamatergic group activates, stimulating MPA and inhibiting DMH. Despite the complexity, this picture is incomplete, as other important nuclei—such as the paraventricular nucleus of the hypothalamus (PVH)—have also implicated. Notably, PVH has been shown to project directly to IML neurons, although these projections appear to reduce SNS activity and BAT thermogenesis²⁶¹.

Innervation in AT has been extensively studied in recent years, thanks to the development of whole-tissue clearing techniques that allow for visualization of intact nerve fibers within the depot. Although clearing techniques have seen considerable success in WAT²⁶²⁻²⁶⁹, leading to elegant analysis of innervation and vascularization density and distribution²⁰⁷, similar analysis in iBAT have lagged behind, with only few studies providing qualitative images for experimental purposes rather than quantified results. One of the main challenges in clearing BAT appears to be the persistence of background dark pigmentation, possibly caused by mitochondria and Fe²⁺ as discussed in section 1.2.1. The field of tissue clearing is advancing rapidly, with new protocols being developed and optimized for different organs every year (recently reviewed in²⁷⁰), and we hope to have a BAT-optimized method sooner rather than later.

BAT activity can be quantified through several different parameters. We have previously mentioned how TH expression serves an indirect indicator of increased sympathetic activity in BAT; thus, many authors use TH protein or *Th* gene expression as a proxies for BAT activity¹⁹³. Other genes commonly used to quantify BAT activity include *Ucp1*, *Dio*, *Pgc1a*, all of which have been extensively shown to be induced upon adrenergic stimulation of brown adipocytes. A limitation of using protein or gene expression is that we lack information about the time dynamic of BAT activity, as we cannot measure protein or gene expression in real time. Consequently,

common methods to assess real-time BAT activation rely on measuring either sympathetic activity through electrophysiological recordings, or changes in temperature and/or blood flow in BAT, which is the outcome of the former. Although nerve recordings have been extensively used in rats^{271,272}, mice nerve recordings have been limited^{192,238,273}, possibly due to the additional difficulties presented by the smaller size of mice. Moreover, these recordings require highly specialized equipment and trained personnel, which further restricts the use of this technique. A valid alternative is measuring BAT temperature in real time (reviewed in ²⁷⁴). In chapter 3, I present a recording technique that I developed to measure temperature and blood flow changes in iBAT in anesthetized mice. Using this technique, we can quantify the intensity and temporal dynamics of these two parameters, and we can compare local intrascapular temperature with the rest of the body to dissect the specific contribution of iBAT to body temperature. This technique is also discussed in chapter 4, where we use it to measure chemogenetic activation of iBAT-projecting SNS.

Artificial stimulation of BAT activity in experimental settings has generally been achieved via pharmacological stimulation. Although this is a valid method, it involves the system-wide diffusion of an active molecule, which could have many potential off-target effects. As such, various molecular techniques have been developed to restrict the activation spatially and temporally to a specific set of neurons. These techniques include chemogenetics and optogenetics (review in²⁷⁵ and in²⁷⁶, respectively), which are typically paired with viral injections to limit the manipulation to a specific organ or region²⁷⁷. By combining these technologies, we can selectively activate the iBAT-projecting SNS to investigate the role of BAT activity in metabolism without any confounding factors. However, there is limited evidence available. Both chemogenetics⁴⁶ and optogenetics²⁷⁸ have been used on adipocytes, yielding the

expected positive outcomes on metabolism. However, as discussed, SNS activity does not only activate adipocytes; a wide variety of cell types in BAT are influenced by the SNS, including immune cells, ECs, and SMCs from the vasculature. Two papers have utilized optogenetics to stimulate iBAT-projecting SNS. The first paper was published in 2018, using a mouse line that conditionally expresses channelrhodopsin (ChR2), the light-sensing receptor which causes an increase in intracellular Ca^{2+} upon activation, in all *Th*-expressing cells. The authors then illuminated the iBAT, restricting sympathetic activation to that region, and they reported an increase in temperature and a reduction in blood glucose, consistent with expectations²⁷⁹. In the second paper, ChR2 expression was restricted to only those nerves that project to iBAT using a viral injection in the interscapular fat pad²⁸⁰. Increased iBAT temperature and *Ucp1* expression were observed after local stimulation with blue light. However, there were several limitations in these studies. First, mouse brown adipocytes in iBAT express opsin 3, a naturally occurring light-sensing receptor, and blue light activates this channel, leading to brown adipocyte activation, with increased lipolysis, oxidation, and temperature²⁸¹. In both papers, the authors placed the light source directly on the iBAT, so we cannot exclude the possibility that their results were partially due to opsin 3 activation. In Chapter 5, I am presenting chemogenetic activation of iBAT-projecting SNS. We restricted the expression of the designer receptor hM₃D to these nerve by injecting a custom-made retrograde virus²⁸², and we explored the impact on thermogenesis, blood flow, and glucose metabolism in mice.

1.3.2 Sympathetic and Sensory cross-talk in BAT

Depicting SNS as the only regulator of BAT activity would be a mistake, as sensory neurons from DRGs also innervate the tissue, and activation of DRGs influences AT activity, both in WAT and BAT (reviewed recently in²⁸³ and in²⁸⁴). Retrograde tracing studies have revealed

important CNS nodes (hindbrain, midbrain, posterior hypothalamus and thalamus) that receive innervation from iBAT-projecting DRGs neurons and simultaneously send their axons to iBAT-projecting sympathetic neurons²⁵⁷. This suggests that sensory feedback can modulate sympathetic tone to iBAT. Crosstalk can also occur within adipose tissue, where neurotransmitters from one system can directly act on the nerve fibers of the other system, modulating their activity²⁸⁵. However, reports on the nature of this interaction have been contrasting. Early studies using chemical sensory denervation with capsaicin injections reported reduced sympathetic outflow and BAT atrophy^{286,287}, supporting the notion of positive feedback from sensory to sympathetic neurons. However, in their follow up study²⁸⁷, capsaicin-treated mice appeared to lose more weight eight months after the treatment, which the authors hypothesized was due to atrophy of other adipose tissues as well. Several other studies using capsaicin-induced sensory denervation have produced similar results²⁸⁸, bolstering the hypothesis that sensory neurons promote sympathetic outflow. However, the use of capsaicin in these experiments can be quite controversial. Capsaicin can be lethal for mice, even at doses reported in literature (discussed in²⁸³), indicating that it could affect other organs as well. Capsaicin kills DRG neurons by inducing an influx of Ca^{2+} and Na^{+} to cytotoxic levels. However, this mechanism can result in a transient high-intensity action potential before cell death, which could be misinterpreted as increased sensory activity. Under this paradigm, capsaicin treatment could potentially lead to high activation of the sensory circuits rather than suppression, supporting the view that sensory neurons inhibit sympathetic activity. Finally, capsaicin directly induces browning in adipocytes precursor in vitro²⁸⁹, which could explain the pro-sympathetic effects. As such, capsaicin denervation studies are challenging to interpret. Similarly, surgical denervation in WAT has led to reduced lipid oxidation in the tissue²⁹⁰, although we have already discussed that

the sectioning of AT-projecting nerve bundles results in both sensory and sympathetic denervation, along with a portion of the blood supply to the tissue. More recent studies using a mix of genetic models and restricted Cre-induced sensory denervation have reported negative feedback from sensory neurons on sympathetic activity in iWAT²⁶⁴ and in iBAT²⁹¹, instead. This negative feedback from sensory nerves logically fits into the overall picture of BAT regulation as a brake on excessive sympathetic activity, especially in the context of hyperthermia. Despite the controversies in the field, it appears evident that sensory and sympathetic systems influence each other. To selectively study the influence of one system on BAT function, we need to employ molecular strategies to restrict the desired manipulation to only the system we are interested in.

1.3.3 Sympathetic control of vascular tone in BAT

We have discussed the importance of vascular tone regulation for AT function and addressed the mechanisms behind general sympathetic regulation of vascular tone. In this section, we will review the specific role of SNS activity on vascular tone in BAT, and how this impacts BAT function.

In small arterioles, ECs line the lumen and serve as the first physical barrier between blood and BAT parenchyma. Nutrients and other factors can leave the blood via two types of transport: paracellular, passing between two ECs, or transcellular, passing through ECs²⁹². Given the continuous endothelium of AT, transcellular transport is thought to be the main pathway for the passage of substances from blood to parenchyma²⁹³. As such, ECs are critical for BAT function, and BAT's uptake of fatty acids and glucose relies on the extraction of these nutrients from circulation by ECs. However, ECs are not directly innervated by the SNS, as sympathetic innervation of blood vessel ceases at the media-adventitial border in small arteries, contacting only the SMCs²⁹⁴. Thus, the effects of SNS on vasculature do not appear to be mediated by ECs,

or at least not directly. Increased sympathetic activity in BAT is associated with enhanced blood flow to the tissue, which is necessary to provide fuel for oxidative processes. However, we have observed that SNS activity is generally associated with vasoconstriction, which seems contradictory with what is observed in BAT, where NE and β ARs agonists induce vasodilation^{295,296}. A possible explanation could be different local relative expression of ARs, as we know that α_1 AR mediates constriction, whereas β_2 AR mediates dilation. However, it has been reported that vasoconstriction can increase vessel permeability by increasing the distance between ECs²⁹⁷, allowing for paracellular transport. The role of NPY is also unclear, as it acts as a vasoconstrictor in the periphery, similar to NE. Surprisingly, the role of NPY in peripheral vascular control is a vastly understudied field, and there is limited information available. Even though the mechanisms behind increased blood flow are fully understood, NE and NPY in blood vessels in BAT (and in AT in general) are essential for inducing neoangiogenesis, which is the first step in both the browning process and expansion of AT. NPY has been reported to stimulate ECs expansion by acting on Y1 and Y2 receptors^{298,299}. SNS activity in BAT induces tissue expansion, as discussed in section 1.2.3. During excessive energy intake, AT expansion is linked to persistence of insulin sensitivity due to avoidance of ectopic lipid accumulation. Conversely, if neoangiogenesis is blocked during periods of excessive energy intake, insulin resistance can develop³⁰⁰. Capillary rarefaction—defined as the increase of distance between two capillaries within a tissue, leading to reduced vascular density—is one of the main factors contributing to AT inflammation. This process occurs when neoangiogenesis fails to keep pace with AT expansion³⁰¹. As such, improved vascular health may provide an explanation for the phenomenon of metabolically healthy obese individuals³⁰², a group characterized by high body weight but otherwise normal blood panels.

Another major factor mediating vasorelaxation and vasodilation in BAT is nitric oxide (NO). NO is a potent vasodilator generated by NO synthase (NOS). There are three known types of NOS: neuronal (nNOS or NOS1), inducible (iNOS or NOS2), and endothelial (eNOS or NOS3)³⁰³. Brown adipocytes have been shown to express iNOS, and its expression is induced upon NE stimulation³⁰⁴. However, other studies have reported significant expression of nNOS and eNOS in iBAT, with brown adipocytes serving as the primary source of eNOS since ECs do not seem to increase NO production in response to adrenergic stimulation³⁰⁵. Regardless of its source, NO production is stimulated by sympathetic activity in BAT, which appears to account for the vasodilatory effects of NE. Nevertheless, NOS-induced effects seem to explain only part of NE-induced vasodilation in BAT³⁰⁶, with the most plausible explanation being an interaction among all the pathways discussed.

Open questions in the field

In this introduction, I have reviewed the current knowledge regarding the SNS, BAT, and the mechanisms by which the former regulates the latter. While it is evident that increased BAT activity is linked to improved metabolic health, how to achieve this increased activity without impacting the entire SNS remains not completely understood. Furthermore, we have observed that many effects generally attributed to BAT may actually arise from contributions of other organs, such as skeletal muscle. One significant gap that is preventing precise quantification of BAT's role in systemic metabolism is the lack of techniques to selectively activate this organ physiologically via the SNS. Another unresolved question in the field concerns the role of NPY and NE double-positive sympathetic fibers that innervate the vasculature. Recent evidence from mice with conditional deletion of *Npy* (cKO) specifically in *Dbh*-expressing cells³²—such as

sympathetic neurons, but also chromaffin cells and other neuronal group in the CNS—has demonstrated a reduced ability to defend body temperatures when exposed to cold. Interestingly, these mice exhibit increased insulin sensitivity, which becomes even more puzzling considering that the authors report reduced GSIS in the pancreatic islets of these mice. There are two main limitations associated with this cKO mouse model: 1) *Npy* conditional deletion driven by *Dbh* results in a whole-body phenotype, including cell types beyond just ganglionic sympathetic neurons, and 2) *Npy* appears to be expressed by all ganglionic sympathetic neurons, although at different levels¹⁰⁷, as will be discussed in Chapter 4. As such, *Npy* is not an appropriate molecular marker for selectively targeting vascular-projecting sympathetic neurons.

The identification of such a marker could enhance our understanding of the mechanisms underlying environmental influences on iBAT innervation. A study from 1969³⁰⁷ reported that blocking SNS development at birth in rats using antibodies against nerve growth factor (NGF)—a potent signal driving neuronal development and axon guidance—resulted in intact parenchymal sympathetic innervation in iBAT. This evidence suggests that axon initiation and elongation from the vasculature-projecting sympathetic neurons start after birth, indicating a later developmental window than that for parenchymal innervation. This hypothesis may help explain why rodents born and raised at thermoneutrality have less iBAT-projecting neurons than their room temperature littermates, as SNS-induced activity in iBAT is linked to the secretion of neurotrophic factors.

During my graduate research, I aimed to bridge the gap in understanding the mechanisms behind sympathetic control of BAT and to leverage this knowledge for the development future therapies for metabolic diseases, such as T2D. Much of the work presented here stems from the results

achieved by Seo Eun Lee, a previous PhD student that worked on this project in our lab. As such, when necessary, I will clarify my specific contributions and those of my predecessor.

Chapter 2: Rearing mice at 22°C programs increased capacity to respond to chronic exposure to cold but not high fat diet

The study presented in the following chapter was originally designed by Seo Eun Lee (S.L.) and Lori Zeltser (L.Z.) and performed by S.L. and Alex Lafonde (A.F.). However, due to technical problems, the results were inconclusive. My (D.N.) original contribution was to analyze the raw metabolic data and to develop an algorithm to address the technical problems that were affecting the analysis (as discussed in the methods section). After addressing the issue, I have reanalyzed the metabolic data, and I found novel results. Angela Ramos Lobos (A.R.L.) analyzed body composition and glucose homeostasis data and generated the figures. S.L. and A.R.L. contributed to early drafts of the manuscript. D.N. and L.M.Z. wrote the manuscript. This study was published in *Molecular Metabolism* in 2023³⁰⁸.

Abstract

Objective: Rodent models raised at environmental temperatures of 21-22°C are increasingly switched to thermoneutral housing conditions in adulthood to better capture human physiology. We quantified the developmental effects of rearing mice at an ambient temperature of 22°C vs. 30°C on metabolic responses to cold and high fat diet (HFD) in adulthood.

Methods: Mice were reared from birth to 8 weeks of age at 22°C or 30°C, when they were acclimated to single housing at the same temperature for 2-3 weeks in indirect calorimetry cages. Energy expenditure attributable to basal metabolic rate, physical activity, thermic effect of food, and adaptive cold- or diet-induced thermogenesis were calculated. Responses to cooling were evaluated by decreasing the ambient temperature from 22°C to 14°C, while responses to HFD feeding were assessed at 30°C. Influences of rearing temperature on thermogenic responses that emerge over hours, days and weeks were assessed by maintaining mice in the indirect calorimetry cages throughout the study.

Results: At an ambient temperature of 22°C, total energy expenditure (TEE) was 12-16% higher in mice reared at 22°C as compared to 30°C. Rearing temperature had no effect on responses in the first hours or week of the 14°C challenge. Differences emerged in the third week, when TEE increased an additional 10% in mice reared at 22°C, but mice reared at 30°C could not sustain this level of cold-induced thermogenesis. Rearing temperature only affected responses to HFD during the first week, due to differences in the timing but not the strength of metabolic adaptations.

Conclusion: Rearing at 22°C does not have a lasting effect on metabolic adaptations to HFD at thermoneutrality, but it programs an enhanced capacity to respond to chronic cold challenges in adulthood. These findings highlight the need to consider rearing temperature when using mice to model cold-induced thermogenesis.

Introduction

There is a growing appreciation that housing rodents at an ambient temperature of 21-22°C (T_a 22) produces metabolic adaptations that diverge from human physiology³⁰⁹⁻³¹². Thus, there has been a call for more studies to be conducted at thermoneutrality. To comply with this recommendation, adult mice are typically acclimated to a T_a of 28-33°C for several weeks before the onset of the study. However, this experimental design does not consider potential developmental influences of rearing temperatures (T_r) below thermoneutrality on energy expenditure and systemic metabolism. Brown adipose tissue (BAT) thermogenesis is activated at parturition and is critical for survival outside the womb in humans and small mammals alike (reviewed in³¹³⁻³¹⁵). The thermogenic capacity of neonates is tuned to meet the demands imposed by the temperature of the extrauterine environment. Exposure to lower temperatures in the early postnatal period enhances cold responsiveness in humans³¹⁶, sheep³¹⁷, rabbits³¹⁸, rats³¹⁹ and mice²⁵⁴. In rodent models, effects of cold exposure during early development on thermogenic capacity persist to adulthood^{253,319-321}, while they only last a few weeks when T_a is manipulated in adulthood^{252,319,320}.

Thermogenesis is induced in response to cold²⁴⁶ and high fat diet (HFD) feeding³²²⁻³²⁴, both are dependent on the sympathetic nervous system (SNS)^{245,246,325,326}. SNS tone onto BAT is programmed in response to T_r ^{253,321}. This raises the possibility that developmental influences of T_r 22 in mice that are subsequently moved to thermoneutrality in adulthood could have unintended effects on thermal biology and/or susceptibility to diet-induced obesity. Here, we explore the impact of T_r 22 vs. T_r 30 on thermogenesis, metabolism and body weight in C57BL6/J mice exposed to cold and HFD.

Cold- and diet-induced thermogenic responses change over time. Both involve an initial acute activation phase, called facultative thermogenesis, that evolves into an adaptive phase during

chronic exposure³¹¹. Cellular processes and cell types engaged in these two phases are best characterized in the context of cold challenges. During facultative thermogenesis, cold activates sympathetic circuits that stimulate lipolysis, blood flow and uncoupled respiration in BAT within minutes^{112,327-330}. The thermal history of the animal determines the capacity for non-shivering thermogenesis; shivering thermogenesis compensates for any shortfall in the response^{311,331-333}. Metabolic acclimation to chronic exposure to cold takes 3-5 days³³⁴. During this adaptive period, increased thermogenic demand is met by recruiting thermogenic adipocytes^{158,328,335-337}. Longer cold exposures lead to remodeling within brown and beige adipose depots. Vascularization of thermogenic adipose tissue expands to increase the flow of oxygen and nutrients needed to support thermogenesis and to distribute the heat produced throughout the body³³⁸. Expansion of the vascular network through sprouting is dependent on SNS signals²⁶⁹. The density of sympathetic fibers in thermogenic adipose tissue increases in parallel to changes in the vasculature^{249,251,339,340}. These adaptations can be detected within 1 week and reach a peak within ~3 weeks^{249,251,339-341}. This is consistent with the idea that there are two phases of adaptive thermogenesis, an initial recruitment phase that primarily engages adipocytes, which is followed by a remodeling phase affecting the neurovascular architecture.

Here we assessed the effects of T_r on cold responses over hours, days and weeks by maintaining mice in metabolic cages throughout the entire study. We first compared responses in T_r22 vs. T_r30 mice to cold (14°C) exposure in adulthood. Then we utilized a similar strategy to assess the impacts of T_r on diet-induced thermogenesis at T_a30 .

Materials and Methods

1.3.4 Animals

Female and male C57BL/6J mice were maintained on a 12 h light: 12 h dark cycle in the Russ Berrie Medical Sciences Pavilion barrier facility with ad libitum access to chow (13.2% fat, 24.7% protein, 62.1% carbohydrate, metabolizable energy 3.07 kcal/g; PicoLab Rodent Diet 20, 5053 irradiated) and autoclaved drinking water unless otherwise indicated. One week before their expected delivery dates, pregnant dams were transferred to a Caron Diurnal Incubator (Catalog #6020) with ad libitum access to breeder chow diet (21.6% kcal from fat; PicoLab Rodent Diet 20, 5058 irradiated) and autoclaved drinking water. Incubators were maintained at a constant ambient temperature of either 22°C (T_{a22}) or 30°C (T_{a30}) on a 12 h light: 12 h dark cycle. We chose 30°C as a compromise between the thermoneutral zone of 13-20°C for lactating dams³⁴² and 34-38°C for pups³⁴³ in rats. While the thermoneutral zone for mouse pups has not been characterized, it is likely to be modestly (1-2°C) higher in mice^{344,345}. Mice were singly housed from weaning throughout the remainder of the study to eliminate contributions of social thermoregulation to thermal physiology³⁴⁶. All procedures were performed within the guidelines of the Institutional Animal Care and Use Committee at the Columbia University Health Science Division.

1.3.5 Responses to cooling

Experimental design (Figure 5A): Cold responsiveness is typically evaluated at a single time point involving an acute (several hours), severe (T_{a2-4}) challenge involving a temperature change of more than 17°C. In rodent models with impaired thermoregulation, this can elicit torpor^{339,347}. We used a milder temperature change of 8-10°C, which can be used to study thermoregulation in these systems^{339,347}. At 7 weeks of age, T_{r22} and T_{r30} offspring were transferred to the Oxymax/Comprehensive Lab Animal Monitoring System (CLAMS, Columbus Instruments),

which was used to measure total energy expenditure (TEE), respiratory exchange ratio (RER, CO₂ produced/ O₂ consumed), locomotor activity by ambulatory beam break and food intake. Mice were first allowed to acclimate to their new housing conditions at their respective T_r for 1 week. Then, all cages were maintained at T_a22 for 3 weeks to allow the T_r30 mice to fully acclimate to the new temperature^{249,339}. Finally, all cages were switched to T_a14 for 3 weeks. Body weights were recorded weekly in conjunction with cage changes, and the average body composition across weeks 6 and 7 were assessed (Bruker minispec). We excluded 7 out of 24 mice started in the experimental protocol due to failing sensors (4) or deaths due to a defect in the food hopper mechanism (3). Offspring in the two experimental groups were born 2 weeks apart. To match the ages for the cold challenge, T_r22 mice started and concluded the experiment two weeks before T_r30 mice.

Processing food intake data: Due to technical problems during the recording, food intake measurements contained sporadic artifacts. We used an unbiased approach to exclude these timepoints from our analyses. For each negative value at a given time point t , we added it to the value at $t+1$. If the result was positive, we replaced the value at t with 0, and $t+1$ with the result. If the result was negative, we replaced t with 0. We took the value at the 97.5th percentile of the distribution of all the food intake data points that were above zero and used it as a threshold for the whole dataset. We recomputed cumulative food intake using the processed dataset.

1.3.6 Responses to HFD

Experimental design (Figure 6A): At 8 wk, T_r22 and T_r30 offspring were transferred to CLAMS cages and maintained at T_a30 for the remainder of the study. After 2 weeks of acclimation, mice were fed HFD (Research Diet D12492 60% fat, 20% protein, 20% carbohydrate; metabolizable

energy 5.24kcal/g) for 6 weeks. To age-match the two experimental groups, T_r22 started HFD feeding a week after T_r30 mice. We excluded one mouse out of the 24 originally involved due to sensor failure.

Food intake measurements: The HFD was more prone to crumbling and could not be measured accurately with the CLAMS, so we manually measured food intake every 3-4 days. Body weights were recorded weekly in conjunction with cage changes, and body composition was assessed weekly (Bruker minispec).

1.3.7 Statistical analyses of CLAMS data (all experiments)

Processing EE data: All data were analyzed using R³⁴⁸. To adjust for different sampling frequencies across the experiment, data were down-sampled to a 1-hour sampling rate before analysis. TEE and RER were averaged across merged intervals, while locomotor activity was summed. When the time interval between two measurements was 26.25 minutes, one datapoint for every 8 consecutive datapoints was removed. To account for this missing data from analyses of locomotor activity, counts were scaled up by 1.142857 (derived from 30/26.25).

Linear modeling: Analysis of variance for mean weekly TEE, body weight, mean weekly locomotor activity, and mean food intake was performed using a linear mixed-effects model using lme4 (ver. 1.1.31,³⁴⁹) and lmerTest (ver. 3.1.3,³⁵⁰) packages. For each variable mentioned above, a model was built with rearing temperature, sex, experimental week, their pairwise interactions, and their three-way interaction as explanatory variables and accounting for repeated measures. These models were analyzed using the anova() function from R. Post-hoc tests were performed using multcomp (ver. 1.4.20,³⁵¹) package, comparing the two groups within each week, and *p* values were adjusted for multiple comparisons.

Quantification of EE components: We built a quadratic model using TEE as the dependent variable, and locomotor activity and its squared value as explanatory variables, as described ³⁵². The Y-axis intercept was taken as the TEE in the absence of physical activity. Thus, the energy expenditure related to physical activity (PAEE) was calculated by subtracting the Y-intercept from mean TEE. Thermic effect of food (TEF) was estimated based on diet composition and thermic effect of food for fat (2.5%), carbohydrate (7.5%), and protein (25%) (0.342 kcal/g for chow diet and 0.419 kcal/g for HFD) and total food ingested ³⁵³. This number was divided by the total number of hours in each dataset. Basal metabolic rate (BMR) was determined as the mean value of the TEE after subtracting PAEE and TEF during the light phase of the last day at T_a30 before the switch to HFD. Cold-induced thermogenesis (CIT) was computed by subtracting PAEE, TEF and BMR from TEE. Similarly, diet-induced thermogenesis (DIT) was calculated by subtracting PAEE, TEF and BMR from TEE. ANOVAs were performed for the absolute values of each component, as well as its proportional contribution to TEE. For each variable, a model was built with group (rearing temperature), experimental weeks, and their pairwise interactions as explanatory variables and accounting for repeated measures. These models were analyzed using the `anova()` function in R. Post-hoc tests were performed using the `multcomp` ³⁵¹ package, comparing the two groups within each week, and p values were adjusted for multiple comparisons. One mouse in the cold challenge dataset was excluded due to persistent food sensor failure.

Accounting for contributions from body weight: We performed ANCOVAs using bodyweight as a covariate, as recommended ^{354,355}. We calculated the mean TEE for each mouse and for each week. We then built linear mixed-effect model for both datasets using `lme4` ³⁴⁹ and `lmerTest` ³⁵⁰ packages with mean heat as the dependent variable and Group, weight, their interaction, and sex as explanatory variables, while accounting for repeated measures and for the weight change of the

animal at each week. These models were analyzed using the `anova()` function from R. Post-hoc tests were performed using `multcomp`³⁵¹ package, comparing the two groups within each week, and p values were adjusted for multiple comparisons.

1.3.8 Glucose homeostasis

After 6 weeks of HFD feeding at T_a30 , we performed glucose tolerance tests (GTT) in the morning after an overnight fast. We measured glycemia from the tail vein (FreeStyle Lite) at baseline and at 15, 30, 60, 90 and 120 minutes after i.p. injection of glucose (2g/kg of BW). We performed insulin tolerance tests (ITT) in the early afternoon in mice that were food-deprived for 4h. We measured glycemia from the tail vein at baseline and at 15, 30, 60, 90 and 120 minutes after i.p. injection of insulin (1IU/kg).

Results

1.4.1 Influence of rearing temperature on metabolic responses to a cold challenge

We examined effects of rearing mice from birth to 8 weeks at 22°C (T_r22) vs. 30°C (T_r30) on responses to a moderate decrease in ambient temperature from T_a22 to T_a14 (Figure 5A). Since T_r30 mice were maintained at 30°C, we first allowed them to acclimate to T_a22 °C for 3 weeks, when SNS and vascular remodeling of thermogenic adipose depots are complete^{340,341}.

2.4.1.1 Effects on body composition

Both sexes gained weight over the course of the study, and males gained more than females (Figures 5B). However, rearing temperature had no effect on body composition in either sex by the end of the study at T_a14 °C (Figures 5C-F).

2.4.1.2 Effects on energy expenditure

We compared responses in T_r22 vs. T_r30 mice to a change in temperature over three timescales: facultative thermogenesis (first 4 hours), thermogenic recruitment (first week) and remodeling period (third week). We did not detect sex differences at any timepoint. At their baseline rearing temperatures, T_r30 mice expended about half as much energy as T_r22 mice (Figures 5G-I, wk1, white shading). Within 1 hour of switching to 22°C , T_r30 mice increased TEE by 49% (Figure 5I) and maintained this level throughout the 3-week period (Figure 5J, wk2-4, light turquoise shading). T_r22 mice transiently increased TEE (Figure 5I), likely caused by the stress of the weekly cage change, but otherwise maintained a consistent output of ~ 0.4 kcal/h (Figure 5J). However, the average weekly TEE of T_r30 mice remained lower than their T_r22 counterparts throughout the $T_a22^\circ\text{C}$ exposure (Figure 5J, wk2-4, light turquoise shading).

Within one hour of the switch from T_a22 to T_a14 , T_r30 mice increased TEE by 48%, while T_r22 mice increased TEE by 40% (Figure 5I), thus producing similar acute responses (Figure 5I), which persisted throughout the first week (Figure 5J, wk5). After 2 weeks at $T_a14^\circ\text{C}$, T_r22 mice increased TEE by an additional 9.8% while T_r30 mice maintained the same levels throughout, resulting in a 9% difference between the groups (Figure 5J, wk7). At no point did we observe a decrease in TEE at the end of the dark cycle that is characteristic of torpor³⁵⁶⁻³⁵⁹. Differences detected at wk 1, 2, 4 and 7 with linear mixed-effect modeling remained significant (Figure 5K), even after including body weight as a covariate^{354,360,361}.

2.4.1.3 Partitioning of total energy expenditure

Contributions of PAEE, TEF, BMR, and CIT to TEE depend on T_a ³⁵². Thus, we assessed the effect of rearing temperature on each individual component, as well as its relative contribution to TEE

during sequential decreases in ambient temperature (see Methods “Quantification of EE components”). As we did not detect sex differences in the partitioning of TEE, we combined data from males and females in these analyses (Figure 5P-Q).

Average weekly locomotor activity decreased as mice were challenged with successively colder temperatures (Figures 5L-N). We observed a significant interaction between sex and time on locomotor activity (Figure 5N). This effect was driven by reduced activity in females in the baseline condition (Figure 5N). Not only did the absolute PAEE decrease at colder temperatures for all conditions (Figure 5P, green), but so did the proportional contribution of PAEE to TEE (Figure 5Q, green).

Decreases in ambient temperature had opposite effects on locomotor activity and food intake, with the latter increasing across the study, independent of sex (Figure 5O). While there was no effect of rearing temperature on caloric intake per se, it influenced changes in TEF across the experiment. This interaction is driven by increased TEF in T_r30 mice after longer exposures to $T_a14^\circ\text{C}$ (Figure 5P, wk 7).

As expected, CIT increased in all mice in response to progressive reductions in ambient temperature. Rearing temperature influenced this response, with less CIT in T_r30 mice across the study (Figure 5P, purple), but only in specific weeks. T_r30 mice exhibited reduced CIT in the first week after the initial 8°C drop from $T_a30^\circ\text{C}$ to $T_a22^\circ\text{C}$ (Figure 5P, wk2), but not after the second 8°C drop from $T_a22^\circ\text{C}$ to $T_a14^\circ\text{C}$ (Figure 5P). Then, strong effects of rearing temperature reemerged after prolonged (3wk) exposure to 14°C (Figure 5P, wk7).

We also evaluated changes in the proportional contributions to TEE at different ambient temperatures. At baseline in T_r30 mice, in the absence of CIT, BMR was $51.3\pm1.9\%$, TEF was $16.5\pm1.8\%$ and PAEE was $32.6\pm0.6\%$ of TEE (Figure 5Q). With successive cold challenges,

increases in CIT ($48.7 \pm 1.0\%$) were accompanied by proportional decreases in PAEE ($11.1 \pm 0.7\%$), resulting in a distribution that was similar to T_r22 mice (BMR: $22.9 \pm 0.6\%$, TEF: $16.3 \pm 1.9\%$, PAEE: $11.6 \pm 1.0\%$, CIT: $49.3 \pm 2.6\%$). While T_r22 mice were able to sustain this level of CIT after prolonged exposure to $T_a14^\circ\text{C}$ (CIT: $52.4 \pm 2.6\%$), T_r30 mice could not (CIT: $42.4 \pm 2.4\%$). They compensated for this by increasing the contribution from TEF ($24.9 \pm 3.1\%$).

In summary, rearing temperature did not influence acute (within 4h) responses to an 8°C drop in T_a . Rearing at 22°C produced a modest (0.5%), but consistent, enhancement in TEE that emerged after the first week of exposure to $T_a22^\circ\text{C}$. The largest impact of rearing at 22°C was to increase the capacity for TEE during longer (>2 wk) exposure to 14°C . T_r30 mice compensated for this deficit by increasing TEF.

1.4.2 Influence of rearing temperature on metabolic responses to HFD at thermoneutrality

Consumption of obesogenic diets are also associated with adaptations that increase BAT thermogenesis in an SNS-dependent manner^{237,246,296}. Given that T_r22 from birth to 8 weeks programs increased SNS tone^{253,321,339} and thermogenic responses to cold (section 2.4.1.2), we examined whether it also programs thermogenic and metabolic responses to HFD feeding for 6 weeks (Figure 6A). These studies were performed at 30°C to minimize contributions from CIT that could obscure thermogenic adaptations to the diet (DIT)^{322,323,328,362,363}. T_r22 mice were acclimated to 30°C for 2wk before the switch to HFD feeding.

2.4.2.1 Effects on body composition

Males weighed more than females and gained weight and adiposity over the course of the study (Figure 6B-D). Interactions between sex and rearing temperature enhanced weight gain in T_r30 males, but not females. Rearing temperature did not influence lean mass or adiposity.

2.4.2.2 Effects on glucose homeostasis

We evaluated the effect of rearing temperature on responses to glucose and insulin tolerance tests. We did not observe sex differences, so we merged the data. At baseline, blood glucose levels were higher in T_r30 mice (Figure 6E). Although we observed a consistent trend of impaired glucose tolerance in T_r30 mice, this did not reach significance (Figure 6F). Rearing temperature did not affect insulin tolerance (Figure 6G).

2.4.2.3 Effects on energy expenditure

We assessed TEE and RER at baseline on a chow diet and in the first 24 hours (acute period), first week (recruitment period) and the sixth week after the switch to HFD (remodeling period)(Figure 7A-D). We did not observe sex differences, so we merged the data. At baseline, average weekly TEE was not impacted by rearing temperature (Figure 7C). As expected, it increased in both groups across the period of HFD exposure (Figure 7C), which was driven by body weight (Figure 7E). Within 24 h of HFD feeding, TEE increased in both groups; this effect was enhanced in T_r22 mice (Figure 7F). Higher TEE in T_r22 mice was associated with a rapid switch to fat metabolism (RER=0.73±0.03), while T_r30 mice continued to favor carbohydrate metabolism (RER=0.80±0.03)(Figure 7I).

The effects of HFD on energy expenditure continued to evolve across the first week of exposure. In T_r22 mice, the initial phase of elevated TEE lasted for only 2 days, and gradually declined thereafter (Figure 7H). In contrast, T_r30 mice slowly increased heat production across the first week of HFD feeding. By the end of the week, T_r30 mice produced more heat than T_r22 mice (Figure 7G). At this time point, all groups primarily utilized fat for energy, but RER of T_r30 mice was now higher than T_r22 mice (Figure 7J). With longer (>2 week) exposure to HFD feeding, impacts of rearing temperature on heat production and RER were lost (Figure 7K).

2.4.2.4 Partitioning of total energy expenditure

We determined the BMR at baseline at T_a30 , after the 2-week acclimation period for T_r22 mice. Then we calculated contributions from PAEE and TEF to TEE. As the studies were conducted at T_a30 , CIT is negligible. The remaining EE was attributed to DIT. As we did not detect sex differences (Figure 7E), we combined data from males and females. Rearing temperature did not affect locomotor activity or food intake (Figure 8A-D).

On a chow diet at baseline, absolute contributions of PAEE and TEF to TEE were similar (Figure 8E, wk2, green and yellow). Both groups of mice responded to chronic HFD exposure by increasing DIT (Figures 8E, F). This adaptation was enhanced in T_r30 mice. Thus, the proportional contributions of PAEE and TEF to TEE decreased accordingly in both groups (Figure 8F). However, they were not impacted by rearing temperature (Figure 8E, F yellow).

In summary, effects of T_r on metabolic responses to HFD at T_a30 depend on the timeframe of the analysis. In the first 24h of HFD, a rapid switch to fat utilization in T_r22 mice is associated with a marked increase in TEE. This is reversed over the course of the first week, so that TEE is higher in T_r30 mice. However, these differences are gradually lost within 2 weeks of HFD feeding.

Discussion

We explored whether rearing at 22°C programs lasting effects on metabolic responses to cold or HFD. Our analyses reveal that the effect of rearing temperature on thermogenic adaptations depends on the nature, severity and chronicity of the challenge.

1.5.1 Rearing at 22°C enhances long-term adaptations to cold.

Cold responsiveness is typically evaluated by exposing T_r22 mice to an acute (<24h), severe (T_a 4) challenge by measuring changes in core body temperature and/or EE at a single timepoint. We analyzed mice continuously over 7 weeks in metabolic cages in which T_a was decreased in 8°C increments. While TEE increased with successive decreases in T_a, body weight was unchanged due to compensatory increases in food intake, as reported by others in mice³⁶⁴ and humans³⁶⁵. Both groups mounted similar acute responses to an 8°C decrease in T_a. This supports the idea that systems regulating shivering, the primary source of facultative thermogenesis^{311,330,333}, are not impacted by rearing temperature. This supports the idea that systems regulating shivering and thermogenic capacity at baseline^{311,331-333} are not impacted by rearing temperature.

Within 3-5 days of chronic cold exposure, recruitment of additional thermogenic capacity gradually replaces shivering thermogenesis^{311,334}. When acclimated at T_a22 for 3 weeks, responses to T_a14 were similar in all mice during the first week of the exposure, when CIT increased more than 2-fold (from ~0.12 kcal/h to ~0.27 kcal/h). This is consistent with a study with a similar design published by the Kozak group²⁵⁴.

Influences of rearing temperature on thermogenic responses to T_a14 emerged after 2 weeks. To meet this persistent challenge, T_r22 mice further increased TEE by ~10%, which was largely driven by increases in CIT (from ~0.27 kcal/h to ~0.33 kcal/h), with no difference in lean mass. While T_r30 mice mounted a robust response during the first week, they could not sustain it over 3 weeks.

They compensated for deficits in CIT by increased contributions from TEF, and not PAEE. The reliance on increased food intake to overcome deficits in CIT has also been reported by others^{352,364,366,367}. The emergence of this CIT deficit in T_r30 mice after 2 wk coincides with peak period of cold-induced remodeling of the SNS and vasculature^{251,340,341}. SNS innervation of BAT is sensitive to T_r²⁵³, supporting a causal link between programmed changes in SNS tone and impaired responses to chronic cold exposure. Experiments to directly test this hypothesis are an important area for future research.

1.5.2 Distinguishing between effects on thermogenic capacity vs. defended body temperature.

In contrast to the situation when all mice were acclimated to T_a22, mice switched from T_a30 to T_a22 at 8 weeks of age consistently produced less heat than mice reared and maintained at T_a22. This deficit cannot reflect an impairment in the thermogenic capacity of T_r30 mice, because they increased EE within 1 hour of switching to T_a14. This observation raises the possibility that reduced responsiveness in T_r30 mice is actively regulated. This is reminiscent of observations in rodents with genetic impairments in leptin signaling, who rapidly lose core body temperature when acutely challenged at T_a4³⁶⁸⁻³⁷⁰ but mount a robust thermogenic response when acclimated to T_a12-15 beforehand^{347,371}. Taken together, it is possible that diminished TEE in T_r30 mice at T_a22 reflects a defense of a lower body temperature (anapyrexia) and not deficits in BAT capacity *per se*.

1.5.3 Effects of rearing at 22°C on thermogenic responses to HFD change over time.

Both groups of mice increased TEE within 1 week of HFD exposure at T_a30, before any increase in body weight. Over the course of the experiment, TEE steadily increased in association with

body weight gain. The contribution of DIT to TEE increased from ~8.5% to ~23.5% across the 6 weeks on the diet. DIT was initially described in rats housed at T_a22 as a 20% increase in oxygen consumption that peaked within 2.5 days³⁷². T_r22 mice acclimated to T_a30 here and in a study from the Cannon and Nedergaard groups³⁷³ exhibited a similar pattern. While the maximal response of T_r30 mice was similar to T_r22 mice, the peak was not reached until 1 wk after the switch to HFD feeding. The delayed responsiveness of T_r30 mice to HFD feeding was also seen with respect to the switch to fat utilization, as reflected in RER. All differences between groups were lost within the second week of exposure. Our findings are consistent with reports in rats that cold acclimation to T_a5 accelerates the timing of the response to a cafeteria diet, but not its magnitude³⁷². Together, these studies highlight the importance of the timing of analyses on metabolic outcomes. Most studies examine DIT at a single timepoint. Had we chosen 24h, we would have reported that T_r22 mice had higher TEE, but we would have seen the opposite result if we had chosen a 1 wk timepoint.

1.5.4 Rearing at 22°C has a modest, but protective, effect on glucose homeostasis.

T_r30 increased susceptibility to diet-induced obesity in males, but not females. These findings are consistent with another study that examined the effects of rearing at sub-thermoneutral temperatures (T_r17 vs. T_r29) in mice²⁵⁴, but differ from a similar experiment in rats³⁷⁴. T_r22 males and females exhibited reduced baseline glycemia after 6 weeks of HFD feeding that is independent of effects on body weight and composition. This is reminiscent of reports that BAT activity in humans is associated with reduced glycemia¹.

1.5.5 Limitations

The thermoneutral zone in small mammals, such as rats and mice, is influenced by strain, diurnal phase, age and lactation status^{167,326,375,376}. In adult mice, it lies within a few degrees of 30°C^{112,167}, but is closer to 35°C in rat pups³⁴³. In contrast, lactating dams prefer cooler temperatures (below T_{a22})³⁴², and housing at higher temperature can reduce milk production and offspring body weight in some strains^{377,378}. Because we had staggered starts for our cohorts in indirect calorimetry, we needed to choose a single temperature at which CIT would be minimized. As we and others found that pups raised at warm temperatures spend less time next to their mothers³⁷⁹, we chose a temperature between what is ideal for pups and lactating dams. We did not observe an effect of T_{r30} on litter size or on body weight at weaning.

There are several additional limitations in the experimental design. Core body temperature was not measured. Rearing temperature could influence the defended body temperature, which would impact TEE^{352,380,381}. The study was likely underpowered to detect the modest effects of rearing temperature on HFD-induced obesity³⁸². Additionally, the 6-week exposure to HFD was too short to rule out an effect on diet-induced obesity in females and on glucose tolerance and insulin sensitivity in both sexes.

1.5.6 Summary and Future Research Questions

By performing these studies involving continuous measurements over many weeks, we uncovered important differences in the temporal dynamics, which should be incorporated into experimental designs. Rearing temperature influences the timing of increases in thermogenesis and a switch to fat utilization in the first week of HFD feeding. As these differences diminished over time, T_{r22} should not represent a major confound in studies of diet-induced obesity. Conversely, T_{r22} did not

affect CIT in the first week of T_r14 but enhanced adaptations that increase thermogenic capacity in response to longer (>2 wk) exposures. This timing is consistent with an effect on remodeling of the vasculature and SNS ^{249,251,339-341}, an important area for future research.

Mounting evidence supports the idea that BAT activity has beneficial metabolic effects, particularly in the context of high body mass index ^{1,133,187,383,384}. Systems that constrain adaptations to chronic cold exposure in mice reared at thermoneutrality could represent novel targets for increasing thermogenic activity in humans, who are also raised near thermoneutrality.

Author Contributions

S.L. and L.M.Z. designed the experiments. S.L. and A.L. ran the experiments and collected the raw data from the CLAMS. A.R.L. analyzed body composition and glucose homeostasis data and generated the figures. S.L. and A.R.L. contributed to early drafts of the manuscript. D.N. analyzed the CLAMS data. D.N. and L.M.Z. wrote the manuscript.

Acknowledgements

This work was funded by NIH/NIDDK 1R01 DK125094. This research was supported by the NIDDK Diabetes Research Center Support Grant P30 DK063608 for the Mouse Metabolic Function and Phenotyping Core.

Conflict of Interest

None declared.

Data availability

Raw data, codes, and statistics can be accessed at Mendeley Data under DOI:

10.17632/vvc66wr5d7.2.

Codes and statistics can also be accessed at <https://github.com/DanieleN90>.

Figures

Figure 1

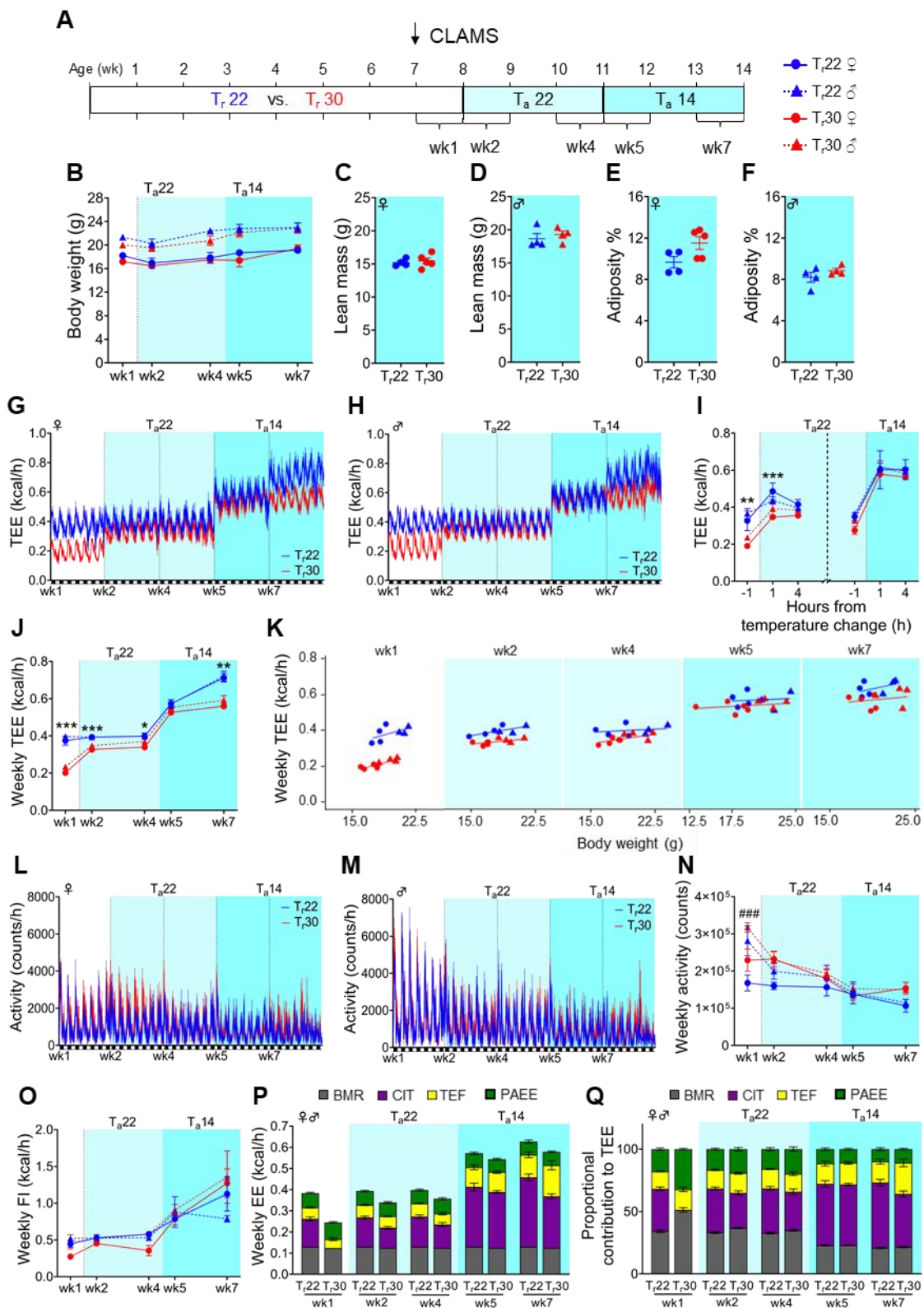


Figure 5. Rearing temperature does not affect body weight and composition during a chronic cold challenge

A. Schematic of the experimental design. Male (triangles) and female (circles) mice were reared at 22°C (Tr22, blue symbols) or 30°C (Tr30, red symbols) from birth until 8 weeks of age. During the last week of the rearing period, they were transferred to indirect calorimetry cages for acclimation (wk1). At 8 weeks of age, all mice were housed at 22°C for three weeks (wk2). At 11 weeks of age, ambient temperature was decreased to 14°C for three weeks (wk5). B. Body weights in the last week when mice were housed at their rearing temperature (wk1), 1 week after all mice were housed at 22°C (wk2), during the transition from 22°C (wk4) to 14°C (wk5), and at the end of the experiment (wk7). C-D. Body composition of females (C, E) and males (D, F); values for lean mass (C, D) and adiposity (E, F) represent an average of weeks 6 and 7 at Ta14. G-H. Total energy expenditure (TEE) across the experiment in female (G) and male (H) mice reared at 22°C vs. 30°C at baseline (wk1), across the 3 weeks at Ta22 (wk2 to wk5), and 3 weeks Ta14 (from wk5 to wk7). I. TEE at baseline rearing temperature 1 hour (-1h) before the temperature switch (to Ta22 and Ta14) and acute changes 1 and 4 hours afterward. J. Average weekly TEE across the rearing temperature transitions from baseline rearing temperatures (wk1) to Ta22 (wk2), from Ta22 (wk4) to Ta14 (wk5), and during the last week of the study (wk7). K. ANCOVA using body weight as a covariate showing the impact of rearing temperature on TEE across the same timepoints assessed in (J). L-M. Hourly locomotor activity across the experiment in females (L) and males (M). N. Total weekly locomotor activity. O. Weekly food intake (FI, kcal/h). P-Q. Components of EE, calculated based on contributions from basal metabolic rate (BMR, gray), cold induced thermogenesis (CIT, purple), thermic effect of food thermogenesis (TEF, yellow), and physical activity (PAEE, green). Absolute (P) and proportional (Q) contributions from each component were calculated from measurements pooled

from females and males Data are mean \pm s.e.m., B, I, J, and N through Q are ANOVAs on linear mixed-effects models, C through F are Wilcoxon rank sum test with continuity correction, K is an ANCOVA on linear mixed-effects model (, $p < 0.05$; **, $p < 0.01$; ***, $p < 0.001$ after post-hoc analysis between rearing temperatures; ###, $p < 0.001$ between sexes).*

Figure 2

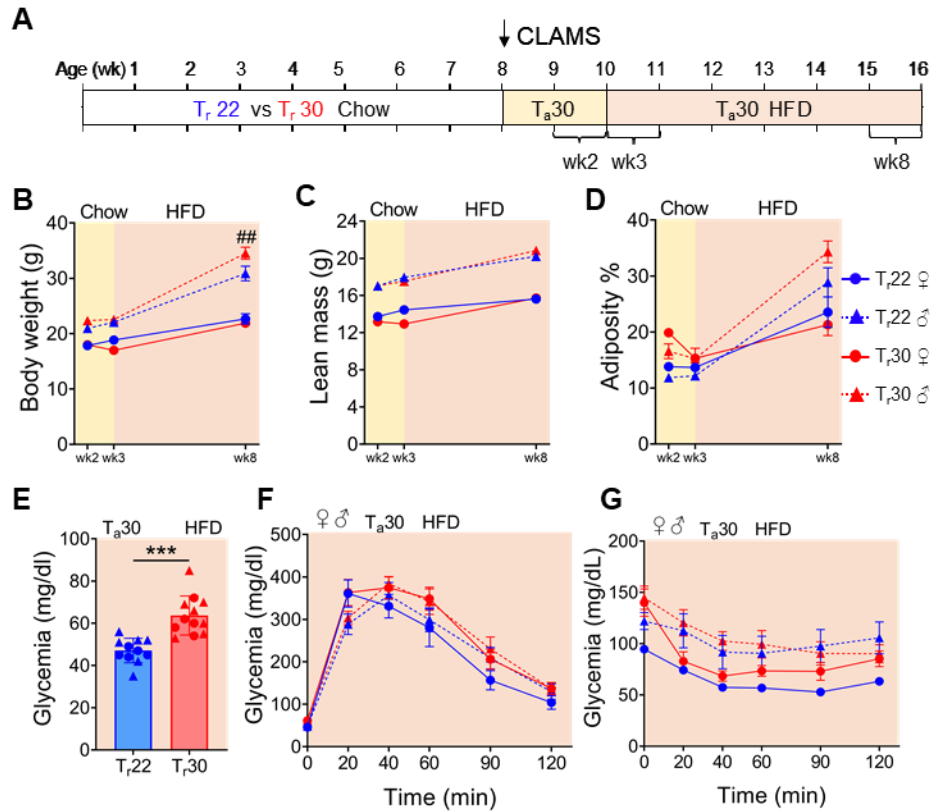


Figure 6. Rearing temperature affects baseline glycemia in mice fed a high fat diet at 30°C.

A. Schematic of the experimental design. Male (triangles) and female (circles) mice were reared at 22°C (Tr22, blue symbols) or 30°C (Tr30, red symbols) from birth until 8 weeks of age. Then they were transferred to indirect calorimetry cages maintained at 30°C (wk1). Two weeks later, all mice were fed a high fat diet (HFD) for 6 weeks. B-D. Body weight (B), lean mass (C) and percent adiposity (D) in mice housed at 30°C across the transition from regular chow (wk2) to HFD (wk3) and in the last week of the experiment (wk8). E-G. Baseline glycemia (E), glucose tolerance test (GTT) (F) and insulin sensitivity test (ITT) (G) after six weeks of HFD feeding at Ta30. For F-G, data were pooled from females and males for analysis (squares). Data are mean \pm s.e.m. B though D are ANOVAs on linear mixed-effect models (##, $p < 0.01$ between sexes after

*post-hoc analysis), E is a two-tailed unpaired t-test (***, $p < 0.001$), F and G are ANOVAs on linear mixed-effects models.*

Figure 3

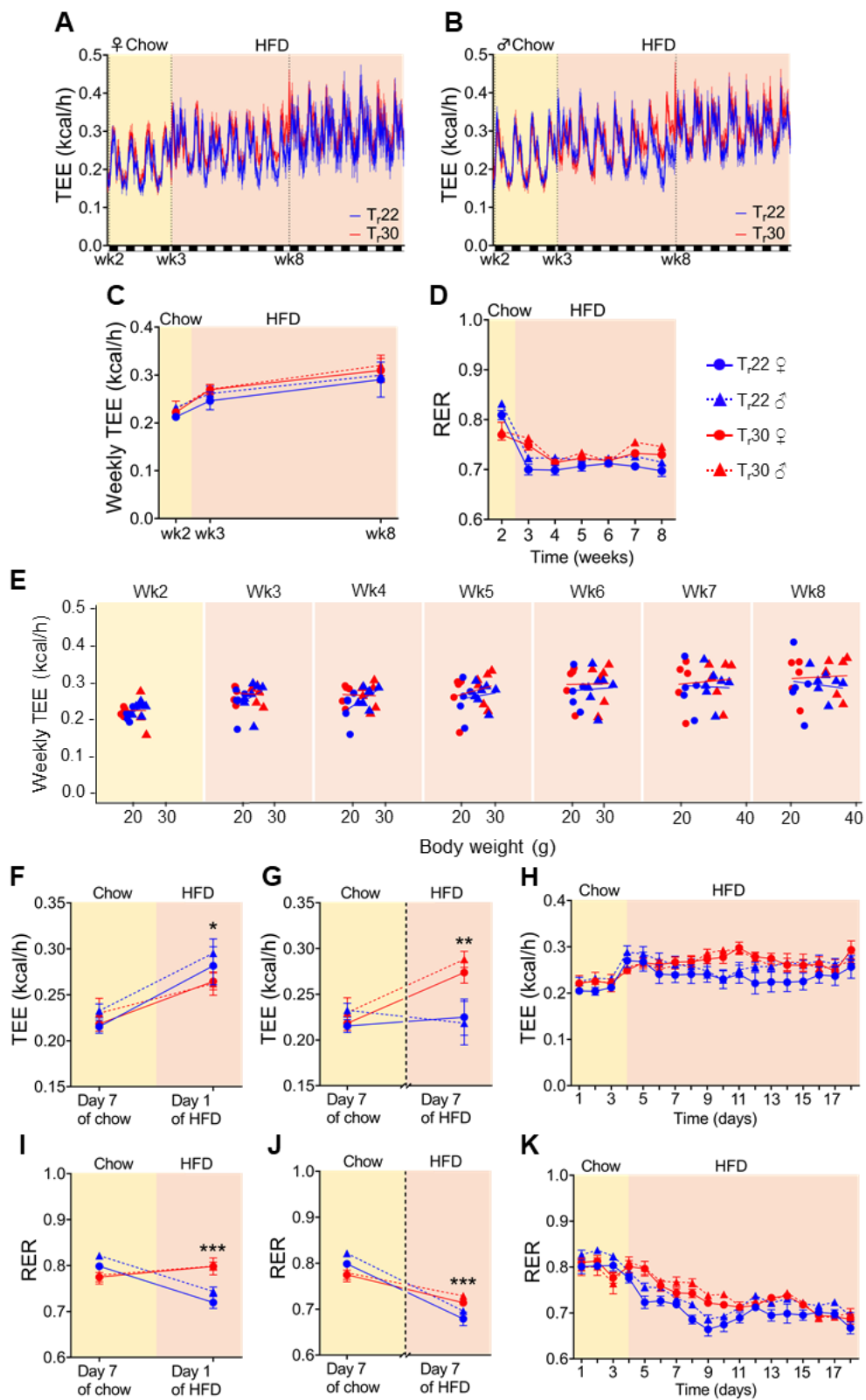


Figure 7. Rearing temperature programs lasting effects on metabolic responses to acute, but not chronic, feeding on high fat diet.

A-C. Hourly (A-B) and weekly (C) total energy expenditure (TEE) across the experiment in female (A) and male (B) mice reared at 22°C (Tr22, blue symbols) vs. 30°C (Tr30) that were maintained in indirect calorimetry cages at 30°C. Measurements when mice were fed a standard chow diet (wk2), after the switch to HFD (wk3) and during the last week of the challenge (wk8). D. Average weekly respiratory quotient (RER) on standard chow (wk2) and every week after the switch to HFD. E. ANCOVA using body weight as a covariate showing the impact of rearing temperature on TEE across the study. F-H. TEE during the transition from standard chow to HFD feeding across the first day (F), the first week (G), and the first two weeks (H) of exposure. I-K. RER during the transition from standard chow to HFD feeding across the first day (I), the first week (J), and the first two weeks (K) of exposure. Data are mean \pm s.e.m. C, F, G, I, and J are ANOVAs on linear mixed-effects models (, $p < 0.05$; **, $p < 0.01$; ***, $p < 0.001$ after post-hoc analysis between rearing temperatures), E is an ANCOVA on a linear mixed-effects model.*

Figure 4

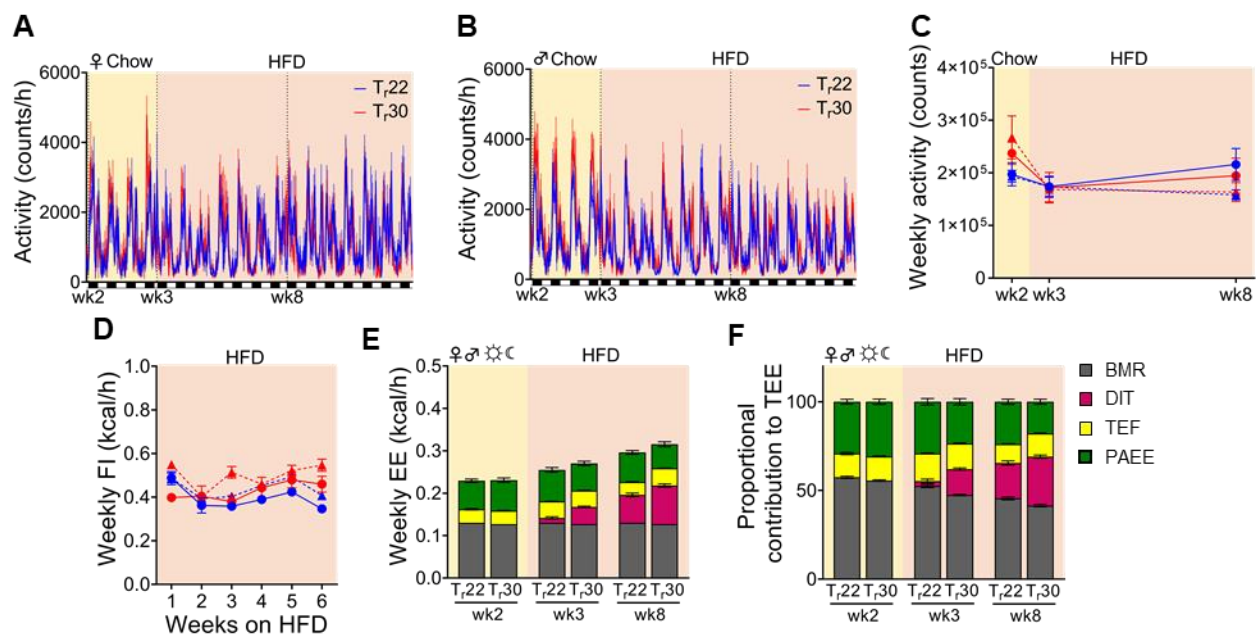


Figure 8. Rearing temperature influences short term adaptations to high fat diet feeding that dissipate with time

Effect of rearing at 22°C (Tr22, blue) vs. 30°C (Tr30, red) on components of total energy expenditure (TEE) under standard chow feeding at baseline (wk2), during the first week (wk3) and last week (wk8) of the HFD challenge at 30°C. A-B. Hourly locomotor activity across the experiment in females (A) and males (B). C. Total weekly locomotor activity. D. Weekly food intake (FI, kcal/h). E-F. Components of EE, calculated based on contributions from basal metabolic rate (BMR, gray), thermic effect of food (TEF, yellow), diet-induced thermogenesis (DIT, red) and physical activity (PAEE, green). Absolute (E) and proportional (F) contributions from each component were calculated from measurements pooled from females and males. Data are mean \pm s.e.m. C through F are ANOVAs on linear mixed-effect models.

1.6.1 Figure 5 Supplementary File

1B

Dependent variable	Independent variable	Sum of squares	Mean sum of squares	Degrees of freedom for numerator	Degrees of freedom for denominator	F value	Pr(>F)
Weekly body weight	Rearing Temperature	1.6877	1.6877	1	13	2.15	0.166
	Sex	35.0941	35.0941	1	13	44.77	<0.001
	Week	77.0051	19.2513	4	52	24.56	<0.001
	Rearing Temperature:Sex	0.1244	0.1244	1	13	0.16	0.697
	Rearing Temperature:Week	5.4995	1.3749	4	52	1.75	0.152
	Sex:Week	7.0695	1.7674	4	52	2.25	0.076
	Rearing Temperature:Sex:Week	2.2269	0.5567	4	52	0.71	0.589

1C

Wilcoxon rank sum test with continuity correction			
Variable	Sex	W	p-value
Lean Mass	F	7	0.556

1D

Lean Mass	M	6	0.686
-----------	---	---	-------

1E

Adiposity	F	4	0.191
-----------	---	---	-------

1F

Adiposity	M	5	0.486
-----------	---	---	-------

11

ANOVA, comparing 1h vs 4h intervals between the end of week 1 and the start of week 2							
Interval length	Independent variable	Sum of squares	Mean sum of squares	Degrees of freedom for numerator	Degrees of freedom for denominator	F value	Pr(>F)
1 hour	Week	0.1372	0.1372	1	13	87.07	<0.001
	Rearing Temperature	0.0205	0.0205	1	13	13.04	0.003
	Sex	0.0009	0.0009	1	13	0.57	0.464
	Week:Rearing Temperature	0.0004	0.0004	1	13	0.25	0.628
	Week:Sex	0.0033	0.0033	1	13	2.13	0.169
	Rearing Temperature:Sex	0.0012	0.0012	1	13	0.77	0.395
	Week:Rearing Temperature:Sex	0.0061	0.0061	1	13	3.85	0.072
4 hours	Week	0.0976	0.0976	1	13	73.40	<0.001
	Rearing Temperature	0.0225	0.0225	1	13	16.90	0.001
	Sex	0.0018	0.0018	1	13	1.37	0.262
	Week:Rearing Temperature	0.0199	0.0199	1	13	14.95	0.002
	Week:Sex	0.0028	0.0028	1	13	2.13	0.168
	Rearing Temperature:Sex	0.0006	0.0006	1	13	0.48	0.499
	Week:Rearing Temperature:Sex	0.0009	0.0009	1	13	0.71	0.414

Post-hoc analysis, p values			
Dependent variable	Contrast	End of week 1	Start of week 2
1 hour	Rearing Temperature	0.007	0.001
4 hours	Rearing Temperature	< 0.001	0.217

ANOVA, comparing 1h vs 4h intervals between the end of week 4 and the start of week 5							
Interval length	Independent variable	Sum of squares	Mean sum of squares	Degrees of freedom for numerator	Degrees of freedom for denominator	F value	Pr(>F)
1 hour	Week	0.5805	0.5805	1	13	99.46	<0.001
	Rearing Temperature	0.0051	0.0051	1	13	0.87	0.368
	Sex	0.0041	0.0041	1	13	0.71	0.415
	Week:Rearing Temperature	0.0036	0.0036	1	13	0.62	0.444
	Week:Sex	0.0001	0.0001	1	13	0.01	0.917
	Rearing Temperature:Sex	0.0029	0.0029	1	13	0.49	0.495
	Week:Rearing Temperature:Sex	0.0015	0.0015	1	13	0.26	0.619
4 hours	Week	0.5527	0.5527	1	13	281.89	<0.001
	Rearing Temperature	0.0091	0.0091	1	13	4.65	0.050
	Sex	0.0020	0.0020	1	13	1.03	0.329
	Week:Rearing Temperature	0.0016	0.0016	1	13	0.84	0.377
	Week:Sex	0.0018	0.0018	1	13	0.93	0.352
	Rearing Temperature:Sex	0.0014	0.0014	1	13	0.73	0.407
	Week:Rearing Temperature:Sex	0.0001	0.0001	1	13	0.02	0.881

1J

ANOVA							
Dependent variable	Independent variable	Sum of squares	Mean sum of squares	Degrees of freedom for numerator	Degrees of freedom for denominator	F value	Pr(>F)
Mean weekly TEE	Rearing Temperature	0.0119	0.0119	1	13	31.48	<0.001
	Sex	0.0007	0.0007	1	13	1.84	0.198
	Week	1.1557	0.2889	4	52	767.06	<0.001
	Rearing Temperature:Sex	0.0004	0.0004	1	13	0.96	0.345
	Rearing Temperature:Week	0.0532	0.0133	4	52	35.34	<0.001
	Sex:Week	0.0009	0.0002	4	52	0.62	0.650
	Rearing Temperature:Sex:Week	0.0002	0.0000	4	52	0.12	0.976

Post-hoc analysis, p values						
Dependent variable	Contrast	Week 1	Week 2	Week 4	Week 5	Week 7
Mean weekly TEE	Rearing Temperature	< 0.001	< 0.001	0.015	0.084	0.001

1K

ANCOVA							
Dependent variable	Independent variable	Sum of squares	Mean sum of squares	Degrees of freedom for numerator	Degrees of freedom for denominator	F value	Pr(>F)
Mean weekly TEE	Rearing Temperature	0.03192	0.03192	1	13.27	30.78	< 0.001
	Weight	0.00223	0.00223	1	10.63	2.15	0.171
	Sex	0.00000	0.00000	1	27.79	0.00	0.985

Post-hoc analysis, p values						
Dependent variable	Contrast	Week 1	Week 2	Week 4	Week 5	Week 7
Mean weekly TEE	Rearing Temperature	< 0.001	< 0.001	0.014	0.164	< 0.001

1N

ANOVA							
Dependent variable	Independent variable	Sum of squares	Mean sum of squares	Degrees of freedom for numerator	Degrees of freedom for denominator	F value	Pr(>F)
Weekly locomotor activity	Rearing Temperature	124656.100	124656.100	1	13	3.77	0.074
	Sex	102153.000	102153.000	1	13	3.09	0.102
	Week	5757280.000	1439320.000	4	52	43.57	<0.001
	Rearing Temperature:Sex	4827.109	4827.109	1	13	0.15	0.708
	Rearing Temperature:Week	284513.700	71128.430	4	52	2.15	0.087
	Sex:Week	924313.800	231078.400	4	52	7.00	<0.001
	Rearing Temperature:Sex:Week	66175.410	16543.850	4	52	0.50	0.735

Post-hoc analysis, p values						
Dependent variable	Contrast	Week 1	Week 2	Week 4	Week 5	Week 7
Weekly locomotor activity	Sex	< 0.001	0.957	0.806	0.979	1.000

10

ANOVA							
Dependent variable	Independent variable	Sum of squares	Mean sum of squares	Degrees of freedom for numerator	Degrees of freedom for denominator	F value	Pr(>F)
Weekly food intake	Rearing Temperature	0.009	0.009	1	13	0.14	0.711
	Sex	0.083	0.083	1	13	1.32	0.272
	Week	5.197	1.299	4	52	20.58	<0.001
	Rearing Temperature:Sex	0.165	0.165	1	13	2.61	0.130
	Rearing Temperature:Week	0.387	0.097	4	52	1.53	0.207
	Sex:Week	0.092	0.023	4	52	0.36	0.834
	Rearing Temperature:Sex:Week	0.202	0.051	4	52	0.80	0.530

1P

ANOVA							
Dependent variable	Independent variable	Sum of squares	Mean sum of squares	Degrees of freedom for numerator	Degrees of freedom for denominator	F value	Pr(>F)
PAEE	Rearing Temperature	0.000023	0.000023	1	14	0.19	0.666
	Week	0.001217	0.000304	4	56	2.58	0.047
	Rearing Temperature:Week	0.000655	0.000164	4	4	1.39	0.249
DIT-O	Rearing Temperature	0.000124	0.000124	1	14	0.19	0.672
	Week	0.070177	0.017544	4	56	26.42	<0.001
	Rearing Temperature:Week	0.007511	0.001878	4	56	2.83	0.033
CIT	Rearing Temperature	0.007130	0.007130	1	14.874	13.45	0.002
	Week	0.454540	0.113636	4	49.187	214.34	<0.001
	Rearing Temperature:Week	0.009790	0.003265	3	49.187	6.16	0.001

Post-hoc analysis, p values						
Dependent variable	Contrast	Week 1	Week 2	Week 4	Week 5	Week 7
DIT-O	Rearing Temperature	0.900	0.998	0.949	1.000	0.013
CIT	Rearing Temperature	/	0.023	0.140	0.622	<0.001

ANOVA							
Dependent variable	Independent variable	Sum of squares	Mean sum of squares	Degrees of freedom for numerator	Degrees of freedom for denominator	F value	Pr(>F)
PAEE, proportion	Rearing Temperature	0.009082	0.009082	1	14	15.56	0.001
	Week	0.224871	0.056218	4	56	96.32	<0.001
	Rearing Temperature:Week	0.055055	0.013764	4	56	23.58	<0.001
DIT-O, proportion	Rearing Temperature	0.008192	0.008192	1	14	4.26	0.058
	Week	0.038739	0.009685	4	56	5.03	0.002
	Rearing Temperature:Week	0.019329	0.004832	4	56	2.51	0.052
CIT, proportion	Rearing Temperature	0.014230	0.014230	1	14.903	7.70	0.014
	Week	0.454860	0.113715	4	49.049	61.57	<0.001
	Rearing Temperature:Week	0.018700	0.006233	3	49.049	3.37	0.026

Post-hoc analysis, p values						
Dependent variable	Contrast	Week 1	Week 2	Week 4	Week 5	Week 7
PAEE, proportion	Rearing Temperature	<0.001	0.377	0.062	0.998	0.950
DIT-O, proportion	Rearing Temperature	0.767	0.995	0.994	0.994	0.002
CIT, proportion	Rearing Temperature	/	0.039	0.2509	0.999	0.001

1.6.2 Figure 6 Supplementary File

2B

Dependent variable	Independent variable	Sum of squares	Mean sum of squares	Degrees of freedom for numerator	Degrees of freedom for denominator	F value	Pr(>F)
Weekly body weight	Rearing Temperature	1.2500	1.2500	1	19	0.29	0.595
	Sex	482.4200	482.4200	1	19	112.93	<0.001
	Week	810.4000	405.2000	2	44	94.86	<0.001
	Rearing Temperature:Sex	24.3900	24.3900	1	19	5.71	0.027

Post-hoc analysis, p values				
Dependent variable	Contrast	Week2	Week3	Week8
Weekly body weight	Sex	<0.001	<0.001	<0.001

Post-hoc analysis, p values					
Dependent variable	Contrast	Contrast subgroup	Week2	Week3	Week8
Weekly body weight	Rearing Temperature	F	0.428	0.940	0.97507
		M	0.994	0.542	0.00186

2C

ANOVA							
Dependent variable	Independent variable	Sum of squares	Mean sum of squares	Degrees of freedom for numerator	Degrees of freedom for denominator	F value	Pr(>F)
Weekly lean mass	Rearing Temperature	0.443	0.443	1	19	1.02	0.325
	Sex	82.349	82.349	1	19	189.70	<0.001
	Week	88.917	44.458	2	44	102.42	<0.001
	Rearing Temperature:Sex	1.214	1.214	1	19	2.80	0.111

Post-hoc analysis, p values				
Dependent variable	Contrast	Week2	Week3	Week8
Weekly lean mass	Sex	<0.001	<0.001	<0.001

2D

ANOVA							
Dependent variable	Independent variable	Sum of squares	Mean sum of squares	Degrees of freedom for numerator	Degrees of freedom for denominator	F value	Pr(>F)
Weekly adiposity	Rearing Temperature	0.003	0.003	1	19	1.84	0.191
	Sex	0.011	0.011	1	19	7.79	0.012
	Week	0.220	0.110	2	44	77.29	<0.001
	Rearing Temperature:Sex	0.004	0.004	1	19	2.53	0.128

Post-hoc analysis, p values				
Dependent variable	Contrast	Week2	Week3	Week8
Weekly adiposity	Sex	0.914	0.307	<0.001

2E

Welch two sample t test, two tails, unequal variances				
Assay performed	Time point	t	Degrees of freedom	p-value
GTT	0	5.19	18.679	<0.001
	20	0.68	20.568	0.507
	40	1.74	19.810	0.097
	60	2.00	19.570	0.059
	90	1.61	20.933	0.122
	120	1.51	19.964	0.146

2F

ANOVA							
Assay performed	Independent variable	Sum of squares	Mean sum of squares	Degrees of freedom for numerator	Degrees of freedom for denominator	F value	Pr(>F)
GTT	Rearing Temperature	6318.0	6318.0	1	20	3.64	0.071
	Sex	323.0	323.0	1	20	0.19	0.671
	Time	1811502.0	362300.0	5	110	208.99	<0.001

2G

ANOVA							
Assay performed	Independent variable	Sum of squares	Mean sum of squares	Degrees of freedom for numerator	Degrees of freedom for denominator	F value	Pr(>F)
ITT	Rearing Temperature	335.0	334.6	1	19	1.58	0.224
	Sex	1849.0	1848.6	1	19	8.72	0.008
	Time	36797.0	7359.4	5	105	34.73	<0.001

1.6.3 Figure 7 Supplementary File

3C

ANOVA							
Dependent variable	Independent variable	Sum of squares	Mean sum of squares	Degrees of freedom for numerator	Degrees of freedom for denominator	F value	Pr(>F)
Mean weekly TEE	Rearing Temperature	0.0005	0.0005	1	19	0.79	0.386
	Sex	0.0003	0.0003	1	19	0.52	0.480
	Week	0.0747	0.0373	2	44	59.38	<0.001
	Rearing Temperature:Sex	0.0001	0.0001	1	19	0.10	0.756

3E

ANCOVA							
Dependent variable	Independent variable	Sum of squares	Mean sum of squares	Degrees of freedom for numerator	Degrees of freedom for denominator	F value	Pr(>F)
Mean weekly TEE	Rearing Temperature	0.00020	0.00020	1	103.93	0.49	0.487
	Weight	0.00814	0.00814	1	17.85	20.27	<0.001
	Sex	0.00035	0.00035	1	23.27	0.88	0.358
	Rearing Temperature:Weight	0.00078	0.00078	1	142.84	1.94	0.166

3F

ANOVA, 24h before and 24h after HFD							
Dependent variable	Independent variable	Sum of squares	Mean sum of squares	Degrees of freedom for numerator	Degrees of freedom for denominator	F value	Pr(>F)
Mean TEE	Rearing Temperature	0.0005	0.0005	1	21	1.37	0.255
	Diet	0.0304	0.0304	1	21	81.73	<0.001
	Rearing Temperature:Diet	0.0019	0.0019	1	21	5.08	0.035

Post-hoc analysis, p values, 24h before and 24h after HFD				
Dependent variable	Tr22 Chow vs Tr30 Chow	Tr22 HFD vs Tr30 HFD	Tr22 Chow vs Tr22 HFD	Tr30 Chow vs Tr30 HFD
Mean TEE	1.000	0.137	<0.001	<0.001

Welch two sample t test, two tails, paired heat gain 24h before and 24h after HFD			
Dependent variable	t	Degrees of freedom	p-value
Mean TEE	2.30	18.377	0.033

3G

ANOVA, 24h before HFD and last 24h of the first week under HFD							
Dependent variable	Independent variable	Sum of squares	Mean sum of squares	Degrees of freedom for numerator	Degrees of freedom for denominator	F value	Pr(>F)
Mean TEE	Rearing Temperature	0.0077	0.0077	1	21	7.37	0.013
	Diet	0.0080	0.0080	1	21	7.61	0.012
	Rearing Temperature:Diet	0.0107	0.0107	1	21	10.18	0.004

Post-hoc analysis, p values, 24h before HFD and last 24h of the first week under HFD				
Dependent variable	Tr22 Chow vs Tr30 Chow	Tr22 HFD vs Tr30 HFD	Tr22 Chow vs Tr22 HFD	Tr30 Chow vs Tr30 HFD
Mean TEE	1.000	<0.001	0.987	<0.001

Welch two sample t test, two tails, paired heat gain 24h before HFD and last 24h of the first week under HFD			
Dependent variable	<i>t</i>	Degrees of freedom	p-value
Mean TEE	-3.26	18.326	0.004

3I

ANOVA, 24h before and 24h after HFD							
Dependent variable	Independent variable	Sum of squares	Mean sum of squares	Degrees of freedom for numerator	Degrees of freedom for denominator	F value	Pr(>F)
Mean RER	Rearing Temperature	0.0018	0.0018	1	21	2.58	0.123
	Diet	0.0093	0.0093	1	21	13.36	0.001
	Rearing Temperature:Diet	0.0284	0.0284	1	21	40.60	<0.001

Post-hoc analysis, p values, 24h before and 24h after HFD				
Dependent variable	Tr22 Chow vs Tr30 Chow	Tr22 HFD vs Tr30 HFD	Tr22 Chow vs Tr22 HFD	Tr30 Chow vs Tr30 HFD
Mean RER	0.016	<0.001	<0.001	0.193

Welch two sample t test, two tails, paired heat gain 24h before and 24h after HFD			
Dependent variable	<i>t</i>	Degrees of freedom	p-value
Mean RER	-5.24	17.037	<0.001

3J

ANOVA, 24h before HFD and last 24h of the first week under HFD							
Dependent variable	Independent variable	Sum of squares	Mean sum of squares	Degrees of freedom for numerator	Degrees of freedom for denominator	F value	Pr(>F)
Mean RER	Rearing Temperature	0.0000	0.0000	1	21	0.01	0.932
	Diet	0.0910	0.0910	1	21	183.71	<0.001
	Rearing Temperature:Diet	0.0132	0.0132	1	21	26.72	<0.001

Post-hoc analysis, p values, 24h before HFD and last 24h of the first week under HFD				
Dependent variable	Tr22 Chow vs Tr30 Chow	Tr22 HFD vs Tr30 HFD	Tr22 Chow vs Tr22 HFD	Tr30 Chow vs Tr30 HFD
Mean RER	0.004	0.007	<0.001	<0.001

Welch two sample t test, two tails, paired heat gain 24h before HFD and last 24h of the first week under HFD			
Dependent variable	<i>t</i>	Degrees of freedom	p-value
Mean RER	-5.12	19.387	<0.001

1.6.4 Figure 8 Supplementary File

4C

ANOVA							
Dependent variable	Independent variable	Sum of squares	Mean sum of squares	Degrees of freedom for numerator	Degrees of freedom for denominator	F value	Pr(>F)
Weekly locomotor activity	Rearing Temperature	1736690589	1736690589	1	19	1.00	0.329
	Sex	337845	337845	1	19	0.00	0.989
	Week	49082550124	24541275062	2	44	14.19	<0.001
	Rearing Temperature:Sex	1830152999	1830152999	1	19	1.06	0.317

4E

ANOVA							
Dependent variable	Independent variable	Sum of squares	Mean sum of squares	Degrees of freedom for numerator	Degrees of freedom for denominator	F value	Pr(>F)
PAEE	Rearing Temperature	0.000112	0.000112	1	21	1.02	0.324
	Week	0.000588	0.000294	2	42	2.67	0.081
	Rearing Temperature:Week	0.001048	0.000524	2	42	4.75	0.014
TEF	Rearing Temperature	0.000082	0.000082	1	21	0.96	0.337
	Week	0.000539	0.000269	2	42	3.18	0.052
	Rearing Temperature:Week	0.000422	0.000211	2	42	2.49	0.095
DIT	Rearing Temperature	0.003162	0.003162	1	21	4.02	0.058
	Week	0.031436	0.031436	1	21	39.94	<0.001
	Rearing Temperature:Week	0.000045	0.000045	1	21	0.06	0.812

Post-hoc analysis, p values				
Dependent variable	Contrast	Week 2	Week 3	Week 8
PAEE	Rearing Temperature	0.823	0.307	0.153

4F

ANOVA							
Dependent variable	Independent variable	Sum of squares	Mean sum of squares	Degrees of freedom for numerator	Degrees of freedom for denominator	F value	Pr(>F)
PAEE	Rearing Temperature	0.005962	0.005962	1	21	3.62	0.071
	Week	0.097325	0.048662	2	42	29.54	<0.001
	Rearing Temperature:Week	0.021096	0.010548	2	42	6.40	0.004
TEF	Rearing Temperature	0.000281	0.000281	1	21	0.28	0.599
	Week	0.011397	0.005698	2	42	3.66	0.034
	Rearing Temperature:Week	0.003971	0.001986	2	42	1.28	0.290
DIT	Rearing Temperature	0.024796	0.024796	1	21	4.93	0.038
	Week	0.259875	0.259875	1	21	51.62	<0.001
	Rearing Temperature:Week	0.005391	0.005391	1	21	1.07	0.313

Post-hoc analysis, p values				
Dependent variable	Contrast	Week 2	Week 3	Week 8
PAEE	Rearing Temperature	0.814	0.034	0.020
DIT	Rearing Temperature	\	0.026	0.198

**Chapter 3: Measuring real-time temperature and blood flow
changes in brown adipose tissue in anesthetized mice**

The study presented here was originally developed and designed by me and L.Z., with experiments conducted by Danya M. Jacobs (D.M.J.) and Lindsay Brandwein (L.B.) under my supervision. I performed the analysis and generated the figure, and I and L.Z. wrote the manuscript. We plan to submit this manuscript as a methods paper in the following months.

Abstract

The study of brown adipose tissue (BAT) has seen significant growth over the past decade due to its critical role in overall health. BAT is predominantly studied in rodents, with interscapular BAT (iBAT) being the most prominent depot in mice. Temperature and blood flow changes are the primary parameters used to measure iBAT activation. However, researchers have often been limited to measuring only one of these parameters at a time, hindering a comprehensive understanding of the coordinated control of iBAT activity. Additionally, measuring BAT activity in awake or anesthetized mice presents challenges: handling awake animals can induce stress-related hyperthermia due to sympathetic activation, while commonly used inhaled anesthetics directly suppress the SNS. Injectable anesthetics, on the other hand, can lead to high variability and inconsistency in the depth of anesthesia. Here, we present a novel protocol that allows for the concurrent recording of local iBAT temperature and blood flow changes in anesthetized mice. We use a combination of intraperitoneal injection and intravenous perfusion of 2,2,2-Tribromoethanol to induce and maintain a stable depth of anesthesia. We record key parameters from three different devices, integrating and analyzing the results through computer programming. Using this protocol, we tested two stimulants, revealing new insights into the coordination of thermogenesis and blood flow in mouse iBAT. This method provides a comprehensive tool for studying BAT function and its regulatory mechanisms, potentially advancing therapeutic strategies for metabolic diseases.

Introduction

Brown adipose tissue (BAT) research has gained significant momentum in the last decade due to its relationship with health health^{1,203}. BAT is almost exclusively present in mammals, making rodents ideal candidates for studying BAT function. In mice, the interscapular BAT (iBAT) is the most prominent depot^{2,385}.

BAT is primarily known for thermogenesis, a process in which uncoupling protein 1 (UCP1) facilitates the flow of protons across the two sides of the inner mitochondrial membrane. UCP1 dissipates the proton gradient generated by the electron transport chain, producing heat instead of regenerating ATP from ADP. As such, thermogenesis serves as a key indicator for measuring BAT activity. This process requires a consistent flux of metabolizable substrates to feed into the electron transport chain, necessitating brown adipocytes to extract glucose and fatty acids from systemic circulation to sustain thermogenesis³⁸⁶.

Blood flow regulation in BAT is tightly controlled, especially during activation, to supply oxygen and metabolites while dissipating the heat produced during thermogenesis. BAT activity is primarily regulated by adrenergic receptors, which are activated upon norepinephrine (NE) release from the sympathetic nervous system (SNS).

The β_3 subtype is the most abundantly expressed adrenergic receptor in BAT, and is considered the primary receptor involved in thermogenesis¹⁶⁹. However, other receptors from both the α - and β - families have also demonstrated roles in this process⁴⁶. The specific adrenergic receptors regulating blood flow remain unclear, with some studies highlighting the β_2 ³⁸⁷ subtype while others point to the α family subtype³⁸⁸. Even though the mechanisms underlying blood flow regulation in BAT are still unclear, it has been established that local blood flow changes during BAT activation, making these changes a valuable indicator of BAT activity³⁸⁹. Unraveling the

mechanisms of blood flow regulation in BAT could provide new insights into BAT activity and potentially lead to novel therapeutic strategies for addressing metabolic disorders.

Numerous methods exist to measure thermogenesis and blood flow changes in mice following iBAT stimulation (reviewed in Meyer et al.²⁷⁴). A common approach for assessing iBAT thermogenesis involves measuring core body temperature in awake mice. However, this method requires repeated handling of the animals, which can induce stress-related thermogenesis³⁹⁰—an effect independent of BAT thermogenesis—and there may be a significant delay between the onset of iBAT thermogenesis and its impact on whole body temperature. Another non-invasive option is to use thermal cameras to focus on the interscapular region³⁹¹. Nevertheless, this method suffers from high variability, even within the same subject, as animal positioning relative to the camera can influence readings, and fur density and type can increase variability between subjects. Finally, implantable transponders coupled with probes are also widely used in the literature³⁹². While this method is more accurate, it is labor-intensive for researchers and invasive for the mice, and the devices are prone to displacement during post-surgery recovery. Blood flow in mice has been measured using Laser Doppler Imaging¹⁶⁸, Computer Tomography^{389,393}, or major vessel cannulation³⁹⁴. Similar to temperature quantification, each method has its advantages and limitations. While whole-body imaging and surgical techniques can yield precise and reliable data, they can be invasive, such as in the case of cannulation, or require specialized equipment that is not commonly available. Laser Doppler Imaging is user-friendly, safe, and capable of providing reliable and repeatable results¹⁶⁸.

Anesthesia can significantly confound the recording of temperature and blood flow in mice. The most commonly used anesthesia methods are inhalants and injectable drugs³⁹⁵. Isoflurane is the most popular inhalant anesthetic, known for its fast induction, consistent maintenance of depth,

and rapid reversal. However, isoflurane activates gamma-aminobutyric acid receptors and reduces excitatory synaptic transmission³⁹⁶, leading to suppression of autonomic responses. Consequently, isoflurane can directly inhibit SNS activity³⁹⁷, blocking SNS-induced BAT activation. Injectable anesthetics do not exhibit the same depressive effects on nerve activity. However, careful calculation of dosage based on mouse weight is essential, as the anesthesia plane is not constant over time—deeper immediately after injection and shallower later on³⁹⁸. This lack of a stable anesthesia plane can result in systemic arousal, leading to inconsistent recordings. Ketamine, a popular injectable agent, stimulates the SNS centrally^{399,400} and induces thermogenesis, making it unsuitable for recording physiological BAT thermogenesis. 2,2,2-Tribromoethanol (TBE) is a safe, widely used, and inexpensive injectable anesthetic that does not exhibit the SNS excitatory effects associated with ketamine (review by Meyer and Fisher⁴⁰¹). Although TBE is not recommended for chronic use due to its association with abdominal inflammation, it is well suited for acute, terminal experiments. Therefore, we chose TBE as our anesthetic of choice. After inducing anesthesia induction via IP injection, we maintain stable levels of anesthesia by providing a constant flow of TBE through intravenous (IV) perfusion. This combination of IP induction and IV perfusion allows for stable recordings lasting over one hour.

Despite the wide array of technologies to quantify changes in iBAT temperature and blood flow, no method has previously allowed for the simultaneous quantification of both signals from the same animal. Here, we present a protocol for recording both local iBAT temperature and blood flow changes in anesthetized mice. Additionally, we can measure core body temperature and local subcutaneous lower back temperature, allowing us to integrate these with iBAT temperature changes to evaluate thermogenic effects on different body regions. Using these

protocol, we tested a range of known and theorized iBAT activity stimulants, unveiling new insights into the coordination of thermogenesis and blood flow in mouse iBAT.

Protocol

All procedures were performed within the guidelines of the Institutional Animal Care and Use Committee at the Columbia University Health Science Division under protocol number AC-AABM6560 and AC-AABN3553.

1.6.5 Anesthetic preparation

NOTE: TBE is sensitive to light and oxygen. Avoid unnecessary and prolonged environmental exposure.

1. Prepare a stock solution of 50% TBE in 2-Methyl-2-butanol (w/v). Warm the solution up to 37°C while rotating or shaking to ensure TBE is fully dissolved. This solution can be kept at 4°C for up to 3 months.
2. Prepare the anesthetic working solution. Warm double-distilled water (ddH₂O) to 37°C, then dilute stock solution in ddH₂O to reach a final concentration of 5% (v/v). The stock solution will not mix immediately with ddH₂O. Warm the working solution up to 37°C while rotating or shaking until the solution looks clear and homogeneous.
3. Filter the solution using a 20 µm filter. This solution can be kept at 4°C for up to 2 weeks.

1.6.6 Set up the heatpad

1. Turn on the heatpad from the button on the Bluetooth Communication Module.
2. Turn on the associated tablet. Open the app provided by the supplier to establish a connection between the tablet and the heatpad.
3. Click on the thermometer icon on top right, set the temperature to “heatpad” and set it at 35°C. The heatpad will adjust itself to keep a constant surface temperature of 35°C.
4. Set the app to visualize the surface temperature and rectal temperature.
5. Connect the rectal probe to heatpad. Verify that the system is working by touching the tip of the probe with your finger; the temperature on the app should show increased temperature.
6. Wrap the heatpad with one layer of tinfoil. We have observed interferences between currents from the metal plates for electrocardiogram present on the heatpad, and the signal received from the thermometer (explained later). Tinfoil will prevent these interferences.
7. Place the heatpad inside of the base of the desktop stand of the laser doppler imager. You don't need to place the imager on its stand yet.

1.6.7 Set up the thermocouple meter

1. Turn on the thermocouple meter and ensure that all the relevant probes are attached. We use two flexible, high-sensitive probes for the mouse, and one more durable probe to measure environmental temperature changes.
2. On the thermocouple meter display, adjust the range to “0°C - 100°C” option.
3. Adjust the digital filtration rate to 1.2s. This passage helps smooth out the signal from the meter without significant temporal accuracy loss.
4. Test the thermal probes are properly functioning by holding the tip of each probe between your thumb and index and observing the temperature going up to 33°C-35°C on the display of the meter.

1.6.8 Connect the thermocouple meter to a computer via a data acquisition system

1. Connect four BNC coaxial cables to the meter, one per channel.
2. Connect the coaxial to terminal block adapters to the other end of each cable.
3. Insert a jumper cable into each opening of the terminal.

4. Insert the other ends of the jumper cables in the Data Acquisition (DAQ) device. Connect signal cable from channel 1 to “FIO4” on the device, and its relative ground to “GRN” on the block of the DAQ device. Connect only the signal cable from channel 2 to “FIO5”. You do not need to connect the ground cable of channel 2. Similarly, connect signal and ground of channel 3 to “FIO6” and “GRN” of the same block, respectively, and only the signal cable of channel 3 to “FIO7”.

5. Connect DAQ device to the computer via USB cable.

6. Open the LJControlPanel software to establish a connection between the system and the computer. Click on “Find Devices (F3)” to detect the DAQ device. Once the device appears on the left side of the software interface, click on it to select it.

7. Click on “Config. Defaults”. Under the “Analog Input” tab, check only FIO4 through 7, and uncheck any other box. Click on “Write Values” and close the window.

8. Click on “Test”. In the new window, under the “Flexible I/O” tab, ensure that for FIO4 through 7 “AIN” is selected (analog input). You can click on “Exit” to close this window, and then close the ControlPanel software.

9. Open the LJLogUD software. There should be “No Error” under the “Error Message” field.

10. Under the “# Channels” select 4.

11. Set “Interval (ms)” to 200 to match the sampling rate from the thermocouple meter.
12. Go to the “+Ch” column and, in the first four rows, set the values to 4 through 7, reflecting the FIO4 through 7 that we set up earlier.
13. For each one of the four rows, set the “Scaling Equation” to “ $y=20x$ ”. For example, for the first row, it will read “ $y=20a$ ”, for the second row it will read “ $y=20b$ ” and so on. Check the values under the “Scaled” column and ensure that they correspond to the values on the thermocouple meter display. You should test this by holding the tip of one of the thermal couples in your hand and observing the change in temperature.
14. Set the “Max File Size (Bytes)” to at least 10 MB to avoid unexpected interruptions.
15. Click on “Change Working Directory” and set it to the folder you prefer.
16. Set “Data File Prefix” with any name that helps you identify the next recording.

1.6.9 Prepare the continuous perfusion of anesthetic

1. Warm up approximately 2 mL of working solution of TBE
2. Break in two parts the needle of 30G syringe using a pair of curved hemostats.

3. Cut approximately 30cm of PE10 tube.
4. Fit the blunt end of the needle in one end of the PE10 tube, and the blunt end of the base of the syringe to the other extremity of the tube.
5. Flush a Heparin solution (1mg/mL in saline) through the tubing to ensure coating, then flush air to remove excess solution.
6. Fill a 1 mL syringe with TBE working solution and prime it to remove any bubble.
7. Connect the syringe to the tubing you prepared. Prime the system to get rid of any air bubble.
8. Place the syringe on the perfusion pump and ensure the plunger is connected to the system.
9. Turn on the pump and set the parameters to match the volume and manufacturer of the syringe.
10. Set the perfusion rate to 8.8 μ L per gram of animal per hour. Use Figure 10 as a reference for your set up.

1.6.10 Prepare the animal for recording

1. Weight the animal. Inject intraperitoneally (IP) 16 μL of pre-warmed TBE working solution per gram of mouse (e.g.: a 20g mouse is injected with 320 μL).
2. Ensure the animal is completely under anesthesia via absence of toe pinch reflex.
3. Move the mouse to a heatpad and apply eye ointment.
4. Shave the interscapular region, and the right quadrant of the lower back of the animal with an electric razor. Remove loose hairs with a wet napkin.
5. Apply hair remover cream on the shaved interscapular region using a cotton tip applicator. Wait 30s, then remove the cream. The skin on the interscapular region should appear completely smooth and hairless.
6. Visually estimate the position of the interscapular fat pad based on the shoulder blades. Cut the skin of the mouse with a 3cm horizontal incision caudal to the estimate position of the fat pad, close to the curvature of the back of the animal. This incision would prevent the doppler from reading blood flow, so you want to cut as far away as possible from the fat pad, but not too far to make it excessively hard to insert thermal probes in the next passage.
7. Use scissors to gently dissociate the skin from the interscapular from the fat pad. Identify the caudal part of the interscapular fat pad. Use fine scissors to cut a small incision (<1cm) between

the caudal part of the fat pad and the connective tissue around, just enough to be able to lift the fat pad and visually inspect the brown adipose tissue on the ventral side of the fat pad.

8. Cut a small incision in the lower back area that you shaved previously. Use the tip of your scissor to dissociate the skin from the tissue underneath.

1.6.11 Set up the recording

1. Bring the animal to the heatpad prepare in section 2. Place the animal in a prone position on the heatpad and tape the four limbs spread out to avoid passive movements of the mouse during probe placement.

2. Insert the rectal probe and tape the exposed end to ensure stability. You can cover the tip of the probe with glycerol to ease the insertion. Confirm probe placement on the tablet, the probe should have gone from room temperature to $\sim 35^{\circ}\text{C}$, reflecting the internal temperature of the animal.

3. Apply the needle from the perfusion system into one of two lateral tail veins. You can apply a napkin soaked in warm water for 60-120s around the tail to cause vasodilation to help with insertion. Confirm a successful insertion by applying soft pressure on the tail, upstream of the needle placement, and observing an influx of blood inside the perfusion tubing. In case of unsuccessful tail vein application, you can insert the needle in the abdomen, resorting to IP perfusion. We found no significant difference in IP vs IV perfusion for recordings below 45 min of length.

4. Estimate the distance between the center of the interscapular brown adipose tissue (iBAT) and the incision. Mark this length on the flexible, implantable thermal probes, starting from the tip, with surgical tape. This will ensure consistency between temperature detected between the two probes.

5. Use a pair of curved forceps to lift the interscapular fat pad and visualize the iBAT. Insert one of the flexible implantable probes between the iBAT and the muscle underneath it is. While holding the probe in position with one hand, use your other hand to place the fat pad and the skin to its initial position. Secure the probe by taping the exterior segment to the table to prevent it from slipping out.

6. Similarly to the previous point, insert the second flexible implantable probe in the lower back section of the animal, and tape the exterior segment for stability.

7. Confirm the successful placement of the probes from the computer, the probes should reflect the internal temperature of the mouse ($\sim 35^{\circ}\text{C}$). See Figure 11 for a drawing of the probes positioning on the mouse.

1.6.12 Set up the laser doppler imager

NOTE: The manufacturer suggests turning on the imager at least 20 minutes before starting recording. You should also calibrate the machine according to the manufacturer instructions with

the calibration kit provided by the manufacturer. The manufacturer also suggests dedicating a computer only to doppler readings to avoid conflict with other software.

1. Place the imager on its frame, pointing down at the mice. Align the red dot from the doppler to the center of the interscapular region of the mouse.

2. Open the moorLDI Laser Doppler Imager Measurement software. Click ok through the initial prompt to get to the main interface. Click on “Setup”.

3. Go to the “Image Scan” tab. Adjust the scan area to cover the interscapular area. We suggest keeping the area size consistent across experiments, as it affects sampling time and resolution.

We used an area of 1.5 x 1.3 cm.

4. Click on “Mark” and ensure that the interscapular area of the mouse is within the path actively drawn by the laser. Click on “Abort” to stop the laser. Adjust the position of the laser or the mouse as needed and repeat the steps above until the area drawn by the laser includes the interscapular region.

5. Go to “Video and Distance” tab. Click on “Auto Distance” and let the software estimate the distance. Click “Ok” to close the Setup window and save settings.

6. Click on “Repeated” on the main menu. Set the number of frames to “unlimited”, and, when prompted, name the recording according to your experiment.

7. Click on the “Start” button. You will be prompted twice: click ok to the first one, then leave the second prompt on the screen. The recording will start as soon as you hit “Ok” on this prompt.

1.6.13 Experimental Recording

NOTE: Warm up to 37°C the solutions you are going to inject into the mouse. We noticed that even room temperature solutions can cause sensitive changes in internal temperature that can bias the outcome of these experiments.

1. Click on “Write To File” on the computer with the LJLogUD software to start recording from the thermocouple meter. Click on “Press to start saving” on the tablet to start recording from the heatpad. Click on “Ok” on the computer with the imager software to start recording from the laser doppler imager. You should be able to start all three recordings within 1s. Start a time to keep track of the experimental time.

2. Record an initial baseline to ensure that everything is running correctly.

3. Load a 1mL syringe with a 27G needle (at least 0.5in long) with the relevant solution. Gently slip the tip of the needle under the belly of the mouse, then enter the peritoneal cavity to inject the solution IP.

4. On the tablet, click on “Add a comment” and type the word “injection”. Click “Ok” to close the prompt. The software will automatically create a text file with the current timestamp, and we can use this information later during data analysis.
5. Repeat the previous point according to your protocol. We injected up to three different solutions at 10 min intervals in these experiments, for a total of up to 40 min of recording.
6. End the experiment by stopping the three different recordings from point 1 of this section, clicking on the same buttons.
7. Euthanize the animal by overdose of anesthetic, then confirm the procedure with thoracotomy.
8. Clean probes and heatpad using 70% ethanol solution.

1.6.14 Collect and decode data

1. Open the moor Laser Doppler Imager Review software on the doppler imager computer.
2. Click on “File”, then “Open”, and open the file from the recording you just concluded.
3. Select the “One” option to view single frames, then navigate to the frame with the highest signal intensity from iBAT.

4. Click on “ROI”, then “Add Poly” and then draw the region of interest around the iBAT. Right click to close the ROI. Click on “Multi” to go back to the view all the frames in the same interface,
5. Check the “Analysis” box in the bottom right.
6. Click on “Statistics”. In the new window, click on “Save” and save the files. You should have a file with a .sta extension now.
7. Connect the tablet to the computer where you saved the thermocouple meter recording.
8. From the computer, navigate to the folder inside the tablet of the experiment you just recorded. Copy the temperature recording file with the .dat extension inside the tablet folder.
9. Connect the tablet to the doppler computer.
10. Copy the .sta file from above into the tablet folder.
11. Connect the tablet to the computer where you will perform data analysis.
12. Open the BinaryConverted.jar file provided by the manufacturer of the heatpad.

13. Select “.csv” in the option at the top, then click on “Open”, navigate to and select the folder on the tablet where you have collected all the data. Click on “Open” to confirm the conversion of the binary files to csv files. You should now have a “csv” subfolder with all the different parameters from the heatpad saved as different .csv files.

1.6.15 Data Analysis and Statistics

NOTE: After the end of the last step, you will have all the information about the recordings that can be opened either with a text reader or with a commonly used spreadsheet software. You can already do your own analysis with these files. However, to ease the analysis process, and to keep consistency, we use a custom written code on R to integrate all the information from the three different devices (heatpad, thermocouple meter, and doppler imager) and to visualize and analyze our data. We will provide an R script to adapt to your analysis as supplemental file, and we will describe, in generic terms, the steps we perform for our usual analysis. All these steps can be easily performed in any other programming language.

1. Calculate the average value of the doppler imager before any injection, during baseline. Use this value to normalize all the imager values.
2. Compute the difference between iBAT temperature and lower back (LB) by subtracting the former from the latter for each timepoint. We can call this new vector “BAT – LB” or thermogenesis.

3. Calculate the effect of every injection. Using the reference time from the “comment.txt”, calculate the average temperature value for each probe between 300s and 600s after the injection. Additionally, calculate the average temperature in the last 120s before the injection. Finally, subtract the pre-injection value to the post-injection value.

4. Repeat the same steps for the blood flow values (doppler imager), considering the frames between 300s and 600s after injection, and those 120s before the injection.

5. Analyze the effects of drug injections with a paired t-test (or the alternative non-parametric test, depending on your data distribution) comparing the saline effects vs the drug effects within each mouse. Analyze temperature and blood flow separately. Report results as mean \pm SEM.

6. If testing multiple concentrations of the same drug, use a repeated-measure one ANOVA (or the non-parametric test) to evaluate the dose dependent effects of the drug. For the experiments presented here, statistical tests were carried out as repeated measures ANOVA with injection (Saline vs Drug), dosage, and their interaction as independent variables, Temperature increase over Baseline or AU fold increase over Baseline as dependent variable, respectively, and controlling for within-mouse measurements. Wilcoxon rank sum exact test was used when comparing only two groups. Analysis were performed on R 4.1.0³⁴⁸ using the lme4 1.1.34³⁴⁹ and lmerTest 3.1.3³⁵⁰ package.

Representative results

We did not observe any significant change from baseline after injecting Saline regarding temperature and blood flow. Specifically, across all the mice reported here (n=24), the effect of saline IP injections on thermogenesis was -0.019 ± 0.024 °C, and the effect on blood flow was 0.024 ± 0.028 AU.

NE strongly increases both thermogenesis and blood flow at every tested dose (**Figure 12**, $F_{1,18} = 122.47$, $p < 0.001$ and $F_{1,9} = 71.15$, $p < 0.001$). At doses of 0.5 and 1 mg/kg, NE increased thermogenesis by 0.645 ± 0.136 °C and 0.661 ± 0.054 °C, respectively, while the 2 mg/kg dose led to an even higher increase at 0.913 ± 0.097 °C. In terms of blood flow, 0.5 and 1 mg/kg doses increase it by 0.913 ± 0.214 AU and 0.988 ± 0.202 AU, respectively, nearly doubling the blood flow to the tissue. However, 2 mg/kg of NE only increased blood flow by 0.617 ± 0.073 AU, a smaller increase than that observed with the lower concentrations. Although there is a trend toward increased thermogenesis and decreased blood flow at 2 mg/kg, this effect is not statistically significant, possibly due to the low sample size.

CL also increases thermogenesis and blood flow at every tested dose (**Figure 13**, $F_{1,9} = 75.32$, $p < 0.001$ and $F_{1,9} = 36.73$, $p < 0.001$). Specifically, the increases in thermogenesis were 0.491 ± 0.062 °C, 0.518 ± 0.085 °C, 0.448 ± 0.031 °C for the 0.1, 0.5, and 1 mg/kg doses, respectively. The corresponding increases in blood flow were 0.432 ± 0.115 AU, 0.607 ± 0.206 AU, and 0.645 ± 0.022 AU for the same doses. In contrast to NE, the effects of CL do not substantially change with dosage, indicating that even at 0.1 mg/kg we may already be evoking the maximum response in terms of thermogenesis and blood flow.

Finally, we observe a complete reversal of NE-induced increases in thermogenesis and blood flow after IP injection of propranolol at 5 mg/kg (**Figure 14**).

Figures

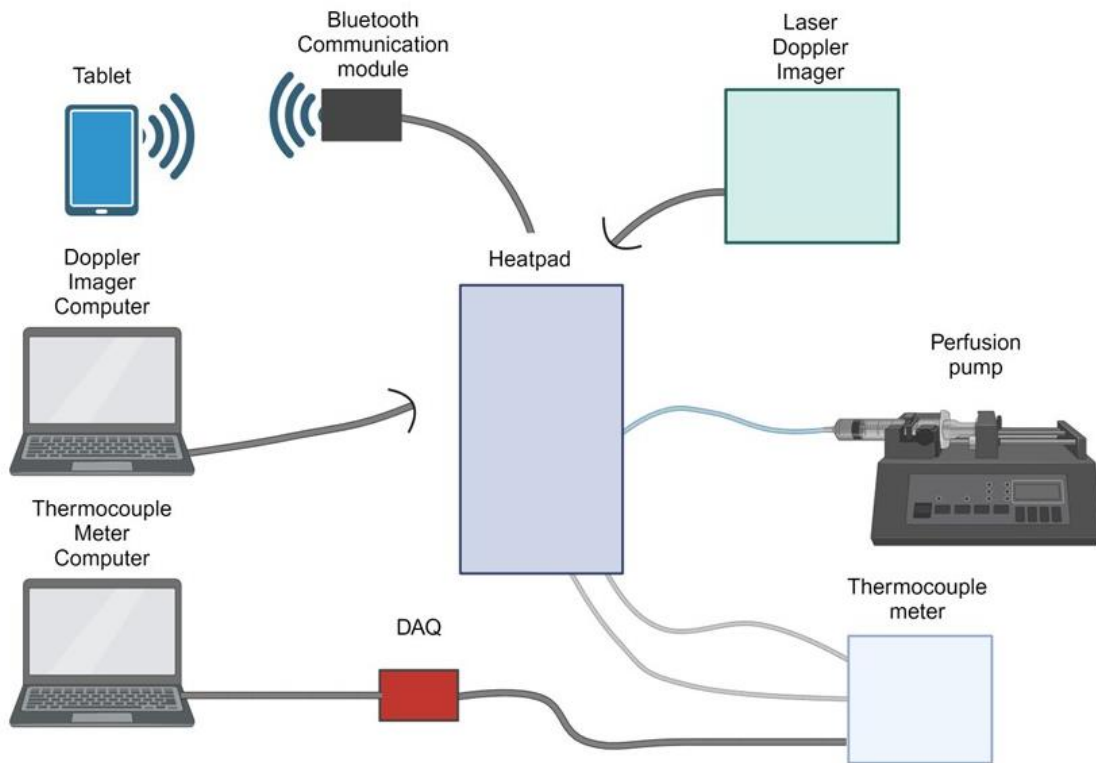


Figure 9. Schematics of the experimental setup

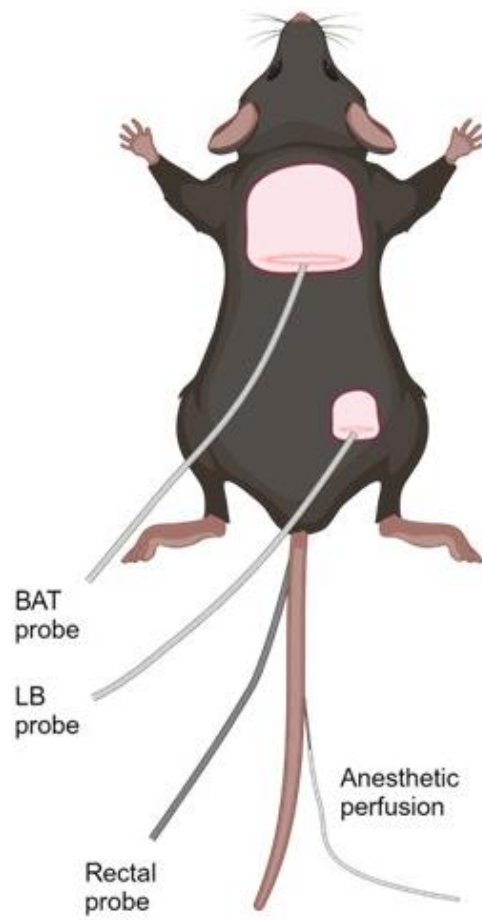


Figure 10. Drawing of probe placement in an experimental animal

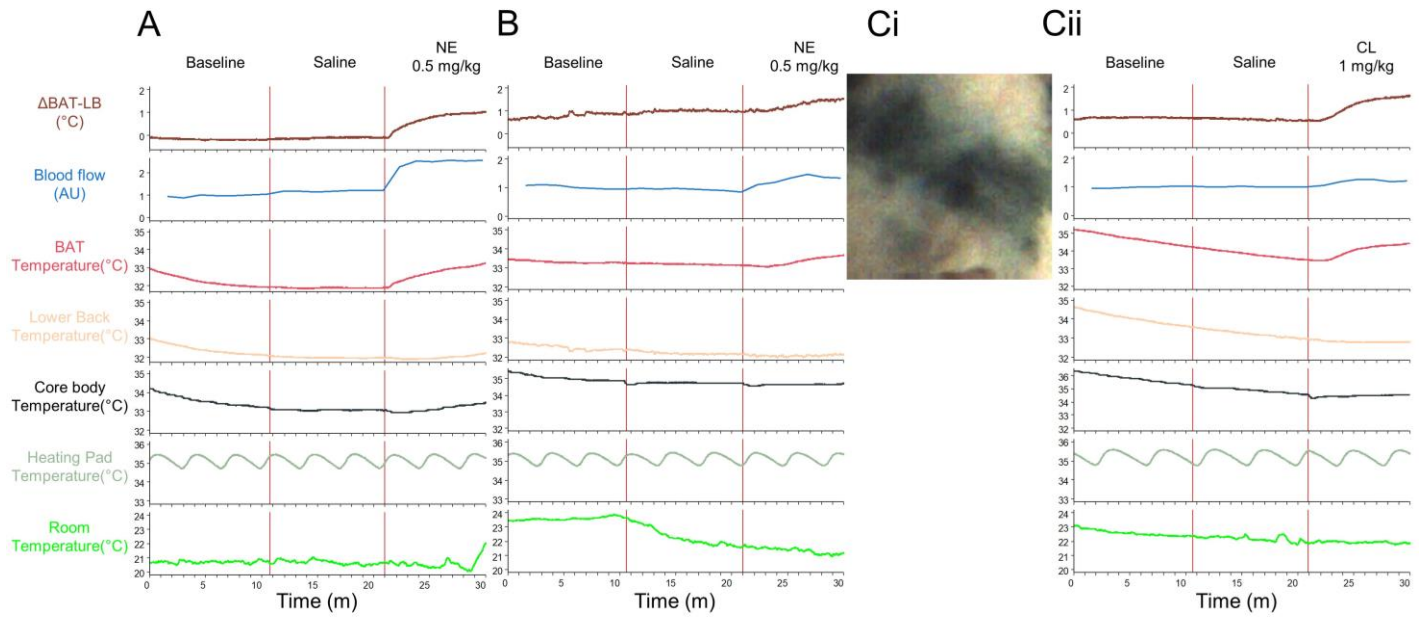


Figure 11. Representative traces obtained with the set up.

A: Example of a successful recording. Baseline and Saline portion of the recording are flat, and both Δ BAT-LB and Blood flow increase upon IP injection of NE 0.5 mg/kg. B: Example of flexible probe misplacement. Notice the noisy signal from the Lower Back Temperature, and the significantly low response evoked by the same IP dose of NE. Ci: Dark, pigmented skin patch on the interscapular region of an experimental animal. Cii: Recording from the animal shown in Ci. Note the shunted Blood flow response to IP injection of CL 1 mg/kg.

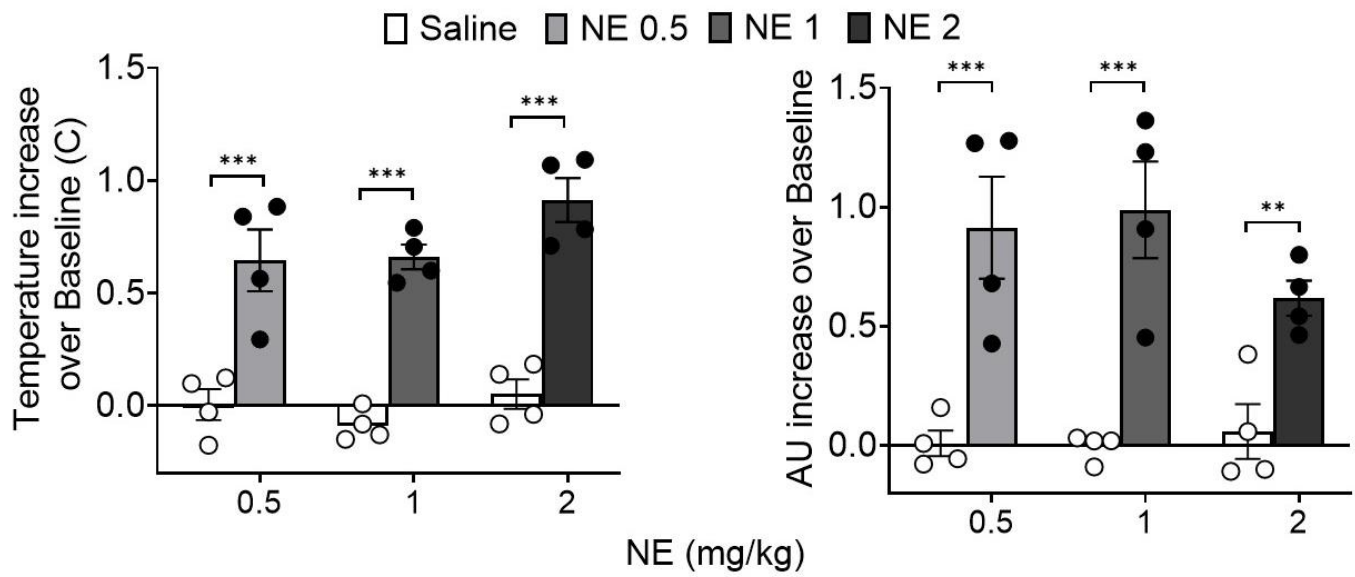


Figure 12. NE effects on Thermogenesis and Blood flow.

Left: IP injections of NE increase thermogenesis at every dose tested. Right: IP injections of NE increase blood flow. Notice the trend of higher thermogenesis and lower blood flow increase for the 2 mg/kg dose.

*** $p < 0.01$, *** $p < 0.001$.*

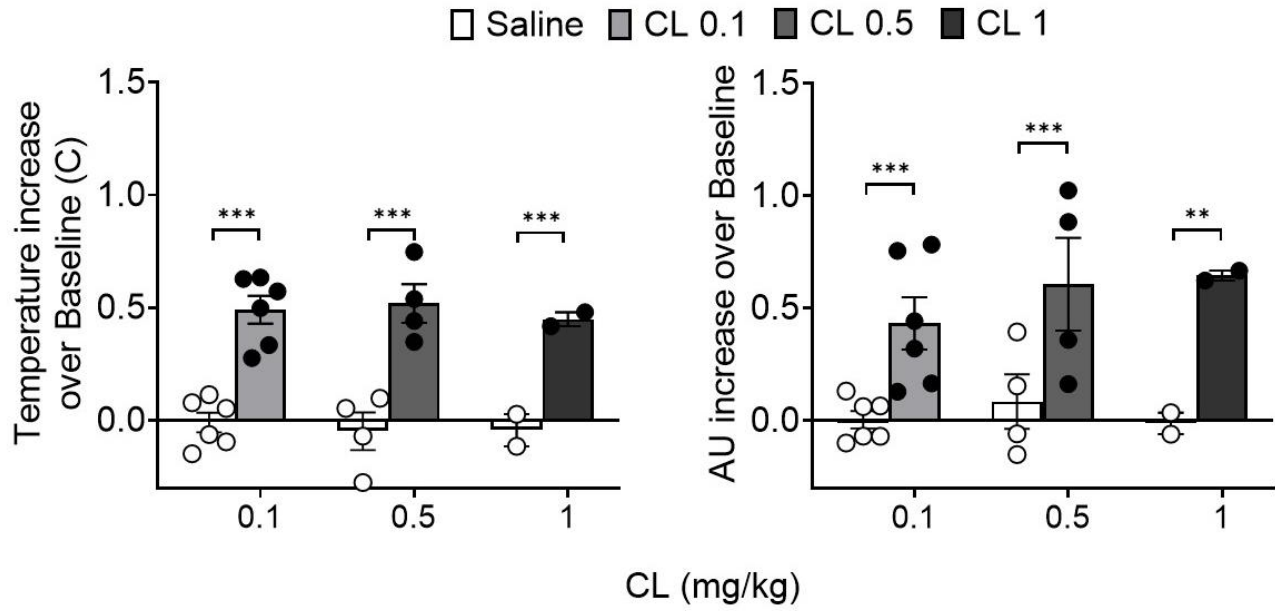


Figure 13. CL effects on Thermogenesis and Blood flow.

*Left: IP injections of CL increase thermogenesis at every dose tested. Right: IP injections of CL increase blood flow. No significant difference between doses is observed. ** $p < 0.01$, *** $p < 0.001$.*

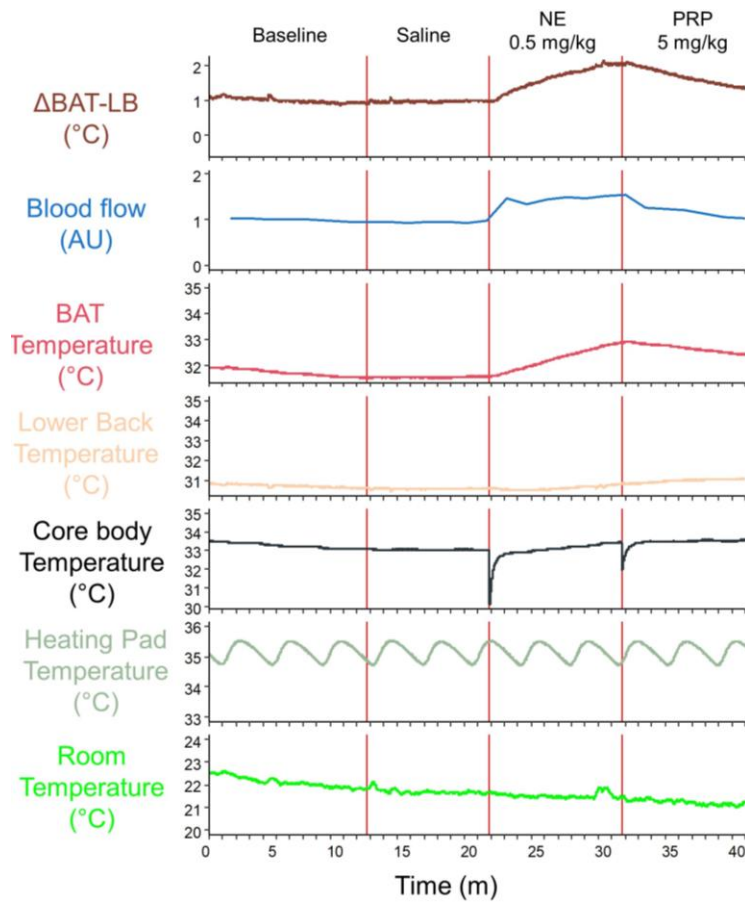


Figure 14. Effects of IP injection of Propranolol (PRP) 5 mg/kg following NE 0.5 mg/kg IP.

Notice the drop both in temperature (BAT and Δ BAT – LB) and in blood flow.

Discussion

Successful recordings from an animal display a flat and stable temperature and blood flow signal during baseline and after saline injection. These two parameters should increase upon injection of a stimulant (**Figure 11A**). Unsuccessful thermal probe placement can be identified immediately. First, a poorly positioned probe may exhibit an unstable signal, frequently oscillating around the true temperature value. This instability is likely due to the probe not being securely held in place, leading to oscillations in response to the mouse's natural breathing movements. This issue can be easily detected during probe placement by inspecting the thermocouple meter display and the signal on the computer. Second, misplaced probes may fail to accurately detect drug responses. **Figure 11B** shows a recording where the BAT probe was incorrectly positioned, resulting in a diminished response and unstable LB probe. Lastly, C57/BL6 mice may exhibit spontaneous patches of heavily pigmented skin that remain hidden until the mouse is shaven (**Figure 11Ci**). These patches can obstruct the Doppler Imager from accurately reading blood flow changes. Consequently, if any of these patches cover the interscapular region, the mouse cannot be used for blood flow recordings. However, it is still possible to successfully record temperature changes in these subjects, as demonstrated in **Figure 11Cii**.

Another relevant aspect of our setup is the use of three different probes to measure temperature from three anatomical regions (BAT, LB and T_c) instead of solely recording from BAT. This combination allows for direct comparison of thermogenesis across different organs and helps mitigate potential whole-body temperature oscillations. This phenomenon is particularly evident in **Figure 11Cii**, where we observe the three temperatures drop by 1.5 °C over the span of 20 minutes. If we were to compare the average BAT temperature during the baseline with the

average temperature after CL injection, we would not find any significant difference. However, by subtracting the LB temperature from the BAT temperature, we can clearly observe an increase in temperature following CL injection, consistent with results presented in **Figure 13**. This method enables us to precisely isolate the effects of BAT thermogenesis, thereby increasing the precision of our measurements and reducing the number of experimental animals needed to achieve statistically significant result.

In agreement with findings by Abreu-Vieira et al.¹⁶⁸, we observed a reduction of the increase in blood flow in mice stimulated with a dose of NE greater than 1 mg/kg. Conversely, thermogenesis increased with NE dosage, suggesting a dissociated control between blood flow and thermogenesis in iBAT

The method presented here is an integrated approach for simultaneously measuring blood flow and thermogenesis in the iBAT of anesthetized mice. Although there is a wide array of methods to measure either temperature or blood flow in mice, and some may offer greater precision, none have been utilized together to measure these two parameters concurrently. Additionally, this method can be adapted for use in other peripheral organs, providing insights into blood flow and temperature regulation under various stimuli.

The primary limitation of this method is the technical expertise required to prepare both the setup and the mouse; however, we have successfully trained other personnel without significant issues. It is important to note that these recordings are terminal procedures, so researchers should consider collecting any behavioral data before performing this procedure. Lastly, while blood flow measurements have a lower sampling rate than temperature measurements, it is still higher than many previously published methods. Users can have the flexibility to adjust the scanning speed and area to reduce the time between intervals according to their preferences.

Author Contributions

D.N. and L.M.Z. designed the experiments. D.N., D.M.J. and L.B. conducted the experiments and collected the raw data. D.N. analyzed the data and generated the figures. D.N. and L.M.Z. wrote the manuscript.

**Chapter 4: Identification and functional characterization of two
distinct sympathetic neuronal populations regulating brown adipose
tissue functions**

The work presented in this chapter is a continuation of S.L. work during her graduate studies. S.L. generated cells for scRNA-Seq and injected mice with CTb. S.L., A.L. and A.R.L. analyzed expression in SG sections and intact BAT in wild type mice. I and Vidhu V. Thaker (V.V.T.) analyzed scRNA-seq data. I performed work on genetically modified mice, injected viruses, and conducted experiments involving chemogenetics. I and Alexis Fohn (A.F) dissected ganglia from mice injected with viruses. I and L.M.Z wrote the manuscript, with discussions and contributions from S.L. and V.V.T.

Summary

Brown adipose tissue (BAT) plays a crucial role in thermogenesis by utilizing glucose and fatty acids, offering potential therapeutic benefits for metabolic disorders. BAT activity is controlled by the Sympathetic Nervous System (SNS), increasing both substrate oxidation and blood flow upon stimulation. Previous studies have suggested the presence of sympathetic neurons selectively innervating BAT vasculature; however, their functional role in BAT remains unexplored. Here, we employed retrograde tracing and single-cell RNA sequencing of stellate ganglion (SG) neurons in mice to identify two distinct sympathetic populations innervating interscapular BAT (iBAT) in mice: one targeting arterioles and the another innervating the parenchyma. Selective activation of these neuronal populations revealed complementary roles, with vasomotor neurons reducing blood glucose and parenchymal neurons driving thermogenesis and increased blood flow. These findings reveal distinct sympathetic pathways that mediate specific aspects of BAT function, suggesting a path toward targeted therapies for metabolic diseases, including type 2 diabetes, by leveraging SNS regulation of BAT.

Introduction

Brown adipose tissue (BAT) is a thermogenic organ specialized in non-shivering thermogenesis¹¹¹, utilizing glucose¹²⁹ and fatty acids^{128,175} from circulation to generate heat. This function has evolved as a protective mechanism for body temperature in cold environments. BAT research has accelerated in the last two decades due to mounting evidence linking its activity to various health benefits in humans^{1,149,150}. While BAT activity can be induced by several stimuli, the Sympathetic Nervous System (SNS) is its primary physiological regulator, particularly during cold exposure¹¹², resulting in increased thermogenesis and localized blood

flow²⁰⁶. Norepinephrine (NE), the main sympathetic neurotransmitter, and its receptors are found abundantly both on brown adipocytes^{46,402} and on other cell types within BAT^{387,403}. As such, enhanced noradrenergic transmission has been the main pharmaceutical approach to leverage BAT activity against metabolic disorders. Despite promising preclinical data and clinical trials⁵⁹, results on human patients have not matched expectations, and increased systemic noradrenergic transmission often led to negative outcomes on the cardiovascular system^{60,177}. Therefore, a more detailed understanding of the sympathetic control of BAT is crucial to leverage the full therapeutic potential of this organ.

The nature and complexity of ganglionic sympathetic neurons is not yet fully understood. Co-transmission of NE with other molecules, such as Neuropeptide Y (NPY) and ATP, is now well-established²⁵, suggesting that adrenergic transmission may not be the sole mediator of SNS influence on BAT. Over 30 years ago⁴⁰⁴, a vasculature-projecting, NPY-positive subset of sympathetic neurons has been identified, showing a role for SNS-derived NPY in regulating peripheral vascular tone by modulating NE effects⁴⁰⁵⁻⁴⁰⁷. Recent evidence indicates that SNS-derived NPY is implicated in regulating whole-body glucose homeostasis and cold induced adaptations³². However, the exact mechanism by which SNS-derived NPY impacts glucose uptake, and the involvement of vasculature-projecting nerves in this process, is still under investigation. Transcriptome studies have identified molecularly distinct sympathetic subgroups^{102,106}, hinting that specialized sympathetic populations may mediate unique aspects of SNS-induced activity on target organs like BAT. Yet, the specific physiological roles of these subgroups in BAT regulation and systemic metabolism remain elusive.

Here, we identify two molecularly distinct groups of ganglionic sympathetic neurons that innervate interscapular BAT (iBAT) in mice. one targets small arterioles, and the other, the

parenchyma. Using targeted activation targeting of iBAT-projecting sympathetic nerves, we demonstrate that acute stimulation enhances energy expenditure and improves glucose homeostasis. Furthermore, our results reveal that these two sympathetic populations mediate complementary roles, with the vasculature-targeting group specifically involved in glucose uptake regulation. These findings highlight the potential for targeted SNS modulation to optimize BAT function and improve metabolic health.

Results

1.6.16 Selective targeting of sympathetic nerves projecting to interscapular brown adipose tissue in mice

We sought to selectively target sympathetic neurons innervating mouse iBAT. Rodent iBAT is innervated both sympathetic and sensory nervous system (SNS and SeNS, respectively, Fig. 15a). In mice, the iBAT-projecting sympathetic second order neurons are located in the stellate ganglion (SG) and thoracic ganglia from T1 to T5, with sparse neurons observed up to T6 and T7¹⁵. While sensory innervation of iBAT in mice has not been extensively studied, research in Siberian hamsters has shown prominent sensory innervation originating from dorsal root ganglia (DRG) C4 to T2²⁵⁷, which may suggest similar patterns in mice.

Consistent with this information, we observed retrograde labeling both in SNS and in SeNS following cholera toxin subunit B (CTb) in mouse iBAT (Fig. 20a). However, since CTb is limited to tracing and cannot modulate neuronal activity, we evaluated a retrograde adeno-associated virus (AAVrg⁴⁰⁸) using the same approach. Although AAVrg produced some sympathetic labeling, its efficiency was less than half that of CTb (Fig. 20b). We next tested an AAV of the MaCPNS1 serotype²⁸² through intra-iBAT injections, observing significantly higher

retrograde labeling efficiency (Fig. 20c). As expected, we observed DRG labeling as well (Fig. 15b). Although the role of SeNS in iBAT is not fully understood, recent data has shown that inguinal white adipose tissue-projecting SeNS antagonizes SNS activity in the same tissue²⁶⁴. To avoid SeNS manipulation, we used a Th-Cre mouse line in combination with a Cre-dependent MaCPNS1 virus, which allowed selective targeting of the SNS. When injected into iBAT of Th-Cre mice, we observed specific SNS labeling with no SeNS labeling (Fig. 15c), providing a precise tool for investigating the sympathetic modulation of iBAT.

1.6.17 iBAT-projecting SNS acutely regulate blood glucose and metabolism, and increase local thermogenesis and blood flow

We next investigated the physiological outcomes of acutely activating iBAT-projecting sympathetic neurons. Th-Cre mice were injected with either a Cre-dependent control virus (Control) or a Cre-dependent excitatory designer receptor exclusively activated by designer drugs (DREADDs, hM₃D) targeting iBAT. After three weeks, both groups were stimulated with intraperitoneal (IP) injections of Clozapine-N-Oxide (CNO, 10 mg/kg) under anesthesia, while temperature and blood flow were recorded from the interscapular region (Fig. 16a). As expected, Control mice showed no response to CNO (Fig. 16b). Conversely, hM₃D mice displayed a rapid increase in BAT temperature and blood flow, which was reversed by an IP injection of Propranolol, confirming the involvement of β -adrenergic receptors (Fig. 16c). This response was consistent across all hM₃D mice (Fig. 16d), with an average increase in iBAT temperature of approximately 0.8 °C and a 25% increase in blood flow within 5 minutes post-CNO injection (Fig. 16e and f).

To explore the effects of selectively and acutely activating iBAT-projecting sympathetic neurons in freely moving, awake mice, we refined our approach by using Deschloroclozapine⁴⁰⁹ (DCZ, 200 µg/kg) to activate DREADDs, aiming to reduce possible off-target effects of CNO (Fig. 16g). Notably, we observed no difference in OGTT outcomes between CNO and DCZ (Fig. 21). Mice stimulated with DCZ exhibited reduced blood glucose levels at 15 minutes during a cross-over oral glucose test (OGTT, Fig. 16h and i), alongside increased energy expenditure (Fig. 16j and k) and a reduced respiratory exchange ratio (RER, Fig. 16l). Collectively, these results demonstrate that iBAT activation exerts a significant and exclusive impact on systemic metabolism.

1.6.18 Characterization of subtypes of Stellate Ganglion neurons innervating distinct targets

To explore factors responsible for the vasodilatory effect of sympathetic signaling in BAT, we performed single cell RNA sequencing (scRNA-Seq) couple with retrograde tracing of distinct peripheral targets in the mouse SG, the main source of sympathetic innervation of BAT^{15,253}. We focused on SG neurons innervating BAT (SG^{BAT}) and forelimb (SG^{FL}), because their projections share a similar anatomical trajectory via the intercostal nerves, and they are both involved in thermoregulation. We performed simultaneous retrograde tracing from BAT and forelimb by injecting CTb conjugated to Alexa Fluor555 (CTB-A555) into BAT and CTB-A488 into the forelimbs. Three days later, we generated z-stacked images of intact cleared ganglia. SG^{BAT} and SG^{FL} neurons were intermingled in the lateral SG but were not overlapping (n=20) (Fig. 17a). We did not observe any sex differences in n=13 males and n=7 females.

Next, we performed scRNA-Seq in conjunction with CTB retrograde tracing from BAT and forelimb (Fig. 22). We collected a total of 1039 single cells by FACS (433 SG^{BAT} (A555+), 220 SG^{FL} (A488+) and 375 non-labeled neurons) from three independent sorts of n=12 SG at eight weeks of age. The FACS data confirmed our observation that SG^{BAT} and SG^{FL} neurons do not overlap (Fig. 22d).

We identified four main clusters of SG neurons (SG1-4, Fig. 17b). The SG1 and SG2 clusters contained 45% and 37% of the analyzed cells, while the smaller SG3 and SG4 clusters contained 12% and 6% of the sorted neurons, respectively. Neurons in all clusters expressed *Th* and *Dbh*, consistent with a sympathetic neuronal identity⁴¹⁰, expression was higher in SG1 and SG2 neurons as compared to SG3 and SG4 neurons (Fig. 17c). Similarly, the gene encoding Neuropeptide Y (*Npy*) was expressed in all clusters, but SG1 neurons expressed it at levels that were 7- to 50-fold higher than the other clusters (Fig. 17c).

We confirmed the specificity of the expression patterns of the marker genes identified in the bioinformatic analyses by multiplex single molecule fluorescent in situ hybridization (smFISH) on SG tissue-sections (Fig. 17f). Since there is little cholinergic innervation of BAT⁴¹¹, we focused our analyses on the three noradrenergic subpopulations of SG neurons (SG1-3). We confirmed that the SG1 markers *Fst*, *Sctr* and *Rfxp1* were co-expressed with *Npy*, but not with *Slc18a1/Vmat1* (SG2), *Colq* (SG2-4) or *Aqp1* (SG3). Nearly all *Slc18a1*⁺ neurons (SG2) expressed *Colq* (SG2-4), but little to no *Aqp1* (SG3). Therefore, the smFISH closely matched the expression pattern predicted by the scRNA-Seq analyses (Fig. 17c).

1.6.19 The molecular signature of vasomotor neurons is not conserved across the Sympathetic chain

Next, we explored why the unique markers of SG subpopulations identified here were not revealed by earlier analyses^{102,106}. The two major differences between the approaches are the age of the mice (postnatal day 27-33 in¹⁰⁶ vs. 6-8 weeks here) and our exclusive focus on the SG, while earlier studies pooled sympathetic ganglia from SG through T13. Since the Ernfors group identified differences in the distribution of the noradrenergic subpopulations across the sympathetic chain¹⁰⁶, we evaluated the expression of the markers for SG1-3 in ganglia at more rostral and caudal positions in the chain.

The superior cervical ganglion (SCG) lies rostral to the SG and innervates the head and neck. We performed multiplex smFISH in *Npy-GFP* reporter mice to map the expression of SG marker genes relative to vasoconstrictor neurons^{405,406}. We confirmed that *Npy* expression is highly enriched in neurons that express high levels of the GFP reporter (Fig. 23). *Npy-GFP^{HI}* neurons co-expressed the SG1 markers *Rfxp1*, *Fst*, *Sctr*, and not markers for SG2-4 neurons, such as *Cckar*, *Colq* or *Aqp1* (Fig. 23, Top). We detected very low levels of the SG2 marker *Slc18a1*, so it was not possible to evaluate its expression relative to other markers. In summary, the pattern of marker gene expression in the SCG paralleled our observations in the SG.

Marker expression in the celiac ganglion (CG), which lies caudal to the SG and innervates the GI tract and liver, diverged substantially from the pattern observed in cervical ganglia. *Npy-GFP^{HI}* neurons co-expressed the SG1 marker *Rfxp1*, but other SG1 markers, such as *Fst* and *Sctr*, were excluded (Fig. 23, Bottom). In addition, the SG2-3 markers *Cckar*, *Colq* and *Aqp1* were preferentially expressed in *Npy-GFP^{HI}* neurons in the CG (Fig. 23, Bottom). The only SG markers assessed that maintained the same pattern of expression relative to *Npy-GFP^{HI}* neurons

in the SCG, SG and CG were *Rfxp1* (SG1) and *Slc18a1* (SG2). The impact of differences in the combination of neuropeptides and receptors expressed across the rostrocaudal axis on the function of vasoconstrictor neurons is an important issue for future investigations.

1.6.20 Cre-driver mouse lines confirm vascular projection of Npy^{HI} Stellate Ganglion neurons

We developed mouse Cre-driver lines to selectively target SG1 and SG2 populations. Although NPY expression is often used to identify vasomotor neurons⁴⁰⁴, our results show that all sympathetic neurons express *Npy* at varying levels. Instead, we chose *Rfxp1*, a gene predominantly expressed in SG1, to generate an *Rfxp1*-Cre mouse line (Fig. 18a). Crossing these mice with a Tomato reporter line (Ai9) and performing smFISH on the SG confirmed coexpression of *Rfxp1* and *tdTomato* within the same SG neurons, with no overlap between *tdTomato* and *Colq* (Fig. 18b). The number of Tomato-expressing neurons was approximately 50% of that in Th-Cre::tdTomato mice (Fig. 18c), matching the proportion of *Rfxp1*⁺ SG neurons in our dataset. Imaging whole iBAT of the *Rfxp1*-Cre::tdTomato mice revealed a selective perivascular innervation pattern (Fig. 18d), validating that *Rfxp1*-Cre line can specifically target iBAT-projecting vasomotor sympathetic neurons.

Similarly, we generated a *Vmat1*-Cre line to target SG2, the parenchyma-projecting neurons (Fig. 18e). Unexpectedly, *Vmat1*-Cre::tdTomato mice showed pan-neuronal tdTomato expression in the SG, observed through whole-ganglion imaging and smFISH (Fig. 24). This may stem from developmental expression of *Vmat1*^{31,412}, as we did not observe significant *Vmat1* expression in SG1, SG3, and SG4 in adult mice. To clarify, we injected a Cre-dependent mCherry retrograde virus into iBAT of *Rfxp1*-Cre or *VMat1*-Cre adult mice (> 12 weeks of age,

Fig. 18f). We observed strong mCherry and GFP overlap in *Rxfp1*-Cre mice but overlap between in *Vmat1*-Cre mice (Fig. 18g, quantified in 4h). These findings confirm that i) *Rxfp1*-Cre targets NPY^{HI} SNS neurons, ii) both *Vmat1* and *Vmat2* are developmentally expressed in SNS, but *Vmat1* becomes restricted to specific neurons in adulthood, iii) all SNS neurons express *Npy*, but only NPY^{HI} neurons show protein-level expression, and iv) *Vmat1*-Cre line can be used to access parenchyma-projecting SNS neurons in post-developmental mice.

Finally, we noted a small but significant proportion of mCherry⁺ and *Npy*⁺ double-positive SG neurons (Fig. 18h). Investigation of our sequencing data showed that, although *Rxfp1* and *Vmat1* expression is strongly negatively correlated, approximately 12% of neurons coexpress both genes (Extended Data Fig.6), explaining these double-positive neurons (Fig. 18h).

1.6.21 Two sympathetic subpopulations of neurons control complementary processes of iBAT physiology

We investigated the phenotypic responses in mice following acute selective stimulation of either *Rxfp1*⁺ (vasomotor) or *Vmat1*⁺ (parenchymal) iBAT-projecting sympathetic neurons. Mice from both Cre-driver lines received a Cre-dependent DREADDs MaCPNS1 injection in iBAT, and we measured blood flow and temperature in the interscapular region three weeks later in anesthetized mice (Fig. 19a and e). Acute chemogenetic stimulation of parenchyma-projecting neurons resulted in a strong and consistent increase in both thermogenesis and blood flow (Fig. 19b), with values comparable to those observed when all iBAT-projecting neurons were stimulated (Fig. 19c and d). In contrast, stimulation of vasomotor neurons did not elicit any changes in temperature or blood flow (Fig 19f-h). Next, we examined the impact of these two subpopulations on systemic metabolism in awake animals (Fig. 19i and m). Consistent with the

anesthetized observations, activation of parenchyma-projecting neurons resulted in an increase in energy expenditure, though this was not significant (Fig. 19j and k), along with a significant decrease in RER (Fig. 19l). Stimulation of vasomotor neurons did not significantly affect energy expenditure or blood flow (Fig. 19n-p).

Surprisingly, stimulation of parenchyma-projecting sympathetic neurons did not influence blood glucose regulation (Fig. 19q and r). Conversely, stimulation of vasomotor neurons during an oral glucose tolerance test (OGTT) resulted in a marked reduction in blood glucose levels at 15 minutes (Fig. 19s, t), similar to the effects observed when all iBAT-projecting sympathetic neurons were activated (Fig. 16h, i).

Discussion

The fundamental role of sympathetic innervation in regulating BAT activity and the molecular mechanisms behind adrenergic receptor activation have been well established in the literature. However, the intricate details of these mechanisms have remained elusive due to experimental limitations, particularly the absence of selective BAT-projecting sympathetic nerve models. Although the existence of two distinct post-ganglionic sympathetic populations has been theorized for nearly three decades, significant advances in understanding the physiology and functions of these subpopulations have been lacking.

In this study, we demonstrated that selective activation of iBAT-projecting sympathetic neurons in mice leads to reduced blood glucose levels, increased energy expenditure, a decrease in the RER, and enhanced iBAT thermogenesis and blood flow. We identified two distinct populations of sympathetic post-ganglionic neurons: one that exhibiting high expression of *Npy* and that preferentially wraps around arterioles, and another with low *Npy* expression that targets iBAT

parenchyma. Notably, these populations displayed complementary roles in modulating iBAT activity. Activation of the parenchyma-projecting neurons resulted in increased thermogenesis and blood flow without affecting glucose levels. Conversely, stimulation of the vasomotor neurons led to decreased blood glucose levels, with no impact on other aspects of iBAT function. Activation of BAT facilitates the uptake of glucose and fatty acids from the bloodstream, a function linked to various health benefits¹. However, sympathetic activity presents a double-edged sword in this context: while it enhances BAT function, it can also strain the cardiovascular system. Based on our findings, we hypothesize that the vasomotor neurons mediate the uptake of relevant nutrients from the circulation, whereas the other population regulates additional functions such as brown adipocyte activation and thermogenesis. The regulation of vascular tone is a finely tuned process occurring virtually in every organ, and evidence suggests that ECs play a role in BAT's regulation lipid uptake⁴¹³. Although sympathetic nerves do not directly contact ECs—since they do not innervate beyond the media-adventitial border in small arteries²⁹⁴—receptors for sympathetic transmitters and co-transmitters are expressed by both ECs and SMCs. Further investigation is required to elucidate the mechanisms underlying the sympathetic vasomotor-induced uptake of nutrients from circulation.

This study has several limitations. First, we focused solely on the activation of sympathetic neurons; future research should explore the phenotypes associated with the suppression or loss of function in one or more of the neuronal subpopulations identified here. Second, we noted minor off-target neuronal infections following MaCPNS1 injections, potentially due to spillover of the virus into the blood, as the main route of administration for MaCPNS1 is IV²⁸². However, the number of off-target neurons was significantly lower than that of the targeted ones, and the influence of off-target effects on our reported results is likely minimal. Nonetheless, additional

strategies are needed to refine the targeting of iBAT-projecting nerves and enhance precision. Finally, while the OGTT is widely used method for assessing whole-body glucose management, newer and more advanced technologies will be necessary to uncover the fine temporal dynamics of SNS-iBAT impact on glucose homeostasis. Special attention should be given to insulin variations during SNS-induced iBAT stimulation.

The findings presented here have the potential to inform new therapeutic approaches for metabolic diseases such as type 2 diabetes. Understanding how different sympathetic neuronal subpopulations regulate activity in peripheral organs and how this regulation affects systemic metabolism could significantly alter our perspective on the SNS. While many studies have examined transcriptomics, lipidomics, and metabolomics of stimulated BAT, these investigations typically involved either cold exposure or pharmacological stimulation. Future studies employing the techniques outlined in this work will help elucidate the metabolic and molecular changes occurring in BAT following selective stimulation, thus avoiding the confounding effects of whole-body activation.

Materials and Methods

1.7.1 Animals

Mice were maintained at an ambient temperature of 22°C ±1°C and on a 12 h light:12 h dark cycle in the Russ Berrie Medical Sciences Pavilion barrier facility. Mice had ad libitum access to chow (13.2% calories from fat, 5053; PicoLab Rodent Diet 20) and autoclaved drinking water. C57BL/6J mice (Jax strain #000664), Ai14 mice (Jax strain # 007914), and NPY-GFP (Jax strain #006417) were purchased from Jackson Labs. B6.Cg-Slc18a1^{tm1(cre)Zel} mouse line (Vmat1-Cre) was generated by the Genetically Modified Mouse Model Shared Resource at Columbia University Irving Medical Center using a CRISPR-based approach to replace the translational

stop codon of the target gene with T2A-nlsCre. Similarly, B6.Cg-Rxfp1^{tm1(cre)Zel} mouse line (Rxfp1-Cre) was generated by the Genetically Modified Mouse Model Shared Resource at Columbia University Irving Medical Center using a CRISPR-based approach to replace the translational stop codon of the target gene with T2A-nlsCre. Rxfp1-Cre mice and Vmat1-Cre mice were crossed to Ai14 mice for ganglia imaging purposes. B6.129X1-Th^{1(cre)Te}/Kieg mouse line (Th-Cre) was acquired from the European Mouse Mutant Archives (RRID:IMSR_EM:00254). All mice that received virus injections were single housed after surgery for the remainder of the study. All procedures were performed within the guidelines of the Institutional Animal Care and Use Committee (IACUC) at the Columbia University Health Science Division.

1.7.2 Retrograde tracing with CTb

Under isoflurane anesthesia, the upper-back was shaved and sterilized with three alternating wipes of betadine and 70% isopropyl alcohol. Buprenorphine (0.1 mg/kg) was administered for analgesia. Mice were placed on a heating pad and covered with a sterile drape, leaving the interscapular area exposed. A 1 cm horizontal incision was made above the interscapular area. The fat pad was carefully extracted with forceps and the superior part of the white adipose tissue layer was dissected to expose the BAT depots. Next, cholera toxin subunit B (CTB) conjugated to Alexa Fluor 555 (A555, ThermoFisher Cat. #C22843) was injected at two sites per depot with a glass pulled needle connected to a mouth pipette (1 μ l of a 1% solution in saline). The fat pad was gently returned to the interscapular cavity, and the wound was closed with a 4-0 PS-4 suture (Ethilon, Cat. #1662G). CTB-Alexa Fluor 488 (A488, ThermoFisher Cat. #C22841) was injected at three sites per forelimb with a glass pulled needle connected to a mouth pipette. The wounds

were cleaned with betadine and 70% isopropyl alcohol and the mice were monitored for any sign of distress. After 72 h, both stellate ganglia (SG) were harvested from mice euthanized with Avertin (2,2,2-tribromoethanol, Fisher, Cat # AC421430100, 500 mg/kg). SG were post-fixed in 4% PFA in 0.1M PB for 1 h at room temperature, followed by a PBS wash at 4°C, and mounted onto glass slides with Vectashield hardset mounting medium (Vector Laboratories) for whole-tissue imaging, or dissociated as described below.

1.7.3 Virus injection

Similarly to the CTb injections, mice were anesthetized, and shaved for surgery. The horizontal incision on the skin was two centimeters below the estimated region of the interscapular fat pad to avoid future scars interfering with Doppler readouts from iBAT. The interscapular fat pad was exposed and then gently separated along the midline using forceps. For each side, the fat pad was flipped to expose the brown depot and held by two bulldog clamps, the virus was injected in 3 to 5 different spots evenly to ensure optimal spread using a 25 μ L Neuros syringe (Hamilton, 65460-11), and then the fat pad was flipped back in place. Each depot was injected with 13 μ L of virus, for a total of 26 μ L per mouse. The wound was closed with suture and sanitized.

1.7.4 Temperature and Blood Flow Recordings

Mice were anesthetized via intraperitoneal injection of 350 mg/kg Avertin, and the interscapular area was shaved. Mice were then placed on a heating pad connected with a rectal probe to keep the subject at a constant temperature of 35 °C (Harvard Apparatus, cat. no. 75-1500) and monitored in real time via a tablet. A perfusion needle connected to a loaded syringe with Avertin was inserted into the lateral vein, and the anesthetic was delivered at a constant rate of

190 mg/kg/g using a small pump (Medfusion 3500, ICU Medical) to keep mice at a constant level of anesthesia throughout the experiment. A small incision was performed on the same spot from previous surgery, and the interscapular fat pad was visually inspected. The fat pad was cut caudally to allow the placement of an implantable thermal probe (IT-21, Physitemp). A small incision was performed on the lower back to insert a second implantable probe subcutaneously. A third probe was positioned next to the experimental setup to monitor environmental temperature. Thermal probes were connected to thermometer (TC-2000, Sable Systems), and the analogic signal was converted to digital and collected on a laptop using a USB DAQ device (LabJack U3-LV, LabJack). A High-Resolution Laser Doppler Imager was placed above the interscapular region to monitor blood flow (MOORLDI2-HIR, Moor Instruments), and data was collected using on a laptop using the manufacturer's software.

Mice were recorded for 10 minutes to establish a baseline, then injected intraperitoneally with saline solution. After 10 minutes, mice were injected with Clozapine-N-Oxide 10 ug/g (Sigma Aldrich, cat. no. SML2304). In some experiments, mice were also injected 10 minutes later with Propranolol (ThermoFisher, cat. no. H26645.06). Before the end of each recording, mice were injected with Norepinephrine (0.5 mg/kg) for positive control. All injections were volume-matched to 5 μ L/g. Finally, recordings were terminated, and mice were euthanized by anesthetic overdose, and ganglia were harvested and processed as previously mentioned.

Doppler recordings were processed using moorLDI Laser Doppler Imager Review V6.0 provided by the manufacturer. We identified the interscapular region based on the most active area following Norepinephrine injection, and we manually delineated the Region Of Interest (ROI) accordingly. We then applied this ROI to all the frames in the recording, and, for each frame, we calculated the average value inside the ROI.

All analyses of these recordings were performed on R³⁴⁸ using a custom script. For each mouse, we first calculated the stepwise difference between brown adipose tissue probe and lower back. Then, for each injection, we calculated the average value in the five to ten minutes time window after injection, and we subtracted this value to the average value in the two minutes preceding the injection. We used the same time window to calculate the relative blood flow values from the Doppler data.

1.7.5 Dissociation of stellate ganglion neurons

The dissociation method was based on published protocols^{414,415}. For each run, SG were harvested bilaterally from two 6-8 week old C57BL/6J males (for a total of 4 SG per batch) in ice-chilled Eagle's Balanced Salt Solution (EBSS) that was equilibrated to 95% CO₂ / 5% O₂ for one hour. Fat and connective tissue attached to the SG were removed, and the clean SG were transferred to a new dish containing cold equilibrated EBSS. SG were cut into 3-4 pieces using a small spring scissor and were gently placed into a low-bind 1.7 mL microcentrifuge tube containing 1,667 µL pre-heated (37°C) digestion solution for 1.5 hours with constant agitation. The digestion solution consisted of 1,034 µL Papain solution, 200 µL Collagenase/Dispase solution (20 mg/ml in EBSS), 167 µL D-trehalose solution (50% in RNase-free water), 3 µL AP-V solution (25mM in EBSS), 13 µL kynurenic acid solution (100mM in EBSS), 250 µL DNase. The digestion-stop and medium solutions were prepared during the digestion. The digestion-stop solution contained 1,050 µL 50% D-trehalose solution, 11 µL 25 mM AP-V solution, 44 µL of the 100 mM kynurenic acid, 250 µL of the DNase solution, and 250 µL fetal bovine serum (FBS). The medium solution contained 1,050 µL 50% trehalose solution, 8 µL the 25 mM AP-V, 19 µL 100 mM kynurenic acid, and 107 µL FBS in 9,450 µL D-MEM/F12. After the digestion,

half of the digestion solution with the tissue was transferred to a fresh low-bind microcentrifuge tube, each tube was filled with the digestion-stop solution. The tubes were gently inverted several times and centrifuged at 300 g at 4°C for 5 min. The supernatant was discarded, and the pellets were gently re-suspended in 500 µL of the digestion-stop solution described above. The suspensions were combined into a single tube and triturated with fire-polished glass Pasteur pipettes that were pre-coated with 0.5% BSA in RNase-free water for at least 1 h at room temperature. The pipette diameter was progressively decreased from 300-400 µm to 150 µm during the trituration process. The contents were then divided into two tubes and washed with 1 mL of the medium solution. The tubes were gently inverted 10 times and centrifuged at 300 g for 5 min. The supernatant was discarded, and the pellets were gently re-suspended in 200 µL of the medium solution. The suspension was filtered using a 40 µm cell strainer and collected in a 15 ml plastic tube. Sytox blue (1:1000) was used to stain dead cells. The suspension was kept on ice during transport to the FACS facility.

1.7.6 Cell sorting

Single cells were sorted into 3-4 96-well plates using a FACSAria sorter with a square cuvette with a 130-µm nozzle at 12 PSI. 2/3 of the plates were filled with either CTB-A555 or CTB-A488 positive neurons and collected non-CTB-labeled neurons in the remaining 1/3 of the plate. The plates were centrifuged at 200g for 2 min and snap frozen on dry ice. 3 sorting runs were performed, collecting a total of 1039 cells in 11 plates from 6 mice.

1.7.7 Plate-based scRNA sequencing of stellate ganglion neurons

The plate-based single cell sequencing was performed by the Sulzberger Columbia Genome Center at Columbia University as previously described⁴¹⁶. Briefly, the library preparation was performed using template-switching reverse transcription with adapter linked oligo(dT) primers containing both cell- and molecule-specific barcodes. The cDNA was pooled for PCR and library construction. Pooled, 3'-end sequencing libraries were sequenced on an Illumina NextSeq 500/550 platform.

1.7.8 Analysis of scRNA-Seq datasets

Reads were aligned to mouse genome, GRCm38, gencode version M13 (Ensembl 88) using STAR v2.5.3a⁴¹⁷. The aligned reads were assigned to genes using featureCounts v1.5.3⁴¹⁸. Next the bam files were sorted and indexed using Samtools v1.4.1 (<http://www.htslib.org/>), duplicated reads were removed and a UMI count matrix was generated using umi tools⁴¹⁹. A total of 1039 cells were obtained from the experiment.

The analysis of gene by cell counts matrix was performed using Seurat v3⁴²⁰. Comparisons of the data from each run confirmed that the clustering is not due to batch differences. Quality control (QC) included removal of cells with < 1000 genes/cell, cells with > 10% mitochondrial genes and those with no assignment of dye (A555, or A488 or A000), resulting in a total of 879 cells for the downstream analysis. From the expression matrix of the filtered cells, highly variable genes were identified followed by scaling and log normalization adjusting for the batch (plate), number of Unique Molecular Identifier (nUMI) and proportion of mitochondrial genes.

Dimension reduction was performed by principal component analysis (PCA). Jackstraw function identified 42 significant principal components (PCs) for the graph-based clustering. In the

iterative analyses, no additional information was gained beyond 30 PCs, and hence these were retained for the final analysis in keeping with the principle of parsimony. Using the FindClusters function of Seurat, cells were clustered using K-nearest neighbor (KNN) graph, with edges drawn between cells with similar gene expression patterns, that were partitioned into highly interconnected “quasi-cliques” or “communities” based on Euclidean distance in the PCA space. Next the edge weights between any two cells were refined based on the shared overlap in their local neighborhood (Jaccard distance), and modularity optimization techniques were used to iteratively group cells together.

Cluster specific markers were identified by differential expression of the genes in one cluster compared to all the other cells using the FindMarkers function with the default Wilcoxon rank sum test. Some of the cells contained genes expressed by satellite glial cells but were included in the analysis since neurons are much larger than these satellite cells and passed the QC for both number of genes and UMI per cell. However, to prevent the interference of the glial genes (n=136) in the clustering, these genes were removed from the highly variable genes resulting in a total of 3555 from the original 3684 to generate the PCs for further analysis⁴²¹. The clustering algorithm was repeated and the relationship between clustering at different resolutions was visualized using the clustree function in the package clustree⁴²² leading to the choice of resolution 0.6. Differential expression was performed to identify the transcriptional markers of the final clusters defined above. Genes with at least 40% difference in the proportion expressed in the specific cluster compared to the rest of the cells were categorized as “cluster markers”. The transcriptional signature of each cluster was visualized using a heatmap and violin plots. Hierarchical clustering was performed to identify the relationship between the clusters using the average transcriptional expression of the cells in each cluster.

To assess the differences in the transcriptional profile of the cells projecting from the forelimb and brown adipose tissue, the cells labeled with A488 (forelimb) and A555 (brown adipose tissue) were extracted separately. These cells were analyzed using Harmony, an algorithm that inputs the PCA embedding of the cells along with their batch (in this case, the dye), and returns batch corrected harmony embeddings⁴²³. After scaling and log-normalization of the cell by gene matrix of the two datasets, the top 2,000 variable genes ranked by coefficient of variation were identified within each dataset. The unique genes from this list were used for the initial step of embedding in a low-dimensional space by the PCA, followed by a soft k-means algorithm that performed 5 iterative clustering cycles to allow similar cells from both the datasets to cluster around a centroid while correcting each cell for a cell-specific factor, which is a linear combination of dataset correction factors weighted by the cell's soft cluster assignment. Based on the information maximization analysis, 10 Harmony embeddings were used to perform clustering and resolution 0.2 was found optimal based on graph-based t-Distributed Stochastic Neighbor Embedding (tSNE) and clustree⁴²² visualization. Differential expression analysis was used to identify the signature markers for each cluster as previously described. The absence of statistically significant differential expression between the cells by the dye within the same cluster validated the harmonization of transcriptome profile of the cells from the two tissue projections. All analyses were performed in R³⁴⁸.

1.7.9 Metabolic cages

Post-recovery mice from after surgery were single housed in Promethion Core Metabolic System for mice (Sable Systems) for one week. The system was at the same ambient temperature as the rearing facility (of 22°C ±1°C) and on a 12 h light:12 h dark cycle, and mice had ad libitum food

and water from the same Russ Berrie Medical Sciences Pavilion barrier facility. Mice were acclimated for three days, during which they received one daily i.p injection of saline solution around 4pm to acclimate them to the procedure. On day four and five, mice received two daily injections of saline solution, one at 10am and one at 4pm. In the last two days, mice received two injections daily of either Deschloroclozapine (DCZ) 200 ng/g or saline solution according to a balanced crossover design. On day six, half of the mice received two injections of DCZ (10am and 4pm), while the other half received two injections of saline solution. On day seven, the first half received two injections of saline solution, and the second half received two injections of DCZ. All injections were volume-matched to 5 μ L/g of mouse. Mice were returned to their original location after the recordings.

Statistical analyses were conducted by comparing, for each mouse and for each relevant parameter, the average values before vs after injection. Briefly, we first excluded the 12 minutes following injection to account for O₂ and CO₂ imbalance due to cage opening and stress-induced hyperthermia. Then, we for each mouse and for each parameter, we took the average value in the 30 minutes before injection (pre) and the average value in the 30 minutes after injection (pro) and compared them using Wilcoxon signed rank test.

1.7.10 Oral Glucose Tolerance Tests

Mice were transferred to clean cages without food four hours prior testing. At the beginning of the test, blood glucose levels were measured from tail vein prick to record the baseline level (Contour Next Ez Blood Glucose Monitoring System, Ascensia). Then, mice received an oral gavage of D-(+)-Glucose solution (2mg/kg; Sigma Aldrich G8769, diluted 1:2 in double distilled water and filtered through a 20 μ m filter) and an i.p. injection of either DCZ 200 ng/g or saline

solution. Gavage solutions were volume matched at 9 $\mu\text{L/g}$, and i.p. injections were volume matched at 5 $\mu\text{L/g}$ of mouse. Blood glucose was measured at 15, 30, 45, 50, 90, and 120 minutes after gavage and injection. Mice received either DCZ or saline solution according to a balanced crossover design, with 7 days between the two blocks to minimize potential carryover effects.

1.7.11 Immunofluorescence staining and counting

Mice injected with MaCPNS1 virus were transcardially perfused with PBS at 4 °C to remove excess blood and then PFA 4% (Electron Microscopy Sciences) in PBS at 4 °C. Vertebral columns were isolated and post-fixed overnight in PFA 4% at 4°C. The next day, columns were washed in PBS 4 °C for 2 hours three times, and then SGs were extracted under an optical microscope. SGs were embedded in Optimum cutting temperature (O.C.T., Andwin Scientific Tissue-Tek) media, frozen at -80 °C, cut into 10 μm sections with a cryostat, mounted on glass slides, and stored at -80 °C.

Slides were thawed and dried at room temperature for one hour protected from light, washed in PBST (PBS + Triton x100 0.1%) for 30 minutes, and then sections were circled with Immedge hydrophobic pen (Vector Laboratories). Slides were incubated with blocking solution (PBST + normal donkey serum 5%, Jackson ImmunoResearch Cat#017-000-121) for one hour at room temperature. After blocking, slides were incubated overnight with primary antibody solution (anti-NPY and anti-RFP, 1:1000 in blocking solution each) overnight at 4 °C. The next morning slides were washed in PBS for five minutes three times, then incubated with secondary antibody solution (secondary antibodies and DAPI, 1:500 in blocking solution each) for one hour at room temperature. Slide were then washed in PBS for five minutes three times, and finally mounted

with ProLong Glass Antifade mountant (Invitrogen, Cat# P36980) with cover glass no. 1.5 (Fisherbrand, Cat#12-541-033).

Slides were imaged with a Zeiss Axio Observer 7 microscope at 20x as a tiled image. Neurons were manually counted using ImageJ⁴²⁴. Negative control slides (incubated without primary antibodies) were used for background subtraction.

1.7.12 In Situ Hybridization

SG were harvested from wild-type, while superior cervical and celiac ganglia were harvested from Npy-GFP mice⁴²⁵ (Jax strain #006417) to aid in their visualization. Ganglia were harvested from adult mice and post-fixed for one hour in PFA 4% as previously described. Ganglia were then mounted embedded in O.C.T. media, frozen at -80 °C, cut into 10 µm sections with a cryostat, mounted on glass slides, and stored at -80 °C. Slides were thawed and dried at room temperature for one hour protected from light prior processing.

Multiplex single molecule Fluoro In Situ Hybridization (smFISH) was performed on mouse sections as directed by the RNAscope™ Multiplex Fluorescent Reagent Kit (Advanced Cell Diagnostics) with the fixed-frozen tissue sample preparation and pretreatment.

Npy-GFP reporter expression was validated in the SCG and CG using IHC for GFP following smFISH. A less stringent antigen retrieval step was used for the smFISH to preserve GFP fluorescence; the target retrieval solution was previously boiled, and sections were incubated for 5 min at room temperature. After smFISH, Immunofluorescence staining for GFP was performed as described with an anti-GFP primary antibody (1:250) and a donkey anti-sheep-A488 secondary (1:500). Images of Npy-GFP fluorescence in SCG and CG sections in Extended Data

Fig 4 were captured without any additional amplification. Sections were imaged with a Zeiss LSM confocal microscope (63X and 40X for mouse sections).

1.7.13 Imaging from Virus-injected mice

Mice injected with MaCPNS1 virus or AAVrg were euthanized, and tissue was harvested and post fixed as described above. SGs and DRGs were then mounted onto glass slides with LIMPID mounting medium, incubated overnight at room temperature and protected from light, and then imaged with a Zeiss 710 LSM confocal microscope at 20x as a tiled image and using the z-stack function with a 5 μ m step.

Figures

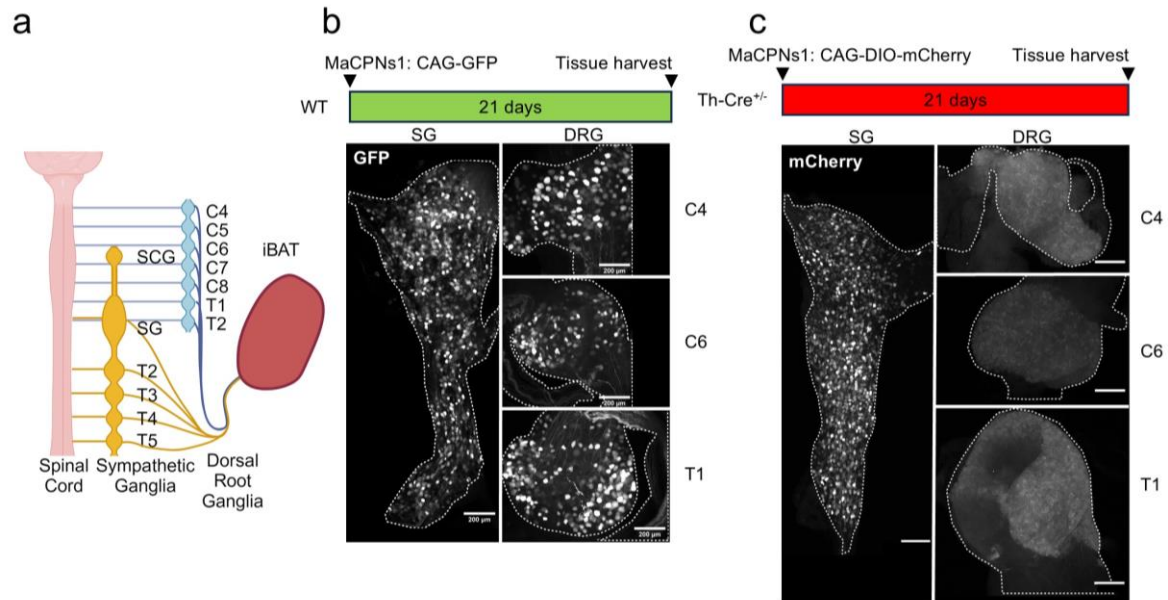


Figure 15. Selective targeting of the interscapular brown fat-projecting sympathetic neurons is achieved via Cre-lox system.

a: Schematics of sympathetic and sensory nervous system innervation in mouse interscapular brown adipose tissue. Created with BioRender.com.

b: Top, experimental timeline of GFP-expressing MaCPNS1 virus injections in iBAT of WT mice. Bottom, representative image of Sympathetic (Stellate Ganglion, SG) and of Sensory ganglia (Dorsal Root Ganglia, DRG) at C4, C6, and T1. Scale bar is 200 μm .

c: Top, experimental timeline of mCherry Cre-dependent expressing MaCPNS1 virus injections in iBAT of Th-Cre mice. Bottom, representative image of SGs and DRGs. Scale bar is 200 μm .

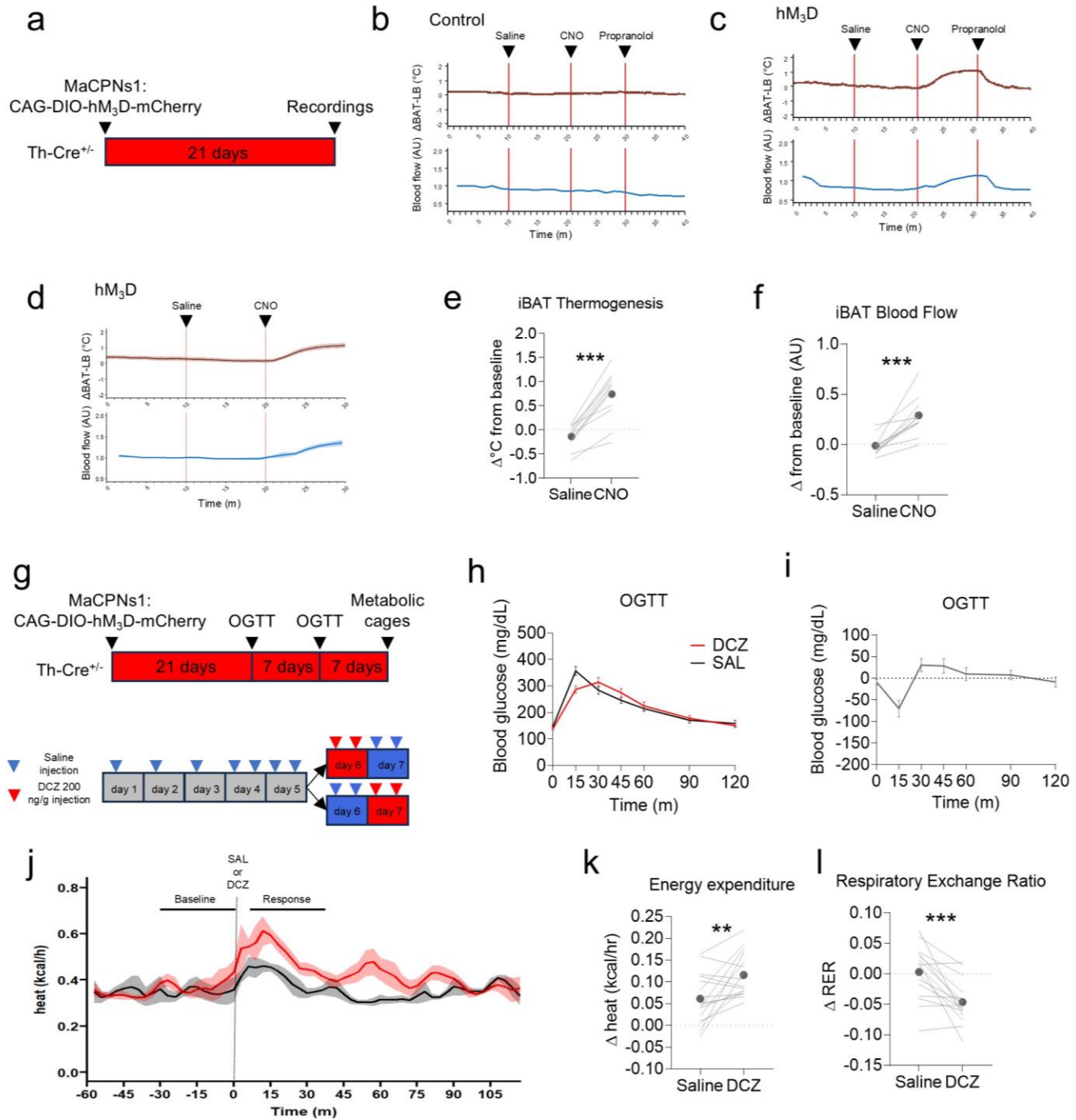


Figure 16. Figure 2: Acute chemogenetic activation of iBAT-projecting SNS neurons results in increased thermogenesis, blood flow, energy expenditure, decreased RER, and better glycemic profile in mice.

- a: Experimental timeline of hM₃D-mCherry Cre-dependent expressing MaCPNS1 virus injections in iBAT of Th-Cre mice.
- b: Representative traces in a Th-Cre mouse injected with mCherry Cre-dependent expressing MaCPNS1 virus.
- c: Representative traces in a Th-Cre mouse injected with hM₃D-mCherry Cre-dependent expressing MaCPNS1 virus.
- d: Average traces in Th-Cre mouse injected with hM₃D-mCherry Cre-dependent expressing MaCPNS1 virus. Data shown as mean, shaded area represents \pm s.e.m., n=12.
- e: Average increase in temperature in iBAT following Saline or CNO 10 mg/kg IP injection in mice shown in d. Dots represent average values, each line represents a mouse. Wilcoxon matched-pairs signed rank test, two-tailed, n=12.
- f: Average increase in blood flow in iBAT following Saline or CNO 10 mg/kg IP injection in mice shown in d. Dots represent average values, each line represents a mouse. Wilcoxon matched-pairs signed rank test, two-tailed, n=12.
- g: Experimental timeline and groups schematics for metabolic cages of hM₃D-mCherry Cre-dependent expressing MaCPNS1 virus injections in iBAT of Th-Cre mice.
- h: Average blood glucose curve. Data shown as mean \pm s.e.m., n=19 per group.
- i: Average within-subject blood glucose curve from data shown in h. Data shown as mean \pm s.e.m., n=19.
- j: Average traces of energy expenditure (kcal/h) in mice from g. Solid lines represent mean, shaded area represents \pm s.e.m., n=8 per group.

k: Average increase in energy expenditure following Saline or DCZ 200 $\mu\text{g}/\text{kg}$ IP injection in mice shown in g. Dots represent average values, each line represents a mouse. Wilcoxon matched-pairs signed rank test, two-tailed, $n=16$.

l: Average decrease in respiratory exchange ratio (RER) following Saline or DCZ 200 $\mu\text{g}/\text{kg}$ IP injection in mice shown in g. Dots represent average values, each line represents a mouse. Wilcoxon matched-pairs signed rank test, two-tailed, $n=16$.

** $P<0.01$, *** $P<0.001$.

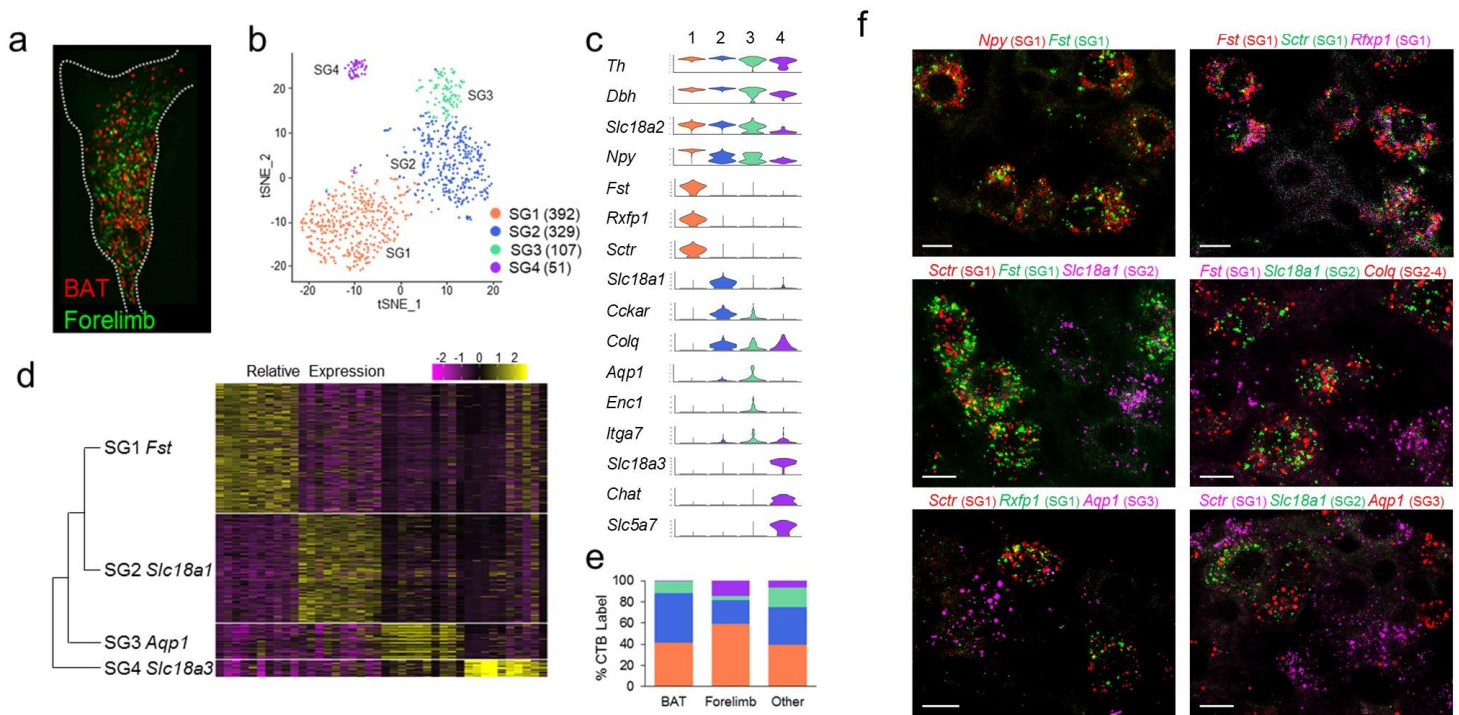


Figure 17. Identifying subpopulations of stellate ganglion neurons with scRNA-Seq.

a: Retrograde labeling of stellate ganglion (SG) neurons that project to BAT (red) and forelimb (green).

b: Single-cell transcriptomes visualized with t-SNE, colored by cluster.

c: Violin plots showing the expression of sympathetic and cluster-specific marker genes.

d: Dendrogram showing relatedness of clusters, followed by a heat map of the expression of cluster-enriched genes in cells sorted by cluster.

e: Percentage of cells of each SG subtype within cells retrogradely labeled from BAT, forelimb or non-labeled cells.

f: Validation of cluster marker genes in the SG using smFISH in n=4 mice. SG1 markers assessed were *Npy*, *Fst*, *Sctr* and *Rfxp1*. Markers for other SG populations were *Slc18a1* (SG2), *Colq* (SG2-4) and *Aqp1* (SG3). Scale bar,

20 μ m

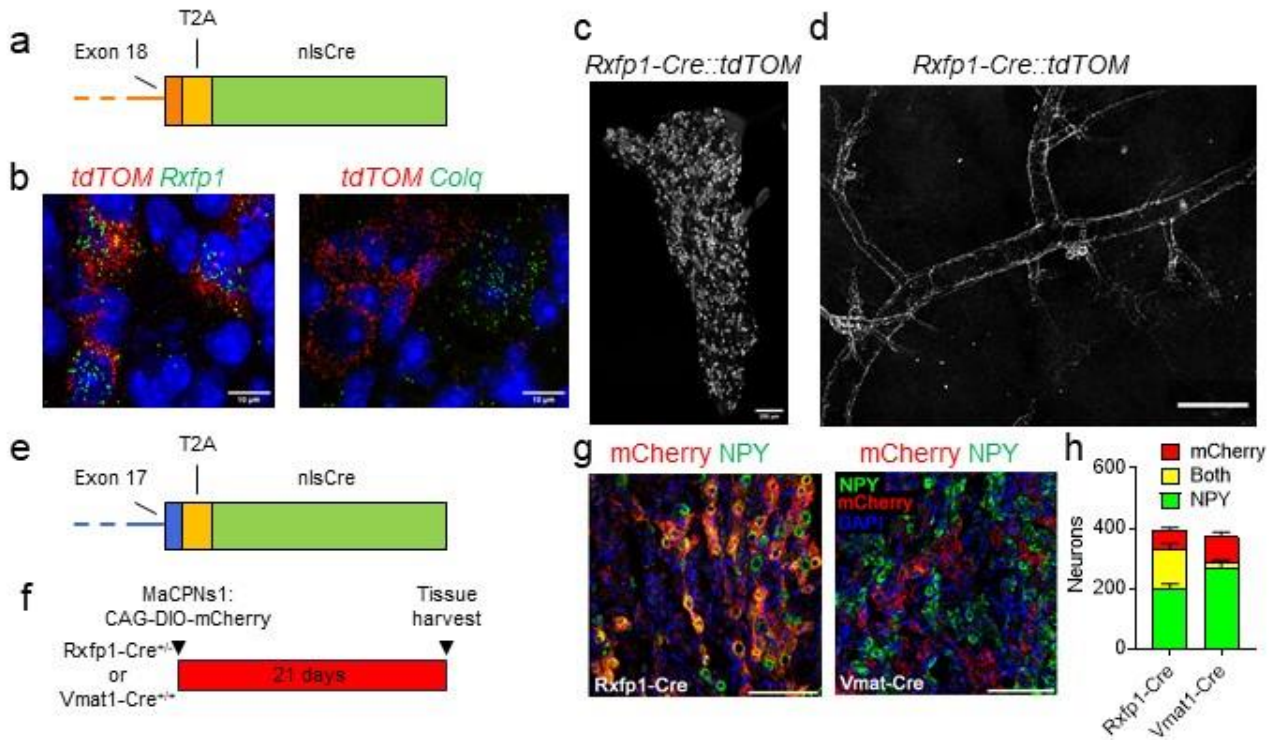


Figure 18. Validation of mouse Cre driver lines for the two sympathetic subpopulations.

a: Gene schematics of Rxfp1-Cre mouse line.

b: Representative images of SG smFISH for cluster-specific markers in a Rxfp1-Cre::tdTomato mouse. Scale bar is 10 μ m.

c: Whole tissue imaging of a SG from a Rxfp1-Cre::tdTomato mouse. Scale bar is 200 μ m.

d: Whole tissue imaging of iBAT from a Rxfp1-Cre::tdTomato mouse. Scale bar is 200 μ m.

e: Gene schematics of Vmat1-Cre mouse line

f: Experimental timeline of mCherry Cre-dependent expressing MaCPNS1 virus injections in iBAT of Rxfp1-Cre or Vmat1-Cre mice.

g: Representative images of mCherry and NPY immunofluorescent staining in the SG in mice from F. Left: Rxfp1-Cre. Right: Vmat1-Cre. Scale bar is 100 μ m.

h: Counts NPY-positive, mCherry-positive, or double positive SG neurons from mice from F. Data is shown as mean \pm s.e.m., n= 3 per genotype (4 sections per mouse).

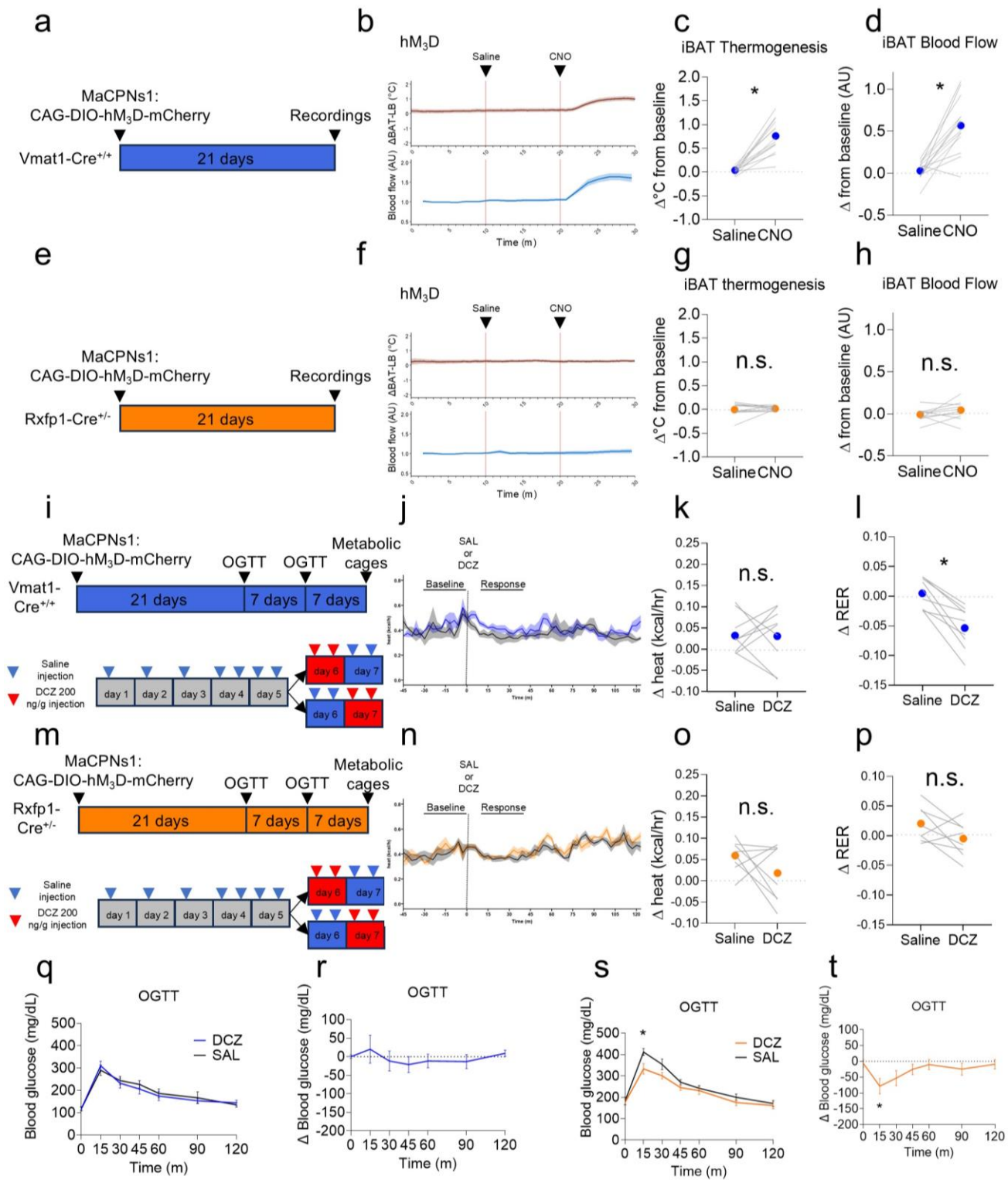


Figure 19. High Npy expressing neurons target large arterioles in iBAT in mice and regulate glucose uptake, while low Npy expressing neurons target parenchyma in iBAT in mice and regulate thermogenesis and blood flow.

- a: Experimental timeline of hM₃D-mCherry Cre-dependent expressing MaCPNS1 virus injections in iBAT of Vmat1-Cre mice.
- b: Average traces in Vmat1-Cre mouse injected with hM₃D-mCherry Cre-dependent expressing MaCPNS1 virus. Data shown as mean, shaded area represents \pm s.e.m., n=14.
- c: Average increase in temperature in iBAT following Saline or CNO 10 mg/kg IP injection in mice shown in a. Dots represent average values, each line represents a mouse. Wilcoxon matched-pairs signed rank test, two-tailed, n=14.
- d: Average increase in blood flow in iBAT following Saline or CNO 10 mg/kg IP injection in mice shown in a. Dots represent average values, each line represents a mouse. Wilcoxon matched-pairs signed rank test, two-tailed, n=14.
- e: Experimental timeline of hM₃D-mCherry Cre-dependent expressing MaCPNS1 virus injections in iBAT of Rxfp1-Cre mice.
- f: Average traces in Rxfp1-Cre mouse injected with hM₃D-mCherry Cre-dependent expressing MaCPNS1 virus. Data shown as mean, shaded area represents \pm s.e.m., n=10.
- g: Average increase in temperature in iBAT following Saline or CNO 10 mg/kg IP injection in mice shown in e. Dots represent average values, each line represents a mouse. Wilcoxon matched-pairs signed rank test, two-tailed, n=10.
- h: Average increase in blood flow in iBAT following Saline or CNO 10 mg/kg IP injection in mice shown in e. Dots represent average values, each line represents a mouse. Wilcoxon matched-pairs signed rank test, two-tailed, n=10.
- i: Experimental timeline and groups schematics for metabolic cages of hM₃D-mCherry Cre-dependent expressing MaCPNS1 virus injections in iBAT of Vmat1-Cre mice.

j: Average traces of energy expenditure (kcal/h) in mice from i. Solid lines represent mean, shaded area represents \pm s.e.m., n=6 per group.

k: Average increase in energy expenditure following Saline or DCZ 200 μ g/kg IP injection in mice shown in i. Dots represent average values, each line represents a mouse. Wilcoxon matched-pairs signed rank test, two-tailed, n=9.

l: Average decrease in (RER) following Saline or DCZ 200 μ g/kg IP injection in mice shown in i. Dots represent average values, each line represents a mouse. Wilcoxon matched-pairs signed rank test, two-tailed, n=9.

m: Experimental timeline and groups schematics for metabolic cages of hM₃D-mCherry Cre-dependent expressing MaCPNS1 virus injections in iBAT of Rxfp1-Cre mice.

n: Average traces of energy expenditure (kcal/h) in mice from m. Solid lines represent mean, shaded area represents \pm s.e.m., n=8 per group.

o: Average increase in energy expenditure following Saline or DCZ 200 μ g/kg IP injection in mice shown in m. Dots represent average values, each line represents a mouse. Wilcoxon matched-pairs signed rank test, two-tailed, n=8.

p: Average decrease in (RER) following Saline or DCZ 200 μ g/kg IP injection in mice shown in m. Dots represent average values, each line represents a mouse. Wilcoxon matched-pairs signed rank test, two-tailed, n=8.

q: Average blood glucose curve in mice from i. Data shown as mean \pm s.e.m., n=6 per group.

r: Average within-subject blood glucose curve in mice from i. Data shown as mean \pm s.e.m., n=6.

s: Average blood glucose curve in mice from m. Data shown as mean \pm s.e.m., n=8 per group.

t: Average within-subject blood glucose curve in mice from m. Data shown as mean \pm s.e.m., n=8.

Supplementary Figures

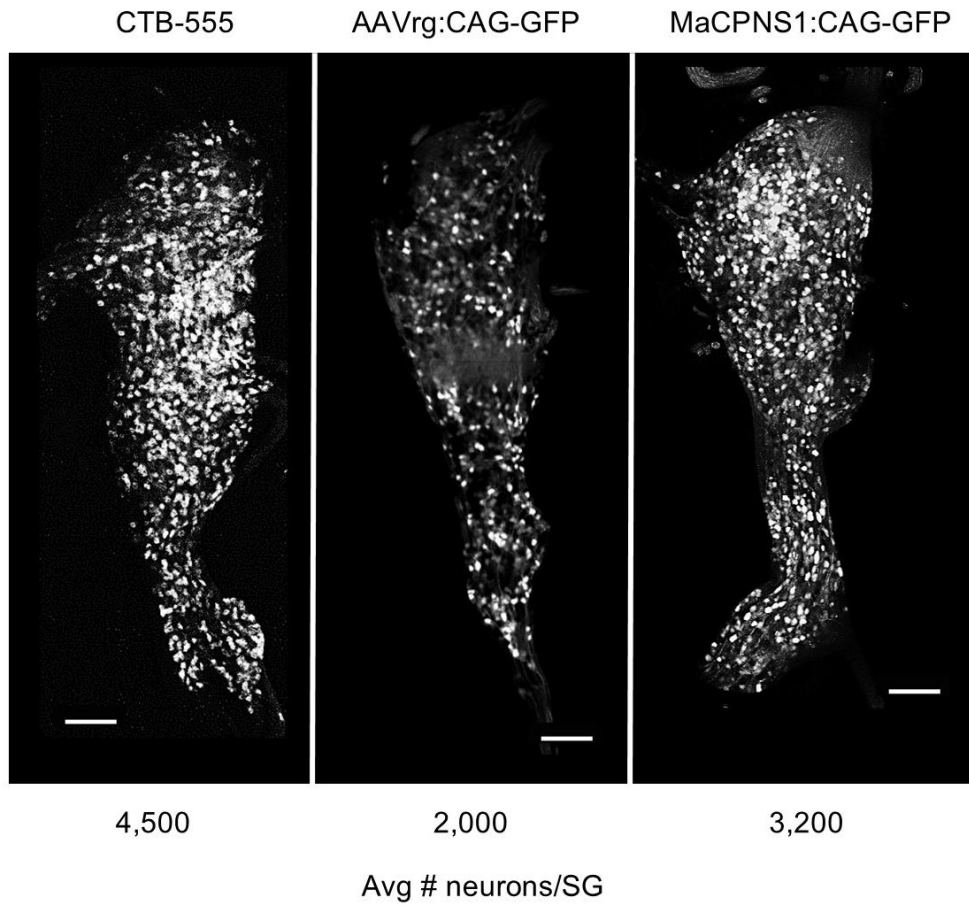


Figure 20. Comparison of retrolabeling efficiency between CTb, AAVrg, and MaCPNS1.

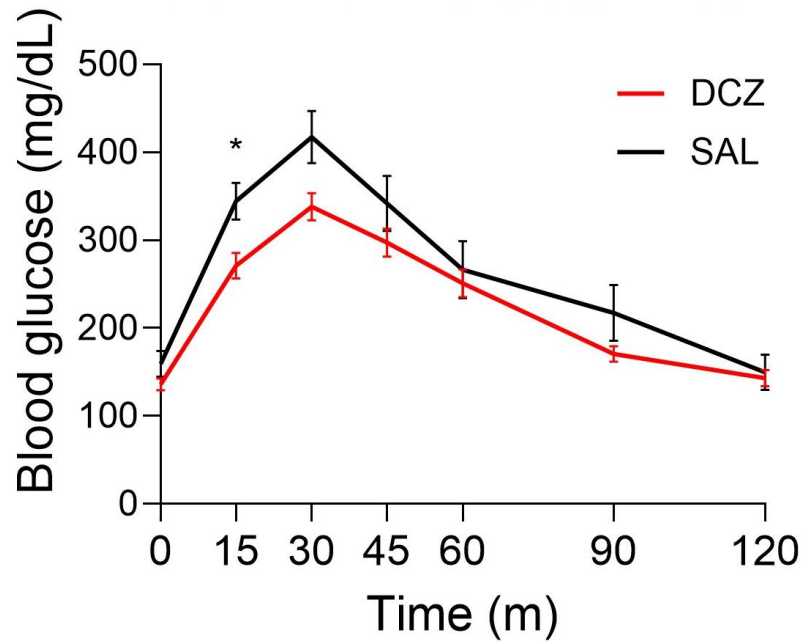


Figure 21. Average blood glucose curve under DCZ in Th-Cre mice expressing hM3D against Th-Cre mice injected with a control virus.

Data shown as mean \pm s.e.m., n=15 per DCZ group, n=8 per SAL group. Wilcoxon rank sum test with continuity correction, unpaired. * P = 0.01

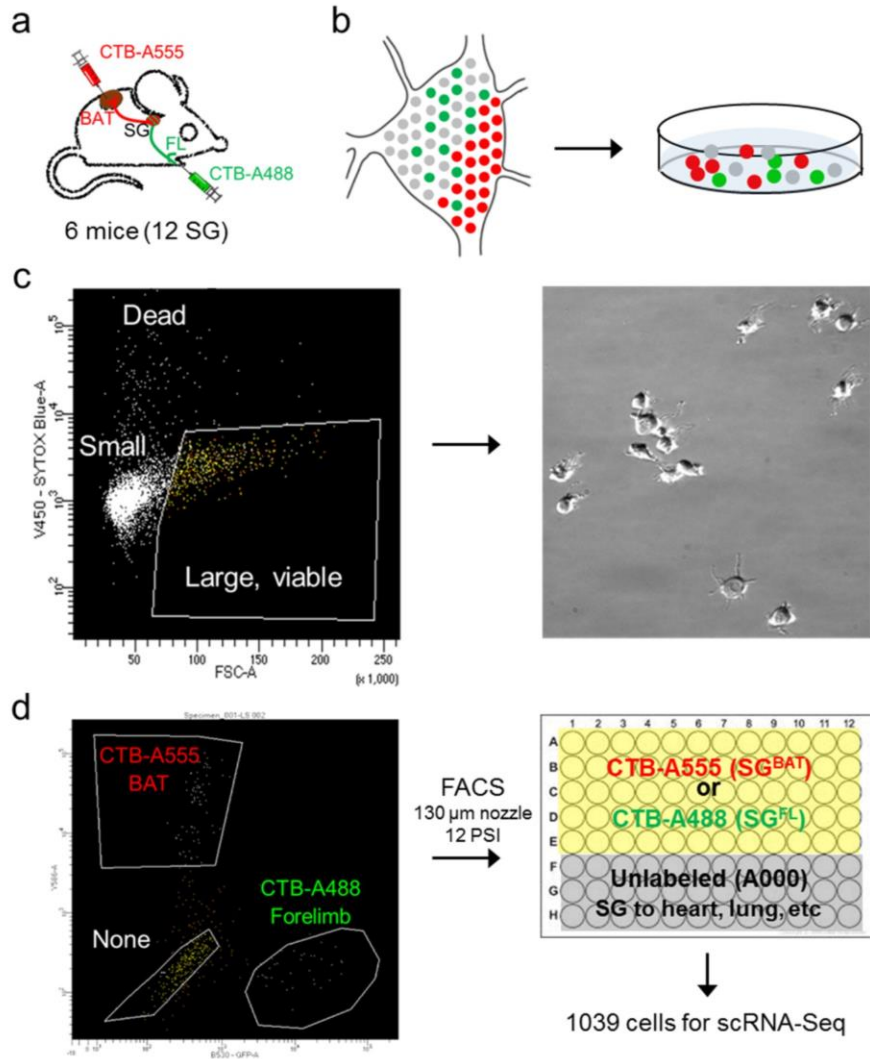


Figure 22. Strategy for scRNA-Seq in conjunction with retrograde tracing.

a: Mice were injected with CTB-A555 into BAT and CTB-A488 into forelimb.

b: Stellate ganglia were harvested and cells were dissociated for FACS.

c: Large, viable neurons were gated based on the absence of Sytox blue staining and forward scatter.

d: A555+, A488+ and unlabeled (A000) cells were sorted into 96-well plates containing lysis buffer for scRNA-Seq.

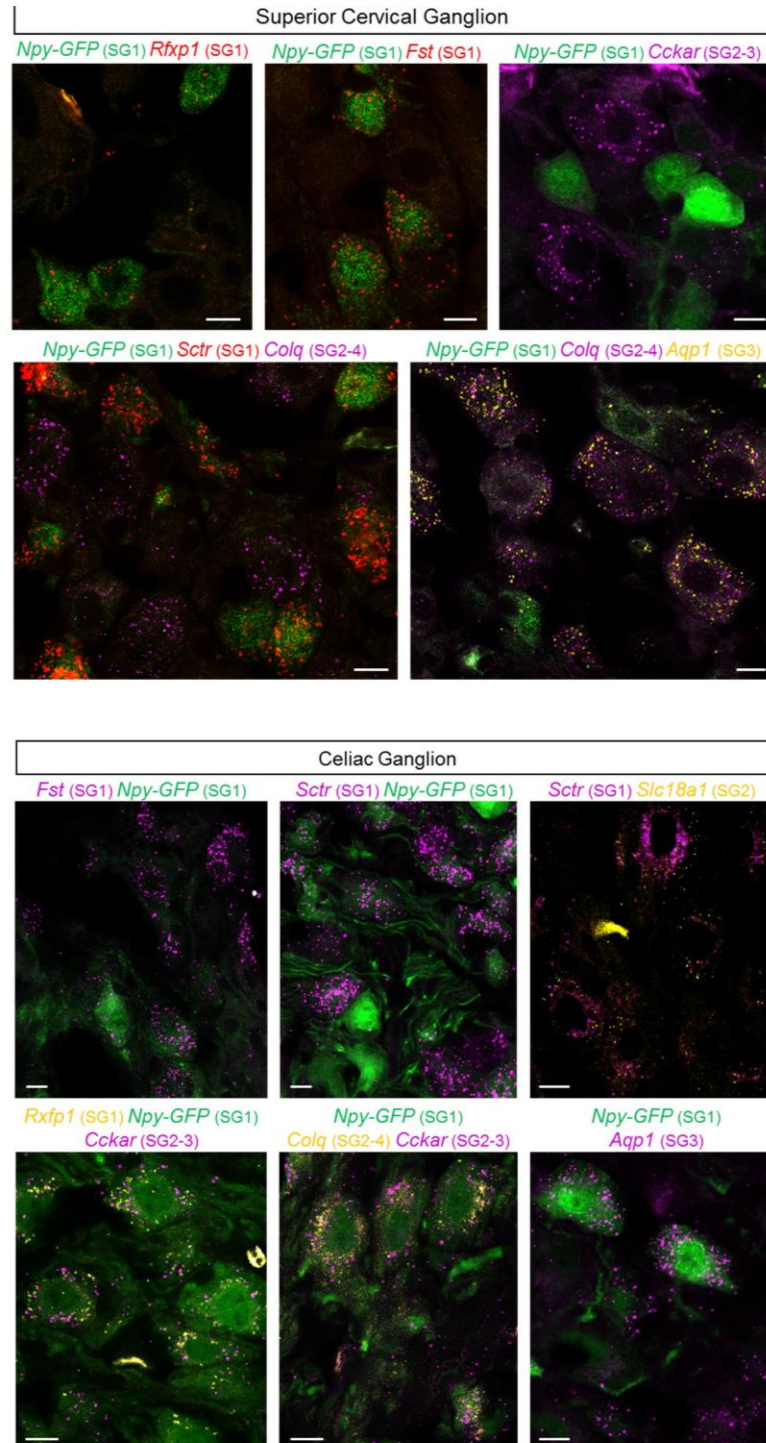


Figure 23. Expression of stellate cluster markers in mouse superior cervical and mouse celiac ganglia.

Top: Validation of SG cluster marker genes in the superior cervical ganglion using smFISH in conjunction with the *Npy-GFP* reporter in n=4 mice. SG1 markers assessed were *Npy-GFP*, *Rfxp1*, *Fst* and *Sctr*. Markers for other SG populations were *Cckar* (SG2-3), *Colq* (SG2-4) and *Aqp1* (SG3). Scale bar, 20 μ m.

Bottom: Validation of SG cluster marker genes in the celiac ganglion using smFISH in conjunction with the *Npy-GFP* reporter in n=4 mice. SG1 markers assessed were *Npy-GFP*, *Fst* and *Sctr* and *Rfxp1*. SG2 and SG3 markers were *Slc18a1* and *Aqp1*, respectively. *Cckar* and *Colq* were also used as markers that are excluded from SG1 neurons. Scale bar, 20 μ m.

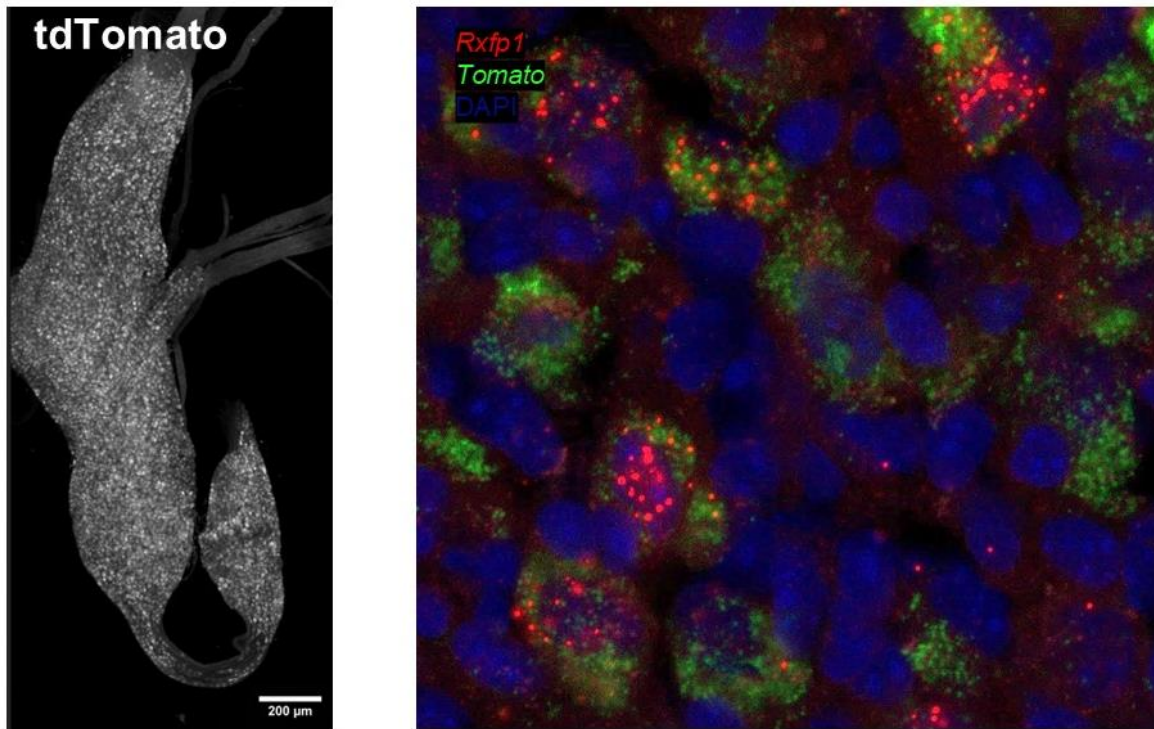


Figure 24. Developmental expression of Cre observed in *Vmat1-Cre::tdTomato* mice.

Left: Whole tissue imaging of a SG from a *Vmat1-Cre::tdTomato* mouse. Scale bar is 200 μm.

Right: Representative images of SG smFISH for *Rxfp1* and *tdTomato* expression in the SG of a *Vmat1-Cre:tdTomato* mouse.

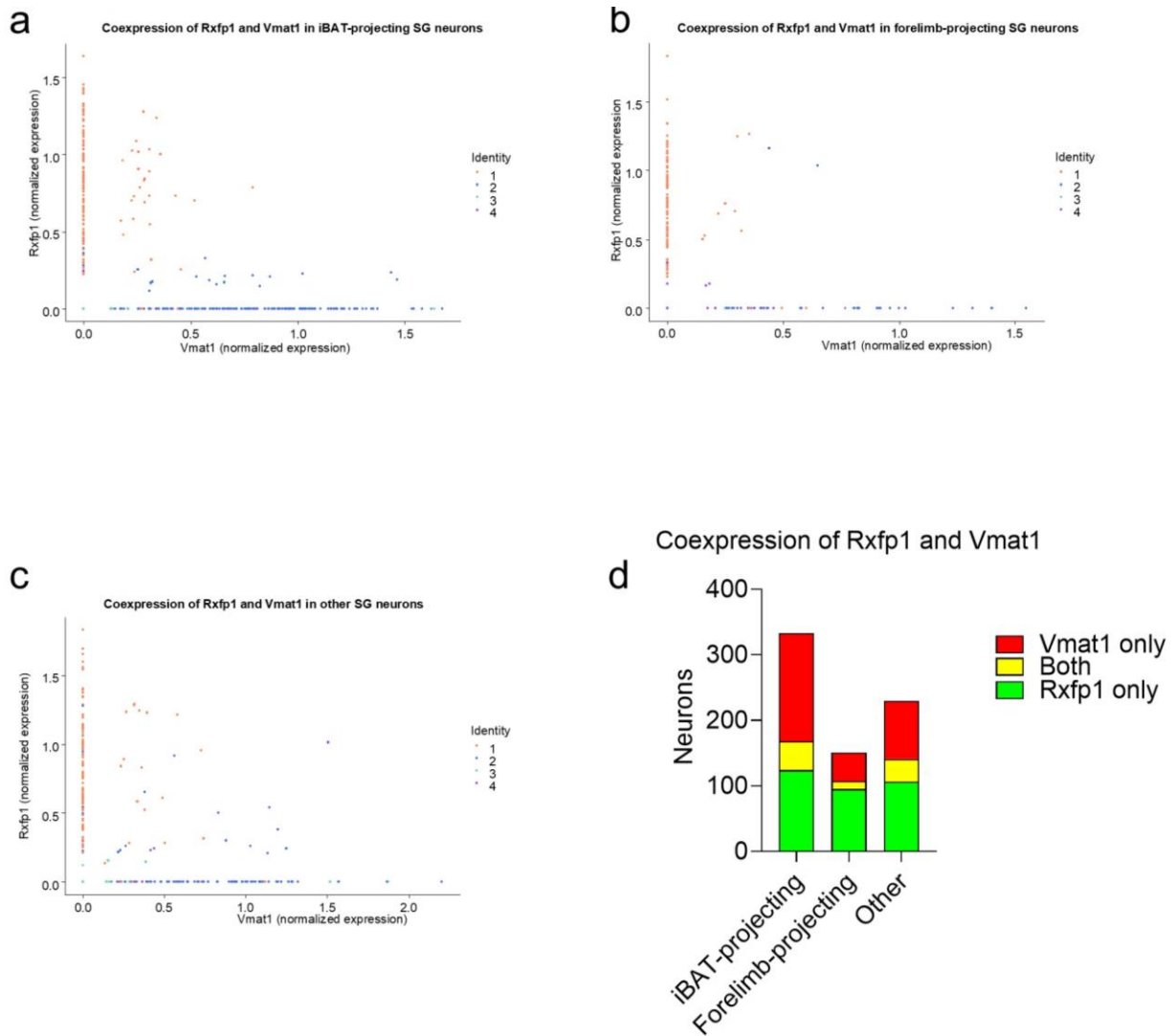


Figure 25. Coexpression of Vmat1 and Rxfp1 in iBAT projecting neurons from scRNASeq.

a: single-cell expression of Rxfp1 and Vmat1 in iBAT-projecting SG neurons from our dataset.

b: single-cell expression of Rxfp1 and Vmat1 in forelimb-projecting SG neurons from our dataset.

c: single-cell expression of Rxfp1 and Vmat1 in the rest of SG neurons from our dataset.

d: Count of SG neurons expressing Vmat1 only, Rxfp1 only, or both from our dataset, divided by retrolabeling identity.

Author Contributions

D.N., S.L., V.V.T. and L.M.Z conceived and designed experiments and interpreted data. S.L. generated cells for scRNA-Seq. S.L., A.J.L. and A.M.R.L. analyzed expression in SG sections and intact BAT. D.N. and V.V.T. analyzed scRNA-seq data. D.N. injected viruses and performed experiments on mice. D.N. and A.F. Dissected ganglia from mice injected with viruses.

L.M.Z and D.N. wrote the manuscript with discussions and contributions from S.L. and V.V.T.

Competing Interest Statement

The authors do not have any competing interests to declare.

Chapter 5: Conclusion and future directions

Summary

In the work that I presented here, I have demonstrated the presence of two molecularly distinct subpopulations of ganglionic sympathetic neurons that project to iBAT in mice, and I have characterized their roles in iBAT function. Specifically, we observed that selectively activating parenchyma-projecting neurons results in increased thermogenesis and blood flow in iBAT, with no impact on glucose tolerance. Conversely, activating only the vasculature-projecting neurons improves glucose tolerance, with no effect on blood flow or thermogenesis. These results have the potential to change the way we study the SNS and the therapeutic approaches we currently use to modulate its activity in pathological conditions.

However, there are some limitations that need to be addressed. I will first discuss the limitations of the current studies and propose possible solutions for the near future. After this, I will present some ideas for future research based on the implications of my graduate work.

Limitations

First, we have only addressed the acute activation of iBAT-projecting neurons, generally restricting the analysis up to 60 minutes post DCZ injection. This limitation was based on the lack of clear differences observed during both the glucose test and metabolic cages recordings after the initial 30 minutes, possibly due to the pharmacokinetics of hM₃D_q ligands⁴²⁶. However, we have discussed how chronic BAT activity is correlated with improved insulin sensitivity. As such, future studies involving chronic exposure to CNO or DCZ will help elucidate the true involvement of BAT in whole-body glucose management.

Another major obstacle during my research was the availability of the AAV serotype that we used. Over the last decade, many different laboratories have engineered viruses to specifically

infect cellular populations of interest. This field of research is rapidly evolving, and there are many valid alternatives to MaCPNS1 that we could try, such as AAV9-retro⁴²⁷, or the canine adenovirus 2 (reviewed in ⁴²⁸ and in ⁴²⁹).

The results from our OGTTs indicate that the effect on glucose homeostasis is generally confined to the first 30 minutes after injection, as previously mentioned. It is possible that homeostatic mechanisms are at play to counterbalance the artificial activation of iBAT-projecting nerves. The SNS innervates the pancreas, and activation of pancreas-projecting sympathetic nerves has hyperglycemic effects. Rats acclimatized to cold (28 hours at 5°C) reportedly have the same glucose tolerance as room temperature mice, albeit with lower plasma insulin levels, indicating that cold acclimatization increases insulin sensitivity⁴³⁰. Notably, the largest differences in insulin levels in cold-acclimated rats are observed at the earliest time point of the glucose tolerance test (between 0 and 30 minutes), with similar levels between the two groups in the later parts of the test, showing a timeline like the one we observed in my experiments. Furthermore, the authors demonstrate that these effects are completely abolished either by acclimating the rats to room temperature for four hours or by treating the animals with phentolamine, a non-selective α ARs antagonist. This result suggests that what appeared to be increased insulin sensitivity might instead reflect an increased localized sympathetic drive into the pancreas, reducing insulin secretion to favor glucose uptake from cold-acclimated organs such as BAT and skeletal muscle, all directed by the CNS to finely tune glucose homeostasis. The implication of this study hints to a crosstalk between thermogenic organs and the CNS, allowing for SNS outflow to be finely tuned to maintain euglycemia. Given the similar timing of our blood glucose-lowering effects, it is possible that counterregulatory mechanisms to balance glucose homeostasis are at play here, such as CNS-induced increased sympathetic activity in the pancreas to reduce insulin output.

Therefore, future studies should employ glucose clamp techniques^{431,432} to elucidate how insulin release and sensitivity are impacted during stimulation of iBAT-projecting sympathetic nerves. BAT is known to lower glucose both directly, by extracting glucose from circulation, and indirectly, via the release of insulin-sensitizing hormones. As such, in our paradigm, we need to understand how much of the glucose-lowering effect is directly mediated by BAT and how much is mediated by other organs. We are planning experiments involving fluorescent glucose analogues, such as 2-(N-(7-nitrobenz-2-oxa-1,3-diazol-4-yl)amino)-2-deoxyglucose (2-NBDG)⁴³³ to track glucose uptake and accumulation throughout the study. Along the same lines, we have observed that activating iBAT-projecting sympathetic nerves results in decreased circulating levels of triglycerides (TGs) while increasing TGs concentration in the iBAT (discussed in Appendix A). We are collaborating with the lab of Jörg Heeren to utilize nanoparticle-based lipoprotein-labeling technology to track lipid uptake in iBAT⁴¹³ and other organs under our selective stimulation.

Finally, we have only explored the effects of activating these neuronal populations using hM₃D_q. We are planning future studies involving the inhibition of these neuronal populations (via hM₄DG_i) or induced cell death through Cre-dependent expression of caspase 3 construct^{434,435}. These technologies can be combined, allowing for the simultaneous manipulation of multiple neuronal groups. Distinct neuronal groups can be targeted using recombinase technologies other than Cre-lox, such as the Flp-FRT⁴³⁶ or the Dre-rox systems^{437,438}. Combining these technologies with excitatory and inhibitory DREADDs would enable us to selectively activate a specific subset of neurons while inhibiting a second neuronal population, thus allowing for a better understanding of how neuronal activity translates into phenotype⁴³⁹.

Impact and future steps

We have shown that the selective activation of iBAT-projecting nerves can induce iBAT to extract glucose from circulation, and that this function is mediated exclusively by the vasculature-projecting sympathetic neurons. However, we do not yet know the specific mechanisms that link neuronal activity to lower glycemia. Literature suggests that this process should involve ECs, as they represent the first physical barrier between blood and parenchyma. However, as discussed in the last section of the Introduction, sympathetic nerves do not pass beyond the medial-adventitial border of the blood vessel, innervating only the SMCs. ECs and SMCs can communicate through both paracrine factors and direct contact (reviewed in ⁴⁴⁰). Therefore, it is possible that SMCs might induce ECs to take up glucose from circulation via some unidentified paracrine factor. Alternatively, direct activation of ECs could occur through myoendothelial gap junctions, which create an electrical continuity between ECs and SMCs⁴⁴¹ and are strongly implicated in vasodilation in resistance arterioles⁴⁴². Finally, increased uptake of glucose from circulation might also be mediated by enhanced paracellular transport due to mechanical stress in the vascular lumen caused by SMCs contraction and relaxation. Understanding the mechanics behind sympathetic-induced glucose uptake in BAT could pave the way for new possible treatments for impaired glucose homeostasis, especially in patients who are not responsive to insulin.

The existence of sympathetic subpopulations that innervate different aspects of adipose tissue has been theorized in the past. In the Introduction, I presented several authors who observed the colocalization of TH and NPY only in proximity to the vessels in BAT. My work has confirmed that this subpopulation does indeed exist; we identified several different markers and described

the functional roles within BAT. Based on these results, we can hypothesize that other peripheral organs might have similar sympathetic vascular-projecting populations, possibly with analogous markers. We have already seen two different populations of heart-projecting sympathetic neurons which modulate cardiovascular functions¹⁰⁷. Therefore, studying the regulation of blood vessels within organs throughout the body could potentially change how we understand the role of the SNS in regulating metabolism. Moreover, we restricted our analysis to the iBAT-projecting sympathetic neurons. However, it is possible that there are more sympathetic populations yet to be identified. While we focused on two populations in these studies, we also found a third adrenergic population and one cholinergic population in our dataset. Furlan et al.¹⁰⁶ identified five noradrenergic and three cholinergic sympathetic populations in mice, although they pooled neurons from several thoracic ganglia. Thus, it is highly likely that other neuronal subpopulations mediate additional aspects of sympathetic-induced activity, either in iBAT or in other organs.

Finally, the techniques presented in this work could be extended to elucidate the interaction between the sympathetic and sensory nervous system in BAT and WAT. We have shown that, in our system, we can achieve selective targeting of sympathetic neurons while avoiding sensory nerves. The selective targeting of iBAT-projecting sensory nerves could be accomplished using custom AAVs with have selective tropism for DRG neurons, such as the ROOT serotype presented by the Ye group²⁶⁴, thus sparing the SNS. This latter option appears particularly interesting given the ongoing discussion about sympathetic and sensory cross-talk in adipose tissue.

Additionally, we need to investigate the role of these sympathetic populations in conditions such as obesity and diabetes. We have discussed how SNS dysfunctions are strongly associated with

excess bodyweight and how SNS activity to BAT is decreased in obesity. It would be intriguing to observe whether one of these populations is more affected than the other during the development of metabolic disorders and whether selectively stimulating one of these populations can help improve glucose tolerance and insulin sensitivity. Similarly, studying changes in these two populations during aging could enhance our understanding of how to sustain EE in later stages of life, where weight gain is more likely to occur.

In conclusion, the findings from this work have the potential to change how we understand the SNS and its impact on systemic metabolism. However, this is only the first step in a long series of studies that, hopefully, will help elucidate how we can treat and prevent metabolic diseases.

References

- 1 Becher, T. *et al.* Brown adipose tissue is associated with cardiometabolic health. *Nat Med* **27**, 58-65, doi:10.1038/s41591-020-1126-7 (2021).
- 2 Zhang, F. *et al.* An Adipose Tissue Atlas: An Image-Guided Identification of Human-like BAT and Beige Depots in Rodents. *Cell Metab* **27**, 252-262.e253, doi:10.1016/j.cmet.2017.12.004 (2018).
- 3 Münzberg, H., Floyd, E. & Chang, J. S. Sympathetic Innervation of White Adipose Tissue: to Beige or Not to Beige? *Physiology* **36**, 246-255, doi:10.1152/physiol.00038.2020 (2021).
- 4 Scott-Solomon, E., Boehm, E. & Kuruvilla, R. The sympathetic nervous system in development and disease. *Nat Rev Neurosci* **22**, 685-702, doi:10.1038/s41583-021-00523-y (2021).
- 5 Biaggioni, I. B., Geoffrey; Low, Phillip; Paton, Julian F.R. *Primer on the Autonomic Nervous System*. (Elsevier Inc., 2012).
- 6 Goldstein, D. S. Differential responses of components of the autonomic nervous system. *Handbook of clinical neurology* **117**, 13-22 (2013).
- 7 McCorry, L. K. Physiology of the autonomic nervous system. *Am J Pharm Educ* **71**, 78, doi:10.5688/aj710478 (2007).
- 8 Cannon, W. B. *Bodily changes in pain, hunger, fear, and rage*. (D. Appleton and company, 1915).
- 9 Selye, H. Stress Without Distress. *School Guidance Worker* **32**, 5-13 (1977).
- 10 Lake, C. R., Ziegler, M. G. & Kopin, I. J. Use of plasma norepinephrine for evaluation of sympathetic neuronal function in man. *Life Sciences* **18**, 1315-1325, doi:https://doi.org/10.1016/0024-3205(76)90210-1 (1976).
- 11 Sauka-Spengler, T. & Bronner-Fraser, M. A gene regulatory network orchestrates neural crest formation. *Nat Rev Mol Cell Biol* **9**, 557-568, doi:10.1038/nrm2428 (2008).
- 12 Stubbusch, J. *et al.* Synaptic protein and pan-neuronal gene expression and their regulation by Dicer-dependent mechanisms differ between neurons and neuroendocrine cells. *Neural Dev* **8**, 16, doi:10.1186/1749-8104-8-16 (2013).
- 13 Chan, W. H., Anderson, C. R. & Gonsalvez, D. G. From proliferation to target innervation: signaling molecules that direct sympathetic nervous system development. *Cell and Tissue Research* **372**, 171+ (2018).
- 14 Feher, J. in *Quantitative Human Physiology (Second Edition)* (ed Joseph Feher) 473-486 (Academic Press, 2012).
- 15 François, M. *et al.* Sympathetic innervation of the interscapular brown adipose tissue in mouse. *Annals of the New York Academy of Sciences* **1454**, 3-13, doi:https://doi.org/10.1111/nyas.14119 (2019).
- 16 Papazoglou, I. *et al.* A distinct hypothalamus-to- β cell circuit modulates insulin secretion. *Cell Metab* **34**, 285-298.e287, doi:10.1016/j.cmet.2021.12.020 (2022).
- 17 Torres, H. *et al.* Sympathetic innervation of the mouse kidney and liver arising from prevertebral ganglia. *American Journal of Physiology-Regulatory, Integrative and Comparative Physiology* **321**, R328-R337, doi:10.1152/ajpregu.00079.2021 (2021).
- 18 Li, Y. F., LaCroix, C. & Freeling, J. Specific subtypes of nicotinic cholinergic receptors involved in sympathetic and parasympathetic cardiovascular responses. *Neurosci Lett* **462**, 20-23, doi:10.1016/j.neulet.2009.06.081 (2009).

- 19 Landis, S. C. & Keefe, D. Evidence for neurotransmitter plasticity in vivo: developmental changes in properties of cholinergic sympathetic neurons. *Dev Biol* **98**, 349-372, doi:10.1016/0012-1606(83)90365-2 (1983).
- 20 Francis, N. J. & Landis, S. C. CELLULAR AND MOLECULAR DETERMINANTS OF SYMPATHETIC NEURON DEVELOPMENT¹. *Annual Review of Neuroscience* **22**, 541-566, doi:https://doi.org/10.1146/annurev.neuro.22.1.541 (1999).
- 21 Zuber, B., Nikonenko, I., Klauser, P., Muller, D. & Dubochet, J. The mammalian central nervous synaptic cleft contains a high density of periodically organized complexes. *Proc Natl Acad Sci U S A* **102**, 19192-19197, doi:10.1073/pnas.0509527102 (2005).
- 22 Bennett, M. R. Transmission at Sympathetic Varicosities. *Physiology* **13**, 79-84, doi:10.1152/physiologyonline.1998.13.2.79 (1998).
- 23 Burnstock, G. Non-synaptic transmission at autonomic neuroeffector junctions. *Neurochemistry International* **52**, 14-25, doi:https://doi.org/10.1016/j.neuint.2007.03.007 (2008).
- 24 Burnstock, G. Autonomic neuroeffector mechanisms: recent developments. *Functional Neurology* **2**, 427-436 (1987).
- 25 Burnstock, G. in *Encyclopedia of Neuroscience* (ed Larry R. Squire) 247-254 (Academic Press, 2009).
- 26 Burnstock, G. & Milner, P. Structural and chemical organisation of the autonomic nervous system with special reference to nonadrenergic, noncholinergic transmission. *Autonomic failure: a textbook of clinical disorders of the autonomic nervous system* (2008).
- 27 Burnstock, G. Physiology and pathophysiology of purinergic neurotransmission. *Physiological reviews* **87**, 659-797 (2007).
- 28 Ernsberger, U., Deller, T. & Rohrer, H. The diversity of neuronal phenotypes in rodent and human autonomic ganglia. *Cell Tissue Res* **382**, 201-231, doi:10.1007/s00441-020-03279-6 (2020).
- 29 Murano, I., Barbatelli, G., Giordano, A. & Cinti, S. Noradrenergic parenchymal nerve fiber branching after cold acclimatisation correlates with brown adipocyte density in mouse adipose organ. *J Anat* **214**, 171-178, doi:10.1111/j.1469-7580.2008.01001.x (2009).
- 30 Goldstein, D. S. & Holmes, C. Neuronal source of plasma dopamine. *Clinical chemistry* **54**, 1864-1871 (2008).
- 31 Schütz, B., Schäfer, M. K., Eiden, L. E. & Weihe, E. Vesicular amine transporter expression and isoform selection in developing brain, peripheral nervous system and gut. *Brain Res Dev Brain Res* **106**, 181-204, doi:10.1016/s0165-3806(97)00196-x (1998).
- 32 Kumari, R. *et al.* Sympathetic NPY controls glucose homeostasis, cold tolerance, and cardiovascular functions in mice. *Cell Rep* **43**, 113674, doi:10.1016/j.celrep.2024.113674 (2024).
- 33 Masliukov, P. M. & Timmermans, J. P. Immunocytochemical properties of stellate ganglion neurons during early postnatal development. *Histochem Cell Biol* **122**, 201-209, doi:10.1007/s00418-004-0692-y (2004).
- 34 Lundberg, J., Rudehill, A., Sollevi, A., Fried, G. & Wallin, G. Co-release of neuropeptide Y and noradrenaline from pig spleen in vivo: importance of subcellular storage, nerve impulse frequency and pattern, feedback regulation and resupply by axonal transport. *Neuroscience* **28**, 475-486 (1989).

- 35 Hanson, E. S. & Dallman, M. F. Neuropeptide Y (NPY) May Integrate Responses of Hypothalamic Feeding Systems and the Hypothalamo-Pituitary-Adrenal Axis. *Journal of Neuroendocrinology* **7**, 273-279, doi:https://doi.org/10.1111/j.1365-2826.1995.tb00757.x (1995).
- 36 Zhang, L., Bijker, M. S. & Herzog, H. The neuropeptide Y system: pathophysiological and therapeutic implications in obesity and cancer. *Pharmacology & therapeutics* **131**, 91-113 (2011).
- 37 Benarroch, E. E. Neuropeptides in the sympathetic system: Presence, plasticity, modulation, and implications. *Annals of Neurology* **36**, 6-13, doi:https://doi.org/10.1002/ana.410360105 (1994).
- 38 LUNDBERG, J. M., PERNOW, J., TATEMOTO, K. & DAHLÖF, C. Pre-and postjunctional effects of NPY on sympathetic control of rat femoral artery. *Acta physiologica scandinavica* **123**, 511-513 (1985).
- 39 Sundler, F., Böttcher, G., Ekblad, E. & Håkanson, R. in *The biology of neuropeptide Y and related peptides* 157-196 (Springer, 1993).
- 40 Burnstock, G., Campbell, G., Satchell, D. & Smythe, A. Evidence that adenosine triphosphate or a related nucleotide is the transmitter substance released by non-adrenergic inhibitory nerves in the gut. *Br J Pharmacol* **40**, 668-688, doi:10.1111/j.1476-5381.1970.tb10646.x (1970).
- 41 Burnstock, G. Purinergic nerves. *Pharmacol Rev* **24**, 509-581 (1972).
- 42 Burnstock, G. in *Primer on the Autonomic Nervous System* 87-93 (Elsevier, 2012).
- 43 Li, E. *et al.* Control of lipolysis by a population of oxytocinergic sympathetic neurons. *Nature* **625**, 175-180, doi:10.1038/s41586-023-06830-x (2024).
- 44 Perez, D. M. *The adrenergic receptors: in the 21st century.* (Springer Science & Business Media, 2006).
- 45 Cotecchia, S. The α 1-adrenergic receptors: diversity of signaling networks and regulation. *Journal of Receptors and Signal Transduction* **30**, 410-419 (2010).
- 46 Rahbani, J. F. *et al.* ADRA1A–Gaq signalling potentiates adipocyte thermogenesis through CKB and TNAP. *Nature Metabolism* **4**, 1459-1473, doi:10.1038/s42255-022-00667-w (2022).
- 47 Flordellis, C., Manolis, A., Scheinin, M. & Paris, H. Clinical and pharmacological significance of α 2-adrenoceptor polymorphisms in cardiovascular diseases. *International journal of cardiology* **97**, 367-372 (2004).
- 48 Angel, I., Niddam, R. & Langer, S. Z. Involvement of alpha-2 adrenergic receptor subtypes in hyperglycemia. *Journal of Pharmacology and Experimental Therapeutics* **254**, 877-882 (1990).
- 49 Madamanchi, A. Beta-adrenergic receptor signaling in cardiac function and heart failure. *Mcgill J Med* **10**, 99-104 (2007).
- 50 Rang, H. P., Dale, M. M., Ritter, J. M., Flower, R. J. & Henderson, G. *Rang & Dale's pharmacology.* (Elsevier Health Sciences, 2011).
- 51 Atgié, C., D'Allaire, F. & Bukowiecki, L. J. Role of β 1- and β 3-adrenoceptors in the regulation of lipolysis and thermogenesis in rat brown adipocytes. *American Journal of Physiology-Cell Physiology* **273**, C1136-C1142, doi:10.1152/ajpcell.1997.273.4.C1136 (1997).
- 52 Johnson, M. Molecular mechanisms of β 2-adrenergic receptor function, response, and regulation. *Journal of Allergy and Clinical Immunology* **117**, 18-24 (2006).

- 53 Philipson, L. β -Agonists and metabolism. *Journal of allergy and clinical immunology* **110**, S313-S317 (2002).
- 54 Gauthier, C., Tavernier, G., Charpentier, F., Langin, D. & Le Marec, H. Functional beta3-adrenoceptor in the human heart. *The Journal of Clinical Investigation* **98**, 556-562, doi:10.1172/JCI118823 (1996).
- 55 Yamaguchi, O. β 3-adrenoceptors in human detrusor muscle. *Urology* **59**, 25-29, doi:https://doi.org/10.1016/S0090-4295(01)01635-1 (2002).
- 56 Dessy, C. *et al.* Endothelial β 3-Adrenoceptors Mediate Vasorelaxation of Human Coronary Microarteries Through Nitric Oxide and Endothelium-Dependent Hyperpolarization. *Circulation* **110**, 948-954, doi:10.1161/01.CIR.0000139331.85766.AF (2004).
- 57 Gauthier, C., Langin, D. & Balligand, J.-L. β 3-Adrenoceptors in the cardiovascular system. *Trends in pharmacological sciences* **21**, 426-431 (2000).
- 58 Arch, J. *et al.* Atypical β -adrenoceptor on brown adipocytes as target for anti-obesity drugs. *Nature* **309**, 163-165 (1984).
- 59 Cypess, A. M. *et al.* Activation of human brown adipose tissue by a β 3-adrenergic receptor agonist. *Cell Metab* **21**, 33-38, doi:10.1016/j.cmet.2014.12.009 (2015).
- 60 Baskin, A. S. *et al.* Regulation of Human Adipose Tissue Activation, Gallbladder Size, and Bile Acid Metabolism by a β 3-Adrenergic Receptor Agonist. *Diabetes* **67**, 2113-2125, doi:10.2337/db18-0462 (2018).
- 61 Dessy, C. & Balligand, J.-L. Beta3-adrenergic receptors in cardiac and vascular tissues: emerging concepts and therapeutic perspectives. *Advances in pharmacology* **59**, 135-163 (2010).
- 62 Emorine, L. J. *et al.* Molecular characterization of the human beta 3-adrenergic receptor. *Science* **245**, 1118-1121, doi:10.1126/science.2570461 (1989).
- 63 Nahmias, C. *et al.* Molecular characterization of the mouse beta 3-adrenergic receptor: relationship with the atypical receptor of adipocytes. *Embo j* **10**, 3721-3727, doi:10.1002/j.1460-2075.1991.tb04940.x (1991).
- 64 Lee, N. J. & Herzog, H. Coordinated regulation of energy and glucose homeostasis by insulin and the NPY system. *Journal of Neuroendocrinology* **33**, e12925, doi:https://doi.org/10.1111/jne.12925 (2021).
- 65 Lin, S., Boey, D. & Herzog, H. NPY and Y receptors: lessons from transgenic and knockout models. *Neuropeptides* **38**, 189-200 (2004).
- 66 Hodges, G. J., Jackson, D. N., Mattar, L., Johnson, J. M. & Shoemaker, J. K. Neuropeptide Y and neurovascular control in skeletal muscle and skin. *Am J Physiol Regul Integr Comp Physiol* **297**, R546-555, doi:10.1152/ajpregu.00157.2009 (2009).
- 67 Zhang, L. *et al.* Peripheral neuropeptide Y Y1 receptors regulate lipid oxidation and fat accretion. *International journal of obesity* **34**, 357-373 (2010).
- 68 Khan, D., Vasu, S., Moffett, R. C., Irwin, N. & Flatt, P. R. Islet distribution of Peptide YY and its regulatory role in primary mouse islets and immortalised rodent and human beta-cell function and survival. *Molecular and cellular endocrinology* **436**, 102-113 (2016).
- 69 Kassir, S., Olasmaa, M., Terenius, L. & Fishman, P. Neuropeptide Y inhibits cardiac adenylate cyclase through a pertussis toxin-sensitive G protein. *Journal of Biological Chemistry* **262**, 3429-3431 (1987).

- 70 Wahlestedt, C., Yanaihara, N. & Håkanson, R. Evidence for different pre-and post-junctional receptors for neuropeptide Y and related peptides. *Regul Pept* **13**, 307-318, doi:10.1016/0167-0115(86)90048-0 (1986).
- 71 Yan, C. *et al.* Peripheral-specific Y1 receptor antagonism increases thermogenesis and protects against diet-induced obesity. *Nature Communications* **12**, 2622, doi:10.1038/s41467-021-22925-3 (2021).
- 72 Heinrich, A., Kittel, A., Csölle, C., Sylvester Vizi, E. & Sperlágh, B. Modulation of neurotransmitter release by P2X and P2Y receptors in the rat spinal cord. *Neuropharmacology* **54**, 375-386, doi:10.1016/j.neuropharm.2007.10.013 (2008).
- 73 Biaggioni, I. Contrasting excitatory and inhibitory effects of adenosine in blood pressure regulation. *Hypertension* **20**, 457-465 (1992).
- 74 Church, V. Economic costs of diabetes in the US in 2002. *Diabetes care* **26**, 917-932 (2003).
- 75 Babic, T. & Travagli, R. A. Neural control of the pancreas. *Pancreapedia: The Exocrine Pancreas Knowledge Base* (2016).
- 76 Woods, S. C. & Porte Jr, D. Neural control of the endocrine pancreas. *Physiological reviews* **54**, 596-619 (1974).
- 77 Schuit, F. C. & Pipeleers, D. G. Differences in adrenergic recognition by pancreatic A and B cells. *Science* **232**, 875-877, doi:10.1126/science.2871625 (1986).
- 78 Lin, E. E., Scott-Solomon, E. & Kuruvilla, R. Peripheral Innervation in the Regulation of Glucose Homeostasis. *Trends Neurosci* **44**, 189-202, doi:10.1016/j.tins.2020.10.015 (2021).
- 79 Ahrén, B. & Lundquist, I. Effects of selective and non-selective beta-adrenergic agents on insulin secretion in vivo. *Eur J Pharmacol* **71**, 93-104, doi:10.1016/0014-2999(81)90390-3 (1981).
- 80 Ahren, B., VEITH, R. C. & TABORSKY JR, G. J. Sympathetic nerve stimulation versus pancreatic norepinephrine infusion in the dog: 1) Effects on basal release of insulin and glucagon. *Endocrinology* **121**, 323-331 (1987).
- 81 Lin, H. V. & Accili, D. Hormonal regulation of hepatic glucose production in health and disease. *Cell metabolism* **14**, 9-19 (2011).
- 82 Moore, M. C., Coate, K. C., Winnick, J. J., An, Z. & Cherrington, A. D. Regulation of hepatic glucose uptake and storage in vivo. *Advances in nutrition* **3**, 286-294 (2012).
- 83 Jensen, K. J., Alpini, G. & Glaser, S. Hepatic nervous system and neurobiology of the liver. *Comprehensive Physiology* **3**, 655 (2013).
- 84 Shimazu, T. Innervation of the liver and glucoregulation: roles of the hypothalamus and autonomic nerves. *Nutrition* **12**, 65-66 (1996).
- 85 Burcelin, R. *et al.* Impaired glucose homeostasis in mice lacking the alpha1b-adrenergic receptor subtype. *J Biol Chem* **279**, 1108-1115, doi:10.1074/jbc.M307788200 (2004).
- 86 Foster, M. T. & Bartness, T. J. Sympathetic but not sensory denervation stimulates white adipocyte proliferation. *American Journal of Physiology-Regulatory, Integrative and Comparative Physiology* **291**, R1630-R1637 (2006).
- 87 Giordano, A. *et al.* White adipose tissue lacks significant vagal innervation and immunohistochemical evidence of parasympathetic innervation. *American Journal of Physiology-Regulatory, Integrative and Comparative Physiology* **291**, R1243-R1255 (2006).

- 88 Bartness, T. J., Liu, Y., Shrestha, Y. B. & Ryu, V. Neural innervation of white adipose tissue and the control of lipolysis. *Front Neuroendocrinol* **35**, 473-493, doi:10.1016/j.yfrne.2014.04.001 (2014).
- 89 Lafontan, M. & Berlan, M. Fat Cell α 2-Adrenoceptors: The Regulation of Fat Cell Function and Lipolysis. *Endocrine reviews* **16**, 716-738 (1995).
- 90 Warner, A. *et al.* Activation of β 3-adrenoceptors increases in vivo free fatty acid uptake and utilization in brown but not white fat depots in high-fat-fed rats. *Am J Physiol Endocrinol Metab* **311**, E901-e910, doi:10.1152/ajpendo.00204.2016 (2016).
- 91 Zhao, J., Cannon, B. & Nedergaard, J. Thermogenesis is β 3-but not β 1-adrenergically mediated in rat brown fat cells, even after cold acclimation. *American Journal of Physiology-Regulatory, Integrative and Comparative Physiology* (1998).
- 92 Morigny, P., Houssier, M., Mouisel, E. & Langin, D. Adipocyte lipolysis and insulin resistance. *Biochimie* **125**, 259-266, doi:https://doi.org/10.1016/j.biochi.2015.10.024 (2016).
- 93 Arner, P. & Langin, D. Lipolysis in lipid turnover, cancer cachexia, and obesity-induced insulin resistance. *Trends in Endocrinology & Metabolism* **25**, 255-262 (2014).
- 94 Mowers, J. *et al.* Inflammation produces catecholamine resistance in obesity via activation of PDE3B by the protein kinases IKK ϵ and TBK1. *eLife* **2**, e01119, doi:10.7554/eLife.01119 (2013).
- 95 Boucher, J., Kleinridders, A. & Kahn, C. R. Insulin receptor signaling in normal and insulin-resistant states. *Cold Spring Harb Perspect Biol* **6**, doi:10.1101/cshperspect.a009191 (2014).
- 96 Grousse, A. *et al.* Partial inhibition of adipose tissue lipolysis improves glucose metabolism and insulin sensitivity without alteration of fat mass. *PLoS biology* **11**, e1001485 (2013).
- 97 Zhang, Y. *et al.* Positional cloning of the mouse obese gene and its human homologue. *Nature* **372**, 425-432, doi:10.1038/372425a0 (1994).
- 98 Dodd, G. T. *et al.* The thermogenic effect of leptin is dependent on a distinct population of prolactin-releasing peptide neurons in the dorsomedial hypothalamus. *Cell Metab* **20**, 639-649, doi:10.1016/j.cmet.2014.07.022 (2014).
- 99 Zhang, Y. *et al.* Leptin-receptor-expressing neurons in the dorsomedial hypothalamus and median preoptic area regulate sympathetic brown adipose tissue circuits. *J Neurosci* **31**, 1873-1884, doi:10.1523/jneurosci.3223-10.2011 (2011).
- 100 Mark, A. L., Correia, M. L., Rahmouni, K. & Haynes, W. G. Selective leptin resistance: a new concept in leptin physiology with cardiovascular implications. *Journal of hypertension* **20**, 1245-1250 (2002).
- 101 Navin, N. *et al.* Tumour evolution inferred by single-cell sequencing. *Nature* **472**, 90-94, doi:10.1038/nature09807 (2011).
- 102 Zeisel, A. *et al.* Molecular Architecture of the Mouse Nervous System. *Cell* **174**, 999-1014, doi:10.1016/j.cell.2018.06.021 (2018).
- 103 Xu, S. *et al.* Behavioral state coding by molecularly defined paraventricular hypothalamic cell type ensembles. *Science* **370**, doi:10.1126/science.abb2494 (2020).
- 104 Van de Sande, B. *et al.* Applications of single-cell RNA sequencing in drug discovery and development. *Nature Reviews Drug Discovery* **22**, 496-520, doi:10.1038/s41573-023-00688-4 (2023).

- 105 Bhuiyan, S. A. *et al.* Harmonized cross-species cell atlases of trigeminal and dorsal root ganglia. *Sci Adv* **10**, eadj9173, doi:10.1126/sciadv.adj9173 (2024).
- 106 Furlan, A. *et al.* Visceral motor neuron diversity delineates a cellular basis for nipple- and pilo-erection muscle control. *Nature Neuroscience* **19**, 1331-1340, doi:10.1038/nn.4376 (2016).
- 107 Sharma, S. *et al.* Tiered sympathetic control of cardiac function revealed by viral tracing and single cell transcriptome profiling. *eLife* **12**, e86295, doi:10.7554/eLife.86295 (2023).
- 108 Mapps, A. A. *et al.* Diversity of satellite glia in sympathetic and sensory ganglia. *Cell Rep* **38**, 110328, doi:10.1016/j.celrep.2022.110328 (2022).
- 109 Sivori, M. *et al.* The pelvic organs receive no parasympathetic innervation. *eLife* **12**, RP91576, doi:10.7554/eLife.91576 (2024).
- 110 Haberman, E. R. *et al.* Immunomodulatory leptin receptor+ sympathetic perineurial barrier cells protect against obesity by facilitating brown adipose tissue thermogenesis. *Immunity* **57**, 141-152.e145, doi:https://doi.org/10.1016/j.immuni.2023.11.006 (2024).
- 111 Smith, R. E. Thermoregulatory and Adaptive Behavior of Brown Adipose Tissue. *Science* **146**, 1686-1689, doi:doi:10.1126/science.146.3652.1686 (1964).
- 112 Cannon, B. & Nedergaard, J. Brown Adipose Tissue: Function and Physiological Significance. *Physiological Reviews* **84**, 277-359, doi:10.1152/physrev.00015.2003 (2004).
- 113 Saito, S., Saito, C. T. & Shingai, R. Adaptive evolution of the uncoupling protein 1 gene contributed to the acquisition of novel nonshivering thermogenesis in ancestral eutherian mammals. *Gene* **408**, 37-44 (2008).
- 114 Hughes, D. A., Jastroch, M., Stoneking, M. & Klingenspor, M. Molecular evolution of UCP1 and the evolutionary history of mammalian non-shivering thermogenesis. *BMC evolutionary biology* **9**, 1-13 (2009).
- 115 Rall, J. A. & Woledge, R. C. Influence of temperature on mechanics and energetics of muscle contraction. *American Journal of Physiology-Regulatory, Integrative and Comparative Physiology* **259**, R197-R203 (1990).
- 116 Cao, Y. Angiogenesis modulates adipogenesis and obesity. *J Clin Invest* **117**, 2362-2368, doi:10.1172/jci32239 (2007).
- 117 Vaughan, C. H., Zarebidaki, E., Ehlen, J. C. & Bartness, T. J. Analysis and measurement of the sympathetic and sensory innervation of white and brown adipose tissue. *Methods Enzymol* **537**, 199-225, doi:10.1016/b978-0-12-411619-1.00011-2 (2014).
- 118 Crabtree, A. *et al.* Quantitative Assessment of Morphological Changes in Lipid Droplets and Lipid-Mito Interactions with Aging in Brown Adipose. *bioRxiv*, doi:10.1101/2023.09.23.559135 (2024).
- 119 Wang, W. & Seale, P. Control of brown and beige fat development. *Nature Reviews Molecular Cell Biology* **17**, 691+ (2016).
- 120 Nedergaard, J. *et al.* UCP1: the only protein able to mediate adaptive non-shivering thermogenesis and metabolic inefficiency. *Biochim Biophys Acta* **1504**, 82-106, doi:10.1016/s0005-2728(00)00247-4 (2001).
- 121 Zhao, J., Cannon, B. & Nedergaard, J. alpha1-Adrenergic stimulation potentiates the thermogenic action of beta3-adrenoreceptor-generated cAMP in brown fat cells. *J Biol Chem* **272**, 32847-32856, doi:10.1074/jbc.272.52.32847 (1997).

- 122 Thonberg, H., Fredriksson, J. M., Nedergaard, J. & Cannon, B. A novel pathway for adrenergic stimulation of cAMP-response-element-binding protein (CREB) phosphorylation: mediation via alpha1-adrenoceptors and protein kinase C activation. *Biochem J* **364**, 73-79, doi:10.1042/bj3640073 (2002).
- 123 Shimizu, Y., Tanishita, T., Minokoshi, Y. & Shimazu, T. Activation of mitogen-activated protein kinase by norepinephrine in brown adipocytes from rats. *Endocrinology* **138**, 248-253 (1997).
- 124 Garlid, K. D., Jabůrek, M., Ježek, P. & Vařecha, M. How do uncoupling proteins uncouple? *Biochimica et Biophysica Acta (BBA)-Bioenergetics* **1459**, 383-389 (2000).
- 125 Roesler, A. & Kazak, L. UCP1-independent thermogenesis. *Biochemical Journal* **477**, 709-725, doi:10.1042/bcj20190463 (2020).
- 126 Sharma, A. K., Khandelwal, R. & Wolfrum, C. Futile cycles: Emerging utility from apparent futility. *Cell Metabolism* **36**, 1184-1203, doi:https://doi.org/10.1016/j.cmet.2024.03.008 (2024).
- 127 Matthias, A. *et al.* Thermogenic responses in brown fat cells are fully UCP1-dependent. UCP2 or UCP3 do not substitute for UCP1 in adrenergically or fatty acid-induced thermogenesis. *J Biol Chem* **275**, 25073-25081, doi:10.1074/jbc.M000547200 (2000).
- 128 Bartelt, A. *et al.* Brown adipose tissue activity controls triglyceride clearance. *Nature Medicine* **17**, 200-205, doi:10.1038/nm.2297 (2011).
- 129 Chondronikola, M. *et al.* Brown adipose tissue improves whole-body glucose homeostasis and insulin sensitivity in humans. *Diabetes* **63**, 4089-4099, doi:10.2337/db14-0746 (2014).
- 130 Schreiber, R. *et al.* Cold-induced thermogenesis depends on ATGL-mediated lipolysis in cardiac muscle, but not brown adipose tissue. *Cell metabolism* **26**, 753-763. e757 (2017).
- 131 Haemmerle, G. *et al.* Defective lipolysis and altered energy metabolism in mice lacking adipose triglyceride lipase. *Science* **312**, 734-737 (2006).
- 132 Wade, G., McGahee, A., Ntambi, J. M. & Simcox, J. Lipid Transport in Brown Adipocyte Thermogenesis. *Front Physiol* **12**, 787535, doi:10.3389/fphys.2021.787535 (2021).
- 133 Matsushita, M. *et al.* Impact of brown adipose tissue on body fatness and glucose metabolism in healthy humans. *International journal of obesity* **38**, 812-817 (2014).
- 134 Sidossis, L. & Kajimura, S. Brown and beige fat in humans: thermogenic adipocytes that control energy and glucose homeostasis. *J Clin Invest* **125**, 478-486, doi:10.1172/jci78362 (2015).
- 135 Maliszewska, K. & Kretowski, A. Brown Adipose Tissue and Its Role in Insulin and Glucose Homeostasis. *Int J Mol Sci* **22**, doi:10.3390/ijms22041530 (2021).
- 136 Gessner, C. *Conradi Gesneri medici Tigurini Historiae animalium liber primus de quadrupedibus viviparis : opus philosophis, medicis, grammaticis, philologis, poetis, & omnibus rerum linguarumque variarum studiosis, vtilissimum simul iucundissimumque futurum.* Editio secunda nouis iconibus nec non obseruationibus non paucis auctior atque etiam multis in locis emendatior. edn, Vol. Lib.1 (1551);Lib.2 (1586) (In Bibliopolio Cambieriano, 1551).
- 137 Trayhurn, P. Brown Adipose Tissue: A Short Historical Perspective. *Methods Mol Biol* **2448**, 1-18, doi:10.1007/978-1-0716-2087-8_1 (2022).
- 138 Trayhurn, P. Brown Adipose Tissue—A Therapeutic Target in Obesity? *Frontiers in Physiology* **9**, doi:10.3389/fphys.2018.01672 (2018).

- 139 Polimanti, O. *Il letargo*. (Tipografia del Senato di G. Bardi, 1912).
- 140 Hampton, M., Melvin, R. G. & Andrews, M. T. Transcriptomic analysis of brown adipose tissue across the physiological extremes of natural hibernation. *PLoS One* **8**, e85157, doi:10.1371/journal.pone.0085157 (2013).
- 141 Hook, W. E. & Barron, E. S. G. THE RESPIRATION OF BROWN ADIPOSE TISSUE AND KIDNEY OF THE HIBERNATING AND NON-HIBERNATING GROUND SQUIRREL. *American Journal of Physiology-Legacy Content* **133**, 56-63, doi:10.1152/ajplegacy.1941.133.1.56 (1941).
- 142 Smith, R. E. Thermogenic activity of the hibernating gland in the cold-acclimated rat. *Physiologist* **4**, 113 (1961).
- 143 Trayhurn, P., Jones, P. M., McGuckin, M. M. & Goodbody, A. E. Effects of overfeeding on energy balance and brown fat thermogenesis in obese (ob/ob) mice. *Nature* **295**, 323-325 (1982).
- 144 Wu, C. *et al.* Activating Brown Adipose Tissue for Weight Loss and Lowering of Blood Glucose Levels: A MicroPET Study Using Obese and Diabetic Model Mice. *PLOS ONE* **9**, e113742, doi:10.1371/journal.pone.0113742 (2014).
- 145 Aherne, W. & Hull, D. Brown adipose tissue and heat production in the newborn infant. *J Pathol Bacteriol* **91**, 223-234, doi:10.1002/path.1700910126 (1966).
- 146 Bouillaud, F. *et al.* Detection of brown adipose tissue uncoupling protein mRNA in adult patients by a human genomic probe. *Clin Sci (Lond)* **75**, 21-27, doi:10.1042/cs0750021 (1988).
- 147 Lean, M. E., James, W. P., Jennings, G. & Trayhurn, P. Brown adipose tissue in patients with pheochromocytoma. *Int J Obes* **10**, 219-227 (1986).
- 148 Warburg, O. On the origin of cancer cells. *Science* **123**, 309-314 (1956).
- 149 Virtanen, K. A. *et al.* Functional Brown Adipose Tissue in Healthy Adults. *New England Journal of Medicine* **360**, 1518-1525, doi:doi:10.1056/NEJMoa0808949 (2009).
- 150 van Marken Lichtenbelt, W. D. *et al.* Cold-activated brown adipose tissue in healthy men. *N Engl J Med* **360**, 1500-1508, doi:10.1056/NEJMoa0808718 (2009).
- 151 Cypess, A. M. *et al.* Identification and importance of brown adipose tissue in adult humans. *New England journal of medicine* **360**, 1509-1517 (2009).
- 152 Leitner, B. P. *et al.* Mapping of human brown adipose tissue in lean and obese young men. *Proc Natl Acad Sci U S A* **114**, 8649-8654, doi:10.1073/pnas.1705287114 (2017).
- 153 Kalinovich, A. V., de Jong, J. M., Cannon, B. & Nedergaard, J. UCP1 in adipose tissues: two steps to full browning. *Biochimie* **134**, 127-137 (2017).
- 154 Peppler, W. T., Townsend, L. K., Knuth, C. M., Foster, M. T. & Wright, D. C. Subcutaneous inguinal white adipose tissue is responsive to, but dispensable for, the metabolic health benefits of exercise. *Am J Physiol Endocrinol Metab* **314**, E66-e77, doi:10.1152/ajpendo.00226.2017 (2018).
- 155 Park, J. *et al.* Progenitor-like characteristics in a subgroup of UCP1+ cells within white adipose tissue. *Developmental cell* **56**, 985-999. e984 (2021).
- 156 Shao, M. *et al.* Cellular origins of beige fat cells revisited. *Diabetes* **68**, 1874-1885 (2019).
- 157 Wang, Q. A., Tao, C., Gupta, R. K. & Scherer, P. E. Tracking adipogenesis during white adipose tissue development, expansion and regeneration. *Nature medicine* **19**, 1338-1344 (2013).

- 158 Rosenwald, M., Perdikari, A., Rüllicke, T. & Wolfrum, C. Bi-directional interconversion
of brite and white adipocytes. *Nature cell biology* **15**, 659-667 (2013).
- 159 Roh, H. C. *et al.* Warming induces significant reprogramming of beige, but not brown,
adipocyte cellular identity. *Cell metabolism* **27**, 1121-1137. e1125 (2018).
- 160 Cinti, S. White, brown, beige and pink: A rainbow in the adipose organ. *Current Opinion
in Endocrine and Metabolic Research* **4**, 29-36,
doi:<https://doi.org/10.1016/j.coemr.2018.07.003> (2019).
- 161 Atit, R. *et al.* Beta-catenin activation is necessary and sufficient to specify the dorsal
dermal fate in the mouse. *Dev Biol* **296**, 164-176, doi:10.1016/j.ydbio.2006.04.449
(2006).
- 162 Seale, P. *et al.* PRDM16 controls a brown fat/skeletal muscle switch. *Nature* **454**, 961-
967 (2008).
- 163 Wu, J. *et al.* Beige adipocytes are a distinct type of thermogenic fat cell in mouse and
human. *Cell* **150**, 366-376 (2012).
- 164 Angueira, A. R. *et al.* Early B cell factor activity controls developmental and adaptive
thermogenic gene programming in adipocytes. *Cell reports* **30**, 2869-2878. e2864 (2020).
- 165 Vinkers, C. H., van Oorschot, R., Olivier, B. & Groenink, L. in *Mood and Anxiety
Related Phenotypes in Mice: Characterization Using Behavioral Tests* (ed Todd D.
Gould) 139-152 (Humana Press, 2009).
- 166 Liu, X., Rossmeisl, M., McClaine, J. & Kozak, L. P. Paradoxical resistance to diet-
induced obesity in UCP1-deficient mice. *The Journal of Clinical Investigation* **111**, 399-
407, doi:10.1172/JCI15737 (2003).
- 167 Škop, V. *et al.* Mouse Thermoregulation: Introducing the Concept of the Thermoneutral
Point. *Cell Rep* **31**, 107501, doi:10.1016/j.celrep.2020.03.065 (2020).
- 168 Abreu-Vieira, G., Hagberg, C. E., Spalding, K. L., Cannon, B. & Nedergaard, J.
Adrenergically stimulated blood flow in brown adipose tissue is not dependent on
thermogenesis. *Am J Physiol Endocrinol Metab* **308**, E822-829,
doi:10.1152/ajpendo.00494.2014 (2015).
- 169 Himms-Hagen, J. *et al.* Effect of CL-316,243, a thermogenic beta 3-agonist, on energy
balance and brown and white adipose tissues in rats. *American Journal of Physiology-
Regulatory, Integrative and Comparative Physiology* **266**, R1371-R1382,
doi:10.1152/ajpregu.1994.266.4.R1371 (1994).
- 170 Ghorbani, M., Claus, T. H. & Himms-Hagen, J. Hypertrophy of brown adipocytes in
brown and white adipose tissues and reversal of diet-induced obesity in rats treated with a
 β 3-adrenoceptor agonist. *Biochemical pharmacology* **54**, 121-131 (1997).
- 171 Grujic, D. *et al.* Beta3-adrenergic receptors on white and brown adipocytes mediate
beta3-selective agonist-induced effects on energy expenditure, insulin secretion, and food
intake. A study using transgenic and gene knockout mice. *J Biol Chem* **272**, 17686-
17693, doi:10.1074/jbc.272.28.17686 (1997).
- 172 Ravussin, Y., Xiao, C., Gavrilova, O. & Reitman, M. L. Effect of intermittent cold
exposure on brown fat activation, obesity, and energy homeostasis in mice. *PLoS One* **9**,
e85876, doi:10.1371/journal.pone.0085876 (2014).
- 173 Nedergaard, J., Bengtsson, T. & Cannon, B. Unexpected evidence for active brown
adipose tissue in adult humans. *American Journal of Physiology-Endocrinology and
Metabolism* (2007).

- 174 Saito, M. *et al.* High Incidence of Metabolically Active Brown Adipose Tissue in Healthy Adult Humans: Effects of Cold Exposure and Adiposity. *Diabetes* **58**, 1526-1531, doi:10.2337/db09-0530 (2009).
- 175 Ouellet, V. *et al.* Brown adipose tissue oxidative metabolism contributes to energy expenditure during acute cold exposure in humans. *The Journal of Clinical Investigation* **122**, 545-552, doi:10.1172/JCI60433 (2012).
- 176 Loh, R. K. C. *et al.* Acute metabolic and cardiovascular effects of mirabegron in healthy individuals. *Diabetes Obes Metab* **21**, 276-284, doi:10.1111/dom.13516 (2019).
- 177 O'Mara, A. E. *et al.* Chronic mirabegron treatment increases human brown fat, HDL cholesterol, and insulin sensitivity. *The Journal of clinical investigation* **130**, 2209-2219 (2020).
- 178 Chen, K. Y. *et al.* Opportunities and challenges in the therapeutic activation of human energy expenditure and thermogenesis to manage obesity. *J Biol Chem* **295**, 1926-1942, doi:10.1074/jbc.REV119.007363 (2020).
- 179 Bel, J. S., Tai, T. C., Khaper, N. & Lees, S. J. Mirabegron: The most promising adipose tissue beiging agent. *Physiol Rep* **9**, e14779, doi:10.14814/phy2.14779 (2021).
- 180 Blondin, D. P. *et al.* Human Brown Adipocyte Thermogenesis Is Driven by β 2-AR Stimulation. *Cell Metab* **32**, 287-300.e287, doi:10.1016/j.cmet.2020.07.005 (2020).
- 181 Straat, M. E. *et al.* Stimulation of the beta-2-adrenergic receptor with salbutamol activates human brown adipose tissue. *Cell Rep Med* **4**, 100942, doi:10.1016/j.xcrm.2023.100942 (2023).
- 182 Ishida, Y. *et al.* Genetic evidence for involvement of β 2-adrenergic receptor in brown adipose tissue thermogenesis in humans. *International Journal of Obesity* **48**, 1110-1117, doi:10.1038/s41366-024-01522-6 (2024).
- 183 Czech, M. P. Mechanisms of insulin resistance related to white, beige, and brown adipocytes. *Molecular Metabolism* **34**, 27-42, doi:https://doi.org/10.1016/j.molmet.2019.12.014 (2020).
- 184 Olsen, J. M. *et al.* β (3)-Adrenergically induced glucose uptake in brown adipose tissue is independent of UCP1 presence or activity: Mediation through the mTOR pathway. *Mol Metab* **6**, 611-619, doi:10.1016/j.molmet.2017.02.006 (2017).
- 185 Wang, T.-Y., Liu, C., Wang, A. & Sun, Q. Intermittent cold exposure improves glucose homeostasis associated with brown and white adipose tissues in mice. *Life Sciences* **139**, 153-159, doi:https://doi.org/10.1016/j.lfs.2015.07.030 (2015).
- 186 Blauw, L. L. *et al.* Diabetes incidence and glucose intolerance prevalence increase with higher outdoor temperature. *BMJ Open Diabetes Research and Care* **5**, e000317 (2017).
- 187 Hanssen, M. J. *et al.* Short-term cold acclimation improves insulin sensitivity in patients with type 2 diabetes mellitus. *Nat Med* **21**, 863-865, doi:10.1038/nm.3891 (2015).
- 188 Ivanova, Y. M. & Blondin, D. P. Examining the benefits of cold exposure as a therapeutic strategy for obesity and type 2 diabetes. *Journal of Applied Physiology* **130**, 1448-1459, doi:10.1152/jappphysiol.00934.2020 (2021).
- 189 Fasshauer, M. & Blüher, M. Adipokines in health and disease. *Trends in pharmacological sciences* **36**, 461-470 (2015).
- 190 Villarroya, J., Cereijo, R. & Villarroya, F. An endocrine role for brown adipose tissue? *American journal of physiology-Endocrinology and metabolism* **305**, E567-E572 (2013).
- 191 Villarroya, F., Cereijo, R., Villarroya, J. & Giralt, M. Brown adipose tissue as a secretory organ. *Nature Reviews Endocrinology* **13**, 26+ (2017).

- 192 Whittle, A. J. *et al.* BMP8B increases brown adipose tissue thermogenesis through both
central and peripheral actions. *Cell* **149**, 871-885, doi:10.1016/j.cell.2012.02.066 (2012).
- 193 Pellegrinelli, V. *et al.* Adipocyte-secreted BMP8b mediates adrenergic-induced
remodeling of the neuro-vascular network in adipose tissue. *Nature Communications* **9**,
4974, doi:10.1038/s41467-018-07453-x (2018).
- 194 Nugroho, D. B. *et al.* Neuregulin-4 is an angiogenic factor that is critically involved in
the maintenance of adipose tissue vasculature. *Biochem Biophys Res Commun* **503**, 378-
384, doi:10.1016/j.bbrc.2018.06.043 (2018).
- 195 Wang, G. X. *et al.* The brown fat-enriched secreted factor Nrg4 preserves metabolic
homeostasis through attenuation of hepatic lipogenesis. *Nat Med* **20**, 1436-1443,
doi:10.1038/nm.3713 (2014).
- 196 Guo, L. *et al.* Hepatic neuregulin 4 signaling defines an endocrine checkpoint for
steatosis-to-NASH progression. *J Clin Invest* **127**, 4449-4461, doi:10.1172/jci96324
(2017).
- 197 Cui, X. *et al.* Adipose tissue-derived neurotrophic factor 3 regulates sympathetic
innervation and thermogenesis in adipose tissue. *Nature Communications* **12**, 5362,
doi:10.1038/s41467-021-25766-2 (2021).
- 198 Zeng, X. *et al.* Innervation of thermogenic adipose tissue via a calsyntenin 3 β -S100b
axis. *Nature* **569**, 229-235, doi:10.1038/s41586-019-1156-9 (2019).
- 199 Cao, H. *et al.* Identification of a lipokine, a lipid hormone linking adipose tissue to
systemic metabolism. *Cell* **134**, 933-944 (2008).
- 200 Lynes, M. D. *et al.* The cold-induced lipokine 12,13-diHOME promotes fatty acid
transport into brown adipose tissue. *Nature Medicine* **23**, 631-637, doi:10.1038/nm.4297
(2017).
- 201 Stanford, K. I. *et al.* 12,13-diHOME: An Exercise-Induced Lipokine that Increases
Skeletal Muscle Fatty Acid Uptake. *Cell Metab* **27**, 1111-1120.e1113,
doi:10.1016/j.cmet.2018.03.020 (2018).
- 202 Leiria, L. O. *et al.* 12-Lipoxygenase Regulates Cold Adaptation and Glucose Metabolism
by Producing the Omega-3 Lipid 12-HEPE from Brown Fat. *Cell Metab* **30**, 768-
783.e767, doi:10.1016/j.cmet.2019.07.001 (2019).
- 203 Verkerke, A. R. P. *et al.* BCAA-nitrogen flux in brown fat controls metabolic health
independent of thermogenesis. *Cell* **187**, 2359-2374.e2318,
doi:10.1016/j.cell.2024.03.030 (2024).
- 204 Chitraju, C., Fischer, A. W., Farese, R. V. & Walther, T. C. Lipid droplets in brown
adipose tissue are dispensable for cold-induced thermogenesis. *Cell reports* **33** (2020).
- 205 Intaglietta, M. & ROSELL, S. Capillary permeability and sympathetic activity in canine
subcutaneous adipose tissue. *Nature* **249**, 481-482 (1974).
- 206 Orava, J. *et al.* Different metabolic responses of human brown adipose tissue to activation
by cold and insulin. *Cell metabolism* **14**, 272-279 (2011).
- 207 Chi, J. *et al.* Three-dimensional adipose tissue imaging reveals regional variation in beige
fat biogenesis and PRDM16-dependent sympathetic neurite density. *Cell metabolism* **27**,
226-236. e223 (2018).
- 208 Barreau, C. *et al.* Regionalization of browning revealed by whole subcutaneous adipose
tissue imaging. *Obesity* **24**, 1081-1089 (2016).
- 209 Huesing, C. *et al.* Sympathetic innervation of inguinal white adipose tissue in the mouse.
Journal of Comparative Neurology **529**, 1465-1485 (2021).

- 210 Morrison, S. F. Differential control of sympathetic outflow. *American Journal of Physiology-Regulatory, Integrative and Comparative Physiology* **281**, R683-R698 (2001).
- 211 Brito, N. A., Brito, M. N. & Bartness, T. J. Differential sympathetic drive to adipose tissues after food deprivation, cold exposure or glucoprivation. *American Journal of Physiology-Regulatory, Integrative and Comparative Physiology* **294**, R1445-R1452, doi:10.1152/ajpregu.00068.2008 (2008).
- 212 Brito, M. N., Brito, N. A., Baro, D. J., Song, C. K. & Bartness, T. J. Differential activation of the sympathetic innervation of adipose tissues by melanocortin receptor stimulation. *Endocrinology* **148**, 5339-5347, doi:10.1210/en.2007-0621 (2007).
- 213 Yoneshiro, T. *et al.* Age-Related Decrease in Cold-Activated Brown Adipose Tissue and Accumulation of Body Fat in Healthy Humans. *Obesity* **19**, 1755-1760, doi:https://doi.org/10.1038/oby.2011.125 (2011).
- 214 Bahler, L. *et al.* Differences in Sympathetic Nervous Stimulation of Brown Adipose Tissue Between the Young and Old, and the Lean and Obese. *Journal of Nuclear Medicine* **57**, 372-377, doi:10.2967/jnumed.115.165829 (2016).
- 215 Kulterer, O. C. *et al.* Brown Adipose Tissue Prevalence Is Lower in Obesity but Its Metabolic Activity Is Intact. *Front Endocrinol (Lausanne)* **13**, 858417, doi:10.3389/fendo.2022.858417 (2022).
- 216 Cesaro, A. *et al.* Visceral adipose tissue and residual cardiovascular risk: a pathological link and new therapeutic options. *Front Cardiovasc Med* **10**, 1187735, doi:10.3389/fcvm.2023.1187735 (2023).
- 217 Sanchez-Rangel, E. *et al.* Norepinephrine transporter availability in brown fat is reduced in obesity: a human PET study with [(11)C] MRB. *Int J Obes (Lond)* **44**, 964-967, doi:10.1038/s41366-019-0471-4 (2020).
- 218 Saari, T. J. *et al.* Basal and cold-induced fatty acid uptake of human brown adipose tissue is impaired in obesity. *Scientific Reports* **10**, 14373, doi:10.1038/s41598-020-71197-2 (2020).
- 219 Ferrante, A. W., Jr. Macrophages, fat, and the emergence of immunometabolism. *J Clin Invest* **123**, 4992-4993, doi:10.1172/jci73658 (2013).
- 220 Mitra, S., Banik, A., Saurabh, S., Maulik, M. & Khatri, S. N. Neuroimmunometabolism: A New Pathological Nexus Underlying Neurodegenerative Disorders. *J Neurosci* **42**, 1888-1907, doi:10.1523/jneurosci.0998-21.2022 (2022).
- 221 Martinez-Sanchez, N. *et al.* The sympathetic nervous system in the 21st century: Neuroimmune interactions in metabolic homeostasis and obesity. *Neuron* **110**, 3597-3626, doi:10.1016/j.neuron.2022.10.017 (2022).
- 222 Ferrante Jr, A. W. Obesity-induced inflammation: a metabolic dialogue in the language of inflammation. *Journal of Internal Medicine* **262**, 408-414, doi:https://doi.org/10.1111/j.1365-2796.2007.01852.x (2007).
- 223 Pirzgalska, R. M. *et al.* Sympathetic neuron-associated macrophages contribute to obesity by importing and metabolizing norepinephrine. *Nat Med* **23**, 1309-1318, doi:10.1038/nm.4422 (2017).
- 224 Guo, T. *et al.* Adipocyte ALK7 links nutrient overload to catecholamine resistance in obesity. *Elife* **3**, e03245, doi:10.7554/eLife.03245 (2014).

- 225 Reynisdottir, S., Ellerfeldt, K., Wahrenberg, H., Lithell, H. & Arner, P. Multiple lipolysis defects in the insulin resistance (metabolic) syndrome. *J Clin Invest* **93**, 2590-2599, doi:10.1172/jci117271 (1994).
- 226 Arner, P. Catecholamine-induced lipolysis in obesity. *Int J Obes Relat Metab Disord* **23 Suppl 1**, 10-13, doi:10.1038/sj.ijo.0800789 (1999).
- 227 Jocken, J. W., Blaak, E. E., van der Kallen, C. J., van Baak, M. A. & Saris, W. H. Blunted beta-adrenoceptor-mediated fat oxidation in overweight subjects: a role for the hormone-sensitive lipase gene. *Metabolism* **57**, 326-332, doi:10.1016/j.metabol.2007.10.006 (2008).
- 228 Valentine, J. M. *et al.* β -Adrenergic receptor downregulation leads to adipocyte catecholamine resistance in obesity. *J Clin Invest* **132**, doi:10.1172/jci153357 (2022).
- 229 Reynisdottir, S. *et al.* Effects of weight reduction on the regulation of lipolysis in adipocytes of women with upper-body obesity. *Clin Sci (Lond)* **89**, 421-429, doi:10.1042/cs0890421 (1995).
- 230 Large, V. *et al.* Decreased expression and function of adipocyte hormone-sensitive lipase in subcutaneous fat cells of obese subjects. *Journal of lipid research* **40**, 2059-2065 (1999).
- 231 Muller, G., Ertl, J., Gerl, M. & Preibisch, G. Leptin impairs metabolic actions of insulin in isolated rat adipocytes. *Journal of Biological Chemistry* **272**, 10585-10593 (1997).
- 232 Martin, L. F. *et al.* Alterations in adipocyte adenylate cyclase activity in morbidly obese and formerly morbidly obese humans. *Surgery* **108**, 228-234; discussion 234-225 (1990).
- 233 Zhao, S. *et al.* Partial Leptin Reduction as an Insulin Sensitization and Weight Loss Strategy. *Cell Metabolism* **30**, 706-719.e706, doi:https://doi.org/10.1016/j.cmet.2019.08.005 (2019).
- 234 Zhao, S. *et al.* Leptin Reduction as a Required Component for Weight Loss. *Diabetes* **73**, 197-210, doi:10.2337/db23-0571 (2023).
- 235 Wirsén, C. Adrenergic innervation of adipose tissue examined by fluorescence microscopy. *Nature* **202**, 913-913 (1964).
- 236 Taylor, K. W. Handbook of Physiology Section 5: Adipose Tissue. *Proc R Soc Med* **59**, 283 (1966).
- 237 Fischer, A. W., Schlein, C., Cannon, B., Heeren, J. & Nedergaard, J. Intact innervation is essential for diet-induced recruitment of brown adipose tissue. *Am J Physiol Endocrinol Metab* **316**, E487-e503, doi:10.1152/ajpendo.00443.2018 (2019).
- 238 Engel, B. T., Sato, A. & Sato, Y. Responses of sympathetic nerves innervating blood vessels in interscapular, brown adipose tissue and skin during cold stimulation in anesthetized C57BL/6J mice. *Jpn J Physiol* **42**, 549-559, doi:10.2170/jjphysiol.42.549 (1992).
- 239 Barrett, M. S., Hegarty, D. M., Habecker, B. A. & Aicher, S. A. Distinct morphology of cardiac- and brown adipose tissue-projecting neurons in the stellate ganglia of mice. *Physiol Rep* **10**, e15334, doi:10.14814/phy2.15334 (2022).
- 240 Rothwell, N. J. & Stock, M. J. Effects of denervating brown adipose tissue on the responses to cold, hyperphagia and noradrenaline treatment in the rat. *J Physiol* **355**, 457-463, doi:10.1113/jphysiol.1984.sp015431 (1984).
- 241 Foster, D. O., Depocas, F. & Zaror-Behrens, G. Unilaterality of the sympathetic innervation of each pad of rat interscapular brown adipose tissue. *Can J Physiol Pharmacol* **60**, 107-113, doi:10.1139/y82-018 (1982).

- 242 Takahashi, A., Shimazu, T. & Maruyama, Y. Importance of sympathetic nerves for the stimulatory effect of cold exposure on glucose utilization in brown adipose tissue. *The Japanese Journal of Physiology* **42**, 653-664 (1992).
- 243 Huesing, C. *et al.* Organization of sympathetic innervation of interscapular brown adipose tissue in the mouse. *J Comp Neurol* **530**, 1363-1378, doi:10.1002/cne.25281 (2022).
- 244 Ungerstedt, U. 6-Hydroxy-dopamine induced degeneration of central monoamine neurons. *Eur J Pharmacol* **5**, 107-110, doi:10.1016/0014-2999(68)90164-7 (1968).
- 245 Depocas, F., Foster, D. O., Zaror-Behrens, G., Lacelle, S. & Nadeau, B. Recovery of function in sympathetic nerves of interscapular brown adipose tissue of rats treated with 6-hydroxydopamine. *Can J Physiol Pharmacol* **62**, 1327-1332, doi:10.1139/y84-222 (1984).
- 246 Young, J. B., Saville, E., Rothwell, N. J., Stock, M. J. & Landsberg, L. Effect of diet and cold exposure on norepinephrine turnover in brown adipose tissue of the rat. *The Journal of clinical investigation* **69**, 1061-1071 (1982).
- 247 Nakamura, K. & Morrison, S. F. A thermosensory pathway that controls body temperature. *Nat Neurosci* **11**, 62-71, doi:10.1038/nn2027 (2008).
- 248 Kawate, R., Talan, M. I. & Engel, B. T. Sympathetic nervous activity to brown adipose tissue increases in cold-tolerant mice. *Physiology & Behavior* **55**, 921-925, doi:https://doi.org/10.1016/0031-9384(94)90080-9 (1994).
- 249 De Matteis, R., Ricquier, D. & Cinti, S. TH-, NPY-, SP-, and CGRP-immunoreactive nerves in interscapular brown adipose tissue of adult rats acclimated at different temperatures: an immunohistochemical study. *Journal of Neurocytology* **27**, 877-886, doi:10.1023/A:1006996922657 (1998).
- 250 Lim, S. *et al.* Cold-induced activation of brown adipose tissue and adipose angiogenesis in mice. *Nature Protocols* **7**, 606-615, doi:10.1038/nprot.2012.013 (2012).
- 251 Jiang, H., Ding, X., Cao, Y., Wang, H. & Zeng, W. Dense Intra-adipose Sympathetic Arborizations Are Essential for Cold-Induced Beiging of Mouse White Adipose Tissue. *Cell Metab* **26**, 686-692.e683, doi:10.1016/j.cmet.2017.08.016 (2017).
- 252 Talan, M. I. & Engel, B. T. Habituation and dishabituation to repeated mild cold exposures in C57BL/6J mice. *Physiology & behavior* **44**, 753-757 (1988).
- 253 Morrison, S. F., Ramamurthy, S. & Young, J. B. Reduced Rearing Temperature Augments Responses in Sympathetic Outflow to Brown Adipose Tissue. *The Journal of Neuroscience* **20**, 9264-9271, doi:10.1523/jneurosci.20-24-09264.2000 (2000).
- 254 Chabowska-Kita, A., Trabczynska, A., Korytko, A., Kaczmarek, M. M. & Kozak, L. P. Low ambient temperature during early postnatal development fails to cause a permanent induction of brown adipocytes. *Faseb j* **29**, 3238-3252, doi:10.1096/fj.15-271395 (2015).
- 255 Oldfield, B. J. *et al.* The neurochemical characterisation of hypothalamic pathways projecting polysynaptically to brown adipose tissue in the rat. *Neuroscience* **110**, 515-526, doi:10.1016/s0306-4522(01)00555-3 (2002).
- 256 Bamshad, M., Song, C. K. & Bartness, T. J. CNS origins of the sympathetic nervous system outflow to brown adipose tissue. *American Journal of Physiology-Regulatory, Integrative and Comparative Physiology* **276**, R1569-R1578, doi:10.1152/ajpregu.1999.276.6.R1569 (1999).

- 257 Ryu, V., Garretson, J. T., Liu, Y., Vaughan, C. H. & Bartness, T. J. Brown Adipose Tissue Has Sympathetic-Sensory Feedback Circuits. *The Journal of Neuroscience* **35**, 2181-2190, doi:10.1523/jneurosci.3306-14.2015 (2015).
- 258 Cao, W. H., Fan, W. & Morrison, S. F. Medullary pathways mediating specific sympathetic responses to activation of dorsomedial hypothalamus. *Neuroscience* **126**, 229-240, doi:10.1016/j.neuroscience.2004.03.013 (2004).
- 259 Morrison, S. F. & Madden, C. J. Central nervous system regulation of brown adipose tissue. *Compr Physiol* **4**, 1677-1713, doi:10.1002/cphy.c140013 (2014).
- 260 Morrison, S. F., Madden, C. J. & Tupone, D. Central neural regulation of brown adipose tissue thermogenesis and energy expenditure. *Cell Metab* **19**, 741-756, doi:10.1016/j.cmet.2014.02.007 (2014).
- 261 Madden, C. J. & Morrison, S. F. Neurons in the paraventricular nucleus of the hypothalamus inhibit sympathetic outflow to brown adipose tissue. *Am J Physiol Regul Integr Comp Physiol* **296**, R831-843, doi:10.1152/ajpregu.91007.2008 (2009).
- 262 Chi, J., Crane, A., Wu, Z. & Cohen, P. Adipo-Clear: A Tissue Clearing Method for Three-Dimensional Imaging of Adipose Tissue. *J Vis Exp*, doi:10.3791/58271 (2018).
- 263 Willows, J. W., Blaszkiewicz, M. & Townsend, K. L. A clearing-free protocol for imaging intact whole adipose tissue innervation in mice. *STAR Protoc* **3**, 101109, doi:10.1016/j.xpro.2021.101109 (2022).
- 264 Wang, Y. *et al.* The role of somatosensory innervation of adipose tissues. *Nature* **609**, 569-574, doi:10.1038/s41586-022-05137-7 (2022).
- 265 Perdikari, A. *et al.* Visualization of sympathetic neural innervation in human white adipose tissue. *Open Biology* **12**, 210345, doi:doi:10.1098/rsob.210345 (2022).
- 266 Gilleron, J. *et al.* Exploring Adipose Tissue Structure by Methylsalicylate Clearing and 3D Imaging. *J Vis Exp*, doi:10.3791/61640 (2020).
- 267 Willows, J. W. *et al.* Visualization and analysis of whole depot adipose tissue neural innervation. *iScience* **24**, 103127, doi:https://doi.org/10.1016/j.isci.2021.103127 (2021).
- 268 Zeng, W. *et al.* Sympathetic neuro-adipose connections mediate leptin-driven lipolysis. *Cell* **163**, 84-94 (2015).
- 269 Cao, Y., Wang, H., Wang, Q., Han, X. & Zeng, W. Three-dimensional volume fluorescence-imaging of vascular plasticity in adipose tissues. *Molecular metabolism* **14**, 71-81 (2018).
- 270 He, C., Yuan, Y., Gong, C., Wang, X. & Lyu, G. Applications of Tissue Clearing in Central and Peripheral Nerves. *Neuroscience* **546**, 104-117, doi:https://doi.org/10.1016/j.neuroscience.2024.03.030 (2024).
- 271 Madden, C. J., Santos da Conceicao, E. P. & Morrison, S. F. Vagal afferent activation decreases brown adipose tissue (BAT) sympathetic nerve activity and BAT thermogenesis. *Temperature (Austin)* **4**, 89-96, doi:10.1080/23328940.2016.1257407 (2017).
- 272 Stocker, S. D. & Muntzel, M. S. Recording sympathetic nerve activity chronically in rats: surgery techniques, assessment of nerve activity, and quantification. *Am J Physiol Heart Circ Physiol* **305**, H1407-1416, doi:10.1152/ajpheart.00173.2013 (2013).
- 273 Rahmouni, K., Morgan, D. A., Morgan, G. M., Mark, A. L. & Haynes, W. G. Role of Selective Leptin Resistance in Diet-Induced Obesity Hypertension. *Diabetes* **54**, 2012-2018, doi:10.2337/diabetes.54.7.2012 (2005).

- 274 Meyer, C. W., Ootsuka, Y. & Romanovsky, A. A. Body Temperature Measurements for Metabolic Phenotyping in Mice. *Frontiers in Physiology* **8**, doi:10.3389/fphys.2017.00520 (2017).
- 275 Kang, H. J., Minamimoto, T., Wess, J. & Roth, B. L. Chemogenetics for cell-type-specific modulation of signalling and neuronal activity. *Nature Reviews Methods Primers* **3**, 93, doi:10.1038/s43586-023-00276-1 (2023).
- 276 Emiliani, V. *et al.* Optogenetics for light control of biological systems. *Nature Reviews Methods Primers* **2**, 55, doi:10.1038/s43586-022-00136-4 (2022).
- 277 Nectow, A. R. & Nestler, E. J. Viral tools for neuroscience. *Nat Rev Neurosci* **21**, 669-681, doi:10.1038/s41583-020-00382-z (2020).
- 278 Tajima, K. *et al.* Wireless optogenetics protects against obesity via stimulation of non-canonical fat thermogenesis. *Nature Communications* **11**, 1730, doi:10.1038/s41467-020-15589-y (2020).
- 279 Jeong, J. H., Chang, J. S. & Jo, Y.-H. Intracellular glycolysis in brown adipose tissue is essential for optogenetically induced nonshivering thermogenesis in mice. *Scientific Reports* **8**, 6672, doi:10.1038/s41598-018-25265-3 (2018).
- 280 Lyons, C. E. *et al.* Optogenetic-induced sympathetic neuromodulation of brown adipose tissue thermogenesis. *Faseb j* **34**, 2765-2773, doi:10.1096/fj.201901361RR (2020).
- 281 Nayak, G. *et al.* Adaptive Thermogenesis in Mice Is Enhanced by Opsin 3-Dependent Adipocyte Light Sensing. *Cell Rep* **30**, 672-686.e678, doi:10.1016/j.celrep.2019.12.043 (2020).
- 282 Chen, X. *et al.* Engineered AAVs for non-invasive gene delivery to rodent and non-human primate nervous systems. *Neuron* **110**, 2242-2257.e2246, doi:10.1016/j.neuron.2022.05.003 (2022).
- 283 Mishra, G. & Townsend, K. L. The metabolic and functional roles of sensory nerves in adipose tissues. *Nature Metabolism* **5**, 1461-1474, doi:10.1038/s42255-023-00868-x (2023).
- 284 Mishra, G. & Townsend, K. L. Sensory nerve and neuropeptide diversity in adipose tissues. *Molecules and Cells* **47**, 100030, doi:https://doi.org/10.1016/j.mocell.2024.100030 (2024).
- 285 Osaka, T. *et al.* Temperature- and capsaicin-sensitive nerve fibers in brown adipose tissue attenuate thermogenesis in the rat. *Pflugers Arch* **437**, 36-42, doi:10.1007/s004240050743 (1998).
- 286 Himms-Hagen, J., Cui, J. & Lynn Sigurdson, S. Sympathetic and sensory nerves in control of growth of brown adipose tissue: Effects of denervation and of capsaicin. *Neurochemistry International* **17**, 271-279, doi:https://doi.org/10.1016/0197-0186(90)90149-N (1990).
- 287 Cui, J. & Himms-Hagen, J. Long-term decrease in body fat and in brown adipose tissue in capsaicin-desensitized rats. *Am J Physiol* **262**, R568-573, doi:10.1152/ajpregu.1992.262.4.R568 (1992).
- 288 Nguyen, N. L. T. *et al.* Separate and shared sympathetic outflow to white and brown fat coordinately regulates thermoregulation and beige adipocyte recruitment. *American Journal of Physiology-Regulatory, Integrative and Comparative Physiology* **312**, R132-R145, doi:10.1152/ajpregu.00344.2016 (2017).
- 289 Baboota, R. K. *et al.* Capsaicin induces "brite" phenotype in differentiating 3T3-L1 preadipocytes. *PLoS One* **9**, e103093, doi:10.1371/journal.pone.0103093 (2014).

- 290 Youngstrom, T. G. & Bartness, T. J. White adipose tissue sympathetic nervous system denervation increases fat pad mass and fat cell number. *American Journal of Physiology-Regulatory, Integrative and Comparative Physiology* **275**, R1488-R1493, doi:10.1152/ajpregu.1998.275.5.R1488 (1998).
- 291 Makwana, K. *et al.* Sensory neurons expressing calcitonin gene-related peptide α regulate adaptive thermogenesis and diet-induced obesity. *Molecular Metabolism* **45**, 101161, doi:https://doi.org/10.1016/j.molmet.2021.101161 (2021).
- 292 Ioannidou, A., Fisher, R. M. & Hagberg, C. E. The multifaceted roles of the adipose tissue vasculature. *Obesity Reviews* **23**, e13403, doi:https://doi.org/10.1111/obr.13403 (2022).
- 293 Krüger-Genge, A., Blocki, A., Franke, R.-P. & Jung, F. Vascular endothelial cell biology: an update. *International journal of molecular sciences* **20**, 4411 (2019).
- 294 Luff, S. E., Young, S. B. & McLachlan, E. M. Ultrastructure of substance P-immunoreactive terminals and their relation to vascular smooth muscle cells of rat small mesenteric arteries. *Journal of comparative neurology* **416**, 277-290 (2000).
- 295 Foster, D. O. & Frydman, M. L. Nonshivering thermogenesis in the rat. II. Measurements of blood flow with microspheres point to brown adipose tissue as the dominant site of the calorogenesis induced by noradrenaline. *Canadian Journal of Physiology and Pharmacology* **56**, 110-122, doi:10.1139/y78-015 %M 638848 (1978).
- 296 Rothwell, N. J. & Stock, M. J. Influence of noradrenaline on blood flow to brown adipose tissue in rats exhibiting diet-induced thermogenesis. *Pflugers Archiv: European journal of physiology* **389**, 237-242 (1981).
- 297 Rosell, S., Axelrod, J. & Kopin, I. J. Release of tritiated epinephrine following sympathetic nerve stimulation. *Nature* **201**, 301-301 (1964).
- 298 Zukowska-Grojec, Z. *et al.* Neuropeptide Y. *Circulation Research* **83**, 187-195, doi:doi:10.1161/01.RES.83.2.187 (1998).
- 299 Movafagh, S. *et al.* Neuropeptide Y induces migration, proliferation, and tube formation of endothelial cells bimodally via Y1, Y2, and Y5 receptorsNeuropeptide Y induces migration, proliferation, and tube formation of endothelial cells bimodally via Y1, Y2, and Y5 receptors. *The FASEB Journal* **20**, 1924-1926, doi:https://doi.org/10.1096/fj.05-4770fje (2006).
- 300 Sun, K. *et al.* Dichotomous effects of VEGF-A on adipose tissue dysfunction. *Proceedings of the national academy of sciences* **109**, 5874-5879 (2012).
- 301 Paavonsalo, S., Hariharan, S., Lackman, M. H. & Karaman, S. Capillary Rarefaction in Obesity and Metabolic Diseases—Organ-Specificity and Possible Mechanisms. *Cells* **9**, 2683 (2020).
- 302 Smith, G. I., Mittendorfer, B. & Klein, S. Metabolically healthy obesity: facts and fantasies. *J Clin Invest* **129**, 3978-3989, doi:10.1172/jci129186 (2019).
- 303 Knowles, R. G. & Moncada, S. Nitric oxide synthases in mammals. *Biochemical Journal* **298**, 249-258, doi:10.1042/bj2980249 (1994).
- 304 Nisoli, E., Tonello, C., Briscini, L. & Carruba, M. O. Inducible Nitric Oxide Synthase in Rat Brown Adipocytes: Implications for Blood Flow to Brown Adipose Tissue*. *Endocrinology* **138**, 676-682, doi:10.1210/endo.138.2.4956 (1997).
- 305 Kikuchi-Utsumi, K. *et al.* Enhanced gene expression of endothelial nitric oxide synthase in brown adipose tissue during cold exposure. *Am J Physiol Regul Integr Comp Physiol* **282**, R623-626, doi:10.1152/ajpregu.00310.2001 (2002).

- 306 Baron, D. M. *et al.* In vivo noninvasive characterization of brown adipose tissue blood flow by contrast ultrasound in mice. *Circ Cardiovasc Imaging* **5**, 652-659, doi:10.1161/circimaging.112.975607 (2012).
- 307 Derry, D. M., Schönbaum, E. & Steiner, G. Two sympathetic nerve supplies to brown adipose tissue of the rat. *Can J Physiol Pharmacol* **47**, 57-63, doi:10.1139/y69-010 (1969).
- 308 Neri, D., Ramos-Lobo, A. M., Lee, S., Lafond, A. & Zeltser, L. M. Rearing mice at 22°C programs increased capacity to respond to chronic exposure to cold but not high fat diet. *Mol Metab* **73**, 101740, doi:10.1016/j.molmet.2023.101740 (2023).
- 309 Lodhi, I. J. & Semenkovich, C. F. Why we should put clothes on mice. *Cell metabolism* **9**, 111-112 (2009).
- 310 Overton, J. M. Phenotyping small animals as models for the human metabolic syndrome: thermoneutrality matters. *International journal of obesity* **34**, S53-S58 (2010).
- 311 Cannon, B. & Nedergaard, J. Nonshivering thermogenesis and its adequate measurement in metabolic studies. *Journal of Experimental Biology* **214**, 242-253 (2011).
- 312 Karp, C. L. Unstressing intemperate models: how cold stress undermines mouse modeling. *The Journal of experimental medicine* **209**, 1069 (2012).
- 313 Symonds, M. E. Brown adipose tissue growth and development. *Scientifica* **2013**, 305763 (2013).
- 314 Zeltser, L. M. Developmental influences on circuits programming susceptibility to obesity. *Frontiers in neuroendocrinology* **39**, 17-27 (2015).
- 315 Symonds, M. E. *et al.* Brown adipose tissue development and function and its impact on reproduction. *Journal of Endocrinology* **238**, R53-R62 (2018).
- 316 Glass, L., Silverman, W. A. & Sinclair, J. C. Effect of the thermal environment on cold resistance and growth of small infants after the first week of life. *Pediatrics* **41**, 1033-1046 (1968).
- 317 Symonds, M. *et al.* Effect of rearing temperature on perirenal adipose tissue development and thermoregulation following methimazole treatment of postnatal lambs. *Experimental Physiology: Translation and Integration* **81**, 995-1006 (1996).
- 318 Cooper, K., Ferguson, A. & Veale, W. Modification of thermoregulatory responses in rabbits reared at elevated environmental temperatures. *The Journal of Physiology* **303**, 165-172 (1980).
- 319 Doi, K. & KUROSHIMA, A. Lasting effect of infantile cold experience on cold tolerance in adult rats. *The Japanese journal of physiology* **29**, 139-150 (1979).
- 320 Ferguson, A., Veale, W. & Cooper, K. Evidence of environmental influence on the development of thermoregulation in the rat. *Canadian Journal of Physiology and Pharmacology* **59**, 91-95 (1981).
- 321 Young, J. B., Weiss, J. & Boufath, N. Effects of rearing temperature on sympathoadrenal activity in young adult rats. *American Journal of Physiology-Regulatory, Integrative and Comparative Physiology* **283**, R1198-R1209 (2002).
- 322 Feldmann, H. M., Golozoubova, V., Cannon, B. & Nedergaard, J. UCP1 ablation induces obesity and abolishes diet-induced thermogenesis in mice exempt from thermal stress by living at thermoneutrality. *Cell metabolism* **9**, 203-209 (2009).
- 323 Rothwell, N. J. & Stock, M. J. A role for brown adipose tissue in diet-induced thermogenesis. *Nature* **281**, 31-35 (1979).

- 324 Din, M. U. *et al.* Postprandial oxidative metabolism of human brown fat indicates thermogenesis. *Cell metabolism* **28**, 207-216. e203 (2018).
- 325 Matsumura, S. *et al.* Voluntary corn oil ingestion increases energy expenditure and interscapular UCP1 expression through the sympathetic nerve in C57BL/6 mice. *Molecular nutrition & food research* **62**, 1800241 (2018).
- 326 Fischer, A. W., Cannon, B. & Nedergaard, J. Optimal housing temperatures for mice to mimic the thermal environment of humans: An experimental study. *Molecular Metabolism* **7**, 161-170, doi:https://doi.org/10.1016/j.molmet.2017.10.009 (2018).
- 327 Foster, D. O. & Frydman, M. L. Tissue distribution of cold-induced thermogenesis in conscious warm-or cold-acclimated rats reevaluated from changes in tissue blood flow: the dominant role of brown adipose tissue in the replacement of shivering by nonshivering thermogenesis. *Canadian journal of physiology and pharmacology* **57**, 257-270 (1979).
- 328 Bukowiecki, L., Collet, A., Follea, N., Guay, G. & Jahjah, L. Brown adipose tissue hyperplasia: a fundamental mechanism of adaptation to cold and hyperphagia. *American Journal of Physiology-Endocrinology and Metabolism* **242**, E353-E359 (1982).
- 329 Himms-Hagen, J. Brown adipose tissue metabolism and thermogenesis. *Annual review of nutrition* **5**, 69-94 (1985).
- 330 Jacobsson, A., Muhleisen, M., Cannon, B. & Nedergaard, J. The uncoupling protein thermogenin during acclimation: indications for pretranslational control. *American Journal of Physiology-Regulatory, Integrative and Comparative Physiology* **267**, R999-R1007 (1994).
- 331 Sellers, E., Scott, J. & Thomas, N. Electrical activity of skeletal muscle of normal and acclimatized rats on exposure to cold. *American Journal of Physiology-Legacy Content* **177**, 372-376 (1954).
- 332 Hart, J., Heroux, O. & Depocas, F. Cold acclimation and the electromyogram of unanesthetized rats. *Journal of applied physiology* **9**, 404-408 (1956).
- 333 Griggio, M. A. The participation of shivering and nonshivering thermogenesis in warm and cold-acclimated rats. *Comparative Biochemistry and physiology. A, Comparative Physiology* **73**, 481-484 (1982).
- 334 Piñol, R. A. *et al.* Preoptic BRS3 neurons increase body temperature and heart rate via multiple pathways. *Cell metabolism* **33**, 1389-1403. e1386 (2021).
- 335 Barbatelli, G. *et al.* The emergence of cold-induced brown adipocytes in mouse white fat depots is determined predominantly by white to brown adipocyte transdifferentiation. *American Journal of Physiology-Endocrinology and Metabolism* **298**, E1244-E1253 (2010).
- 336 Lee, Y.-H., Petkova, A. P., Konkar, A. A. & Granneman, J. G. Cellular origins of cold-induced brown adipocytes in adult mice. *The FASEB Journal* **29**, 286 (2015).
- 337 Song, A. *et al.* Low-and high-thermogenic brown adipocyte subpopulations coexist in murine adipose tissue. *The Journal of clinical investigation* **130**, 247-257 (2020).
- 338 Xue, Y. *et al.* Hypoxia-independent angiogenesis in adipose tissues during cold acclimation. *Cell metabolism* **9**, 99-109 (2009).
- 339 Ashwell, M. & Dunnett, S. B. Fluorescent histochemical demonstration of catecholamines in brown adipose tissue from obese (ob/ob) and lean mice acclimated at different temperatures. *Journal of the autonomic nervous system* **14**, 377-386 (1985).

- 340 Cao, Y., Wang, H. & Zeng, W. Whole-tissue 3D imaging reveals intra-adipose
sympathetic plasticity regulated by NGF-TrkA signal in cold-induced beiging. *Protein &
cell* **9**, 527-539 (2018).
- 341 Luo, X. *et al.* Cold exposure differentially stimulates angiogenesis in BAT and WAT of
mice: implication in adrenergic activation. *Cellular Physiology and Biochemistry* **42**,
974-986 (2017).
- 342 Roberts, S. B. & Coward, W. Effect of ambient temperature on the energy requirements
of the lactating rat. *The Journal of nutrition* **115**, 980-985 (1985).
- 343 Taylor, P. Oxygen consumption in new-born rats. *The Journal of Physiology* **154**, 153
(1960).
- 344 SCHOLANDER, P. F., HOCK, R., WALTERS, V. & IRVING, L. ADAPTATION TO
COLD IN ARCTIC AND TROPICAL MAMMALS AND BIRDS IN RELATION TO
BODY TEMPERATURE, INSULATION, AND BASAL METABOLIC RATE. *The
Biological Bulletin* **99**, 259-271, doi:10.2307/1538742 (1950).
- 345 Riek, A. & Geiser, F. Allometry of thermal variables in mammals: consequences of body
size and phylogeny. *Biological Reviews* **88**, 564-572,
doi:https://doi.org/10.1111/brv.12016 (2013).
- 346 Škop, V., Xiao, C., Liu, N., Gavrilova, O. & Reitman, M. L. The effects of housing
density on mouse thermal physiology depend on sex and ambient temperature. *Molecular
Metabolism* **53**, 101332, doi:https://doi.org/10.1016/j.molmet.2021.101332 (2021).
- 347 Trayhurn, P. & James, W. P. Thermoregulation and non-shivering thermogenesis in the
genetically obese (ob/ob) mouse. *Pflugers Archiv : European journal of physiology* **373**,
189-193, doi:10.1007/bf00584859 (1978).
- 348 R: A language and environment for statistical computing (R Foundation for Statistical
Computing, Vienna, Austria, 2023).
- 349 Bates, D., Mächler, M., Bolker, B. & Walker, S. Fitting Linear Mixed-Effects Models
Using lme4. *Journal of Statistical Software* **67**, 1 - 48, doi:10.18637/jss.v067.i01 (2015).
- 350 Kuznetsova, A., Brockhoff, P. B. & Christensen, R. H. B. lmerTest Package: Tests in
Linear Mixed Effects Models. *Journal of Statistical Software* **82**, 1 - 26,
doi:10.18637/jss.v082.i13 (2017).
- 351 Hothorn, T., Bretz, F. & Westfall, P. Simultaneous Inference in General Parametric
Models. *Biometrical Journal* **50**, 346-363, doi:https://doi.org/10.1002/bimj.200810425
(2008).
- 352 Abreu-Vieira, G., Xiao, C., Gavrilova, O. & Reitman, M. L. Integration of body
temperature into the analysis of energy expenditure in the mouse. *Molecular Metabolism*
4, 461-470, doi:https://doi.org/10.1016/j.molmet.2015.03.001 (2015).
- 353 Trumbo, P., Schlicker, S., Yates, A. A. & Poos, M. Dietary reference intakes for energy,
carbohydrate, fiber, fat, fatty acids, cholesterol, protein and amino acids. (Commentary).
Journal of the American Dietetic Association **102**, 1621+ (2002).
- 354 Tschöp, M. H. *et al.* A guide to analysis of mouse energy metabolism. *Nature Methods* **9**,
57-63, doi:10.1038/nmeth.1806 (2012).
- 355 Mina, A. I. *et al.* CalR: A Web-Based Analysis Tool for Indirect Calorimetry
Experiments. *Cell Metabolism* **28**, 656-666.e651, doi:10.1016/j.cmet.2018.06.019 (2018).
- 356 Stehling, O., Doring, H., Ertl, J., Preibisch, G. & Schmidt, I. Leptin reduces juvenile fat
stores by altering the circadian cycle of energy expenditure. *American Journal of*

- Physiology-Regulatory, Integrative and Comparative Physiology* **271**, R1770-R1774, doi:10.1152/ajpregu.1996.271.6.R1770 (1996).
- 357 Gavrilova, O. *et al.* Torpor in mice is induced by both leptin-dependent and -independent mechanisms. *Proceedings of the National Academy of Sciences* **96**, 14623-14628, doi:10.1073/pnas.96.25.14623 (1999).
- 358 Geiser, F. Metabolic Rate and Body Temperature Reduction During Hibernation and Daily Torpor. *Annual Review of Physiology* **66**, 239-274, doi:https://doi.org/10.1146/annurev.physiol.66.032102.115105 (2004).
- 359 Chong, A. C. N., Greendyk, R. A. & Zeltser, L. M. Distinct Networks of Leptin- and Insulin-Sensing Neurons Regulate Thermogenic Responses to Nutritional and Cold Challenges. *Diabetes* **64**, 137-146, doi:10.2337/db14-0567 (2014).
- 360 Fernández-Verdejo, R., Ravussin, E., Speakman, J. R. & Galgani, J. E. Progress and challenges in analyzing rodent energy expenditure. *Nature Methods* **16**, 797-799, doi:10.1038/s41592-019-0513-9 (2019).
- 361 Corrigan, J. K. *et al.* A big-data approach to understanding metabolic rate and response to obesity in laboratory mice. *eLife* **9**, e53560, doi:10.7554/eLife.53560 (2020).
- 362 Goldgof, M. *et al.* The Chemical Uncoupler 2,4-Dinitrophenol (DNP) Protects against Diet-induced Obesity and Improves Energy Homeostasis in Mice at Thermoneutrality *. *Journal of Biological Chemistry* **289**, 19341-19350, doi:10.1074/jbc.M114.568204 (2014).
- 363 Hoevenaars, F. P. M. *et al.* Thermoneutrality results in prominent diet-induced body weight differences in C57BL/6J mice, not paralleled by diet-induced metabolic differences. *Molecular Nutrition & Food Research* **58**, 799-807, doi:https://doi.org/10.1002/mnfr.201300285 (2014).
- 364 Zhao, Z. *et al.* Effects of ambient temperatures between 5 and 35 °C on energy balance, body mass and body composition in mice. *Molecular Metabolism* **64**, 101551, doi:https://doi.org/10.1016/j.molmet.2022.101551 (2022).
- 365 Carey, A. L. *et al.* Ephedrine activates brown adipose tissue in lean but not obese humans. *Diabetologia* **56**, 147-155, doi:10.1007/s00125-012-2748-1 (2013).
- 366 Zhao, Z.-J., Chi, Q.-S., Cao, J. & Han, Y.-D. The energy budget, thermogenic capacity and behavior in Swiss mice exposed to a consecutive decrease in temperatures. *Journal of Experimental Biology* **213**, 3988-3997, doi:10.1242/jeb.046821 (2010).
- 367 Virtue, S., Even, P. & Vidal-Puig, A. Below Thermoneutrality, Changes in Activity Do Not Drive Changes in Total Daily Energy Expenditure between Groups of Mice. *Cell Metabolism* **16**, 665-671, doi:10.1016/j.cmet.2012.10.008 (2012).
- 368 Hogan, S. & Himms-Hagen, J. Abnormal brown adipose tissue in genetically obese mice (ob/ob): effect of thyroxine. *American Journal of Physiology-Endocrinology and Metabolism* **241**, E436-E443, doi:10.1152/ajpendo.1981.241.6.E436 (1981).
- 369 Wilson, S., Arch, J. R. S. & Thurlby, P. L. Genetically obese C57BL/6 ob/ob mice respond normally to sympathomimetic compounds. *Life Sciences* **35**, 1301-1309, doi:https://doi.org/10.1016/0024-3205(84)90102-4 (1984).
- 370 Schmidt, I., Stahl, J., Kaul, R. & Carlisle, H. J. Cold-rearing normalized capacity for norepinephrine-stimulated thermogenesis but not body temperature in 16-day-old fatty Zucker rats. *Life Sciences* **38**, 129-136, doi:https://doi.org/10.1016/0024-3205(86)90004-4 (1986).

- 371 SEYDOUX, J., ASSIMACOPOULOS-JEANNET, F., JEANRENAUD, B. &
GIRARDIER, L. Alterations of Brown Adipose Tissue in Genetically Obese (ob/ob)
Mice. I. Demonstration of Loss of Metabolic Response to Nerve Stimulation and
Catecholamines and Its Partial Recovery after Fasting or Cold Adaptation*.
Endocrinology **110**, 432-438, doi:10.1210/endo-110-2-432 (1982).
- 372 Rothwell, N. J., Saville, M. E. & Stock, M. J. Factors influencing the acute effect of food
on oxygen consumption in the rat. *International journal of obesity* **6**, 53-59 (1982).
- 373 von Essen, G., Lindsund, E., Cannon, B. & Nedergaard, J. Adaptive facultative diet-
induced thermogenesis in wild-type but not in UCP1-ablated mice. *American Journal of
Physiology-Endocrinology and Metabolism* **313**, E515-E527,
doi:10.1152/ajpendo.00097.2017 (2017).
- 374 Young, J. B. & Shimano, Y. Effects of rearing temperature on body weight and
abdominal fat in male and female rats. *American Journal of Physiology-Regulatory,
Integrative and Comparative Physiology* **274**, R398-R405,
doi:10.1152/ajpregu.1998.274.2.R398 (1998).
- 375 Gordon, C. J. Thermal biology of the laboratory rat. *Physiology & Behavior* **47**, 963-991,
doi:https://doi.org/10.1016/0031-9384(90)90025-Y (1990).
- 376 Keijer, J., Li, M. & Speakman, J. R. What is the best housing temperature to translate
mouse experiments to humans? *Molecular Metabolism* **25**, 168-176,
doi:https://doi.org/10.1016/j.molmet.2019.04.001 (2019).
- 377 Król, E. & Speakman, J. R. Limits to sustained energy intake VII. Milk energy output in
laboratory mice at thermoneutrality. *Journal of Experimental Biology* **206**, 4267-4281,
doi:10.1242/jeb.00675 (2003).
- 378 Zhao, Z.-J. *et al.* Limits to sustained energy intake XXV: milk energy output and
thermogenesis in Swiss mice lactating at thermoneutrality. *Scientific Reports* **6**, 31626,
doi:10.1038/srep31626 (2016).
- 379 Leon, M., Croskerry, P. G. & Smith, G. K. Thermal control of mother-young contact in
rats. *Physiology & Behavior* **21**, 793-811, doi:https://doi.org/10.1016/0031-
9384(78)90021-5 (1978).
- 380 Klaus, S., Münzberg, H., Trüloff, C. & Heldmaier, G. Physiology of transgenic mice with
brown fat ablation: obesity is due to lowered body temperature. *American Journal of
Physiology-Regulatory, Integrative and Comparative Physiology* **274**, R287-R293,
doi:10.1152/ajpregu.1998.274.2.R287 (1998).
- 381 Meyer, C. W. E., Klingenspor, M., Rozman, J. & Heldmaier, G. Gene or Size: Metabolic
Rate and Body Temperature in Obese Growth Hormone-Deficient Dwarf Mice. *Obesity
Research* **12**, 1509-1518, doi:https://doi.org/10.1038/oby.2004.188 (2004).
- 382 Zhao, Z.-J. *et al.* Late lactation in small mammals is a critically sensitive window of
vulnerability to elevated ambient temperature. *Proceedings of the National Academy of
Sciences* **117**, 24352-24358, doi:doi:10.1073/pnas.2008974117 (2020).
- 383 Orava, J. *et al.* Blunted metabolic responses to cold and insulin stimulation in brown
adipose tissue of obese humans. *Obesity* **21**, 2279-2287,
doi:https://doi.org/10.1002/oby.20456 (2013).
- 384 Chondronikola, M. *et al.* Brown Adipose Tissue Activation Is Linked to Distinct
Systemic Effects on Lipid Metabolism in Humans. *Cell Metabolism* **23**, 1200-1206,
doi:10.1016/j.cmet.2016.04.029 (2016).

- 385 Bal, N. C. *et al.* Sarcolipin is a newly identified regulator of muscle-based thermogenesis in mammals. *Nat Med* **18**, 1575-1579, doi:10.1038/nm.2897 (2012).
- 386 Heine, M. *et al.* Lipolysis Triggers a Systemic Insulin Response Essential for Efficient Energy Replenishment of Activated Brown Adipose Tissue in Mice. *Cell Metab* **28**, 644-655.e644, doi:10.1016/j.cmet.2018.06.020 (2018).
- 387 Ernande, L. *et al.* Relationship of brown adipose tissue perfusion and function: a study through β 2-adrenoreceptor stimulation. *J Appl Physiol (1985)* **120**, 825-832, doi:10.1152/jappphysiol.00634.2015 (2016).
- 388 Flaim, K. E., Horwitz, B. A. & Horowitz, J. M. Coupling of signals to brown fat: alpha- and beta-adrenergic responses in intact rats. *Am J Physiol* **232**, R101-109, doi:10.1152/ajpregu.1977.232.3.R101 (1977).
- 389 Li, Y. *et al.* Secretin-Activated Brown Fat Mediates Prandial Thermogenesis to Induce Satiating. *Cell* **175**, 1561-1574.e1512, doi:10.1016/j.cell.2018.10.016 (2018).
- 390 Zethof, T. J. J., Van Der Heyden, J. A. M., Tolboom, J. T. B. M. & Olivier, B. Stress-induced hyperthermia in mice: A methodological study. *Physiology & Behavior* **55**, 109-115, doi:https://doi.org/10.1016/0031-9384(94)90017-5 (1994).
- 391 Kordić, M., Dugandžić, J., Ratko, M., Habek, N. & Dugandžić, A. Infrared Thermography for the Detection of Changes in Brown Adipose Tissue Activity. *JoVE*, e64463, doi:doi:10.3791/64463 (2022).
- 392 Clement, J. G., Mills, P. & Brockway, B. Use of telemetry to record body temperature and activity in mice. *Journal of Pharmacological Methods* **21**, 129-140, doi:https://doi.org/10.1016/0160-5402(89)90031-4 (1989).
- 393 Garside, J. C., Livingston, E. W., Frank, J. E., Yuan, H. & Branca, R. T. In vivo imaging of brown adipose tissue vasculature reactivity during adrenergic stimulation of non-shivering thermogenesis in mice. *Sci Rep* **12**, 21383, doi:10.1038/s41598-022-25819-6 (2022).
- 394 Sabater, D. *et al.* Cafeteria diet induce changes in blood flow that are more related with heat dissipation than energy accretion. *PeerJ* **4**, e2302, doi:10.7717/peerj.2302 (2016).
- 395 Oh, S. S. & Narver, H. L. Mouse and Rat Anesthesia and Analgesia. *Current Protocols* **4**, e995, doi:https://doi.org/10.1002/cpz1.995 (2024).
- 396 Wang, H.-Y., Eguchi, K., Yamashita, T. & Takahashi, T. Frequency-Dependent Block of Excitatory Neurotransmission by Isoflurane via Dual Presynaptic Mechanisms. *The Journal of Neuroscience* **40**, 4103-4115, doi:10.1523/jneurosci.2946-19.2020 (2020).
- 397 Boban, N. *et al.* Direct comparative effects of isoflurane and desflurane on sympathetic ganglionic transmission. *Anesth Analg* **80**, 127-134, doi:10.1097/00000539-199501000-00022 (1995).
- 398 Buitrago, S., Martin, T. E., Tetens-Woodring, J., Belicha-Villanueva, A. & Wilding, G. E. Safety and efficacy of various combinations of injectable anesthetics in BALB/c mice. *J Am Assoc Lab Anim Sci* **47**, 11-17 (2008).
- 399 Sinner, B. & Graf, B. M. Ketamine. *Handb Exp Pharmacol*, 313-333, doi:10.1007/978-3-540-74806-9_15 (2008).
- 400 Lee, J. S., Morrow, D., Andresen, M. C. & Chang, K. S. Isoflurane depresses baroreflex control of heart rate in decerebrate rats. *Anesthesiology* **96**, 1214-1222, doi:10.1097/00000542-200205000-00026 (2002).

- 401 Meyer, R. E. & Fish, R. E. A review of tribromoethanol anesthesia for production of
genetically engineered mice and rats. *Lab Animal* **34**, 47-52, doi:10.1038/labani1105-47
(2005).
- 402 Bachman, E. S. *et al.* β AR signaling required for diet-induced thermogenesis and obesity
resistance. *Science* **297**, 843-845 (2002).
- 403 Evans, B. A., Merlin, J., Bengtsson, T. & Hutchinson, D. S. Adrenoceptors in white,
brown, and brite adipocytes. *British Journal of Pharmacology* **176**, 2416-2432,
doi:https://doi.org/10.1111/bph.14631 (2019).
- 404 Cannon, B. *et al.* 'Neuropeptide tyrosine' (NPY) is co-stored with noradrenaline in
vascular but not in parenchymal sympathetic nerves of brown adipose tissue. *Exp Cell
Res* **164**, 546-550, doi:10.1016/0014-4827(86)90052-2 (1986).
- 405 Lundberg, J. M. *et al.* Neuropeptide Y (NPY)-like immunoreactivity in peripheral
noradrenergic neurons and effects of NPY on sympathetic function. *Acta Physiol Scand*
116, 477-480, doi:10.1111/j.1748-1716.1982.tb07171.x (1982).
- 406 Pernow, J., Ohlén, A., Hökfelt, T., Nilsson, O. & Lundberg, J. M. Neuropeptide Y:
presence in perivascular noradrenergic neurons and vasoconstrictor effects on skeletal
muscle blood vessels in experimental animals and man. *Regul Pept* **19**, 313-324,
doi:10.1016/0167-0115(87)90173-x (1987).
- 407 Ellis, J. L. & Burnstock, G. Neuropeptide Y neuromodulation of sympathetic co-
transmission in the guinea-pig vas deferens. *British Journal of Pharmacology* **100**, 457-
462, doi:https://doi.org/10.1111/j.1476-5381.1990.tb15828.x (1990).
- 408 Tervo, D. Gowanlock R. *et al.* A Designer AAV Variant Permits Efficient Retrograde
Access to Projection Neurons. *Neuron* **92**, 372-382, doi:10.1016/j.neuron.2016.09.021
(2016).
- 409 Nagai, Y. *et al.* Deschloroclozapine, a potent and selective chemogenetic actuator enables
rapid neuronal and behavioral modulations in mice and monkeys. *Nat Neurosci* **23**, 1157-
1167, doi:10.1038/s41593-020-0661-3 (2020).
- 410 Laduron, P. & Belpaire, F. Transport of noradrenaline and dopamine-beta-hydroxylase in
sympathetic nerves. *Life Sci* **7**, 1-7, doi:10.1016/0024-3205(68)90355-x (1968).
- 411 Giordano, A., Frontini, A., Castellucci, M. & Cinti, S. Presence and distribution of
cholinergic nerves in rat mediastinal brown adipose tissue. *J Histochem Cytochem* **52**,
923-930, doi:10.1369/jhc.3A6246.2004 (2004).
- 412 Hansson, S. R., Mezey, E. & Hoffman, B. J. Ontogeny of vesicular monoamine
transporter mRNAs VMAT1 and VMAT2. II. Expression in neural crest derivatives and
their target sites in the rat. *Brain Res Dev Brain Res* **110**, 159-174, doi:10.1016/s0165-
3806(98)00103-5 (1998).
- 413 Fischer, A. W. *et al.* Lysosomal lipoprotein processing in endothelial cells stimulates
adipose tissue thermogenic adaptation. *Cell Metabolism* **33**, 547-564.e547,
doi:https://doi.org/10.1016/j.cmet.2020.12.001 (2021).
- 414 Saxena, A. *et al.* Trehalose-enhanced isolation of neuronal sub-types from adult mouse
brain. *Biotechniques* **52**, 381-385, doi:10.2144/0000113878 (2012).
- 415 Campbell, J. N. *et al.* A molecular census of arcuate hypothalamus and median eminence
cell types. *Nat Neurosci* **20**, 484-496, doi:10.1038/nn.4495 (2017).
- 416 Snyder, M. E. *et al.* Generation and persistence of human tissue-resident memory T cells
in lung transplantation. *Sci Immunol* **4**, doi:10.1126/sciimmunol.aav5581 (2019).

- 417 Dobin, A. *et al.* STAR: ultrafast universal RNA-seq aligner. *Bioinformatics* **29**, 15-21,
doi:10.1093/bioinformatics/bts635 (2013).
- 418 Liao, Y., Smyth, G. K. & Shi, W. featureCounts: an efficient general purpose program for
assigning sequence reads to genomic features. *Bioinformatics* **30**, 923-930,
doi:10.1093/bioinformatics/btt656 (2014).
- 419 Smith, T., Heger, A. & Sudbery, I. UMI-tools: modeling sequencing errors in Unique
Molecular Identifiers to improve quantification accuracy. *Genome Res* **27**, 491-499,
doi:10.1101/gr.209601.116 (2017).
- 420 Stuart, T. *et al.* Comprehensive Integration of Single-Cell Data. *Cell* **177**, 1888-
1902.e1821, doi:10.1016/j.cell.2019.05.031 (2019).
- 421 Bai, L. *et al.* Genetic Identification of Vagal Sensory Neurons That Control Feeding. *Cell*
179, 1129-1143 e1123, doi:10.1016/j.cell.2019.10.031 (2019).
- 422 Zappia, L. & Oshlack, A. Clustering trees: a visualization for evaluating clusterings at
multiple resolutions. *Gigascience* **7**, doi:10.1093/gigascience/giy083 (2018).
- 423 Korsunsky, I. *et al.* Fast, sensitive and accurate integration of single-cell data with
Harmony. *Nat Methods* **16**, 1289-1296, doi:10.1038/s41592-019-0619-0 (2019).
- 424 Schneider, C. A., Rasband, W. S. & Eliceiri, K. W. NIH Image to ImageJ: 25 years of
image analysis. *Nature Methods* **9**, 671-675, doi:10.1038/nmeth.2089 (2012).
- 425 van den Pol, A. N. *et al.* Neuromedin B and gastrin-releasing peptide excite arcuate
nucleus neuropeptide Y neurons in a novel transgenic mouse expressing strong Renilla
green fluorescent protein in NPY neurons. *J Neurosci* **29**, 4622-4639,
doi:10.1523/JNEUROSCI.3249-08.2009 (2009).
- 426 Jendryka, M. *et al.* Pharmacokinetic and pharmacodynamic actions of clozapine-N-oxide,
clozapine, and compound 21 in DREADD-based chemogenetics in mice. *Scientific
Reports* **9**, 4522, doi:10.1038/s41598-019-41088-2 (2019).
- 427 Zhang, Z. *et al.* Spinal projecting neurons in rostral ventromedial medulla co-regulate
motor and sympathetic tone. *Cell* **187**, 3427-3444.e3421, doi:10.1016/j.cell.2024.04.022
(2024).
- 428 Lavoie, A. & Liu, B.-h. Canine Adenovirus 2: A Natural Choice for Brain Circuit
Dissection. *Frontiers in Molecular Neuroscience* **13**, doi:10.3389/fnmol.2020.00009
(2020).
- 429 del Rio, D. *et al.* CAV-2 Vector Development and Gene Transfer in the Central and
Peripheral Nervous Systems. *Frontiers in Molecular Neuroscience* **12**,
doi:10.3389/fnmol.2019.00071 (2019).
- 430 Morton, G. J. *et al.* Evidence That the Sympathetic Nervous System Elicits Rapid,
Coordinated, and Reciprocal Adjustments of Insulin Secretion and Insulin Sensitivity
During Cold Exposure. *Diabetes* **66**, 823-834, doi:10.2337/db16-1351 (2017).
- 431 DeFronzo, R. A., Tobin, J. D. & Andres, R. Glucose clamp technique: a method for
quantifying insulin secretion and resistance. *Am J Physiol* **237**, E214-223,
doi:10.1152/ajpendo.1979.237.3.E214 (1979).
- 432 Ayala, J. E. *et al.* Hyperinsulinemic-euglycemic clamps in conscious, unrestrained mice.
J Vis Exp, doi:10.3791/3188 (2011).
- 433 Sheth, R., Josephson, L. & Mahmood, U. Evaluation and clinically relevant applications
of a fluorescent imaging analog to fluorodeoxyglucose positron emission tomography.
Journal of Biomedical Optics **14**, 064014 (2009).

- 434 Yang, C. F. *et al.* Sexually Dimorphic Neurons in the Ventromedial Hypothalamus Govern Mating in Both Sexes and Aggression in Males. *Cell* **153**, 896-909, doi:10.1016/j.cell.2013.04.017 (2013).
- 435 Gray, D. C., Mahrus, S. & Wells, J. A. Activation of specific apoptotic caspases with an engineered small-molecule-activated protease. *Cell* **142**, 637-646, doi:10.1016/j.cell.2010.07.014 (2010).
- 436 Kranz, A. *et al.* An improved Flp deleter mouse in C57Bl/6 based on Flpo recombinase. *Genesis* **48**, 512-520, doi:10.1002/dvg.20641 (2010).
- 437 Anastassiadis, K. *et al.* Dre recombinase, like Cre, is a highly efficient site-specific recombinase in *E. coli*, mammalian cells and mice. *Disease Models & Mechanisms* **2**, 508-515, doi:10.1242/dmm.003087 (2009).
- 438 Han, X. *et al.* A suite of new Dre recombinase drivers markedly expands the ability to perform intersectional genetic targeting. *Cell Stem Cell* **28**, 1160-1176.e1167, doi:10.1016/j.stem.2021.01.007 (2021).
- 439 De Solis, A. J. *et al.* Reciprocal activity of AgRP and POMC neurons governs coordinated control of feeding and metabolism. *Nature Metabolism* **6**, 473-493, doi:10.1038/s42255-024-00987-z (2024).
- 440 Méndez-Barbero, N., Gutiérrez-Muñoz, C. & Blanco-Colio, L. M. Cellular Crosstalk between Endothelial and Smooth Muscle Cells in Vascular Wall Remodeling. *Int J Mol Sci* **22**, doi:10.3390/ijms22147284 (2021).
- 441 Takano, H., Dora, K. A. & Garland, C. J. Spreading vasodilatation in resistance arteries. *Journal of Smooth Muscle Research* **41**, 303-311 (2005).
- 442 Triggle, C. R. *et al.* The endothelium: influencing vascular smooth muscle in many ways. *Canadian Journal of Physiology and Pharmacology* **90**, 713-738, doi:10.1139/y2012-073 %M 22625870 (2012).
- 443 Liu, Y., Watanabe, M., Rollins, A. M. & Jenkins, M. W. in *Three-Dimensional and Multidimensional Microscopy: Image Acquisition and Processing XXV*. 104991J (SPIE).
- 444 Love, M. I., Huber, W. & Anders, S. Moderated estimation of fold change and dispersion for RNA-seq data with DESeq2. *Genome Biol* **15**, 550, doi:10.1186/s13059-014-0550-8 (2014).
- 445 Guangchuang Yu, L.-G. W., Yanyan Han, and Qing-Yu He. clusterProfiler: an R Package for Comparing Biological Themes Among Gene Clusters. *OMICS: A Journal of Integrative Biology* **16**, 284-287, doi:10.1089/omi.2011.0118 (2012).
- 446 Bay, B. *et al.* Sex differences in lipidomic and bile acid plasma profiles in patients with and without coronary artery disease. *Lipids Health Dis* **23**, 197, doi:10.1186/s12944-024-02184-z (2024).

Appendix A

Transcriptomics and lipidomics on acutely activated mice iBAT

To investigate the molecular changes induced by acute stimulation of iBAT-projecting SNS, we studied 12 Th-Cre^{+/-} mice (6 males and 6 females) that have been injected in iBAT with MaCPNS1: pAAV-CAG-DIO-hM₃D(Gq)-mCherry as described above. Mice were anesthetized with an IP injection of Avertin (350 mg/kg) and received either DCZ 200 ng/g or Saline 0.9% by IP injection, depending on the experimental condition. Mice were placed on a heating pad at 35 °C for 30 minutes before euthanasia via thoracotomy. Blood was collected via cardiac puncture into tubes containing 5 µL of EDTA 0.5M pH 8.0 and centrifuged at 5000 rpm at 4 °C for 10 minutes to obtain plasma. Mice were then transcardially perfused with 5 mL of 4 °C PBS to clear excess blood, and then iBAT and SG were harvested. Each iBAT was split along the midline in the two lobes, weighed, and snap-frozen in liquid nitrogen; one lobe was used for RNA extraction, and the other was for lipidomic analysis alongside plasma samples. SG were post-fixed, washed, and then in Limpid⁴⁴³ for imaging as previously described.

RNA analysis revealed a small but consistent set of genes upregulated or downregulated in DCZ-treated mice, controlling for sex (Fig. 26a). Gene set enrichment analysis (GSEA) indicated “cell activation” as the top enriched term (Fig. 26b), followed by terms generally consistent with increased iBAT activity. No downregulated terms were identified. Plasma lipidomics showed a significant decrease in TGs concentration in DCZ-treated animals (Fig. 27a, top). In iBAT, TGs were significantly elevated in DCZ-treated animals, but this increase was observed only in females (Fig. 27a, bottom), suggesting that iBAT clears TGs in response to DCZ as expected. To understand why only females displayed TGs enrichment in iBAT, we re-examined the bulkSeq data for sex-specific gene expression differences while controlling for treatment. Surprisingly, a long list of

genes differed between males and females (Fig. 27b). Gene ontology enrichment (GOE) analysis revealed that male mice exhibited significantly increased lipid oxidation in iBAT relative to females, independent of DCZ treatment (Fig. 27c). This inherent difference in lipid metabolism may explain why, despite similar reductions in plasma TG concentrations, DCZ-treated male iBATs do not show TG enrichment.

Methods

RNA from iBAT was extracted using Tri-Isolate RNA Pure Kit (IBI Scientific, IB47631), following the manufacturer's instructions. The RNA samples were tested for RIN by the Columbia Genome Center before sequencing. We used poly-A pull-down to enrich mRNAs from total RNA samples, then proceeded with library construction using Illumina TruSeq chemistry. The final PCR step was modified using the KAPA HiFi HotStart Ready Mix. Libraries were sequenced using Element AVITI at Columbia Genome Center. Samples were multiplexed in each lane to obtain a targeted number of paired-end 75bp reads per sample. bases2fastq version 1.4.0.833301531 was used for converting BCL to fastq format, coupled with adaptor trimming. Pseudoalignment to a kallisto index created from transcriptomes (Ensembl v96, Mouse:GRCm38.p6) was performed using kallisto (0.44.0).

Gene count matrices were analyzed on R³⁴⁸ with DESeq 2⁴⁴⁴, while gene set enrichment analysis and gene ontology over representation analysis were done with clusterProfiler⁴⁴⁵.

Lipidomics were carried out by the lab of Joerg Heeren following to a similar protocol⁴⁴⁶.

Figures

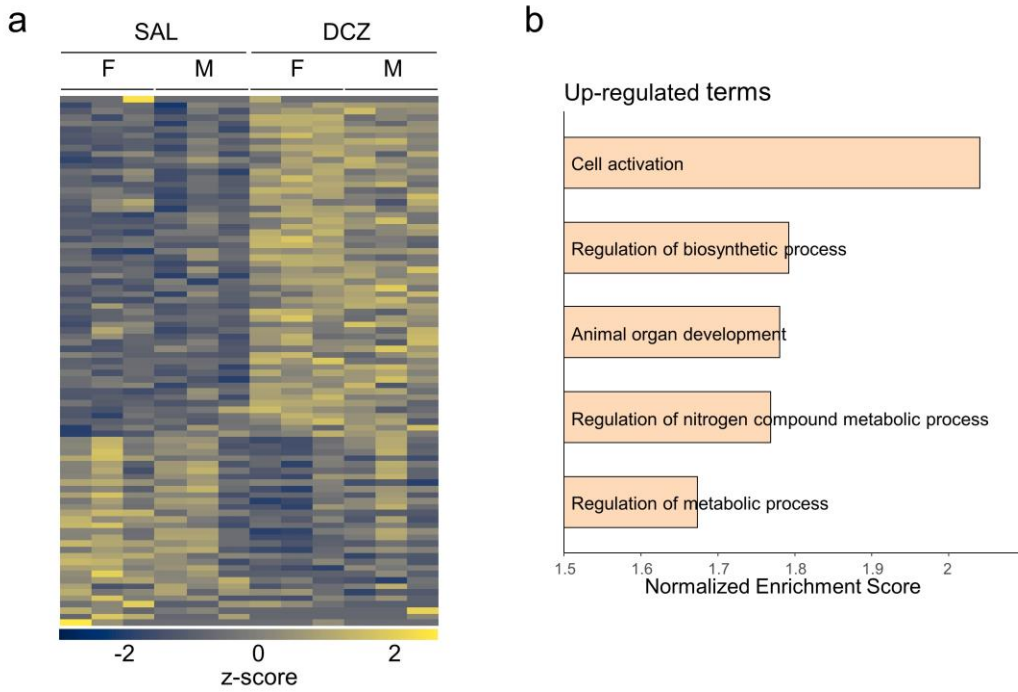


Figure 26. Transcriptomic analysis of chemogenetically activated iBAT-projecting sympathetic nerves reveals metabolic activation in iBAT

a: Heatmap of statistically significant genes between mice treated with DCZ and mice treated with Saline, while controlling for sex.

b: GSEA of the genes shown in A, selected significant terms.

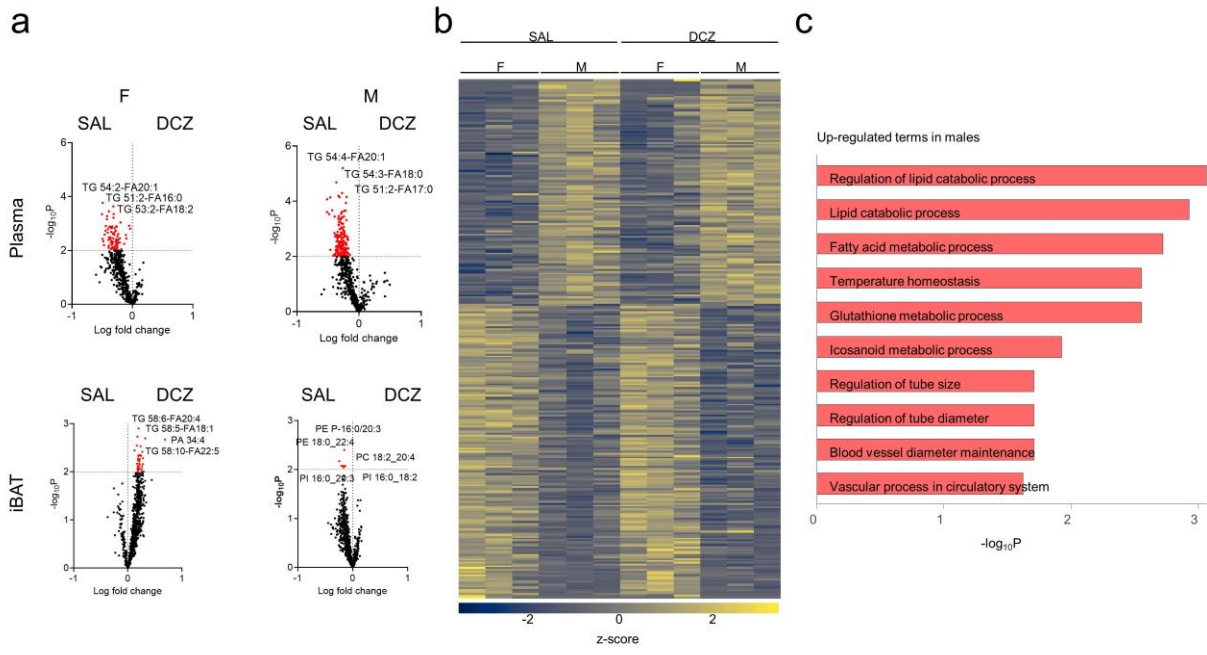


Figure 27. Lipidomics analysis suggests iBAT involvement with circulating TGs clearance and different lipid metabolism based on sex

A: Lipidomics on plasma (top) and on iBAT (bottom) in mice from Fig. 26, split by sex (females on the left, males on the right).

b: Heatmap of statistically significant genes between male and female mice, while controlling for treatment.

c: GOE of the upregulated genes for males shown in b.

Appendix B

Systemic effects of sympathetic transmitters and peptides on glucose tolerance

The sympathetic regulation of glucose homeostasis remains relative underexplored field. For instance, NPY is hypothesized to play a role in glucose regulation, its mechanisms of action are not well understood. While we have extensively discussed the role of NE in glucose homeostasis, there have been no studies investigating the acute antagonism of different ARs during a glucose test. To address this gap, we aimed to elucidate the role of the SNS on glucose regulation by testing different adrenergic and non-adrenergic receptor agonists and antagonists, along with other molecules hypothesized to modulate sympathetic activity. Ten WT mice (C57BL/6J, five males and five females) were tested with OGTTs under eight experimental and two control conditions, with a minimum of three-day interval between each test. All tests followed a balanced crossover design.

We observed reduced glycemia in mice injected with NPY (1 mg/kg, Fig. 28a), indicating a direct role of NPY in glucose regulation. Based on scRNA Seq results presented in chapter 4, we saw that vasculature-projecting neurons express follistatin (*Fst*), the receptor for secretin (*Sctr*), and *Rxfp1*, a known receptor for relaxin. As such, we tested IP injections of follistatin (100 ug/kg), relaxin (RX2, 100 ug/kg), and secretin (1.5 mg/kg). Only secretin significantly lowered blood glucose levels (Fig. 28b-d).

BIBO 3304, a selective NPY1R antagonist that cannot cross the blood-brain barrier, was tested in combination with NPY and secretin, separately, to test whether the effects of these peptides were centrally or peripherally mediated. Our results show that BIBO does not inhibit the glycemia-lowering effects of NPY (Fig. 28e), suggesting either an exclusive central mechanism

or involvement of additional NPYRs. Conversely, BIBO effectively blocked the blood glucose-lowering effects of secretin (Fig. 28f).

We then tested NE in combination with propranolol (a non-selective β ARs antagonist), phentolamine (a non-selective α ARs antagonist), and BIBO. Mice injected with NE + propranolol exhibited a substantial increase in blood glucose levels, while the combination of NE and phentolamine strongly reduced glycemia (Fig. 29a and b). Blocking β ARs reduces glucose uptake across multiple organs, including BAT, and decreases NE-induced glucagon release from pancreatic α cells. On the other hand, blocking α ARs prevents NE from reducing GSIS in the pancreas while promoting glucagon release. Could the glucose-lowering effects be solely insulin-mediated? This seems unlikely, as a selective β_3 AR agonist (CL) co-injected with BIBO produced a similar glycemic pattern as the NE + phentolamine combination (Fig. 29d), indicating a non-insulin-dependent glucose uptake in peripheral tissues due to β ARs activation. Future studies should also measure insulin plasma levels within this framework to better understand the interaction between these systems. Finally, we tested a combined injection of NE and BIBO to examine whether NPY1R blockade could modulate NE's effects on glycemia. Surprisingly, this combination led to the highest glycemic levels in mice (Fig. 29c). Moreover, we could only test this condition on four mice, since this condition resulted in a 50% mortality rate, with two of the four mice found deceased in their cages within 48 hours post-glucose test, despite exhibiting normal behavior prior to death.

Methods

Mice were transferred to clean cages without food four hours prior to testing. At the beginning of the test, baseline blood glucose levels were measured from a tail vein prick (Contour Next Ez

Blood Glucose Monitoring System, Ascensia). Mice then received an oral gavage of D-(+)-Glucose solution (2mg/kg; Sigma Aldrich G8769, diluted 1:2 in double distilled water and filtered through a 20 μ m filter) and an IP injection of one of the drug combinations. Gavage solutions were volume-matched at 9 μ L/g. Saline (Saline 0.9%), Saline + 1% DMSO (Thermo Scientific Chemicals #036480.AP), Neuropeptide Y (1 mg/kg in Saline, Hello Bio # HB2935), BIBO 3304 (1 mg/kg in Saline + 1%DMSO, Tocris #2412), Relaxin-2 (100 ug/kg in Saline, Pheonix pharmaceuticals #035-62A), Secretin (1.5 mg/kg in Saline, Tocris #1919), Follistatin (100 ug/kg in Saline, R&D Systems #769-FS-025), Norepinephrine (0.5 mg.kg in Saline, Sigma Aldrich #A9512-250MG), Propranolol (5 mg/kg in Saline, ThermoFisher Scientific #H26645.06), Phentolamine (20 mg/kg in Saline, Sigma Aldrich #P7561-100MG), and their respective combinations were volume-matched at 5 μ L/g of mouse. Blood glucose was subsequently measured at 15, 30, 45, 50, 90, and 120 minutes post-gavage and injection.

Figures

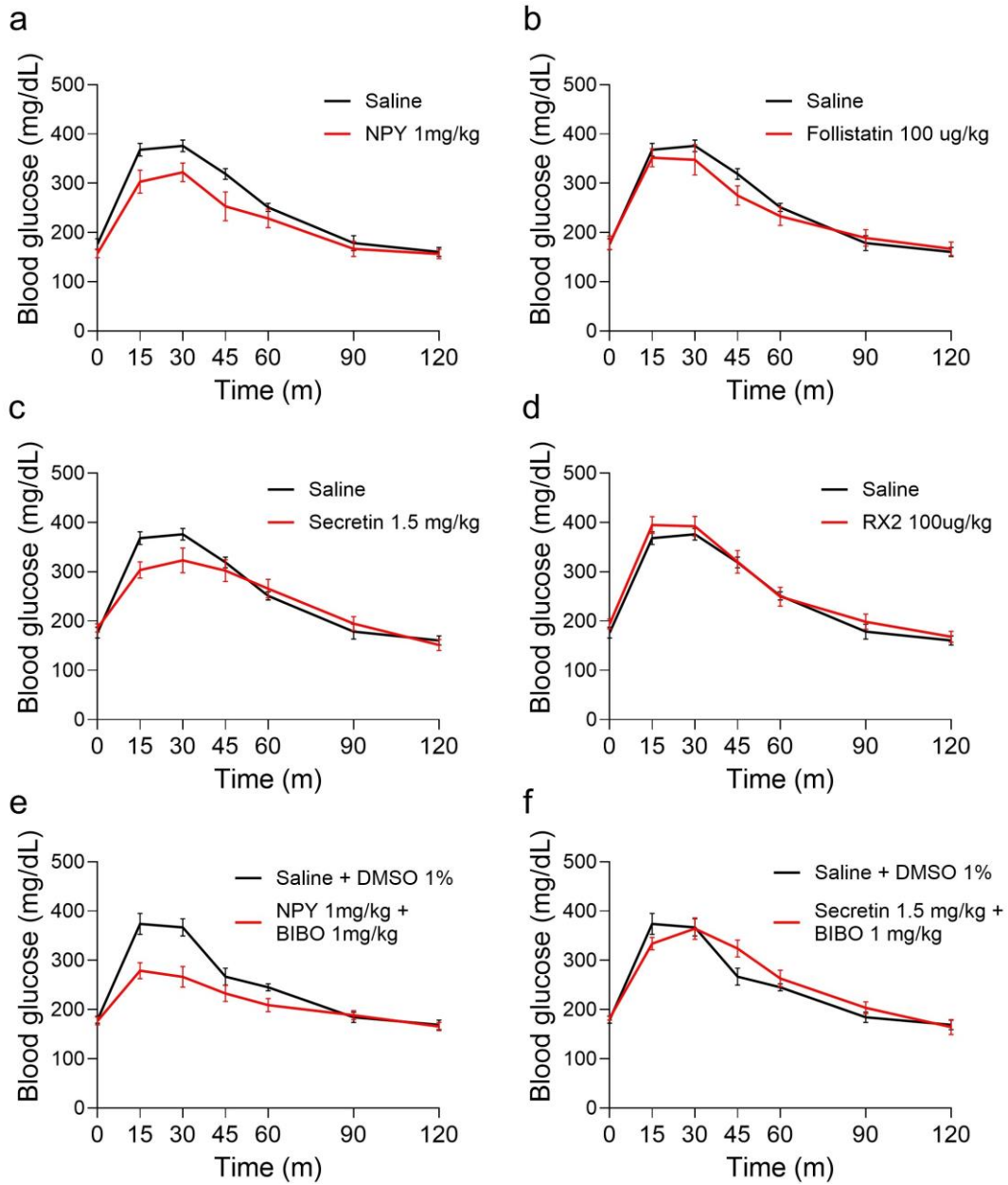


Figure 28.OGTTs on mice under stimulation of adrenergic-related peptides

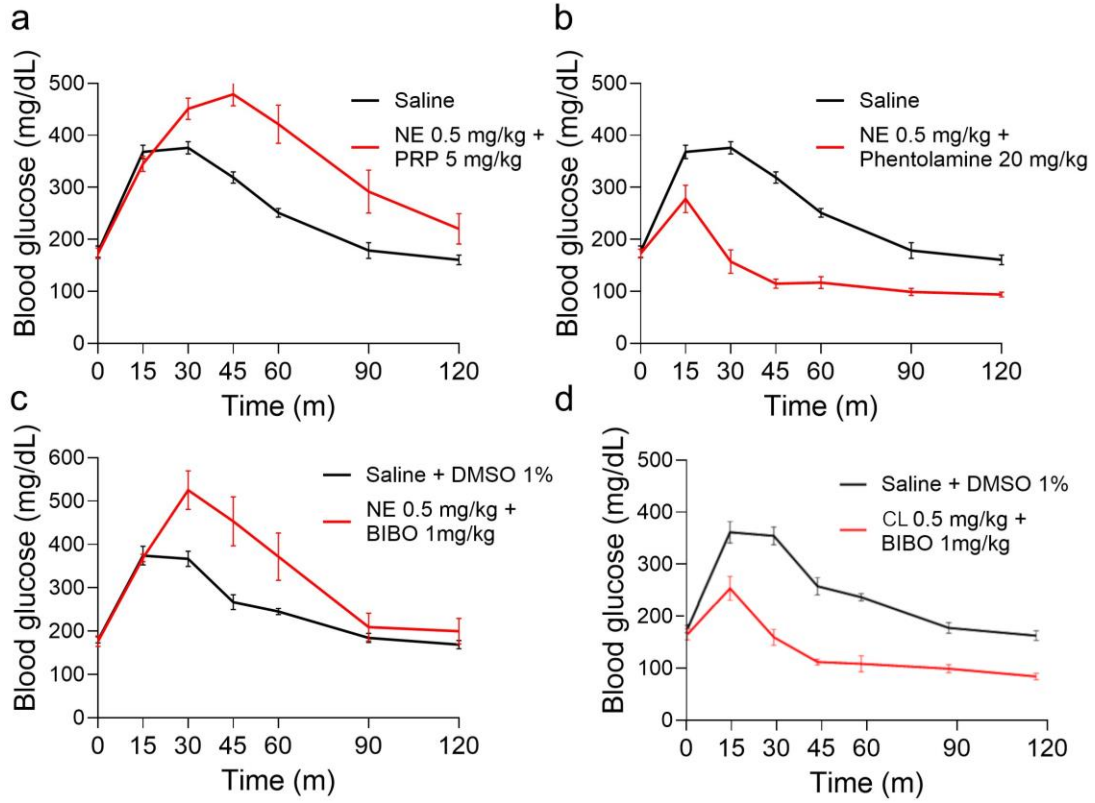


Figure 29. OGTTs using combinations of adrenergic transmitters and adrenergic-related receptor antagonists